https://doi.org/10.15388/vu.thesis.687
https://orcid.org/0000-0001-7173-7454

VILNIUS UNIVERSITY
CENTER FOR PHYSICAL SCIENCES AND TECHNOLOGY

Greta Inkrataitė

Synthesis and Characterization of Inorganic Garnet Structure Scintillators

DOCTORAL DISSERTATION

Natural Sciences,
Chemistry (N 003)

VILNIUS 2024

The dissertation was prepared between 2020 and 2024 at Vilnius University. The research was supported by Research Council of Lithuania via scholarships for academic achievements and travel grants. Additional support was received from German Academic Exchange Service and The Lithuanian Academy of Sciences for scientific works.

Academic supervisor – Prof. Dr. Ramūnas Skaudžius (Vilnius University, Natural Sciences, Chemistry, N 003)

This doctoral dissertation will be defended in a public meeting of the Dissertation Defense Panel:

Chairman – Prof. Dr. Rasa Pauliukaitė (Center for Physical Sciences and Technology, Natural Sciences, Chemistry, N 003).

Members:

Prof. Dr. Aldona Beganskienė (Vilnius University, Natural Sciences, Chemistry, N 003),

Assoc. Prof. Dr. Inga Grigoravičiūtė (Vilnius University, Natural Sciences, Chemistry, N003),

Dr. Teresė Rauckytė-Žak (Bydgoszcz University of Science and Technology, Natural Sciences, Chemistry, N 003),

Prof. Dr. Jaunius Urbonavičius (Vilnius Gediminas Technical University, Technological Sciences, Chemistry Engineering, T 005).

The dissertation shall be defended at a public meeting of the Dissertation Defence Panel at 2 p.m. on 15th November 2024 in Room Inorganics Chemistry auditorium (141 room) of the Institute of Chemistry Faculty of Chemistry and Geosciences, Vilnius University.

Address: Naugardukas street, 24, LT-03225, Vilnius, Lithuania.

Tel. +37052193105; e-mail: info@chgf.vu.lt

The text of this dissertation can be accessed at the libraries of Vilnius University and Center for Physical Sciences and Technology, as well as on the website of Vilnius University:

www.vu.lt/lt/naujienos/ivykiu-kalendorius

https://doi.org/10.15388/vu.thesis.687
https://orcid.org/0000-0001-7173-7454

VILNIAUS UNIVERSITETAS
FIZINIŲ IR TECHNOLOGIJOS MOKSLŲ CENTRAS

Greta Inkrataitė

Neorganinių granato struktūros scintiliatorių sintezė ir charakterizavimas

DAKTARO DISERTACIJA

Gamtos mokslai,
Chemija (N 003)

VILNIUS 2024

Disertacija rengta 2020–2024 metais Vilniaus universitete.
Mokslinius tyrimus rėmė Lietuvos mokslo taryba, skirdama stipendijas mokslinėms išvykoms ir už akademinius bei mokslinius pasiekimus. Papildoma parama moksliniams darbams buvo gauta iš Vokietijos akademinių mainų tarnybos ir Lietuvos mokslų akademijos.

Mokslinis vadovas – prof. dr. Ramūnas Skaudžius (Vilniaus universitetas, gamtos mokslai, chemija, N 003).

Gynimo taryba:
Pirmininkė – prof. dr. Rasa Pauliukaitė (VMTI Fizinių ir technologijos mokslų centras, gamtos mokslai, chemija N 003).
Nariai:
prof. dr. Aldona Beganskienė (Vilniaus universitetas, gamtos mokslai, chemija N 003),
doc. dr. Inga Grigoravičiūtė (Vilniaus universitetas, gamtos mokslai, chemija N 003),
dr. Teresė Rauckytė-Žak (Bydgoščiaus Jono ir Andriaus Sniadeckių technikos ir gamtos mokslų universitetas, gamtos mokslai, chemija N 003),
prof. dr. Jaunius Urbonavičius (Vilniaus Gedimino technikos universitetas, technologijos mokslai, chemijos inžinerija T 005).

Disertacija ginama viešame Gynimo tarybos posėdyje 2024 m. lapkričio mėn. 15 d. 14.00 val. Vilniaus universiteto Chemijos ir geomokslų fakulteto Chemijos instituto Neorganinės chemijos (141 aud.) auditorijoje.
Adresas: Naugarduko g. 24, LT-03225, Vilnius, Lietuva.
Tel. +37052193105; el. paštas info@chgf.vu.lt.

Disertaciją galima peržiūrėti Vilniaus universiteto ir Fizinių ir technologijos mokslų centro bibliotekose ir VU interneto svetainėje adresu:
https://www.vu.lt/naujienos/ivykiu-kalendorius

LIST OF ABBREVIATIONS

CCD – Charge-Coupled Device

CERN – The European Organization for Nuclear Research

CIE – International Commission on Illumination

CT – Computed Tomography

DAAD – German Academic Exchange Service

EQE – External Quantum Efficiency

GdAG – Gadolinium Aluminum Garnet

GdASG – Gadolinium Aluminum Scandium Garnet

ICP-OES – Inductively Coupled Plasma Optical Emission Spectroscopy

IR – Infrared Light

LED – Light Emitting Diode

LHC – Large Hadron Collider

LuAG – Lutetium Aluminum Garnet

LuASG – Lutetium Aluminum Scandium Garnet

MRI – Magnetic Resonance Imaging

NR – Non-Radiative Decay

PDF – Powder Diffraction File

PET – Positron Emission Tomography

PL – Photoluminescence

PMT – Photomultiplier Tube

PVA – Polyvinyl Alcohol

PWO – $PbWO_4$

QE – Quantum Efficiency

RL – Radioluminescence

SEM – Scanning Electron Microscopy

SPECT – Single Photon Emission Computed Tomography

UV – Ultraviolet Light

VUV – Vacuum Ultraviolet Light

XRD – X-Ray Diffraction

YAG – Yttrium Aluminum Garnet

YLuAG – Yttrium Lutetium Aluminum Garnet

TABLE OF CONTENTS

INTRODUCTION

One of the key areas where many technological advances are achieved is related to the use of electromagnetic radiation, i.e. materials or technical systems that interact with light. Such materials range from light emitting diodes (LEDs) for general and special lighting purposes, security inks used to prevent counterfeiting of valuables such as banknotes, to more scientific ones in detector devices or optical sensors [1–3].

Some of the most common light-based detectors are used in computerized detection devices for medical imaging of the human body, such as CT (computed tomography) or PET (positron emission tomography). These devices are based on the conversion of high-energy radiation, such as gamma rays or X-rays, into visible light. The materials that perform this conversion are commonly referred to as scintillators [4,5]. Improving the quality of scintillators is particularly important in the production of high-quality detectors. The improvement and then the usage of such detectors would allow for much more accurate and reliable information obtained during the analysis. The main way to achieve this is to discover new compounds or to improve well known structures that fit all the relevant requirements raised for these materials: high-thermal stability, high-density, high-emission intensities, and good excitation properties (especially when it comes to excitation with high-energy radiation) [6–8]. A high-quantum yield value is also relatively important. Nevertheless, the majority of scientific attention has been directed towards the adjustments and improvements in the decay time. This is due to the fact that for scintillators, the shortest possible decay time is currently a key priority. It is the duration of the decay time that is one of the limitations of scintillators that is being attempted to be solved. A reduction in decay time will result in an increase in the number of signals captured by the device during a given period. This will lead to an improvement in image quality and energy resolution, thereby enhancing the reliability of the detector system [9,10].

An almost ideal matrix for scintillators is deemed to be a class of inorganic garnet oxides. In particular, a lot of attention is paid to cerium doped yttrium aluminum and lutetium aluminum garnets (YAG:Ce; LuAG:Ce). The aforementioned garnets fit all of the prerequisites needed for a good scintillator, including relatively high-density. Furthermore, the mentioned garnets have excellent decay times in the nano-second range, which is one of their key properties making them so desirable [8,11,12].

Despite the already rapid decay processes observed in Ce^{3+} based garnets, there is a continued need to further enhance the properties of these

compounds. One of the ways to reach this is to change their elemental composition. Compounds can be doped/substituted by replacing one ion with another, thus producing changes in structural, morphological, and luminescent properties. There have been numerous studies performed on the doping effect of various ions (for example Ga^{3+}, Ca^{2+}, or In^{3+}). However, based on current data the obtained improvements are still not enough. Recently, boron doping has been shown to provide significant benefits for the luminescence properties of garnet. Boric acid, which can be used for the synthesis has a low melting/decomposition point (170 °C), therefore it not only acts as a boron source, but also as a flux. The dual nature of boron allows to improve the emission, excitation properties, the increase quantum efficiency values of the garnets while also allowing for a reduction in decay times [9,13,14]. The aforementioned factors make boron ions an excellent dopant that can improve the required properties of scintillators, especially in terms of photoluminescence and radioluminescence emission and decay. It is important to note that there is a paucity of information on the subject of boron doping strategies.

While boron provides an immense improvement in the luminescent character of garnets additional doping may also be used. In order to find out the benefits of co-doping with boron ions systematic analysis in this work was performed not only for the most popular YAG:Ce and LuAG:Ce compounds but also for numerous other garnet compounds. The investigated compounds included mixed Y/Lu garnets, as well as Gd based aluminum garnets. The chemical composition of the aforementioned initial garnets was even further modified with magnesium and scandium in hopes that it may potentially lead to the improvement of optical properties [15]. Along with cerium, garnets doped with trivalent praseodymium are also often used as scintillators, mainly due to the fact that these garnets have an even shorter decay time than cerium doped compounds [16]. Due to the short nature of Pr^{3+} garnet-based decay times, they were also investigated in this work alongside the Ce^{3+} based ones.

In this work, in addition to the luminescent properties required for scintillators, structural and morphological properties were also investigated. Furthermore, although powder samples are popular for investigating various properties, their form may not be suitable for many practical applications. For this reason, a group of the analyzed compounds were also prepared and investigated in the form of ceramics and thin films on quartz and sapphire substrates.

The objective of this dissertation is to synthesize and characterize inorganic oxides with a garnet structure that would exhibit the optimal properties required for scintillators, with particular emphasis on a short decay time.

The following tasks were formulated for the dissertation:

1. To prepare powder, thin film, and ceramic forms of garnet structure compounds based on Y^{3+}/Lu^{3+}/Gd^{3+} and Al^{3+} and further doped with cerium (Ce^{3+}) or praseodymium (Pr^{3+}) and co-doped with boron (B^{3+}), magnesium (Mg^{2+}) or scandium (Sc^{3+}) ions by aqueous sol-gel synthesis method,
2. To study the structural and morphological properties of the synthesized compounds in order to determine the purity, crystal structure, and elemental composition of garnet and the particle shape and size of the obtained compounds,
3. To study the optical properties, especially decay times, of garnets in order to determine their potential for scintillator applications.

The novelty and importance of the work are as follows:

In order to obtain the requisite properties for use as scintillators, cerium or praseodymium doped garnets have been synthesized. In addition, the garnets were doped with boron, magnesium, or scandium ions.

For the first time, garnet structures powders containing boron and scandium ions were synthesized. Boron and cerium doped garnets thin films, and ceramic forms were also prepared for the first time. Compounds with novel elemental compositions exhibited superior luminescent properties as compared to garnets that do not contain boron ions. The main differences were observed in both radioluminescence and photoluminescence emission intensity, quantum efficiency values, and most importantly, a reduction in the decay process.

The key statements for defenses:

1. The aqueous sol-gel synthesis method can be used to manufacture successfully get single phase compounds with a garnet structure compositions which are doped with Ce^{3+}, Pr^{3+}, B^{3+}, Sc^{3+}, and/or Mg^{2+} ions,
2. Doping of garnet with B^{3+} ions improves the optical properties of garnet. It increases radioluminescence and photoluminescence emission intensity, quantum efficiency values, and shortens decay time,
3. The form of the garnet compounds (powder, coatings, ceramics) has an important influence on the emission intensity and decay time values,

4. Lutetium aluminum garnets doped with praseodymium and boron exhibit shorter decay times than cerium doped yttrium and gadolinium aluminum garnets compositions.

1. LITERATURE OVERVIEW

1.1. The Phenomena of Luminescence

The term luminescence has been used since 1888, when it was first mentioned by German physicist Eilhard Wiedemann. It was then defined as “cold light”, which is obtained from energy sources other than the usually created light. This light can be emitted at room or lower temperatures and does not require high temperatures the way conventional light sources do [17,18]. Currently, the term luminescence is used to define the processes that occur when a material emits visible light, after being excited by a secondary source, such as ultraviolet light (UV), X-rays or even a chemical reaction [19]. In terms of electromagnetic induced luminescence, the processes can be divided into several stages. The aforementioned stages and the entire process itself can be explained with Jablonski diagram, shown in Figure 1 [20]. Firstly, the optically active ion absorbs X-ray, UV, VUV (Vacuum Ultraviolet Light), IR (Infrared Light), or visible light and electron goes from a stable ground state to an excited one [21–23]. During excitation, an electron moves from a lower energy level to a higher energy level. This transition is represented by a green arrow in the Jablonski diagram. Subsequently, some of the energy is released as heat via lattice vibrations or so-called phonons, causing the electron transition from S_2 to S_1 level. Finally, when the electron returns from the excited state to the ground state (S_0), it emits a photon [20,24–26]. The energy difference between the absorbed and emitted photons is referred to as the Stokes shift. In most cases, the emitted light has a longer wavelength than the absorbed light. The number of possible states to which an electron can be excited depends on the electronic configuration of the atom. When the electronic configurations of atoms are $[Xe]4f^n$, and the number of electrons in the element ion (n) ranges from 0 to 14, the theoretical number of microstates can be calculated using the formula $14!/(n!(14-n)!)$. For instance, Gd^{3+} ion has a total of 3432 different states [27–29].

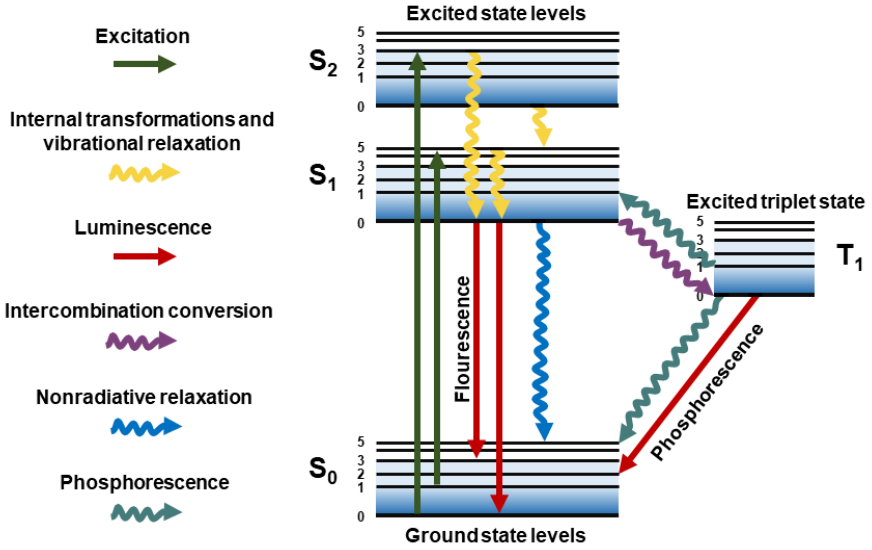

Figure 1. Fluorescence and phosphorescence fragment of Jablonski diagram. The figure is adapted from [26]

1.1.1. Photoluminescence and Radioluminescence

Luminescence can be classified into several distinct categories (Figure 2) based on the excitation source or type. For illustrative purposes, bioluminescence is caused by living organisms undergoing chemical reactions, cathodoluminescence is caused by an electron beam and thermally stimulated luminescence is called thermoluminescence. It is noteworthy that while each type of luminescence is fundamentally distinct, each plays a crucial role in different scientific fields. Nevertheless, photoluminescence and radioluminescence types have attracted an incredible amount of attention due to their applications in the everyday human environment [17,30–34].

Photoluminescence (PL) can be described as emission of light that occurs when electromagnetic radiation excites a substance. The excited electron eventually decays and then returns to their ground state (as depicted in the fragment of Jablonski diagram in Figure 1). The light that is emitted during radiative relaxation is commonly referred to as photoluminescence [35–37]. Depending on the decay time (the time it takes for the electron to return from excited to the ground state) photoluminescence can be further subdivided into fluorescence (fast time $\tau < 10^{-8}$ s) and phosphorescence (long time $\tau > 10^{-8}$ s), referring to the process of light emission. Photoluminescence as a process is

characterized not only by emission intensity but also by other parameters, such as decay time (time after which the phosphor stops emitting) and quantum efficiency (the ratio of absorbed and emitted photons) [38–41].

During the fluorescence process, materials are usually excited with ultraviolet light [42]. The entire process is very fast and the excited electrons quickly return to their ground state, which is why such materials stop emitting light rather quickly when the excitation source is turned off. Fluorescence is particularly important when it comes to the application of compounds in the LED and detector manufacturing industries [43,44].

As opposed to fluorescence, phosphorescence does not re-emit the absorbed radiation immediately as seen in Figure 1. Instead, the electrons undergo further intercombination transition to triplet state. The energy is then emitted during the transition from T_1 (excited triplet state) to S_o (ground singlet state). When the excitation source is removed, emission still continues for a substantial amount of time, as the emission process form triplet to ground state is much slower. It can be summarized that a phosphorescent material will glow by absorbing light of a shorter wavelength and emitting it at a longer wavelength, similarly as during fluorescence, however at a much slower pace [45–47]. Most phosphorescent materials are used in medicine as markers as well as in part of safety signs, house interior items or various paints [48,49].

Radioluminescence is similar to photoluminescence, however in this case X-rays or gamma rays are used as an excitation source. The material is bombarded with high-energy radiation and then emits visible lights [50,51]. This type of luminescence is particularly important and is used in high-energy radiation detectors that consist of scintillating materials. Such detectors are used in computer tomography, magnetic resonance, and X-ray inspection devices. Short wavelengths also was used for photodynamic therapy, radiological and radionuclide imaging [52,53].

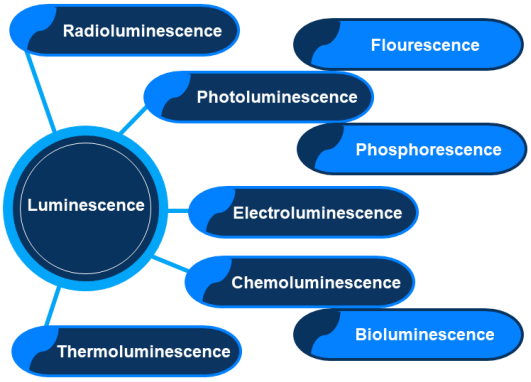

Figure 2. Different types of luminescence.

1.1.2. The Influence of Lanthanides on the Luminescence Process

Lanthanide luminescence serves as a fundamental component in a wide range of applications, including but not limited to lighting, luminescent molecular thermometers, lasers, optical medical imaging, security marking and barcoding. Electronic levels of lanthanide luminescence are generated from different electronic configurations, according to the previously mentioned formula [54–58]. Most of the trivalent lanthanides Ln^{3+} are used as luminescent activator ions. In essence, they are characterized by electron transitions between $[Xe]4f^2 \rightarrow [Xe]4f^2$ (f-f) orbitals, but there are cases, such as trivalent cerium/praseodymium or divalent europium, whose electron transitions occur between $[Xe]4f^2 \rightarrow [Xe]4f^15d^1$ (f-d) orbitals as well. Electron transitions, depending on the probability of their occurrence, can be allowed or forbidden. The f-d transitions are allowed, resulting in a broad, single emission band. In contrast, f-f transitions are forbidden, and observing this emission spectrum will show many peaked bands at a wider range of band lengths [59]. The possible electron transitions of lanthanides are often displayed in the so-called Dieke diagram [60]. This diagram shows how many excited states each lanthanide can have. Also, whether if electron transitions take place between f-f or f-d orbitals [61,62]. A small fragment of the Dieke diagram in Figure 3 shows the electron transitions of praseodymium Pr^{3+} and cerium Ce^{3+}, that were used the most in this work [63].

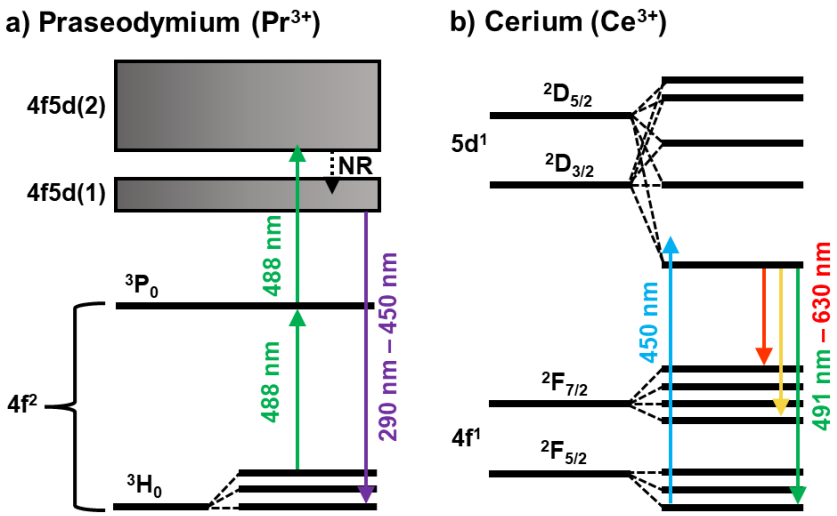

Figure 3. Praseodymium (a) and cerium (b) electron transitions in the fragment of Dieke diagrams. The figure is adapted from [63].

Trivalent praseodymium ions are stimulated through emission process, where a diode laser with a wavelength of 488.25 nm is used for excitation [64,65]. Upon excitation, the first step involves a spectrally narrow forbidden 4f-4f transition from the ground $^3H_0$ to the excited $^3P_0$ state. In the $^3P_0$ state, the electron absorbs another photon, so it can go back to another 4f5d (2) excited state. Due to the resulting non-radiative decay, the electron moves to a lower energy level 4f5d (1) (therefore, not only forbidden f-f transitions, but also allowed f-d transitions are observed in praseodymium ions spectra) [66,67]. From this state, the electron returns to the ground $^3H_4$ state. As a result of these transitions, the Pr^{3+} emission spectrum contains emission peaks throughout the visible light region from 290 nm to 760 nm [68,69].

Trivalent cerium ions only exhibit an allowed f-d electron transition between the ground level $4f^1$ orbital, to the lowest energy $5d^1$ orbital by exciting electron with a 450 nm laser [70–72]. In the case of Ce^{3+} ions, the emission band profile depends on the temperature. In the low temperatures cerium ions emission band split into the two parts which are attributed to interconfigurational transitions between states of the $[Xe]5d^1$ and the $[Xe]4f^1$ configuration, while the latter is composed of the spin-orbit split $^2F_{5/2}$ and $^2F_{7/2}$ ground state terms. In the higher temperatures emission bands overlaps and only an intense single emission band of Ce^{3+} ions is observed in the 491–630 nm spectral window which results from a return to the lowest $4f^1$ orbital [73–75].

1.1.3. Inorganic Luminescent Phosphors

Almost all good quality inorganic phosphors are composed of a crystalline "host material" and a small amount of activator ion. Activator ions are usually impurities, additional ions added to the compound. They absorb energy and emit an electron causing an emission process [76]. As mentioned earlier, the most common activators ions in the inorganics compounds are various lanthanides and their pairs [77]. Activators are responsible for the luminescence process in the inorganic matrix. Depending on the activator and its amount, the compounds can have different properties and emission/excitation wavelengths. For instance, if cerium Ce^{3+} ion is used as an activator in the compound, then the emission will be visible in the spectrum at a wavelength of 491–630 nm, and if europium Eu^{3+} ion – the main emission lines will be at a wavelength of 575–635 nm and 715–720 nm [78–82]. However, the host materials are also particularly important in the luminescence process. By changing the inorganic matrix, emission can be further modified, by either introducing shifting of the wavelengths or even by

regulating the intensity of certain transitions. One example of such a change can be observed when a compound is doped with praseodymium. When doping lutetium aluminum garnet with praseodymium (LuAG:Pr), an intense emission band at 300–460 nm is visible, which is attributed to $[Xe]4f^2 \rightarrow [Xe]4f^15d^1$ emission. However, the $[Xe]4f^2 \rightarrow [Xe]4f^2$ electron transition is also observed. Meanwhile after slightly modifying the inorganic matrix and replacing lutetium (Lu^{3+}) with gadolinium (Gd^{3+}), the allowed f-d transition is quenched and there is no emission in the higher energy range. Only the $[Xe]4f^2 \rightarrow [Xe]4f^2$ electron transition peaks are observed [83–86].

The biggest advantage of inorganic phosphors as compared to others (e.g., organics) is their high stability, durability and thermal resistance thus explaining their particular popularity and their wide applicability in various fields [87–89]. The most commonly used inorganic host materials are various oxides ($Y_3Al_5O_{12}$, La_2O_3), silicates (Mg_2SiO_4, $Ca_3Al_2Si_3O_{12}$), phosphates ($LaPO_4$, $Ca_2P_2O_7$), borates (YBO_3, $YAl_3B_4O_{12}$), aluminates ($YAlO_3$, $CaAl_2O_4$) amongst others. Each compound can be doped with different lanthanides like Ce^{3+}, Eu^{3+}, Pr^{3+} or Dy^{3+} to produce a material that emits at a specific wavelength depending on the needed application [90–94].

1.2. Garnet Structure Materials

Inorganic garnets as abrasives have been used for thousands of years however, using X-ray diffraction analysis, their crystal structure was first identified only in 1920 [95,96]. Meanwhile, the first synthetic garnets were synthesized in 1928. Additionally, at that time, Menzers scientific group identified that all garnet compounds also have the same crystal structure with $Ia\bar{3}d$ space group. This space group belongs to the cubic crystal symmetry group with in this case a body centered variant, and as previously mentioned, even now all of the prepared synthetic or natural garnets possess this structure [75,97]. The cubic crystal structure of garnet compounds can be defined by formula $(A)_3(B_1)_2(B_2)_3(X)_{12}$. In this formula, A is often a rare earth element, but other larger elements are often present in this position. The B_1 and B_2 positions usually contain aluminum, silicon, gallium or other relatively small cations. X refers to oxygen ions in the lattice. The A, B_1, and B_2 sites are coordinated by eight, six, and four oxygen ions to form dodecahedral (Wyckoff position 24c – 1/8,0,1/4), octahedral (16a – 0,0,0), and tetrahedral (24d – 3/8,0,1/4) sites, respectively. It should be emphasized that quite often even the same type of ion can occupy B1 and B2 sites that have different oxygen coordination [98].

The garnet crystal structure is rather flexible and allows for a substantial number of elemental compositions and thus a wide variety of properties. It is a relatively large lattice, it is relatively large lattice, containing 160 atoms. As in all cubic lattices, the unit cell parameter $a = b = c$ and can vary drastically depending on the chemical compounds, for $Y_3Al_5O_{12}$ it is around 12.000 Å, meanwhile for $Y_3Fe_5O_{12}$

a = 12.376 Å [99]. The visual representation structure of garnet can be also found in Figure 4. The figure highlights the crystal lattice of praseodymium doped gadolinium aluminum scandium garnet, visualized from data obtained after Rietveld refinement performed on samples analyzed in this thesis. The coordination polyhedral forming the crystal lattice are also displayed separately on the right side of the figure. The dodecahedral formed by the rare earth element (Gd^{3+}) in the center and coordinating oxygen atoms can be seen marked in green color. The aluminum and scandium octahedra and tetrahedra are visible in blue.

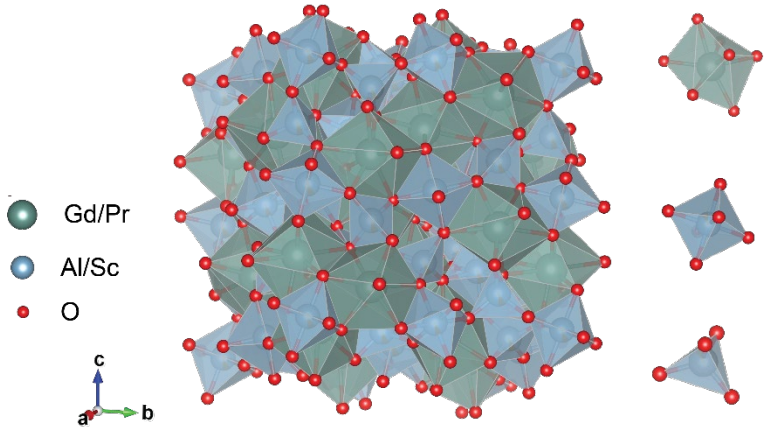

Figure 4. Crystal structure of gadolinium garnets: Cubic unit cell; Local polyhedral environment experienced by Al^{3+} (B_1, B_2), Sc^{3+} (B_1, B_2) and Gd^{3+} (A) ions from their neighboring oxygen ions.

1.2.1. Garnet Matrix Modification with Lanthanides

Due to the aforementioned ability of the garnet matrix to accommodate numerous ions it is a relatively popular matrix used for modifications [100]. Depending on the methods used during the synthesis, it is quite easy to work with such compounds and dope them with other elements. This is because various water soluble nitrates and oxides are used for synthesis, especially if

aqueous sol-gel synthesis is used [101]. In most cases, the main matrix of garnet is replaced by various lanthanides. Quite often the element in the A position will be changed in order to achieve the desired properties. Some of the popular dopants include: Ce^{3+}, Pr^{3+}, Eu^{3+}, Nd^{3+}, Yb^{3+} and other Ln^{3+} ions. However, excessive amounts of lanthanides cannot be inserted into the matrix. This is because concentration quenching can occur if there are too many activator ions. During such quenching, electron transitions take place between the activator ions themselves, as a result of which the intensity of the emission is strongly reduced. For this reason, only the optimum amount of activator ions should always be used [102–105].

Furthermore, not only the quantity and the nature of the ion, but also its local environment is important for compounds applications. In particular, as previously mentioned, garnet structure has 3 distinct positions for atoms with coordination numbers of 8, 6, and 4. The different coordination geometry in these positions results in different size spaces that accommodate the ions, thus limiting or preferring certain sized ones. Additionally, the crystal splitting energy is also dependent on the geometry of the aforementioned coordination, thus influencing its luminescence properties by modulating the energy levels. As such, not only the ion and its concentration but also the understanding of the lattice position it is in and the coordination of it are important for getting a clear picture of the luminescent behavior [82,104,106].

Our work focuses on structural modifications of yttrium, lutetium and gadolinium aluminum garnets $Y_3Al_5O_{12}$ (YAG); $Lu_3Al_5O_{12}$ (LuAG); $Gd_3Al_5O_{12}$ (GdAG). The aforementioned garnets are near perfect materials for further modifications, due to their excellent physical properties [107]. Although this process is not complicated, not all modifications are possible, as not all elements are suitable for doping in the respective structures. Structural modification is usually divided into two similar groups: doping, when a small amount of one element is replaced by another, and substitution, when the existing lattice element is replaced by a large amount of another element [108,109].

One of the main factors that is taken into account in order to obtain a compound with a stable structure during doping is to appropriately choose the radius of the exchangeable ion [110]. For this reason, the radius of the dopant should be as similar as possible to the radii of the exchanged ion. If the difference between these sizes were too large (dopant is larger than the lattice atom), then the synthesized garnet structure would be destroyed. At the same time, if the dopant was too small, then it would not replace the ions and would not remain in the crystal lattice and result the destruction of the lattice, via impurity formation [111–113]. Overall, Goldschmidt's rule states that if the

difference of ionic radius is less than 15%, the ions can be fully interchanged, however that is not always the case in practice [114]. These changes in the lattice are called substitution defects. Figure 5 shows the effects of defects on the crystal lattice with different size substitution ions, (a) when atom was changed with smaller atom, it can be seen lattice contraction, and (b) when atom was changed with larger atom, it can be seen crystal lattice expansion [115].

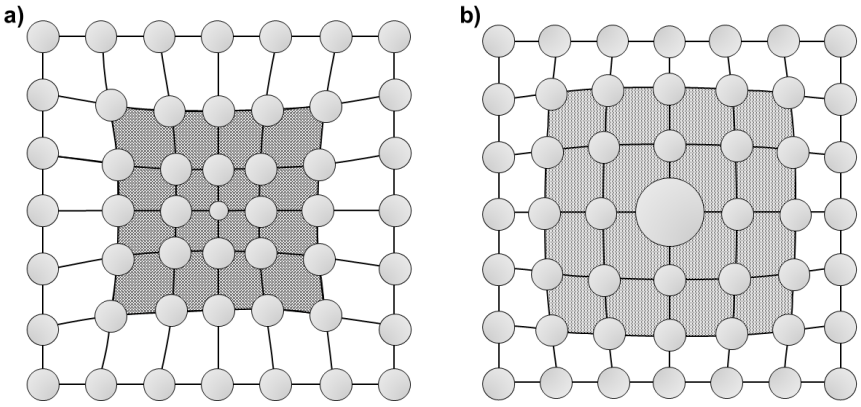

Figure 5. Atoms that are (a) smaller or (b) larger than the solvent atoms in the crystal structure are known as substitutional atoms. The shaded area highlights the region of high strain resulting from the substitutional defect. The figure is adapted from [115].

When carrying out modification and replacing one element with another, differences in ionic charges must be taken into account and electroneutrality must be maintained in all cases. The main reasons why electroneutrality can change is if that during doping non-stoichiometric amounts are removed or if they have different oxidation states. Most often, such defects are vacancies or intercalated atoms created by participation of oxygen atoms. For example, if Ce^{3+} cations are used, oxygen vacancies ($V_O^{\cdot\cdot}$) are formed in the LuAG structure during additional doping with ions of lower charge. Therefore, usually trivalent cerium Ce^{3+} ions must be oxidized to tetravalent cerium Ce^{4+} ions to restore the overall charge. The defect equilibrium equation is shown in the first (1) equation [116–118].

$$V_O^{\cdot\cdot} + 2Ce_{Lu}^{\times} + O_2 \rightarrow 2O_O^X + 2Ce_{Al}^{\cdot} \quad \textbf{(1)}$$

Where, $Ce_{Lu}^{\times}$ is cerium interstitials in place of lutetium, $O_o^{\times}$ – oxygen interstitials and $Ce_{Al}^{\cdot}$ – cerium interstitials in place of aluminum.

The crystal lattice can be modified not only with one, but also with several elements at the same time. A second cation can enhance the existing properties of the compound. Cerium or praseodymium ions impart luminescent properties to garnet. However, if such a compound is additionally doped with trivalent boron (B^{3+}) ions, then these properties can be improved even further. The boron ion occupies the tetrahedral sites of Al^{3+}, thereby reducing the size of the lattice parameters as well as changing the local environment of the activator ion. As a result, we have a compound with a similar structure, however with additional improved structural and also luminescence properties [119–121]. Doping with boron is possible for various compounds according to literature data, but the information about the influence of this ion on garnet structure compounds is relatively scarce.

1.2.2. Applications of Garnets Compounds

By doping the host material matrix with different elements, it can be modified to show unique properties, which allow it to be used in various areas of application [98]. For example garnets could used in jewelry as gemstone or like abrasives in abrasives paper. As was mentioned before, yttrium/lutetium/gadolinium aluminum garnets are a near perfect material for further modifications. If neodymium (Nd^{3+}) or chromium (Cr^{3+}) ions are included, the garnets will possess the necessary luminescent properties for use in high-power lasers. On the other hand, if europium (Eu^{3+}) ions are added to the garnet structure, this inorganic compound can be beneficial for enhancing photodynamic therapy in cancer treatment. Cerium (Ce^{3+}) ions doped garnets are perfect material for LED and scintillator manufacturing. Synthesis of cerium ion doped garnets was one of the first steps in the evolution in the production of these lighting applications [75,122–124] Praseodymium (Pr^{3+}) also is very popular activator ions in the scintillators materials [125,126].

1.3. Scintillators and Scintillation Process

Compounds that can convert high-energy radiation, such as gamma rays or X-rays, into near visible or visible light is referred to as a scintillators [127,128]. The scintillators themselves can be of two types, organic and inorganic. Their possible application also depends on the type. Organic ones are usually made of plastic or polyester. Such scintillators cost relatively low and can be of practically any shape, but the biggest disadvantage is that the received signal

is of lower quality than that of inorganic compounds. Meanwhile, inorganic scintillators are very limited in shape due to more complex synthesis methods and are limited by the size of crystals to around 75 mm × 75 mm × 25 mm [129–131].

In particular, single crystals scintillators have received the most attention. This is due to the fact that materials in this form are most commonly adapted and used in industry. Larger crystals with better atomic structure and higher chemical purity are the main component of various detectors [132]. Single crystals also have better mechanical properties compared to other forms of scintillators [130]. Other, less commonly used, but popular forms of scintillators are ceramics, powders, thin films, or fibers. Ceramics, due to their durability, shape stability and the ability to be transparent, are also often used instead of single crystals in various detectors. Only in this case, due to the nature of fabrication from bulk powder, the mechanical properties are usually slightly worse as compared to single crystals, as such they do not have the same popularity. The advantage is that the synthesis of ceramics is somewhat faster and simpler as compared to single crystals [133].

Although powders are not widely used in practice, they are the easiest to work with, synthesize and explore new properties and structural modifications in terms of research. Complex and expensive equipment is usually not required in powder synthesis. Also, modifications are made relatively quickly, so the analysis results are also obtained in a short period of time [134,135].

Thin film scintillators provide positivity to use relatively small amount of sample for detection or the ability to be used wherein ceramics/single crystals are not convenient. In this case, thin coatings are synthesized on different substrates. Thin films of material are obtained on the required (quartz (SiO_2), silicon (Si), sapphire (Al_2O_3)) surface which can drastically influence the obtained properties and even allow for changes in the crystal structure via strain. The strain in the case of films is produced due to the lattice mismatch between the substrate and the deposited film. Additionally, interface effects at the boundary between the substrate and the film itself may produce interesting changes to the obtained properties. Lastly, as previously mentioned, relatively very small amounts of precursor materials are used to synthesize coatings, as such and overall reduction in the price of already expensive materials is usually achieved [136,137].

The last type of scintillators that are often used is fibers. In order to efficiently transport scintillation photons over long distances, fibers are commonly used. The scintillating fiber serves the dual function of acting as both a scintillator and a light guide. The combined functionality allows for a direct transfer of light toward the detector, minimizing the loss or noise

associated with the process. It is also important to note that while using synthesized fibers, large size light detectors can be obtained. However, the main disadvantages of these scintillators are a low density and an average atomic number (Z_{eff}). These parameters reduce the absorption efficiency of ionizing radiation [138–140].

1.3.1. Essential Characteristics of High-Quality Scintillators

For ideal scintillators, an exceedingly good stopping power, which can be explained as the force that causes alpha and beta particles to lose their kinetic energy when interacting with matter, is required. In this case, materials with a high-density and a high Z_{eff} would be advantageous. In high-count-rate and fast sampling rate applications, it is necessary for the light emission pulse of the ideal crystal to have a fast rise and decay times, without any lingering afterglow. These properties effectively eliminate the accumulation of signal pulses during electronic signal processing [130]. In particular the value of the decay time is especially important because the shorter it is, the more signals can be recorded simultaneously and it is less likely that those signals will overlap. For this reason, data of higher quality and resolution is obtained as compared to compounds that have longer decay times [9,10].

Other important luminescence properties for high-quality scintillators are high-quantum efficiency (QE), high-emission intensity and emission wavelength. The wavelength emitted by the scintillator and the value of the quantum efficiency can determine the use and importance of the scintillator. This is due to the fact that the intensity of detectors differs based on the measured wavelength, as such the combination of high QE and correct emission wavelength can allow for detection of low intensity radiation. Furthermore, the improvement of QE is crucial for enhancing accuracy and spatial resolution. The energy resolution and proportionality are also reliant on the quantum efficiency. [141,142].

In addition to the properties mentioned above, high-quality scintillators must have other excellent, non-luminescent, properties, such as: stability in air, thermal stability and negligible self-absorption. Both air stability and thermal stability define the environmental stability of the compound itself and limit the areas of potential application. For example, it is not uncommon to use scintillators for the detection of X-ray under elevated temperatures, or for their temperature to increase due to excitation. If scintillator material is not stable, it will have the potential to decompose or react. As a result, the potential use of the material in industry and practice suffers [6,143,144].

Another feature that scintillators try to avoid is self-absorption. This is a process where an atom can absorb a photon emitted by another atom before it leaves the source. During this process, the intensity of the spectral band decreases. Negligible self-absorption has a significant influence on the scintillation response to X-rays. If the compound exhibits excellent luminescence properties together with negligible self-absorption, it will guarantee a good quality scintillation response [143].

Overall, it can be said that in order to have high-quality practically applicable scintillators, such materials must be characterized by high-density, high-atomic number, high-emission intensity, low rise and decay times, and high-quantum efficiency value. It is also important that the materials are stable in air and at high-temperatures and have negligible self-absorption.

1.3.2. The Scintillation Detectors Based on Inorganic Materials

Inorganic crystalline scintillators are the most important part in devices aimed at the detection of various particles and high-energy electromagnetic radiation [145]. These detectors can be found in computed tomography devices (CT), single photon emission computed tomography (SPECT), positron emission tomography (PET) or various security cameras and etc. [4,5,9,10]. The necessity for such detectors to meet specific demands necessitates the use of scintillating materials that exhibit optimal properties. In particular, the use of materials with short decay time allows for the acquisition of images with superior quality and resolution [9,74].

The main task of the detector is to convert the radiation absorbed by the scintillator itself, which then emits visible light and to convert it into an electronic signal for further detection and analysis. This process is initiated when a scintillator, which is a highly efficient and linear converter of kinetic energy into visible light, is employed in conjunction with a photodetector [146,147].

A schematic diagram of a standard scintillator and photomultiplier tube (PMT) detector setup is shown in Figure 6. Instead of a PMT a photodiode can be also used as a photodetector [148,149]. However, photomultipliers are the most common photodetectors used in regard to scintillation. The photodetector of this type is composed of a scintillator, photocathode, series of dynodes, and a final anode. After high-energy photon is converted to visible light by the scintillator, the photon of light strikes the photocathode in the photomultiplier. In this way, a photoelectron is emitted. These photoelectrons are focused on the first dynode. During this process, the generated electrons

are multiplied at the second dynode. This sequence follows until the end of the photodetector. Amplified electron signal is collected after reaching the anode and passed on to the measuring circuit. The resulting electric current pulse is proportional to the number of observed photons. Since this process is rather fast, and in most cases the liming factor to distinguish between individual pulses is the afterglow of the scintillator, it explains why a fast decay/rise times are needed. With fast decay/rise times, more precise data is obtained differentiating between different instances of detection [147,148,150–152].

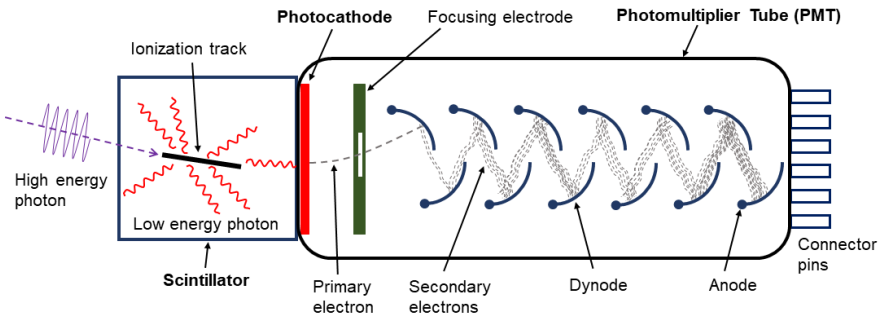

Figure 6. Schematic diagram of the detector consisting of a crystalline inorganic scintillator and a photomultiplier tube. The figure is adapted from [148].

1.3.3. Significance of Scintillators in Different Applications

As already mentioned, inorganic scintillators are very often used in different application such as medicine or particle physics [153].

In medicine the use of scintillator materials is mostly focused on improved detection of different diseases. As currently, when people are getting sick with cancer, one of the most popular diagnostic routes for cancer disease relies on the use of images obtained from computed tomography. The advantage of CT technology is that it is possible to detect and observe the formation tumors or other growths, without changing or damaging them. Furthermore, due to the non-invasive nature of the analysis it also helps prevent unnecessary operations and harm to the patient. In order to enhance the diagnostic efficiency of this method and facilitate the detection of cancer at an earlier stage, it is essential to develop and utilize materials in CT detectors that exhibit a low detection limit, a short decay time, and a high-resolution. Having such materials could reduce the damage to the body from computed tomography using X-rays, due to faster procedures by reducing the exposure time of the

patient to harmful radiation, while also maintaining high-quality and high-contrast images [154–156]. Currently, CT is the one of the few diagnostic devices, like also MRI, that allows fast and complicated high-resolution analysis.

In particle physics, scintillators are employed in the Large Hadron Collider (LHC) particle accelerator in the European Organization for Nuclear Research (CERN), situated on the border between Switzerland and France [157]. LHC particle accelerator can accelerate charged positive particles to extremely high-speed and energies. When such a high-speed is reached, the particles collide with each other releasing an extremely high-amount of energy, up to tens of TeVs. During such collisions, special particles are created, which can help to better understand the basics of physics and about the world around us. Then the scintillator based detectors are used for the analysis of the obtained radiation and created particles [158,159].

One part of LHC, the so-called Electromagnetic Calorimeter, is the main area where scintillators are used [160]. Scintillators that could work properly under such extreme conditions must have very good properties with special requirements. The main required properties are: extremely short decay time (less than 25 ns); resistance to extremely strong magnetic field; must be able to operate at extremely high incident particle energies [161–163]. PWO ($PbWO_4$) was the scintillator that best fit according to all the listed properties and was most widely used. While PWO crystals have high-density, the entire detector is estimated to contain around 100 tons of scintillating material, which is exceeding large amount. Thus making the price of such systems prohibitively expensive as well, and causing a need for cheaper or better materials [146,164].

Currently, a lot of work and research is being put into replacing PWO with another, more universal material that adapts better to each different situation with a different response time. Such materials could be lutetium aluminum garnets doped with cerium (LuAG:Ce), or more precisely, scintillation fibers of such materials [165,166]. The adaptability garnets is a major advantage compared to PWO materials [166]. In order to create optimal and practical materials, a lot of scientific research is currently being carried out. This work was based on the aforementioned need and lack of novel high-quality scintillating materials expressed by CERN and other industry leaders. Particularly intense focus was given towards the reduction of decay times in high-potential having Lu^{3+}, Y^{3+}, or Gd^{3+} based garnets by incorporating doping induced structural distortions to the lattice.

2. EXPERIMENTAL

2.1. Precursors and Substrates Materials

All synthesis powder compounds were prepared using Y_2O_3 (99.9% Alfa Aesar), Lu_2O_3 (99.9% Alfa Aesar), Gd_2O_3 (99.9% Aldrich), Sc_2O_3 (99.9% ThermoFisher), $Al(NO_3)_3 \cdot 9H_2O$ (99.999% Alfa Aesar), $Pr(NO_3)_3 \cdot 5H_2O$ (99.9% Aldrich), $(NH_4)_2Ce(NO_3)_6$ (99.5% Roth), H_3BO_3 (99.5% Chempur), $Mg(NO_3)_2 \cdot 6H_2O$ (99.0% Chempur), $C_6H_8O_7 \cdot H_2O$ (99.5% Chempur) as precursors.

All synthesis thin films compounds were prepared using Y_2O_3 (99.9% Alfa Aesar), Lu_2O_3 (99.9% Alfa Aesar), $Al(NO_3)_3 \cdot 9H_2O$ (99.999% Alfa Aesar), $(NH_4)_2Ce(NO_3)_6$ (99.5% Roth), H_3BO_3 (99.5% Chempur), $Mg(NO_3)_2 \cdot 6H_2O$ (99.0% Chempur), $C_6H_8O_7 \cdot H_2O$ (99.5% Chempur), Polyvinylalcohol (98.8% Acros organics), H_2SO_4 (98,08% Chempur), and H_2O_2 (30% Chempur) as precursors. Sapphire C-cut (0001), 10x10 mm (>90 % Altechna); Quartz UVFS, 10x10 mm (>90 % Altechna) were used as substrates.

All synthesis ceramic compounds were prepared using Y_2O_3 (99.9% Alfa Aesar), Lu_2O_3 (99.9% Alfa Aesar), $Al(NO_3)_3 \cdot 9H_2O$ (99.999% Alfa Aesar), $(NH_4)_2Ce(NO_3)_6$ (99.5% Roth), H_3BO_3 (99.5% Chempur), $Mg(NO_3)_2 \cdot 6H_2O$ (99.0% Chempur), $C_6H_8O_7 \cdot H_2O$ (99.5% Chempur) as precursors.

2.2. Synthesis Procedure

The aqueous sol-gel method was used for the yttrium/lutetium/gadolinium aluminum garnets. Cerium concentration was kept at 0.5 mol% of the dodecahedral coordinated yttrium/lutetium/gadolinium for all the samples. For compounds doped with praseodymium, its amount was kept at 1 mol%.

Full descriptions of the syntheses and lists of synthesized samples can be found in the publications P1, P2, P3, P4 and P5.

2.2.1. Synthesis of Garnet Powders

For the garnet powders, firstly, oxides (Y_2O_3, Gd_2O_3, Lu_2O_3, or Sc_2O_3) were dissolved in an excess of concentrated nitric acid at 50 °C. Then, acid was evaporated, and the remaining gel was washed with distilled water 2-3 times, followed by further evaporation of added water. An additional 50 ml of H_2O was added and nitrates ($Al(NO_3)_3 \cdot 9H_2O$, $(NH_4)_2Ce(NO_3)_6$, or $Pr(NO_3)_3 \cdot 5H_2O$,

H_3BO_3) were dissolved. The solution was left under magnetic stirring for 2 h at 50 – 60 °C. After that, citric acid was added to the solution, and it was left to stir overnight. The solution was then evaporated and obtained gels were dried at 140 °C for 24 h in a drying furnace. The obtained powders were ground and firstly heated at 1000 °C for 2 hours in air, with a 5 °/min heating pace, secondly the same powders were heated in a muffle furnace at 1200 °C for 4 h under air (or reducing atmosphere) [1], with 5 °/min heating pace [13,168]. The synthesis scheme of garnets doped with praseodymium is shown in Figure 7. This synthesis scheme is similar for all powders samples.

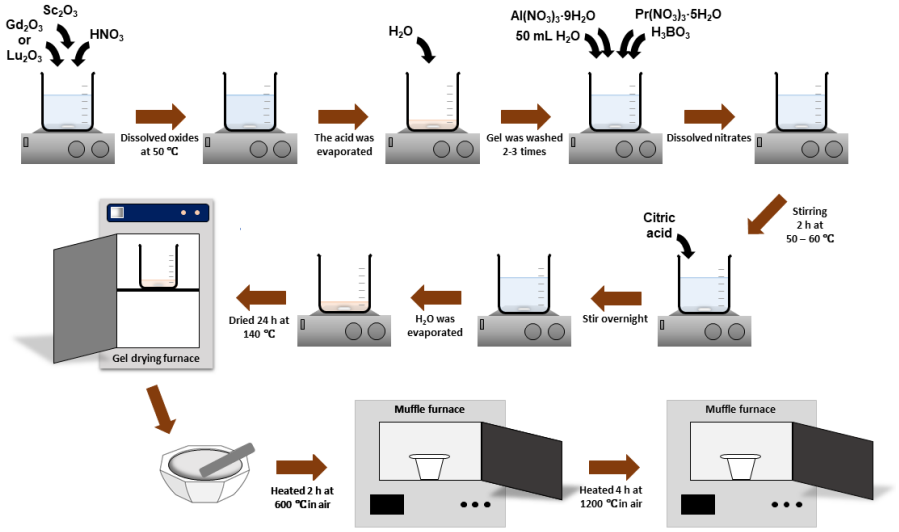

Figure 7. Scheme of praseodymium doped garnet sol-gel synthesis procedure.

2.2.2. Synthesis of Garnet Thin Films

Synthesis of thin films consist of three steps. First, synthesis of sol using sol-gel method. Secondly, follows the making of aqueous solution with 3% polyvinyl alcohol (PVA) and substrate preparation. The final stage of the process is the deposition of coating on the substrate. In this instance, the substrates employed were sapphire and quartz.

Sol synthesis. Firstly, Y_2O_3 or Lu_2O_3 were dissolved in an excess of concentrated nitric acid at 50–60 °C. Then, the excess of nitric acid was evaporated and the remaining gel was washed with distilled water 3 times, followed by further evaporation of added water each time. An additional 200 ml of water were added, after the washing, and $Al(NO_3)_3 \cdot 9H_2O$,

$(NH_4)_2Ce(NO_3)_6$, H_3BO_3, and $Mg(NO_3)_2 \cdot 6H_2O$ were then dissolved. The solution was left under magnetic stirring for 2 hours at around 50–60 °C. After that, citric acid was added to the solution with a ratio of 1:1 to metal ions and was left to stir overnight [167,168].

PVA and sol solution. When the sol was prepared, the 3% PVA solution was introduced into the already prepared sol in order to improve the wettability of the substrate. The volume ratio of the PVA and precursor solutions was kept at a 1:1. The final concentration in the solution was left at 0.1 M for all samples. The substrates were washed for about 30 minutes in boiling acidic piranha solution, after that they were soaked in distilled water and then washed in an ultrasonic bath for 3 min.

Coating procedure. When the coating solution was ready and the substrates were washed, the coating processes were started. First, sol-gel dip-coating technique was used. For dip-coating procedure a KSV Dip Coater device was used. For $Y_{2,985-y}Al_2Al_{3-x}O_{12}:Ce_{0,015},B_x,Mg_y$ or $Lu_{2,985-y}Al_2Al_{3-x}O_{12}:Ce_{0,015},B_x,Mg_y$ films, five layers were deposited by a single-dipping process. During the process, the immersion time of the substrate is 85 mm/min and holding time in the solution is 20 s. Withdrawal from the solution takes place at a speed of 40 mm/min, with support for 30 s after withdrawal. During a single dipping process (marked – 1 by 1), each deposited layer is calcined for 2 hours at 900 °C in air, with heating pace of 1°/min. Then the second layer is deposited using the same procedure as before. After final deposition, films were annealed once again at 900 °C for 2 hours in air, with 1°/min heating pace, and lastly at 1000 °C for 2 hours in air, with the same heating rate as before [169]. Samples (marked - together) are that of which the layers were coated one after the other, with brief annealing of each layer at a temperature of 200 °C ant then all five layers are calcinated as mentioned earlier.

Secondly, sol-gel spin-coating technique was used for thin film synthesis. For it a “Spincoater model P6700” device was used. The substrate is placed on the head of the device, and then is attached to it by the forming vacuum. Several drops of coating solution are placed on the substrate using a membrane syringe. Using spin-coating method (spin rate = 2000 rpm for 60 seconds,), the excess solution is eliminated because of centrifugal forces, resulting in a smooth coating throughout the surface of the substrate. One layer is applied at one time and is calcined at 900 °C for 2 hours in air, with 1°/min heating pace. After final deposition, the films were annealed for the first time at 900 °C for 2 hours in air, with 1°/min heating pace, and the second time at 1000 °C for 2 hours in the air, with 1°/min heating pace. The heating rates were all the same as in the dip-coating procedure. Both spin and dip-coating processes are shown in Figure 8.

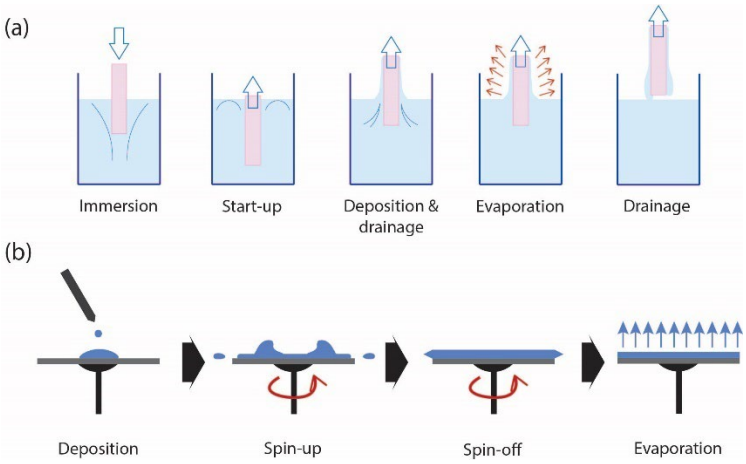

Figure 8. Examples of different coating processes: (a) dip-coating; (b) spin-coating.

2.2.3. Synthesis of Garnet Ceramics

Firstly, Y_2O_3 or Lu_2O_3 were dissolved in an excess of concentrated nitric acid at 50 °C. Then, acid was evaporated, and the remaining gel was washed with distilled water 2 or 3 times, followed by further evaporation of added water. An additional 50 ml of water was added, after the washing $Al(NO_3)_3 \cdot 9H_2O$, $(NH_4)_2Ce(NO_3)_6$, H_3BO_3, and $Mg(NO_3)_2 \cdot 6H_2O$ were dissolved. The solution was left under magnetic stirring for 2 hours at 50–60 °C. After that, citric acid was added to the solution with a ratio of 1:1 to metal ions and the solution was left to stir overnight. The solution was evaporated at the same temperature, and obtained gels were dried at 140 °C for 24 h in the drying furnace. In order to remove the organic residue as well as for all powders to still be amorphous, the compounds were heated at 600 °C for 2 hours under air [13,175].

The resulting white powders were ground in "Retsch Emax" ball mill with ZrO_2 balls (5 mm diameter) at 1200 rpm for 10 minutes to reduce and homogenize the size of the synthesized powders resulting in stronger ceramics later on. After that 0.1 g of the fine powder was initially compressed into a 10 mm diameter tablet using "Perken Elmer Hydraulic press" under a force of 4 kN for 10 minutes. Then the tablet was embedded between two 10 mm diameter metal plates, vacuum sealed in a plastic container and placed in an "P/O/Weber" isostatic press for 30 minutes under a force of 400 kN. The

obtained tablet was heated at 1000 ℃ for 2 hours in air and then further calcined at 1500 ℃ for 4 hours in air.

While synthesizing ceramics, various different tablet pressing times (from 30 s to 30 min) and pressures (from 0.5 to 4 kN) were tested. Attempts were also made to make ceramics from different amounts of materials (from 0.05 to 1 g). The obtained ceramics were also heated in different conditions, changing the temperature (from 800 to 1700 ℃) and the heating time (from 1 to 6 h) in order to adjust the most appropriate heating temperature and time. It was only after testing many different parameters that the best were selected.

Nominal formulas of the synthesized samples are the following: $Y_{2,985-y}Al_2Al_{3-x}O_{12}:Ce_{0,015},B_x,Mg_y$, $Lu_{2,98-y5}Al_2Al_{3-x}O_{12}:Ce_{0,015}B_x,Mg_y$. According to previous studies, YAG and LuAG ceramics were doped with 5% or 0% of boron, and/or with 0.03, or 0% of magnesium [13,170,171].

2.3. Structure Characterization

2.3.1. X-Ray Diffraction Analysis

Powder and ceramics samples. X-ray diffraction analysis (XRD) was performed using a "Rigaku MiniFlex II" X-ray diffractometer. Before analysis about 0.05 g of samples were dispersed using 0.1 ml of ethanol on a glass sample holder and left to dry for 5 min in the air. Then diffraction patterns were recorded in the range of 2θ angles from 15 ° to 80 ° for all compounds. For analysis, CuKα radiation (λ = 1.542 Å) was used. Other parameters of measurement: current – 15 mA, voltage – 30 kV, dwell time – 5.0 s, X-ray detector movement step – 0.010 °. The FullProf program for Rietveld refinement was used.

Thin film samples. XRD measurements of thin films were performed using "Bruker D8 Advance" X-ray diffractometer. Monochromatic $CuK\alpha_1$ radiation (λ = 1.541 Å) was used for analysis. Substrates with thin films were placed in sample holder, dwell time was 1.0 s. Measurements were performed under glancing angle conditions.

The PDF numbers used in the dissertation were generated by the Match! software using crystallography open database datasets (COD). The generation is based on such formula 960000000 + COD file number + 1. For example the used PDF card number for YAG 96-152-9038 would result in 1529037 COD number.

2.3.2. Scanning Electron Microscopy

Scanning electron microscopy (SEM) for the determination of particle morphology was done, using a "Hitachi SU-70" scanning electron microscope. For the measurement of the powder samples were prepared by dispersing them on a conductive double-sided carbon tape, that was attached to an aluminum sample holder. For the thin films and ceramics, samples were fixed onto the alumina sample holder by copper holders.

2.3.3. Inductively Coupled Plasma Optical Emission Spectroscopy

Quantification of B in the synthesized species was performed by inductively coupled plasma optical emission spectrometry (ICP-OES) using "Perkin-Elmer Optima 7000 DV" spectrometer (Perkin-Elmer, Walthman, MA, USA). The powders were dissolved in concentrated nitric acid (HNO_3, Rotipuran® Supra 69%, Roth) in a beaker and diluted to an appropriate volume with deionized water. Calibration solutions were prepared by dilution of the stock standard solution (single-element ICP standard, 1000 mg/L, Roth).

2.4. Photoluminescence Properties

2.4.1. Photoluminescence Measurements in Room Temperature

Emission and excitation. „Edinburgh Instruments FLS980" spectrometer equipped with excitation and emission monochromators and 450 W Xe arc lamp, and single-photon counting photomultiplier tube (Hamamatsu R928P) which was cooled to -20 °C. Obtained photoluminescence emission spectra were corrected using a correction file obtained from a tungsten incandescent lamp certified by "NPL" (National Physics Laboratory, UK). Excitation spectra were corrected by a reference detector [13].

VUV excitation. Collection of excitation spectra in the VUV range was performed on a commercial "Edinburgh Instruments FL920" spectrometer, which was modified by the integration of VUV monochromators for the excitation branch. The excitation branch consists of a D_2 lamp (DS-775) as VUV radiation source, an "Acton Research VM-504" VUV monochromator and a mirror based focusing unit. The monochromator has manually adjustable (by a micrometer screw) inlet and outlet openings, as well as a 1200 grooves per mm (F/mm) grid. The inside of the monochromator and the focusing unit are operated under much reduced pressure ($< 5 \times 10^{-}$ mbar the focusing unit

are operated and the lamp radiates through an MgF_2 window directly into the radiation path being under vacuum. The remaining distance between the exit of the focusing unit, which is also closed by an MgF_2 window, and the sample is continuously flushed with dry nitrogen. The sample is fixed in the standard FLS920 sample chamber in a modified sample holder at a 45° angle to the excitation beam. The measurement is carried out in a 90° arrangement. The emission arm of the spectrometer consists of a convex quartz collecting lens, a TMS300 monochromator with an 1800 F/mm grating (Czerny-Turner Optics) and a photomultiplier tube (PMT, Hamamatsu R928) which is operated in single photon counting mode and is cooled to -20 °C by a Peltier element. To consider that the excitation source exhibits intensity fluctuations over the measured spectral range, all VUV excitation spectra are divided by the excitation spectrum of a standard compound. Sodium salicylate (≥99.5%, Merck KGaA) was used for this purpose because it exhibits relatively constant excitability over the relevant spectral range.

Calculation of Quantum Efficiency. Quantum yield like were measured by using an "Edinburgh Instruments FL920" or "Edinburgh Instruments FLS980" spectrometers with an integration sphere coated by the white polymer Spectralon®. External quantum efficiencies were calculated by comparing the emission spectrum of the $BaSO_4$ sample (99% Merck) and the desired compounds that were measured in Teflon coated integration sphere. The EQE values were obtained employing the following formula 2 [172]:

$$EQE = \frac{\int I_{em,sample} - \int I_{em,BaSO_4}}{\int I_{ref,BaSO_4} - \int I_{ref,sample}} \times 100\% = \frac{N_{em}}{N_{abs}} \times 100\% \quad \textbf{(2)}$$

where $\int I_{em,sample}$ and $\int I_{em,BaSO4}$ are integrated emission intensities of the phosphor sample and $BaSO_4$, respectively. $\int I_{ref,sample}$ and $\int I_{ref,BaSO4}$ are the integrated reflectance of the phosphor sample and $BaSO_4$, respectively. N_{em} and N_{abs} stand for the number of emitted and absorbed photons.

Time resolved spectroscopy. For the cerium doped garnets decay kinetics were studied for powders thin films and ceramics using the "Edinburgh Instruments FLS980" or "Edinburgh Instruments FLS920" spectrometers. 450 nm laser was used as an excitation source.

Photoluminescence decay curves of the praseodymium doped garnet samples were recorded by using an Edinburgh Instruments FLS920 spectrometer. For lutetium aluminum/scandium garnet samples, photoluminescence decay times were measured using a 265 nm laser excitation source. For gadolinium aluminum scandium garnets decay times

were performed with a millisecond pulsed xenon flashlamp (Edinburgh Instruments μF920H).

2.4.2. Photoluminescence Temperature Resolved Spectroscopy

Temperature resolved spectroscopy measurements were performed using "Edinburgh Instruments FLS920" or "Edinburgh Instruments FLS980" spectrometers, with an ozone generating 450 W Xe lamp (Osram AG) and a single-photon counting photomultiplier tube (Hamamatsu R928) which was cooled to -20 °C. Analysis in the temperature range from 77 – 500 K with 50 K intervals was used and recorded by using a liquid nitrogen cooled cryostat (Oxford Instruments MicrostatN2). Stabilization duration for each temperature point was kept at 90 s while the allowed temperature tolerance interval was chosen as ± 5 K. Also, to prevent the water from condensing on the cryostat window dried nitrogen was being flushed during the procedure on its surface.

2.5. Radioluminescence Properties

For the first samples X-ray lamp (W anode, 40 kV, 30 mA) was used for the excitation of the radioluminescence. Radioluminescence spectra were measured by Andor iSTAR DH734_18 mm CCD camera coupled to Andor SR-303i-B spectrometer.

Other samples radioluminescence emission spectra were recorded using an "Edinburgh Instruments FLS980" spectrometer equipped with a photomultiplier tube (PMT, Hamamatsu R928P) which is cooled to -20 °C by Peltier elements. X-ray analysis "Oxford Instruments Neptune 5200" tube was used as an X-ray radiation source.

3. THE MAIN RESULTS

3.1. Investigation of Atmospheric Conditions During Calcination of Boron Doped YAG:Ce, YLuAG:Ce and LuAG:Ce

Cerium doped yttrium aluminum and lutetium aluminum are very popular scintillating materials. Short decay times are particularly important for good quality scintillators. The decay time in YAG:Ce and LuAG:Ce is about 60 ns, therefore the essential task for their improvement would be to shorten it as much as possible. For this reason, in this work, the aforementioned garnets were doped with different amounts of boron. B^{3+} ion has a suitable neutron capture cross section and can therefore absorb gamma radiation. Because of the extremely strong absorption of thermal neutrons and the weak interaction with MeV gamma rays the material is an exciting new inorganic scintillator candidate for the detection a thermal and epithermal neutrons. B^{3+} stimulates and improves the absorption of such radiation. To investigate the influence of the annealing atmosphere, because compound with Ce^{3+} ions in most cases are heated in reducing atmosphere in order to reduce any existing Ce^{4+} ions, all samples were heated either under air or reducing atmospheres.

All the information presented is published in the scientific article **P1**. In addition, a list of synthesized and described compounds, emission spectra at different temperatures and CIE chromaticity diagram can be found in the publication.

3.1.1. X-Ray Diffraction Analysis

In order to determine the purity of the garnet powder samples X-ray diffraction analysis was performed. All samples, which contain 5 or less % of boron, independently of the atmosphere under which they were heated, exhibit pure garnets phase (Powder Diffraction File, (PDF) #96-152-9038). Compounds with 10% and 20% of boron also contain aluminum boride (AlB_{10}) impurity phase. This secondary phase displays peaks at 20.1, 27.1, 34.0, 47.9 and 49.9 2θ degrees. These reflections are marked with * sign in the given diffraction patterns. From the given diffractograms (Figure 9 and P1) it could be said that increasing the amount of boron, causes an increase of the volume fraction of the impurity phase as well as to a larger intensity of its specific reflections. Also, it is noticeable that the introduction of lutetium into the garnet structure, from YAG, to LuAG with intermediate YLuAG stage, causes shifting of peaks towards larger angle values. This trend can be attributed to

the fact that yttrium and lutetium have different ionic radii, 1.02 Å and 0.98 Å respectively. According to Bragg's law, this determines the resulting shift. [173]. The difference between yttrium/lutetium and boron/cerium in ionic radii is even higher. However, due to the relatively low doping concentration of cerium and boron, this lattice modification does not affect peak position to a noticeable degree. Boron is a light element, for this reason it is complicated to determine its occupancy by the XRD method. Based on the literature it occupies a tetrahedral position in the garnet matrix [174,175]. However, when comparing peaks of PDF cards to that of the measured samples, no shift can be noticed for yttrium and lutetium aluminum garnets, but yttrium/lutetium aluminum garnet shows a small displacement from PDF card peaks. This can be explained by the fact that for identification of YLuAG samples, YAG Powder Diffraction File card was used as no phase transitions occur and only the cell parameters are affected by the substitution. In summary from the measured data, it can be argued that garnets could be doped with no more than 5% of boron with no additional impurity phase formation.

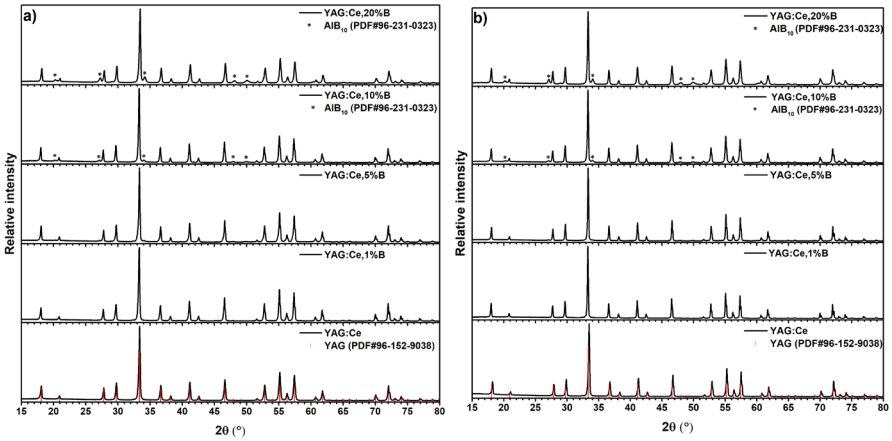

Figure 9. YAG:Ce powder samples diffractions patterns heated under different atmospheres: (a) air atmosphere; (b) reducing atmosphere (*– phase of AlB_{10}).

3.1.2. Scanning Electron Microscopy Analysis

Scanning electron microscopy (SEM) analysis was performed in order to determine the morphology and particle size of the synthesized materials. All samples were measured using two different magnifications. The smaller magnification was used to see the larger aggregation of the particles, while the

larger, to get a clearer vision of the individual particles. SEM images are shown in Figures 10 and 11. It is clearly seen that the size of garnet particles as well as porosity increases, when garnets are doped with more boron ions and annealed under air. Size of particles varies around 180 nm when no boron is introduced and increased up to 300 nm when sample is doped with 1% of B^{3+}, 400 nm when doped with 5% of boron, 600 nm – 10% of B^{3+} and lastly, up to 800 nm when boron amount reaches 20% B^{3+}.

From these images, it is clear that a higher boron content gives a larger particle size with an almost uniform increase in diameter. This change is likely due to a lower melting point of boron doped garnet phase as compared to pure garnet. The lower melting point may be influenced by the fact that the melting point of the boric acid is 170 ℃. Therefore, in this case, the acid may also act as a flux. As a result, the particles agglomerate faster, resulting in larger and more discrete particles [176].

Similarly, to particle size the addition of boron causes increased formation of pores. Samples without boron show only small and sparse pores, while the samples with 20% show an abundant amount of larger pores. One of the most likely explanations for this difference is that at sintering temperature of 1200 ℃, the inner pores are transferred to the surface of the sample where they form open pores. By increasing the amount of boron in the sample, the melting point of the compound potentially decreases, which results in quicker sintering and a faster transfer of pores. The results of the mentioned process are then seen in the SEM images [177]. The effect of the different heating atmospheres and the introduction of lutetium ions on particle size and morphology was also investigated. However, the SEM images show neither the sintering atmosphere nor the introduction of lutetium induced any significant changes to the particle size or morphology.

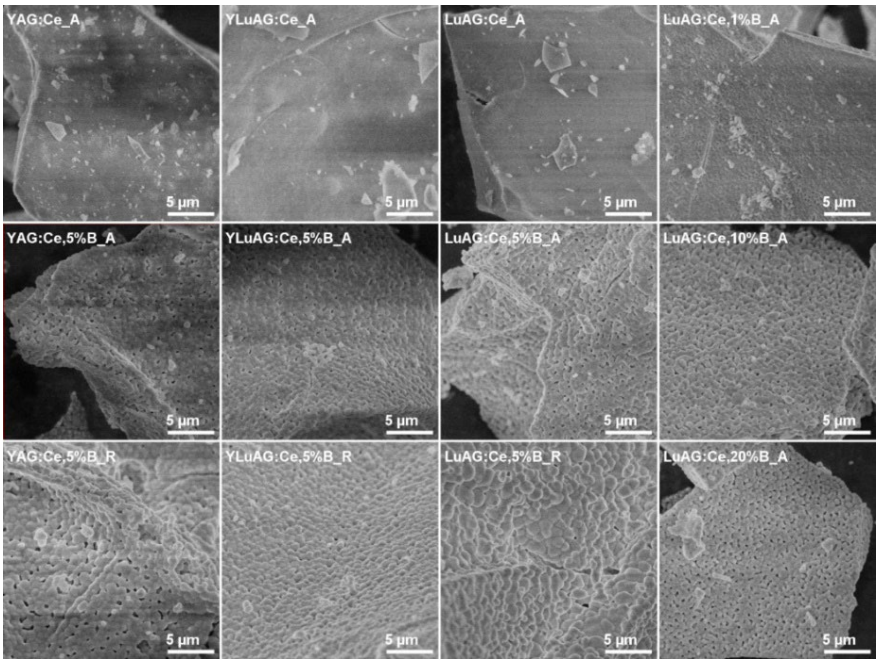

Figure 10. SEM images of garnet powder samples made under 2.5 k magnification.

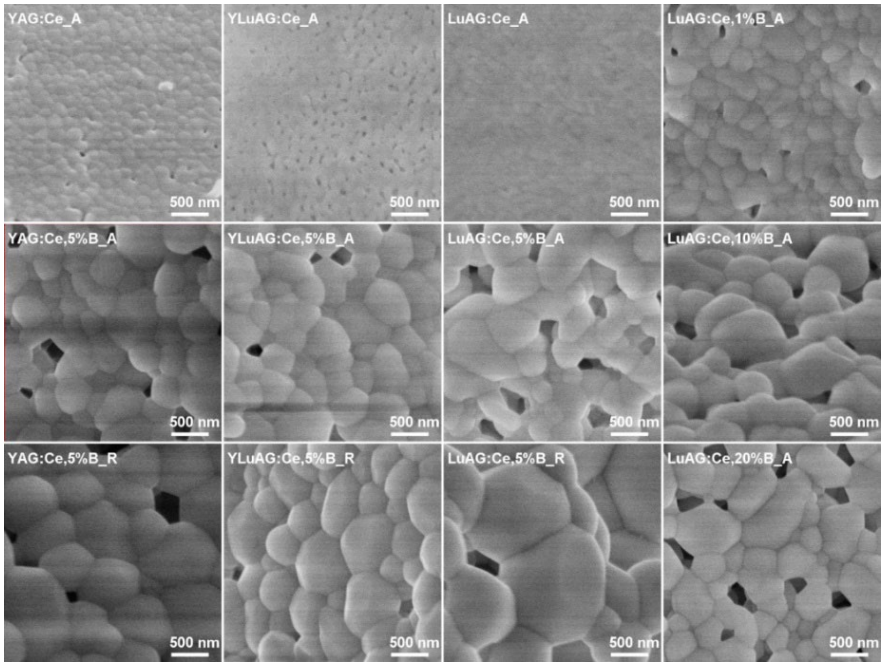

Figure 11. SEM images of garnet powder samples made under 20 k magnification.

3.1.3. Luminescence Properties

Luminescence properties are the most important characteristic of all of the samples synthesized in this work. These are caused by the doping of garnet with a rare earth element and in this case cerium. Cerium distinguishes itself from the other lanthanides because of the allowed nature of its electron transitions from $5d^1$ to $4f^1$ orbitals and vice versa. During these jumps, energy is either radiated or absorbed, which gives the garnet its optical properties. For the practical application of scintillators, it is essential to produce devices with the best optical properties, and thus important to find the most appropriate modifications to the material structure.

Figures 12, 13 and, 14 show excitation and emission spectra of different compounds measured at room temperature. From these graphs, it can be noted that, all YAG, YLuAG, and LuAG garnet samples, are characterized by wide excitation and emission bands. It was already mentioned that this is caused by electron transitions from $4f^1$ to $5d^1$ in the excitation process and from $5d^1$ to $4f^1$ orbitals in emission process [75]. These transitions are allowed therefore, figures show neat single-transition spectra. It was decided to excite all different garnets with the same wavelength light that would give the best emission intensity. From the excitation spectra given in Figures 12a, 13a and, 14a it was concluded that the best choice for excitation is the 450 nm wavelength light. Apart from the basic excitation intensities, an additional peak at 368 nm can be seen for several of the samples. This additional peak increases in intensity when increasing the amount of boron in the samples. Third excitation peak at 340 nm in YAG phase, 342 nm in YLuAG phase and 345 nm in LuAG phase is attributed to the electron transition from $4f^1$ to $5d^2$ orbitals [178].

According to Figures 12b, 13b and, 14b, all the samples exhibit band emission in green region. YAG has emission maximum at λ = 533 nm, YLuAG – λ = 525 nm and LuAG has the greatest shift towards higher energy when compared with yttrium aluminum garnet with emission maximum at λ = 514 nm. This shift can be explained by the difference in the covalence of the compounds, this is the due different electronegativity of the bond. The higher the covalence of the bond, the greater the shift to longer waves. In this case, the electronegativity of lutetium is 1.27 and that of yttrium is 1.22. Although small, the difference is what influences the shift of the emission maximum of lutetium compounds towards the higher energy range [179]. From the figures it can also be noticed that the samples demonstrating the highest luminescence intensity were all annealed under air and not under reducing atmosphere. This effect of the heating atmosphere has been

previously observed by other scientists, but it is still not fully understood as to what may be the cause of it [180,181].

Other important difference of all synthesized garnets is the boron amount inside the garnet structure. This difference gives obvious emission intensity changes. It could be said, that compounds when the boron amount is the highest, whilst no secondary phase has formed, have the highest luminescence intensity. The addition of boron causes an increase of particle size. And since particles with bigger size have a relatively larger amount of dopant ions in bulk as compared to the surface resulting in higher emission intensity [182,183]. When AlB_{10} phase is formed, the emission weakens. One of the possible explanations why boron ions affect the luminescent properties, could be, that boron can create extra defects in Y/LuAG phosphors. While, equivalent substitution between boron and aluminum occurs in the $Y_3Al_5O_{12}$ matrix, the defects in order to compensate for charge difference, cannot form since the charge is equal. However, since the radii of B^{3+} ions is much smaller in comparison to that of Al^{3+} ions, the irregularity of the coordination polyhedron of the dopant site can increase, which causes an exceptionally large increase in local strain. This strain could be partially reduced by the formation trigonal planar units of BO_3, which tends to then form oxygen vacancies and thus finally decreases the emission intensity [121].

For YAG samples, the compounds with 1% of boron that were annealed under air atmosphere show the most intensive luminescence. Samples that were doped with 5% of boron show slightly lower emission intensities. Compounds, of which the dodecahedral position partially occupied by Y^{3+} and Lu^{3+} ions, have emission intensities similar to that of YAG powders. The highest luminescence intensity is seen for sample doped 1% of boron and the second highest – doped with 5% of boron, all of these samples were annealed under air atmosphere. LuAG sample emission spectra are shown in Figure 7b. Similarly, to the aforementioned YAG and YLuAG, in LuAG spectra, the most intensive emission was detected for heated calcinated under air atmosphere with 1% of boron. Second and third most intensive luminescence having compounds are samples doped with 5% of boron. From all emission spectra it can be clearly seen that samples doped 20% of boron and heated under reducing atmosphere exhibit the weakest emission. To sum up, from Figures 12, 13 and 14, it could be said, that all of the synthesized garnet powders have almost the same excitation and emission intensities independently of which element occupied the dodecahedral structure position. So in turn, the majority differences are caused by addition of different B^{3+} amounts into the structure.

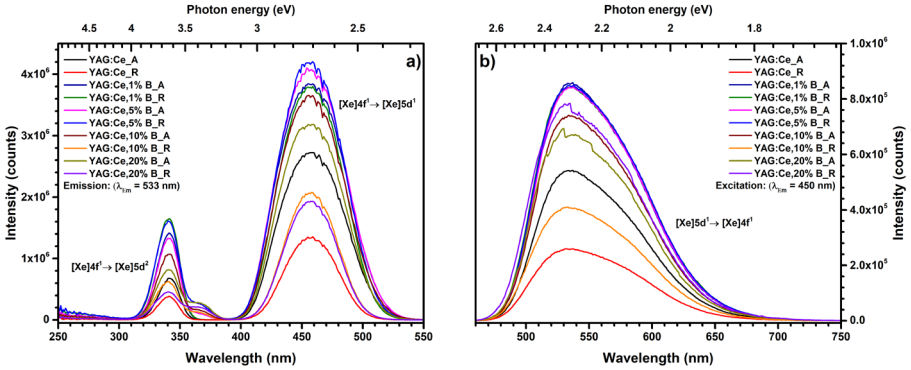

Figure 12. Yttrium aluminum garnet samples excitation (a) and emission (b) spectra.

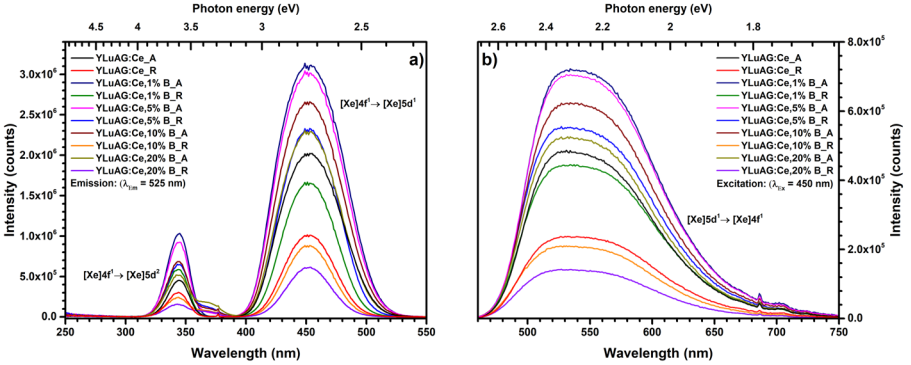

Figure 13. Yttrium-lutetium aluminum garnet samples excitation (a) and emission (b) spectra.

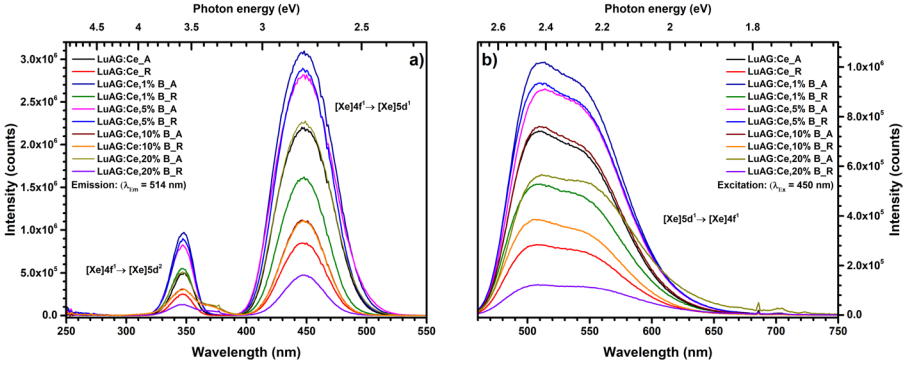

Figure 14. Lutetium aluminum garnet samples excitation (a) and emission (b) spectra.

For materials that could be used as scintillators, in this case all of the synthesized compounds: YAG, YLuAG and LuAG, it is important to measure the emission when using shorter excitation wavelengths than the blue laser light. Devices incorporating such materials operate on the principle that compounds emit light when they are excited by X-rays. Therefore, one of the most important studies that can change the value of garnets synthesized in this work as potential scintillating materials is the measurement of the emission spectrum when X-rays are used for excitation. However, due to the fact that such procedure is not readily available, only yttrium aluminum garnets samples were measured.

From Figure 15 it is clear that, as in the usual emission spectrum, one broad band, attributed permissible [Xe]5d1 → [Xe]4f1 transitions is visible. The emission maxima were located at $\lambda = 535$ nm, overall, the sample that was without boron and was heated under air atmosphere showed the highest luminescence intensity. The second most intensive emission is almost identical to that of the first compound was measured for sample also heated under air atmosphere, but doped with 5% of boron. Note that at about 700 nm several additional peaks for several of the samples were observed. These extra peaks may be attributed to Cr^{3+} emission, which may be incorporated to the compound during synthesis from precursor impurities. The emission of these ions is very strong under X-ray excitation, even if the amount is negligible. This can be confirmed because in Figure 12b, in the measured spectrum of the same samples, no additional peaks are observed [184].

To conclude this measurement, it is obvious that the compounds that are heated under air atmosphere are better suited to be used as scintillators, due to higher emission intensity. Therefore, other more significant studies will be conducted on the boron-containing compound with the highest emission – YAG:Ce,5%B_A.

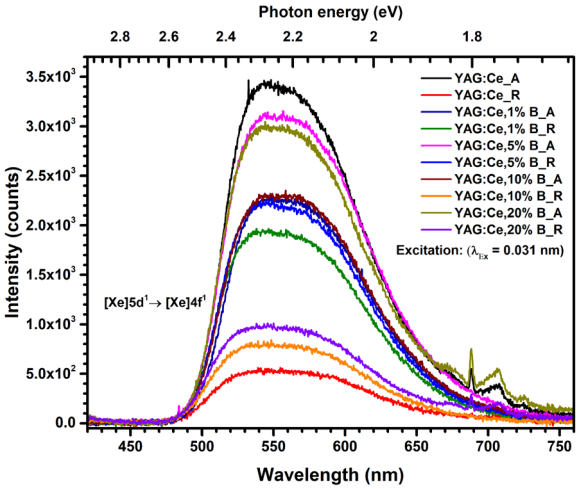

Figure 15. Yttrium aluminum garnets sample emission spectra, excited with X-rays.

The main idea of all work is to synthesize such compounds, that have shorter decay times, as this is the most important characteristic of the samples. The improvement of this property would give scintillators of a much better quality in different devices. Garnets, such as cerium doped YAG, YLuAG and LuAG have fast decay times, which are in nanosecond scale. Of course, this property could still be improved upon and by shortening decay time as a result of co-doping. In this case materials are co-doped with boron ions.

The influence of B^{3+} ions on the decay times is visible in Figure 16a. Garnets with an appropriate amount of boron exhibit a decay time that is shorter than that of the samples doped with only cerium, except YAG:Ce_A and LuAG:Ce. Surely, it is necessary to emphasize that only samples with 1% and 5% boron have a pure garnet phase. Larger doping may reduce the duration due to the resulting AlB_{10} phase. As expected, yttrium garnets exhibit longer decay times by more than 10 ns as compared to lutetium garnets [174]. If talking about pure garnets, then the shortest decay time was observed for cerium and 5% of boron co-doped lutetium aluminum garnet heated under reducing atmosphere, which is 54.7 ns. Of course, the decay times of all garnets were affected by the addition of the appropriate amount of boron. However, no clear dependency was observed since the decay times of other samples change rather unevenly. Of course, the shortening of the decay times themselves can be based on the fact that boron has a higher electronegativity than that of aluminum. The shortened decay time again could be associated with the polarization of the local activator ion environment. Therefore, when

the ions electronegativity increases, then the polarization decreases and the decay time becomes shorter. Different electronegativity of boron as compared to aluminum can cause the decrease photoluminescence decay time which also correlated with blue wavelength shift of emission [185]. The reason why the decay time decreases less when the samples are heated under a reducing atmosphere, may be due to the fact that boron incorporates in the structure less well in such a case and thus does not create the desired effect. Although scintillation decay has not been measured for some samples, it should be noted that there have been previous reports drawing a direct correlation between luminescence and scintillation decays, which are very similar in most cases [186]. The commercial factor can be emphasized. Lutetium aluminum garnets are known to be one of the most popular materials used as scintillators because of their short decay time. From the obtained data, it can be seen that replacing a part of the lutetium with yttrium and doping with 5% boron gives almost the same decay time. It is possible to calculate how much more commercially viable it would be to synthesize cerium and boron doped yttrium and lutetium aluminum garnets. Such compounds would cost about half as much as just lutetium aluminum garnet doped with cerium. The main difference comes from the high cost of lutetium oxide.

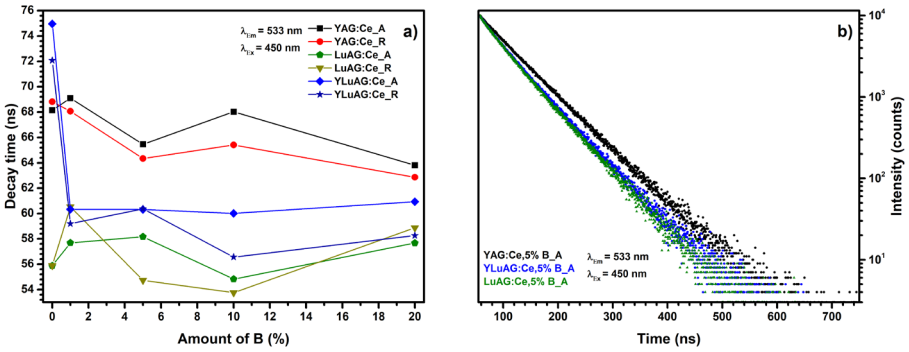

Figure 16. (a) Different garnet decay times at room temperature; (b) 5% of boron doped garnet decay lines.

All materials capable of luminescence exhibit one or another value of quantum efficiency (QE). This property demonstrates the quality of the synthesized phosphor. Of course, quality is indicated by the approximation of the yield in percentages up to one hundred [187].

Materials, prepared in this work have broadly distributed efficiency values which are shown in Figure 17. Ranging from 19.8% - LuAG:Ce_R to 93.0% - YAG:Ce,5%B_R. Upon further examination of the graph, it becomes evident

that the optimal boron content in the compounds is 5%, as this is the quantity that yields the highest quantum efficiency (QE) value. While yttrium aluminum garnets exhibit a higher initial QE compared to lutetium ones, the addition of boron enhances the QE value for each matrix. This effect is much more pronounced for LuAG compounds, especially for LuAG:Ce_R Also, most compounds doped with more than 5% boron have lower quantum efficiency as compared to the ones doped with 5%, except for LuAG:Ce_A sample. This can be explained by the presence of an impurity phase in all of these garnets, which results in a darker (grayer) color from the yellowish or greenish tones. Furthermore impurity phase compound contains number of defects, which can absorb part of the photons falling on the sample, thus reducing the amount of absorbed and emitted by the desired phase [188]. Another point is that in this case, although the decay time of the compounds with doped boron is reduced. The quantum efficiency is not that which is due to the collar ability of these properties (QE = 1/τ), but rather increases, especially in the case of garnets doped with 5% boron.

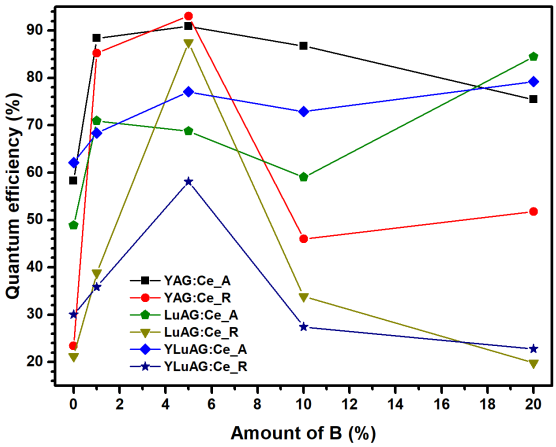

Figure 17. Quantum efficiency of different garnet samples.

Based on these studies, it is clear that boron has a positive effect on all scintillation-specific characteristics. That is, increasing the emission intensity, shortening the decay time, and improving the quantum yield in most cases. These changes are particularly pronounced for YAG:Ce_A, YAG:Ce_R and LuAG:Ce_R sample series. Summarizing the results obtained, it is obvious that the addition of boron has a positive effect on the required optical properties.

3.2. Determination of Different Garnet Films Characteristics Prepared via Sol-Gel Spin or Dip-Coatings Techniques

The usage of coatings opens up new areas of practical application that would be otherwise inaccessible for powders obtained by other methods. As the actual incorporation of the powder into devices requires extra attention, while the coatings do not as they retain their shape no matter how they are placed. The most commonly synthesized compounds either in powder form or coatings and used as scintillators are different lanthanide doped yttrium or lutetium aluminum garnets. These materials are also important in that their coatings are transparent, which opens up even more additional practical and research avenues. Transparent coatings coupled with transparent substrates are required to study high-quality luminescence characteristics. For this reason, sapphire and quartz wafers are usually used.

All the information presented is published in the scientific article **P2**. In addition, a list of synthesized and described thin films, results of atomic force microscopy, CIE chromaticity diagrams can be found in the publication.

3.2.1. X-Ray Diffraction Analysis

When performing X-ray diffraction analysis of the as prepared thin films, samples must be measured using the glancing angle method. This method is necessary because the quartz substrate is highly-amorphous, as seen from increased background intensity visible from 20 to 25 2θ degrees [189]. When recording diffraction patterns by the conventional method only this high-intensity amorphousness remains visible, the phase peaks merge with the background due to the relatively low intensity. This low intensity of the peaks is due to the thinness of the coating, as only five layers were deposited.

Figures 18 and 19 show diffractograms of two out of four series of prepared coatings of YAG and LuAG on quartz substrates. From these Figures, it can be said that all samples have pure garnets phase with cubic symmetry and $Ia\bar{3}d$ (#230) space group. It can also be observed that the most intense peaks, remain narrow. They also have a slight shift to larger angles in the case of LuAG samples due to the replaced element in the dodecahedral positions, since yttrium ions are larger (1.02 Å) as compared to lutetium (0.98 Å) [173]. From the results of this measurement, it can be stated that all coatings independently of the doping still retain their pure garnet phase structures.

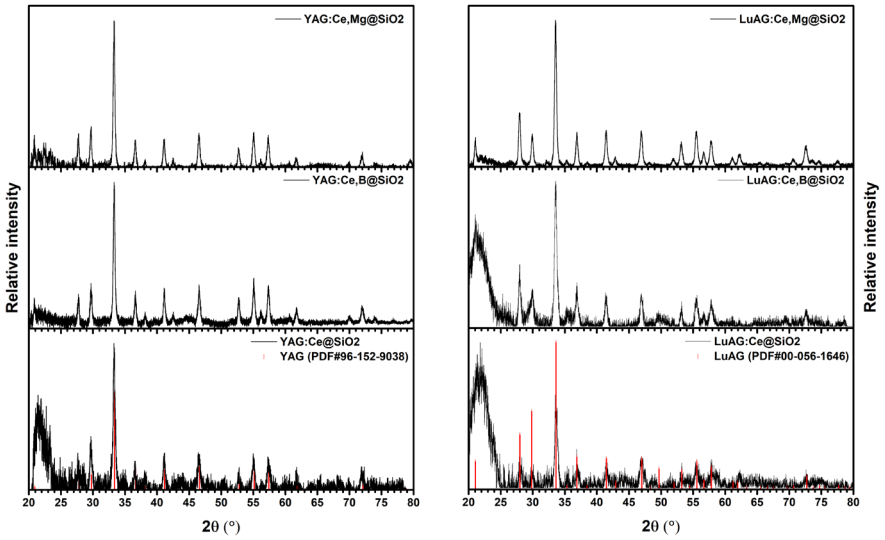

Figure 18. Thin film diffractograms of YAG and LuAG garnets on quartz (SiO_2) substrate using dip-coating technique when all layers were coated without intermittent heating.

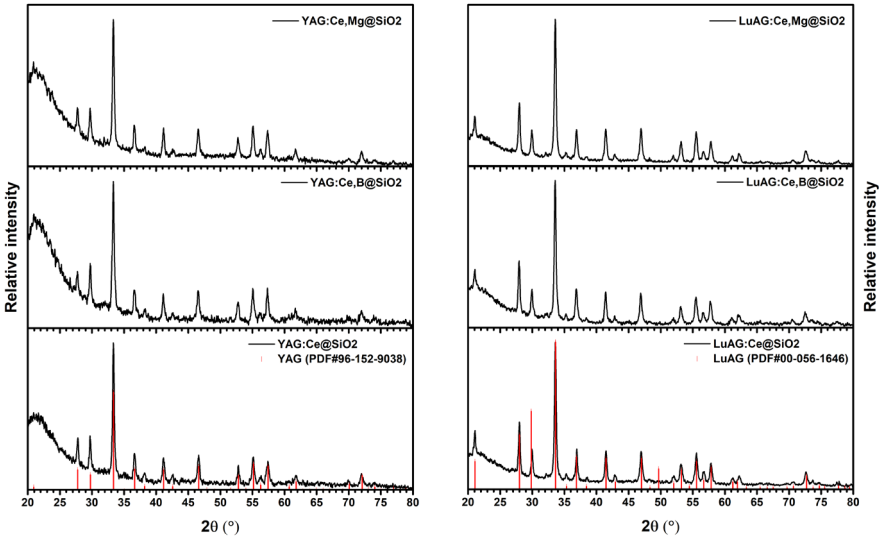

Figure 19. Thin film diffractograms of YAG and LuAG garnets on quartz (SiO_2) substrate using spin-coating technique when each layer is heated separately.

3.2.2. Scanning Electron Microscopy Analysis

Scanning electron microscopy, revealed the fact that different coating methods and substrates resulted in different morphologies of thin films [190].

From the micrographs it can be observed that using the dip-coating technique (Figures 20, 21) the coatings are uneven, split and layered. In principle, it can be argued that such coatings do not have the same properties over their entire area, as different parts of them have different material thickness and are inhomogeneous. Of course, when analyzing SEM data, the two different ways of deposition can be compared in case of the dip-coating methodology. Figure 20 shows the samples of which the layers were coated one after the other, with brief annealing of each layer at a temperature of 200 °C, this method was referred to as coating all the layers without intermittent heating, in micrograph titles. Meanwhile, in Figure 21, each layer was heated at 900 °C with the 1°/min pace. It can be seen that in the first case, the coatings are less layered, but they have many more cracks and voids on the substrate. This difference in morphology can be explained by the fact that with short annealing time, the sample is already placed on a heated hot plate, so that heating and the release of organic impurities and the evaporation of the remaining water take place rapidly. This causes cracks and tears in the coatings [191]. Also, looking at the images with higher magnification, it can be seen that coating the layers together results in less smooth coatings and formation of more cracks and empty, uncovered gaps. In this case, it can be said that the coating with annealing at a higher temperature gives, albeit layered, but less cracked thin films.

Thin films were much tidier, smoother and less cracked when spin-coating technique was used for their preparation. Figures 22 and 23 show that the coatings are evenly distributed over the entire substrate, with no protrusions and empty, uncovered gaps. Figure 22 shows that on the quartz substrates cracks in the thin films that may have been caused by the shrinkage of the substrate during heating. While the higher magnification figures show individual particles in the garnet layer that are about 50 nm in size. The essential difference with using different, sapphire substrate shown in Figure 23, is only that there are no visible cracks in the coatings on it. This retention of the smooth surface of the coatings may have been influenced by a high-coefficient of thermal expansion of Al_2O_3 which ranges from 4.5 to 5.8×10^{-6} K^{-1}. Meanwhile, the coefficient of thermal expansion of quartz is almost 10 times lower and can be from 0.55 to 0.75×10^{-6} K^{-1}. It is obvious that in order for the sapphire to start to expand the same distance as this

substrate, a higher temperature is required, so when heated at the same temperature, the coating on this substrate remains unbroken [192,193]

Summarizing the obtained data, it can be stated that in order to obtain better quality thin films, it is essential to use the spin-coating technique. This method helps to avoid unnecessary layering of coatings, which affects the inhomogeneity of the coating at different locations on the substrate.

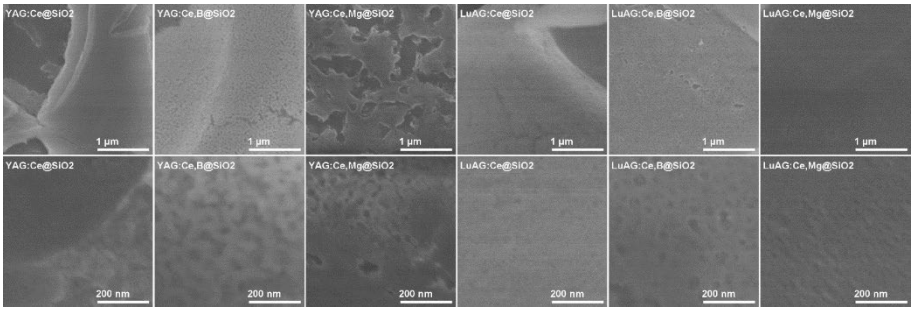

Figure 20. SEM images of garnet coatings on quartz (SiO_2) substrate using dip-coating technique when all layers were coated without intermittent heating.

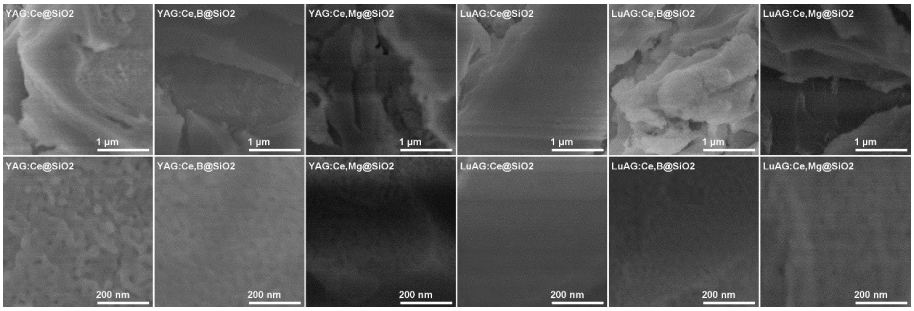

Figure 21. SEM images of garnet coatings on quartz (SiO_2) substrate using dip-coating technique when each layer is heated separately.

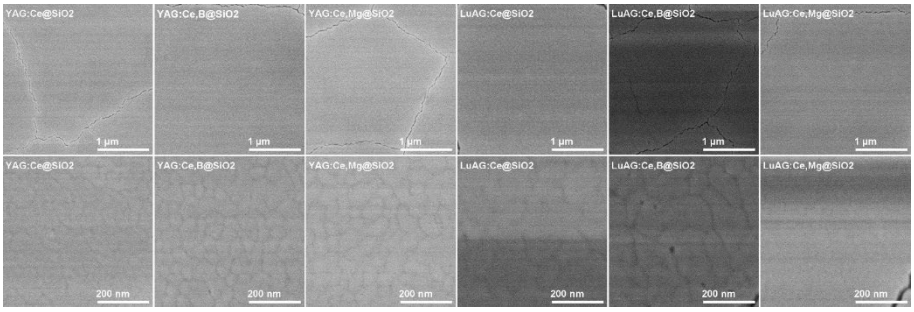

Figure 22. SEM images of garnet coatings on quartz (SiO_2) substrate using spin-coating technique when each layer is heated separately.

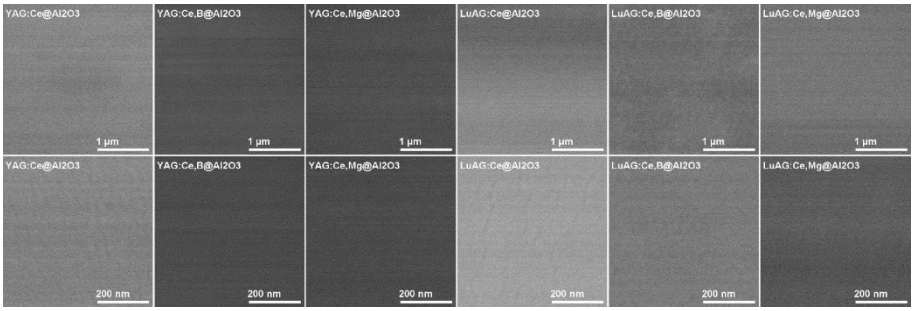

Figure 23. SEM images of garnet coatings on sapphire (Al_2O_3) substrate using spin-coating technique when each layer is heated separately.

3.2.3. Luminescence Properties

The luminescence of the compounds and its efficiency are highly dependent on the active centers in the sample. Since for preparation of films a much diluted solution is used, only a thin layer is deposited on the substrate. Moreover, the number of active emission centers is much smaller if compared to that of powders or ceramics. This disparity leads to the much more reduced emission and excitation intensity [13].

The Figures 24–27 show that the coatings have luminescent properties. Note, a self- made sample holder was used for the luminescent measurement of the thin films. For this reason, emission intensity is very sensitive and not a comparable parameter, because even the smallest displacement in the coating can have a huge effect on the emission and excitation strength.

Despite the fact that the luminescence intensity cannot be compared between different compounds samples, the properties of YAG and LuAG garnets can be seen in Figures 24–27. The excitation spectra (Figures a) show two intense peaks, which, are assigned to the transitions characteristic to Ce^{3+} ions.

From the emission spectra (images b in all of the figures) one main emission band characteristic to Ce^{3+} ions is observed and is attributed to the $5d^1 \rightarrow 4f^1$ electron transitions. Its maximum varies from 505 nm to 550 nm depending on the composition of the garnet. The figures also show extraneous peaks of different intensities located in the region from 660 nm to 740 nm. All of these peaks are attributed to Cr^{3+} ion emission [184]. Given the composition of the materials and substrates used, it can be stated that the influence of chromium ions seen in the spectrum may be caused by the impurities in used substrates. All substrates seem to contain appropriate amounts of chromium

impurities. In Figure 25b this area particularly stands out. This can be explained by the fact that sapphire contains about 10% of other elements, including chromium, impurities.

A different quartz substrate has also been used for dip-coating (Figure 24b) where all layers were coated without intermittent heating. It can be seen that higher levels of chromium ions impurities are also observed in this substrate. The substrates used in the synthesis of the other two compounds have the lowest amount of parasitic phase. These quartz substrates, and impurities are the smallest and less than 8%.

From the obtained spectra for the thin films, it can be said that regardless of the coating technique and the substrate used, the optical properties that are characteristic of synthesized garnets are observed. This confirms that these coating deposition methods retain their characteristic luminescent properties.

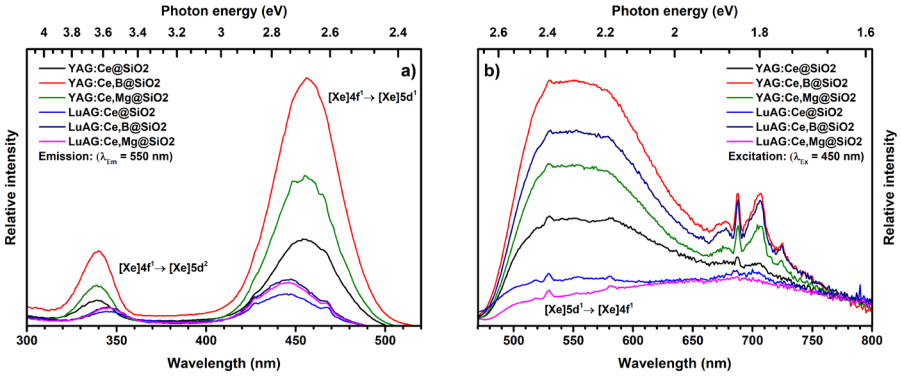

Figure 24. Excitation (a) and emission (b) spectra of garnet coatings on quartz (SiO_2) substrate using dip-coating technique when all layers were coated without intermittent heating.

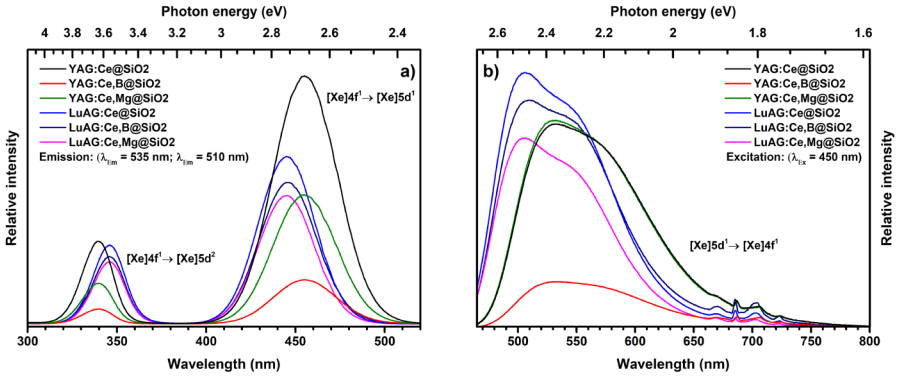

Figure 25. Excitation (a) and emission (b) spectra of garnet coatings on quartz (SiO_2) substrate using dip-coating technique when each layer is heated separately.

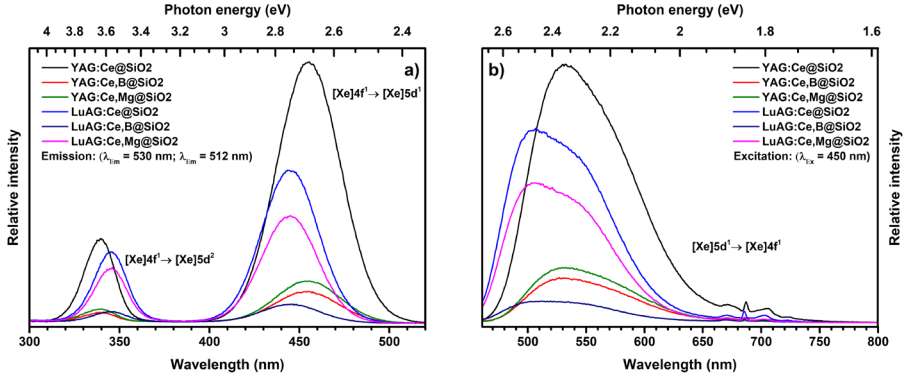

Figure 26. Excitation (a) and emission (b) spectra of garnet coatings on quartz (SiO_2) substrate using spin-coating technique when each layer is heated separately.

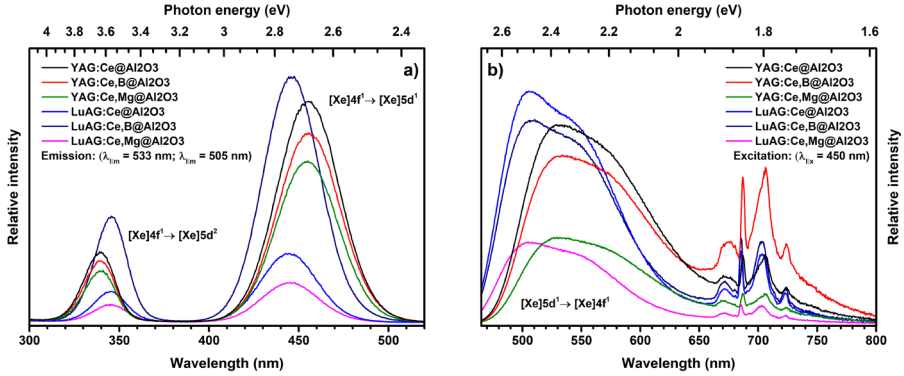

Figure 27. Excitation (a) and emission (b) spectra of garnet coatings on sapphire (Al_2O_3) substrate using spin-coating technique when each layer is heated separately.

While the fact that the emission and excitation intensities of the garnet coatings cannot be compared between each other stands, the decay times can be compared because the same number of counts were used for all samples.

Depending on the intensity of the emission, only the duration of the measurement itself varied. The luminescence decay time was also measured for the prepared compounds. According to the literature, the specific trends and values applicable for luminescence decay times (decreases and increases) correlate well with ones obtained during scintillation decay [186,194–196]. The basic idea is that the added boron and magnesium shortens the decay time. Indeed, as seen from the Table 1, both YAG and LuAG samples show a decrease in decay times when adding boron and magnesium with only slight reduction for some samples. In some cases the reduction is even up to 6 ns (YAG:Ce,B – dip-coating, SiO_2, 1by1). Determination of the sample decay times shows that in this case the introduction of boron to the structure gives more of an advantage as compared to magnesium, although there are more literature sources on magnesium doping [197]. As expected and mentioned in literature LuAG garnets have shorter decay times than YAG compounds [174]. Slightly longer durations are observed on sapphire substrate, but this can be affected by the replacement of the substrate itself. Looking at all the obtained data, it can be seen that the shortest decay time is for LuAG:Ce,B sample, which is coated by dip-coating method, when each layer is heated separately 900 ℃. Based on the visible emission spectra in Figures 24–27, it cannot be ruled out that the values of the decay times are also influenced by Cr^{3+} ions present as an impurity, which has longer decay times than Ce^{3+} ions.

Table 1. Decay times of different garnets thin films.

Sample	**Decay time (ns)**			
	Dip-coating, SiO_2, together	Dip-coating, SiO_2, 1by1	Spin-coating, SiO_2, 1by1	Spin-coating, Al_2O_3, 1by1
YAG:Ce	59.64 ± 0.2	65.73 ± 0.3	67.67 ± 0.2	68.83 ± 0.1
YAG:Ce,B	59.13 ± 0.2	49.44 ± 0.2	64.97 ± 0.2	77.46 ± 0.3
YAG:Ce,Mg	59.54 ± 0.2	48.69 ± 0.2	71.22 ± 0.3	74.22 ± 0.2
LuAG:Ce	53.47 ± 0.1	47.07 ± 0.1	63.31 ± 0.2	66.37 ± 0.2
LuAG:Ce,B	50.60 ± 0.2	45.46 ± 0.1	65.74 ± 0.2	62.50 ± 0.1
LuAG:Ce,Mg	61.88 ± 0.3	46.65 ± 0.2	60.52 ± 0.1	72.93 ± 0.2

3.3. Synthesis and Investigation of Novel Boron and Magnesium Doped YAG:Ce and LuAG:Ce Phosphor Ceramics

In addition to the scintillation properties themselves, applicability is an important factor as well. For this reason, materials synthesized in form of ceramics are much more viable to fashion into actual devices as compared to powders which are impractical in this case. In view of this paragraph, boron and/or magnesium doped YAG:Ce and LuAG:Ce ceramics are synthesized. The resulting ceramics are durable and have a suitable tablet shape, which were synthesized under isostatic pressure and finally heated to form crystalline ceramic.

All the information presented is published in the scientific article **P3**. In addition, a list of synthesized and described ceramics, results of particle size distribution histograms, the profiles of decay time curves and CIE chromaticity diagrams can be found in the publication.

3.3.1. X-Ray Diffraction Analysis

X-ray diffraction analysis was performed to determine the purity of the synthesized ceramics. The diffraction patterns of the garnet samples are shown in Figure 28. Every peak corresponds to garnet phase according the reference data (YAG: PDF#96-152-9038 and LuAG: PDF#00-056-1646, respectively). No additional and unassigned reflection were observed that could be attributed to any impurity phases. Thus, from the given results it can be clearly seen that all of the obtained yttrium aluminum (part a) and lutetium aluminum (part b) garnet ceramics exhibit a single phase structure. A cubic garnet crystal lattice was observed with a $Ia\bar{3}d$ (#230) space group for all compounds.

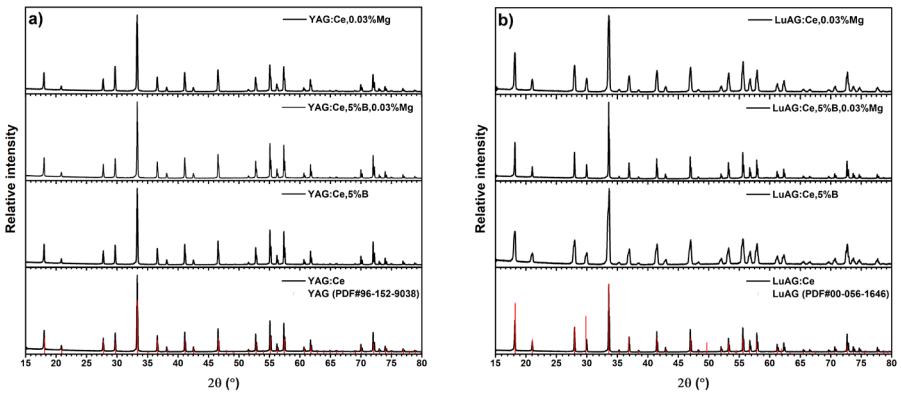

Figure 28. Diffractions patterns of YAG (a) and LuAG (b) ceramics.

3.3.2. Scanning Electron Microscopy Analysis

SEM analysis was performed to determine the surface morphology of the ceramics as well as to estimate the particle size. Figures 29 and 30 show the surfaces of YAG and LuAG ceramics under different magnifications. This was done in order to investigate both the broader surface of the ceramics as well as the individual particles that make up the ceramics.

It can be clearly seen from the figures that the incorporation of boron into the garnet structure has a significant influence on the morphology of the ceramics. This was expressed mostly in the fact that the particle size increased drastically when comparing the samples doped with boron to the ones doped with only cerium (in both LuAG and YAG cases). This can be explained by a couple of reasons. Firstly, in some cases when compounds are alloyed with other elements their melting point decreases and as such the particle size increases due to a more rapid mass transport. And secondly, due to the fact that boron can also act as a flux not just dopant in this case, this also drastically increases grain growth and results in larger individual particles [176].

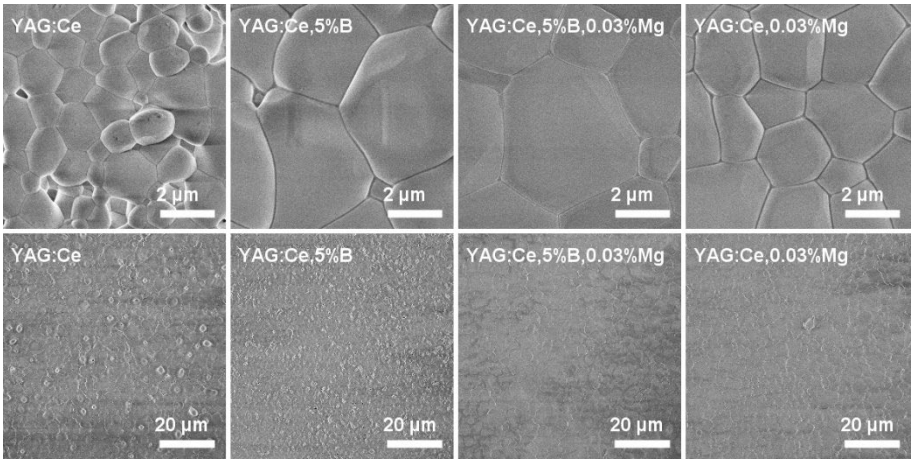

Figure 29. SEM images of YAG ceramic samples.

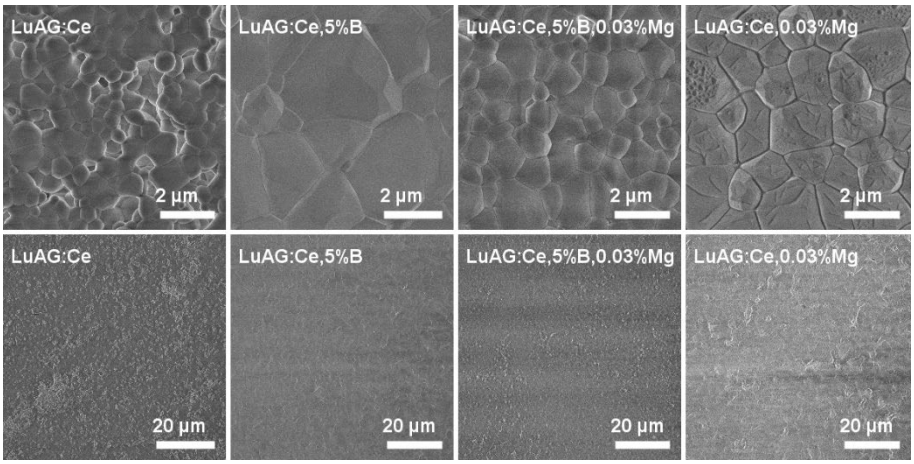

Figure 30. SEM images of LuAG ceramic samples.

In addition to surface morphology, the thickness of ceramics was determined by scanning electron microscopy. Figure 31 shows a side view of YAG:Ce,5%B ceramic. It can be seen that the thickness of the ceramic is around 749 µm. It is therefore clear that a sufficiently thin ceramic was obtained during the synthesis.

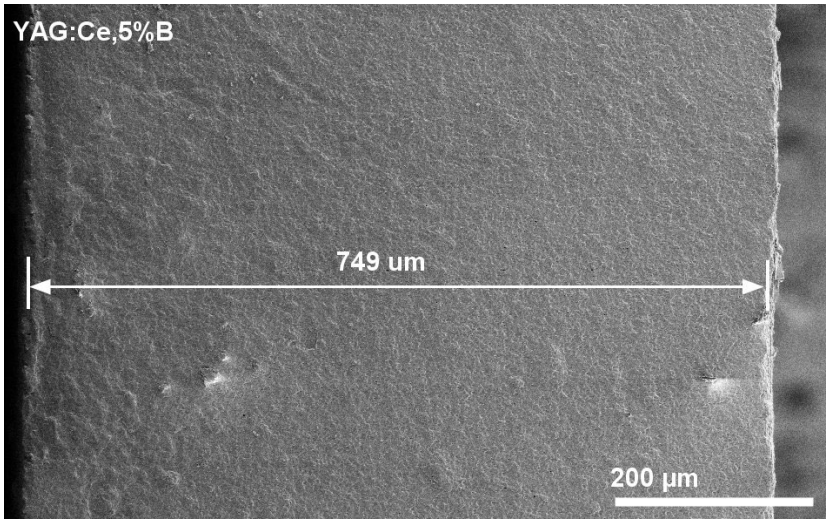

Figure 31. SEM images of YAG:Ce,5%B ceramic sample side view.

3.3.3. Luminescent Properties

Photoluminescence emission and excitation spectra were measured for all ceramic samples and are shown in Figures 32 and 33. For all ceramics, electron transitions between $4f^1$, $5d^1$and $5d^2$ levels are observed [3]. The excitation spectra (part a) consist of two broad bands. These bands are located at 342 nm and 457 nm for yttrium aluminum garnet and at 347 nm and 450 nm lutetium aluminum garnet. The first (less intensive) band is attributed to the electron transition that occurs between $4f^1$ and $5d^2$ levels, and the second band – between $4f^1$ and $5d^1$ levels [178]. It can be observed that the YAG:Ce,B and LuAG:Ce,Mg compounds have the most intense bands in the excitation spectra.

Figures 32b and 33b show a broad band emission spectrum of the Ce^{3+} ions. The emission maxima are seen at 545 nm and 512 nm for YAG and LuAG ceramics, respectively. The lutetium aluminum garnet samples have their emission maxima shifted towards the higher energy side. This blue shift can be explained by the different covalency of the samples which originated from the different electronegativity of the (Lu^{3+} and Y^{3+}) bonds inside the matrix [179]. Similarly to the excitation spectra, the emission spectra show that the YAG:Ce,B and LuAG:Ce,Mg samples have the highest emission intensity. The increase in emission intensity can be explained by the change in particle size (from SEM data). Both YAG:Ce,B and LuAG:Ce,Mg have the largest particles, and since larger particles in most cases have higher emission intensity due to relative small surface area to volume ration. This occurs due to the fact that most luminesce quenching defects exist on the surface of the particles, hence less surface area as compared to volume means that less of these defects are present [180,181].

In addition to Ce^{3+} emissions, Cr^{3+} ion emission is also observed in the emission spectra at about 700 nm. The emission of chromium ions originates from the $^2E \rightarrow {}^4A_2$ electron transitions [198]. The chromium ions are most likely introduced as impurities from the precursors used during synthesis as even extremely small amounts have been reported to show reasonably intensive emission [170].

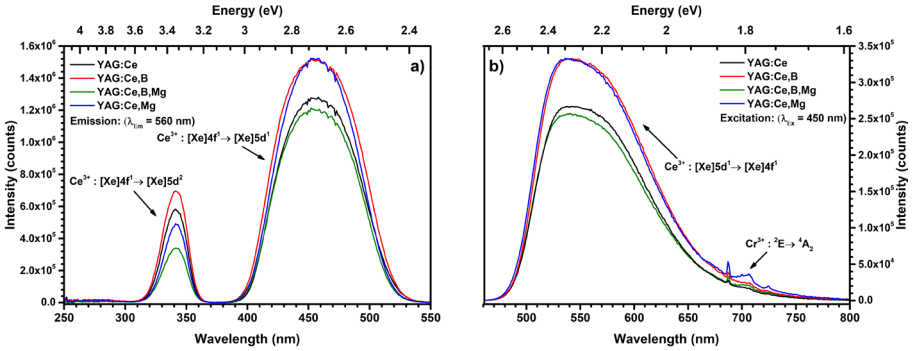

Figure 32. YAG ceramics excitation (a) and emission (b) spectra.

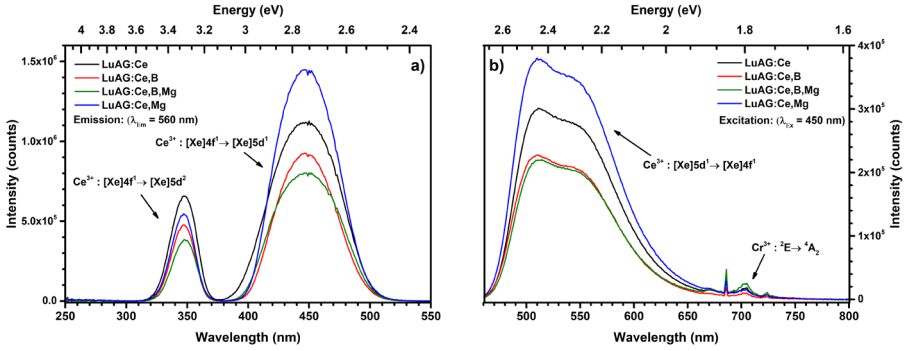

Figure 33. LuAG ceramics excitation (a) and emission (b) spectra.

The main idea behind the boron and/or magnesium doping was to reduce the decay times. From decay curves it was determined that the two-component process is happening. Bi-exponential decay occurred due to doping of YAG:Ce and LuAG:Ce with boron and magnesium ions. As a result of this doping, defects appear in the samples that trap electrons and delay recombination, and as such cause the bi-exponential decay profile [199].

For more clarity the decay times of all synthesized samples are displayed in Table 2. Due to the two-component nature of the process average decay times were calculated. The obtained results suggest that the doping of ceramics with boron was successful and as a result the decay times of the compounds decreased. For YAG:Ce that was not doped with boron the decay time is 55.79 ns, and after doping it decreased to 52.74 ns. In the case of lutetium aluminum garnets, this change is even more visible and the decay times decrease from 52.17 ns to 48.86 ns.

However, in the case of magnesium and combination doping the decay times have increased, in most cases. This may potentially show that

magnesium doping is not suitable for ceramics, at least in the case of YAG and LuAG. Comparing the results seen from the emission spectra (Figures 32 and 33) it can be observed that magnesium improves the emission intensity, which may be caused by increase of particle size and changes in morphology of the compounds. While the decay time depends on the electronegativity difference of the different ions [180,185].

Table 2. Decay times of different garnets ceramics.

Sample	Decay time (ns)		
	τ_1	τ_2	τ_{Av}
YAG:Ce	18.59 ± 0.8	58.48 ± 0.8	55.79 ± 0.9
YAG:Ce,5%B	16.04 ± 0.4	56.44 ± 0.4	52.74 ± 0.8
YAG:Ce,5%B,0.03%Mg	18.41 ± 0.5	67.84 ± 0.5	66.51 ± 0.8
YAG:Ce,0.03%Mg	21.44 ± 0.4	60.06 ± 0.4	60.16 ± 0.8
LuAG:Ce	21.24 ± 0.9	51.97 ± 0.9	52.17 ± 1.1
LuAG:Ce,5%B	21.32 ± 0.9	52.68 ± 0.9	48.86 ± 1.1
LuAG:Ce,5%B,0.03%Mg	17.55 ± 0.9	51.92 ± 0.9	48.67 ± 1.2
LuAG:Ce,0.03%Mg	32.24 ± 0.4	57.47 ± 0.4	54.86 ± 1.1

Based on the obtained results, it can be concluded that boron doped ceramics have a shorter decay time, which is required for scintillators. The decay times of this synthesized ceramic are one of the shortest as compared to the work of other scientists (for YAG:Ce varies from 58 to 60 ns, for LuAG – from 54 to 50 ns) [200–202].

Although scintillation decay times have not been measured in this work, it can be argued from the literature that in both photoluminescence and scintillation decay times (decreases and increases), specific trends and values correlate [170,186,194,196].

3.4. The Effect of Boron and Scandium Doping on the Luminescence of LuAG:Ce and GdAG:Ce

This section concerns cerium and boron doped $Lu_3Al_4Sc_1O_{12}$ and $Gd_3Al_3Sc_2O_{12}$ garnet μ-crystalline powders, which were synthesized for the first time. No information about of such elemental composition garnets was found in the literature. The incorporation of B^{3+} and Sc^{3+} ions into the garnet matrix corresponds to the improvement of the scintillating properties. Boron in these compounds could act like a flux and thus modulate particle

morphology, while scandium solely changes the physical and luminescent properties of these garnets. From the measured radioluminescence emission spectra, it could be concluded that boron doping results in a higher emission intensity when the compounds are excited by high-energy radiation.

All the information presented is published in the scientific article **P4** and article supplementary material file. In addition, a list of synthesized and described garnets powders, results of particle size distribution histograms, the profiles of decay time curves and temperature dependent luminescence properties can be found in the publication.

3.4.1. Inductively Coupled Plasma Optical Emission Spectrometry

The boron content in gadolinium aluminum scandium garnets was determined by using ICP-OES and the results are listed in Table 3. In all samples, the measured boron amount was slightly smaller than the calculated amounts used for the synthesis. This trend is expressed more in the compounds with higher total boron amount values (samples with 3 and 5% of Boron).

Table 3. Boron content in % in GdASG samples measured by ICP-OES.

Sample	Amount of boron (weighed in)	Amount of boron (determined)
$Gd_3Al_3Sc_2O_{12}$:1%Ce	0%	0%
$Gd_3Al_3Sc_2O_{12}$:1%Ce,1%B	1%	0.9%
$Gd_3Al_3Sc_2O_{12}$:1%Ce,3%B	3%	2.3%
$Gd_3Al_3Sc_2O_{12}$:1%Ce,5%B	5%	3.5%

3.4.2. X-Ray Diffraction Analysis

Lutetium aluminum garnet sample purity was checked based on Powder Diffraction File, (PDF) #00-056-1646. The purity of gadolinium aluminum scandium garnet is checked based on the same structure since no material PDF card of this garnet was found. The diffraction patterns show (Figure 34) that garnets containing less than 3% of boron (except LuAG) have a pure garnet phase, regardless of whether doped with Ce^{3+} ions or not.

Lutetium or gadolinium aluminum scandium garnet compounds with more boron contain aluminum boride AlB_{10} ((PDF) #96-231-0323) impurities. The reflections attributed to these impurities are marked with a ♦ sign in the XRD patterns. When increasing the boron amount in gadolinium aluminum

scandium garnets, impurities of scandium oxide Sc_2O_3 ((PDF) #96-100-8929) are also observed in the samples. Sc_2O_3 phase is marked with a * sign. From the given diffraction patterns, it could be said that the increasing amount of boron, leads to a rise in intensity and number of reflections that are ascribed to the impurities phase. As is commonly know the ionic radii of Gd^{3+} (1.05 Å) is larger than that of Lu^{3+} (0.98 Å) ions [203]. We can also observe this difference in ionic size in the diffractograms, as they show a shift to smaller angle values when gadolinium ions are present in the garnet lattice. Low amounts of Ce^{3+} and B^{3+} ions do not significantly affect peak position [174].

In summary from the measured data, it can be said that synthesized garnets could be doped with no additional impurity phase formation in LuAG with up to 5% of boron. In lutetium or gadolinium aluminum scandium garnets the single-phase compounds are only obtained up to 3% of boron.

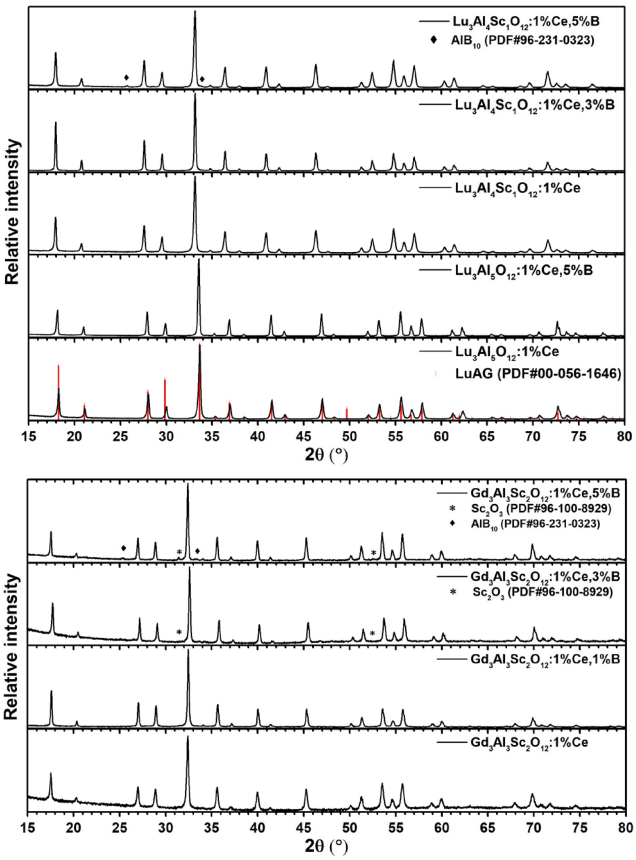

Figure 34. Diffraction patterns of $Lu_3Al_5O_{12}$, $Lu_3Al_4Sc_1O_{12}$ (above) and $Gd_3Al_3Sc_2O_{12}$ (below) doped with 1% of cerium and different concentrations of boron.

3.4.3. Scanning Electron Microscopy Analysis

Scanning electron microscopy (SEM) images were taken to determine the morphology of the garnet powders. All samples were imaged at different magnifications.

While analyzing the obtained results, all samples, regardless of the composition have similar morphological characteristics. This is mainly reflected in the particle shape, porosity, and particle arrangement, while in the case of particle size, significant differences were observed. These characteristics were most likely determined by chemical composition, synthesis procedure, and doping with B^{3+} ions.

Figure 35 displays images of cerium and different amount of boron doped gadolinium aluminum scandium garnet. All compounds have irregularly shaped interconnected particles, between which no significant porosity is observed. However, the particle size changes when compounds are co-doped with boron. The higher the boron content is used during the garnet synthesis, the larger the particle size is observed. These changes can be explained by the fact that boron can act as a flux. Since the melting point of boric acid used in the synthesis is 170 °C. Furthermore, boron most likely lowers the melting point of garnet. As a result, when heated at the same temperatures, garnets doped with a higher amount of boron show accelerated grain growth. For these reasons, larger garnet particles are obtained [176]. As can be seen from Figure 35 as the boron content in the compounds increases, the porosity of the samples decreases. In boron-free garnets, relatively high-porosity is observed, which disappears when samples are doped with 5% of boron. This change can also be explained by boron acting as a flux and thus increasing grain growth.

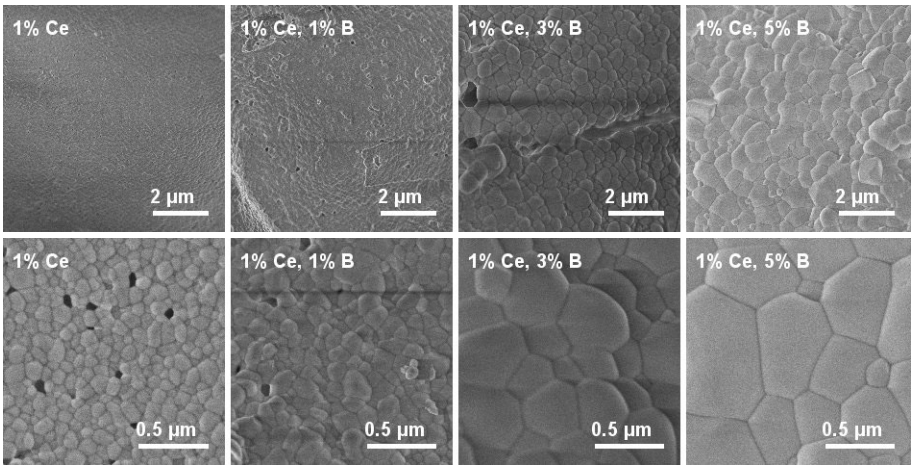

Figure 35. SEM images of 1% Ce^{3+} and different amounts of B^{3+} doped $Gd_3Al_3Sc_2O_{12}$ garnet powder samples.

3.4.4. Luminescent Properties

The operation mechanism of scintillators is based on the high-energy conversion to visible light in the form of luminescence. In this case, the photo and radio luminescent properties are determined by the presence of cerium ions in the composition of garnets. Ce^{3+} ions are characterized by interconfigurational electron transitions between the $[Xe]5d^1$ and $[Xe]4f^1$ configuration with light emitted in the green to yellow spectral range [204]. The luminescence properties were the main indicator which was sought to be modified, by adjusting the materials in such a way that they could be most applicable as scintillators.

The reflection spectra of the synthesized lutetium aluminum and gadolinium aluminum garnets doped with scandium, cerium, and boron are shown in Figure 36. It can be also noted that doping with other ions affects absorption strength, this is also observed when doping with B^{3+} and Sc^{3+} ions. However, scandium also causes the absorption band to red shift from 430 to 450 nm [205]. Similar trends are observed for the gadolinium garnets. In this case, it is not possible to estimate the shift due to scandium ions, since the compound without scandium is not stable in bulk form. However, B^{3+} influences the absorption strength. As the boron content increases, absorption becomes stronger. Electron transitions characteristic of Ce^{3+} can be observed, however, additionally, characteristic transitions of Gd^{3+} can also be observed at 340 nm and are identified as the intraconfigurational transitions $^8S_{7/2} \rightarrow {}^6P_j$.

These transitions are not present in Lu based garnet samples because of the lack of Gd^{3+} [206].

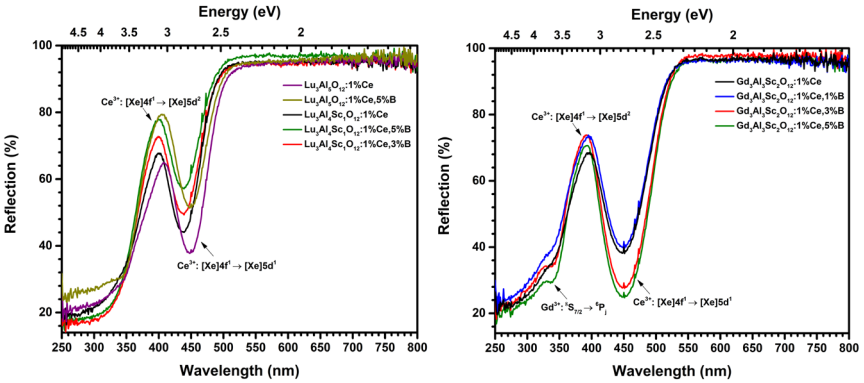

Figure 36. Reflection spectra of 1% cerium and different amounts of boron doped $Lu_3Al_5O_{12}$, $Lu_3Al_4Sc_1O_{12}$ and $Gd_3Al_3Sc_2O_{12}$.

Figures 37 and 38 show excitation and emission spectra of different compounds measured at room temperature.

As was already observed from the reflection spectra, LuAG samples (Figure 36) show the same tendency, when garnet was doped with Sc^{3+} the emission and excitation spectra shifted to lower energy waves and the intensity of the spectra decreased [205]. In this case, boron does not have a significant effect on the emission intensity, but a small amount of it does not reduce the intensity as well. However, a larger amount reduces the intensity. XRD showed that the compounds with higher boron content show AlB_{10} impurities that could be responsible for the reduction in intensity. Other possible explanation for effect of boron on luminescence intensity is that B^{3+} can cause additional defects in lutetium or gadolinium phosphors. Although equivalent substitution of Al^{3+} and B^{3+} ions occur in matrix, defects that appear to compensate for the ionic charge cannot form because the ionic charges are the same and equal to 3+. However, the B^{3+} radii is much smaller than the Al^{3+} ion in tetrahedral and octahedral coordination and the irregularity of the coordination polyhedron of the dopant site can increase, which causes an exceptionally large increase in local strain. This strain could be partially reduced by the formation of trigonal-planar moieties of $[BO_3]$, which tend to then form oxygen vacancies and thus finally decreases the emission intensity [121].

The emission spectra also show two peaks, which are specific to cerium doped garnets, as they indicate two different electronic transitions, which are

the interconfigurational transitions $^5D \rightarrow {}^4F_{5/2}$ at higher energy and $^5D \rightarrow {}^4F_{7/2}$ at lower energy [75].

Emission and excitation spectra of gadolinium aluminum scandium garnet samples are plotted in Figure 38. An $^8S_{7/2} \rightarrow {}^6I_j$ electron transition at 260 nm, which is attributed to Gd^{3+}, is additionally visible in the excitation spectra [207]. In contrast to LuAG, boron has an obvious influence on the intensity of these luminescence spectra. From the emission and excitation spectra, it can be derived that compounds doped with 5% and especially 3% B^{3+} show the highest intensities, while the boron free compound shows the lowest. From the SEM data, it is known that compounds with more boron have larger particles. The particle growth was likely responsible for the increase in intensity, due to the lower surface area to volume ratio resulting in less surface quenching and thus higher PL intensity [182,183]. In this case, it can also be observed that the emission maximum is red-shifted towards 580 nm. This shift can be explained by the different covalency of these compounds, which results from the different electronegativity of constituent atoms [179].

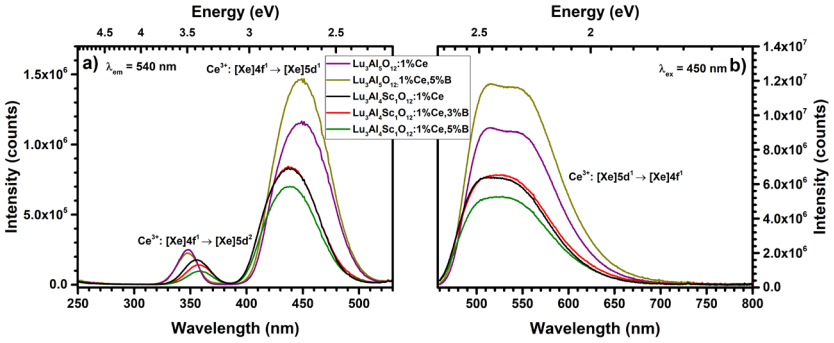

Figure 37. Excitation (a) and emission (b) spectra of 1% cerium and different amounts of boron doped $Lu_3Al_5O_{12}$ and $Lu_3Al_4Sc_1O_{12}$.

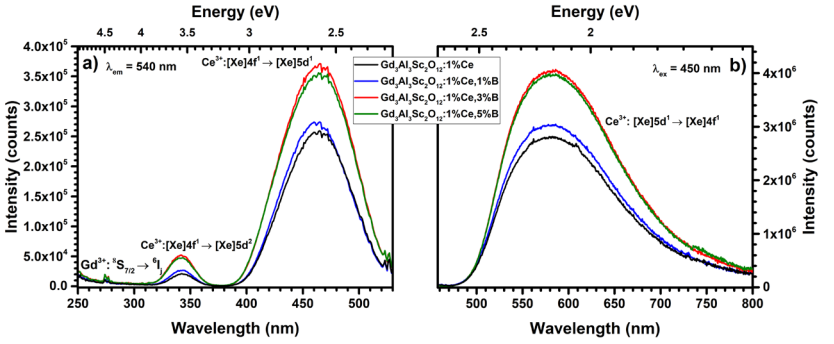

Figure 38. Excitation (a) and emission (b) spectra of 1% cerium and different amounts of boron doped $Gd_3Al_3Sc_2O_{12}$.

To find out how effective the synthesized materials are as scintillators, radioluminescence emission measurements were also performed for all samples. All cerium and boron doped lutetium and gadolinium aluminum scandium garnets were excited with X-rays (50 kV, 1.8 mA).

From the left part of Figure 39, lutetium garnets without scandium have a more intense emission. This was to be expected since the scandium extinguishes the intensity of the emission [208]. However, garnet doped with 5% of boron has the most intense emission characteristic of cerium ions $[Xe]5d^1 \rightarrow [Xe]4f^1$ with maxima at a wavelength of 550 nm. The emission intensity of this sample is as much as 1.5 times higher than that of the boron-free sample. This, as in the case of photoluminescence, can be explained by the different particle sizes [182,183]. An additional peak at around 685 nm can be attributed to the photoluminescence of a Cr^{3+} impurity, which was most likely caused due to the use of chromium containing aluminum nitrate as a starting material. The emission of these ions when excited by X-rays is relatively strong, so impurity is very clearly visible even at extremely low content. This is quite a common occurrence and the low content of impurities can be confirmed due to the fact that these emission peaks are not observed under regular excitation conditions (Figure 37) [184].

The right graph of Figure 39 shows the emission spectra of cerium and boron doped gadolinium aluminum scandium garnets. From these spectra, it can be seen that boron increases the intensity of the emission like in LuAG samples. The most intense emission was observed for garnet doped with 3% of boron, and the least intense emission for the boron-free garnet. This garnet indeed has an additional peak at approximately 608 nm, however, this is an artifact stemming from the measurement procedure and not a property of the sample. From the results of the radioluminescence emission spectra, it can be concluded that the addition of boron has a large and important influence on the compounds that are used for excitation with X-rays. In this case, boron ions increase the intensity of radioluminescence emission.

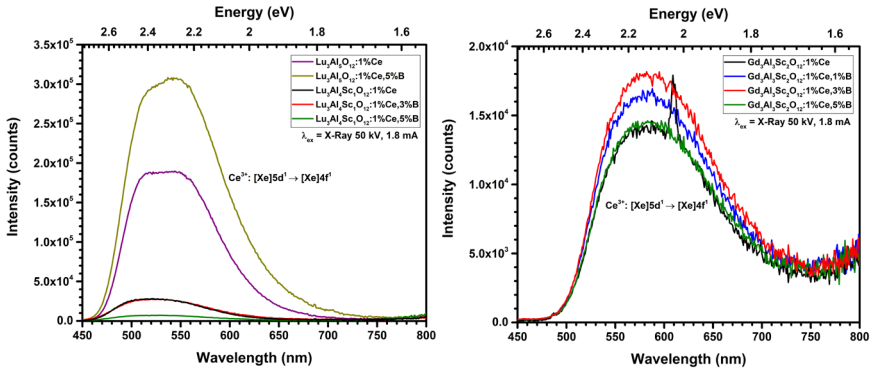

Figure 39. Emission spectra of 1% cerium and different amounts of boron doped $Lu_3Al_5O_{12}$, $Lu_3Al_4Sc_1O_{12}$ (left) and $Gd_3Al_3Sc_2O_{12}$ (right) under X-ray excitation.

Ce^{3+} activated garnets have a decay time in the ns range [75]. In this case, the same trend is obtained. The measured decay time of the compounds and the B^{3+} influence of these values is shown in Table 4.

The decay time of the synthesized samples range from 60 to 46 ns. It should be noted that in this synthesized series, the decay time of lutetium aluminum garnet are slightly shorter than the usual ones mentioned in other sources, where they equal to 68 ns [11]. In this case, lutetium aluminum garnet doped only with cerium has the longest decay time, which is 60.6 ns. Increasing the boron content and adding scandium shortens the decay time. Lutetium garnet doped with scandium and 3% boron, most likely due to the formation of recombination centers has the shortest decay, equaling 53.1 ns [208].

As expected, the decay time of gadolinium aluminum scandium garnets is shorter than that of lutetium garnets [107]. It can be seen from Table 4 that increasing the amount of boron in the compounds decreases the decay time. The decay time is even 4.2 ns shorter for the compound doped with 5% of boron compared to the compound without boron.

Table 4 also shows the quantum efficiency values of the compounds. Lutetium aluminum garnets exhibit higher EQE values than gadolinium aluminum scandium garnets. A significant difference can again be seen due to the addition of boron to the compounds. Boron increases the quantum efficiency of the compounds. For LuAG, the EQE increases by more than 19%. The corresponding change is also seen in gadolinium garnets, although it is smaller.

Table 4. Synthesized samples decay time and quantum efficiency.

Sample	Decay time [ns]	Quantum efficiency [%]
$Lu_3Al_5O_{12}$:1%Ce	60.6 ± 0.1	39
$Lu_3Al_5O_{12}$:1%Ce,5%B	58.8 ± 0.1	59
$Lu_3Al_4Sc_1O_{12}$:1%Ce	54.9 ± 0.1	31
$Lu_3Al_4Sc_1O_{12}$:1%Ce,3%B	53.1 ± 0.1	35
$Lu_3Al_4Sc_1O_{12}$:1%Ce,5%B	54.0 ± 0.1	33
$Gd_3Al_3Sc_2O_{12}$:1%Ce	50.8 ± 0.2	12
$Gd_3Al_3Sc_2O_{12}$:1%Ce,1%B	49.6 ± 0.2	13
$Gd_3Al_3Sc_2O_{12}$:1%Ce,3%B	46.8 ± 0.2	15
$Gd_3Al_3Sc_2O_{12}$:1%Ce,5%B	46.6 ± 0.2	14

However, it can be observed that garnets containing scandium doped with 5% of boron have a lower EQE value. This can be explained by the appearance of impurities, which are confirmed by X-ray diffraction analysis. Compounds doped with larger amounts of B^{3+} have more defects that absorb part of the photons falling on the sample. This is reducing in the amount of photons absorbed and emitted by the desired phase [188].

3.5. Effect of Boron and Scandium Modification of Pr^{3+} Doped LuAG and GdAG on the Luminescence Properties

Both lutetium and gadolinium aluminum garnets doped with praseodymium (Pr^{3+}), according to literature sources, have shorter decay times than, for example, compounds doped with cerium (Ce^{3+}). It was decided to synthesize praseodymium doped garnets with a completely new elemental composition and to see what influence the modification of compounds with scandium and boron has on the structural and luminescent properties. To our best knowledge, elemental composition of $Gd_3Al_3Sc_2O_{12}$:B,Pr has been reported for the first time.

All the information presented is published in the scientific article **P5** and article supplementary material file. In addition, a list of synthesized and described garnets powders, results of particle size distribution histograms, reflection spectra, profiles of decay time curves and temperature dependent luminescence properties can be found in the publication.

3.5.1. Inductively Coupled Plasma Optical Emission Spectrometry

The $Gd_3Al_3Sc_2O_{12}$ garnets were analyzed by ICP-OES to determine the molar concentration of Pr^{3+} and B^{3+} in the samples. The results are shown in Table 5. Praseodymium amount varies slightly but is close to 1%, the discrepancies may most likely be caused by the small amount present and the inaccuracies of the analysis itself. The amount of boron in the compounds varied from 0% to 5% during the synthesis. From the obtained results, it can be seen that the actual measured amount is not identical to the calculated one. However, the difference is quite small in all cases. Despite the existing differences and the overall trend remains as expected, the more B^{3+} was added to the structure, the more was detected. Garnets, which should contain 3% and 5% boron, show slightly lower values of 2.6% and 4.2% respectively. This reduction may have occurred because of the low melting point of boric acid which causes some of the B^{3+} have evaporated.

Table 5. Praseodymium and boron content % in GdASG samples measured by ICP-OES.

Sample	Praseodymium		Boron	
	Weighed in	Measured	Weighed in	Measured
$Gd_3Al_3Sc_2O_{12}$:1%Pr	1.0%	1.2%	0.0%	0.0%
$Gd_3Al_3Sc_2O_{12}$:1%Pr,1%B	1.0%	1.0%	1.0%	1.3%
$Gd_3Al_3Sc_2O_{12}$:1%Pr,3%B	1.0%	1.3%	3.0%	2.6%
$Gd_3Al_3Sc_2O_{12}$:1%Pr,5%B	1.0%	1.3%	5.0%	4.2%

3.5.2. X-Ray Diffraction Analysis

Since the luminescence properties are dependent on the phase composition of the materials it is imperative to fully investigate the compositional makeup of each sample. As such, the phase purity of the samples was investigated by X-ray diffraction analysis and Rietveld refinement.

The XRD patterns and the results of Rietveld refinement of GdASG doped with Pr^{3+} and B^{3+} are plotted in Figure 40, while the results for LuAG, and LuASG doped with Pr^{3+} and B^{3+} can be found in article P5. From the Rietveld refinement results displayed in Figure 40 (left), it can be observed that samples containing 0 and 1% of boron possess a single phase garnet structure with a space group $Ia\bar{3}d$. The model shows quite a good fit with no unattributed reflections. However, when the sample is doped with 3% of B^{3+} additional

diffraction peak is observed at around 32 2θ(°). This impurity phase was identified as Sc_2O_3 with a space group of $I\bar{a}3$ and when 5% B^{3+} is added, another impurity phase of $GdAl_3(BO_3)_4$ with an *R*32 space group (Powder Diffraction File, (PDF) #04-002-9348) is observed as indicated by new reflection at around 33.5 2θ(°). However, while the impurities in these cases are indeed present, their fractions are rather insignificant. In the case when 3% of boron was used the impurities consisted of only 0.64%, and in the second case (5% of Boron) – 1.73%.

Figure 40 (bottom right) shows the variation of unit cell parameters based on the B^{3+} content in the samples. In all cases when boron was introduced into the unit cell a reduction of the lattice parameter was observed. This is due to the ionic radii difference between Al^{3+} (0.54 Å) in octahedral, (0.39 Å) in tetrahedral and B^{3+} (0.27 Å) in octahedral, (0.11 Å) in tetrahedral as boron is much smaller [209]. In GdASG:Pr, the unit cell parameter *a* slightly reduces from 12.331 Å to 12.328 Å, in LuASG:Pr from 12.068 Å to 12.060 Å, and in LuAG:Pr from 11.914 Å to 11.900 Å. The unit cell parameter of $Lu_3Al_5O_{12}$ garnet was reported to be around 11.906 Å [210]. Overall, the gadolinium based garnet showed the largest size, followed by the Al-Sc garnet, and the simple Lu-Al garnet exhibited the smallest lattice parameter. Consequently, it can be stated that Sc^{3+} (0.75 Å) and Pr^{3+} (1.13 Å) increased doping level leads to an expansion of the crystal lattice, while the introduction of B^{3+} ions causes it to contract as expected from the ionic radii differences [209].

The visualization of the garnet structure from the data obtained after Rietveld refinement can be found in Figure 40 (top right). Visualization was made with the program "Vesta" [211]. Garnets have a cubic crystal structure with the $Ia\bar{3}d$ space group. In such a structure there are three independent positions, an 8-fold coordinated dodecahedral, a 6-fold coordinated octahedral, and a 4-fold coordinated tetrahedral positions. Depending on the size, elements can occupy different positions in the structure. In this case, $Sc^{3+,}$ $Al^{3+,}$ and B^{3+} occupy tetrahedral and octahedral sites, and Lu^{3+}, $Gd^{3+,}$ and Pr^{3+} the dodecahedral sites. All of the coordination polyhedrons are shown in Figure 2. Overall, the obtained crystallographic results fit well with the ones reported in the literature [212,213].

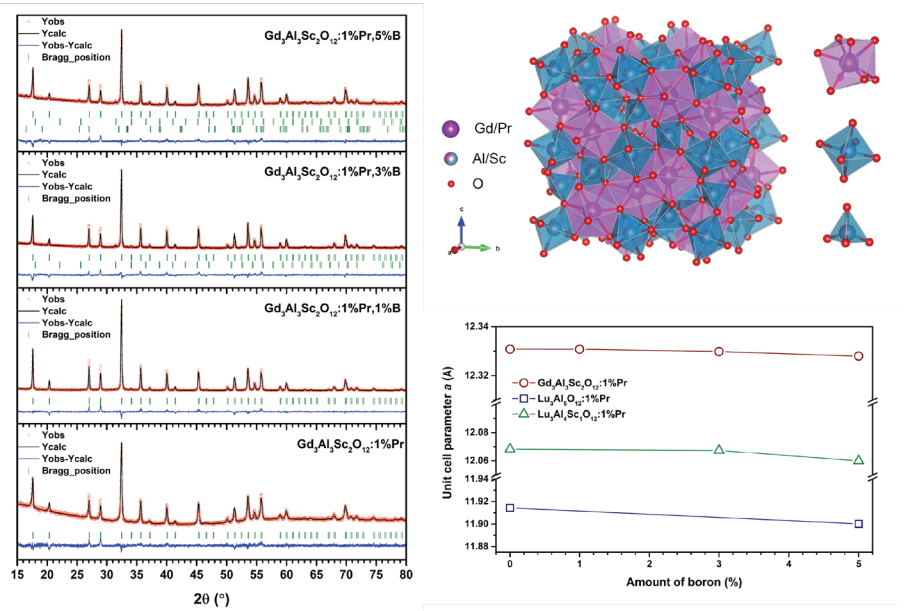

Figure 40. Rietveld refinement results of XRD data recorded for Pr^{3+} and B^{3+} doped $Gd_3Al_3Sc_2O_{12}$ at room temperature (red dots are the experimental data; black lines are calculated data), Bragg reflections are indicated by vertical ticks. Top right – a structure of garnet cell after Rietveld refinement. Bottom right – unit cell parameter *a* after Rietveld refinement of all synthesized samples.

3.5.3. Scanning Electron Microscopy Analysis

SEM images of $Lu_3Al_5O_{12}$ and $Lu_3Al_4Sc_1O_{12}$ garnets doped with Pr^{3+} and different amounts of boron are shown in Figure 41. $Gd_3Al_3Sc_2O_{12}$ garnets – in Figure 4. Garnet samples that are prepared by the sol-gel method, commonly are characterized by irregularly shaped individual and interconnected particles that may have unfilled pores between them [214–216].

It can be seen that samples without boron have smaller particles as compared to those containing B^{3+} ions. As the boron content increases, the particle size also increases. This is observed for LuAG and LuASG samples. However, it is especially noticeable in the $Gd_3Al_3Sc_2O_{12}$ samples. This may be caused by the fact that the initial particle size for this composition is much smaller as compared to the Lu based garnets as well as by a more gradual increase in boron content from 0%, 1%, 3% to 5%. In this case, particle size increases from nanometer scale to micrometer one.

In Figure 42, it can be observed that the porosity of garnets decreases as the boron content increases. Overall, the incorporation of B^{3+} leads to a larger particle size as well as a reduction in porosity.

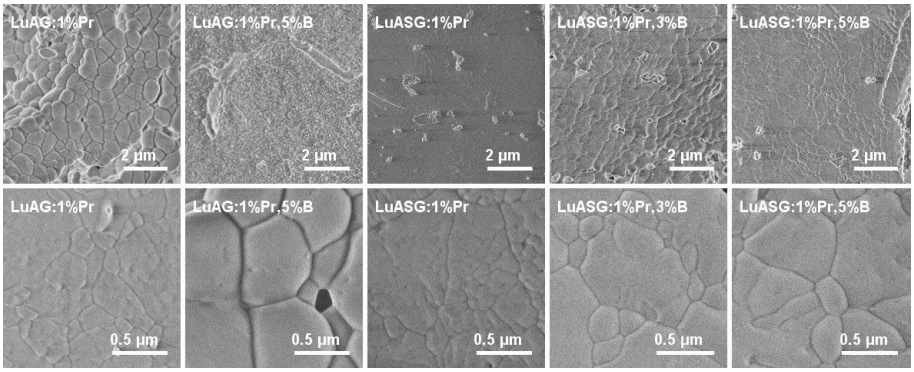

Figure 41. SEM images of 1% Pr^{3+} and different amounts of B^{3+} doped $Lu_3Al_5O_{12}$ and $Lu_3Al_4Sc_1O_{12}$ garnet samples in different magnifications.

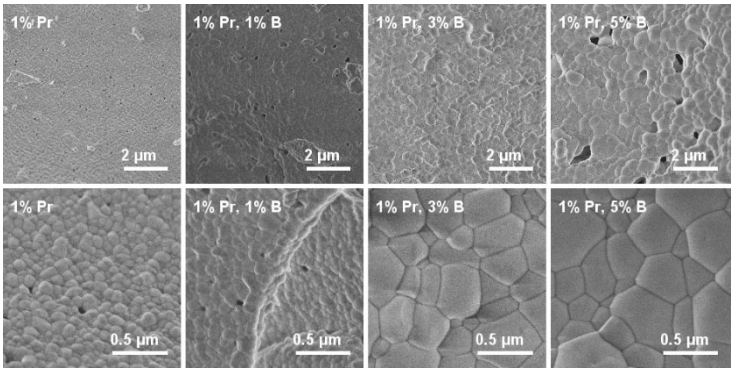

Figure 42. SEM images of 1% Pr^{3+} and different amounts of B^{3+} doped $Gd_3Al_3Sc_2O_{12}$ garnet samples in different magnifications.

3.5.4. Luminescent Properties

VUV and UV excitation spectra were measured for all synthesized samples using 312 nm as emission wavelength. Figure 43 (left) shows the normalized excitation spectra of lutetium garnets in the range from 120 nm to 310 nm with an intense band being visible at 172 nm. It is assigned to host the absorption of LuAG. From 230 nm two intense bands are assigned to praseodymium ion excitation [217].

The normalized excitation spectra of the GdASG samples are shown in Figure 43 (right). It is quite difficult to ascribe the bands existing in the 120 nm

to 200 nm region as not much data is present in the literature for such composition, however similarly as before, at least in part it could arise from the band gap of the matrix compound. Bands from 200 nm are attributed to Pr^{3+} centered $^3H_4 \rightarrow [Xe]4f^15d^1$ transitions and Gd^{3+} centered $^8S_{7/2} \rightarrow {}^6I_J$ and $^8S_{7/2} \rightarrow {}^6P_J$ transitions.

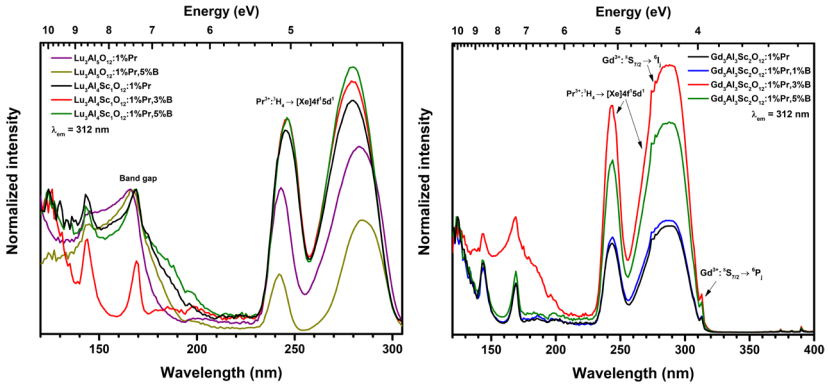

Figure 43. VUV and UV excitation spectra of 1% of praseodymium and different amounts of boron doped $Lu_3Al_5O_{12}$, $Lu_3Al_4Sc_1O_{12}$ (left) and $Gd_3Al_3Sc_2O_{12}$ (right) samples.

Figures 44 and 45 show the excitation (a) and emission (b) spectra of LuAG, LuASG, and GdASG phosphors measured at room temperature. From the data given in Figure 44, it can be observed that $Lu_3Al_5O_{12}$ and $Lu_3Al_4Sc_1O_{12}$ garnets exhibit characteristic excitation spectra of praseodymium ion with (a) and $^3H_4 \rightarrow [Xe]4f^15d^1$ electron transitions.

Additionally, a peak shift is observed between different samples. LuAG samples have excitation peaks at lower energy waves than samples containing Sc^{3+}. This shift occurrence can be explained by the covalency effect, because of the reduction of the energy between the lowest 5d and lowest 4f energy levels [218]. The presence of Sc^{3+} in the structure also affects the intensity of the excitation spectra, mainly resulting in a reduction in intensity. However, samples containing B^{3+} have higher intensity, with the most intense being the compound with 3% of B^{3+}.

Electron transitions ascribed to praseodymium ions are also visible in the emission (b) spectrum [219,220]. During the measurement of emission spectra λ_{ex} = 285 nm was used for the excitation. In the wavelength range of 300 – 460 nm, characteristic, allowed, and more intense $[Xe]4f^2 \rightarrow [Xe]4f^15d^1$ electron transitions are visible.

As in the excitation spectra, garnets without Sc^{3+} have the most intense emission, while out of the LuASG samples, garnet doped with 3% boron

showed the most intense emission. The $[Xe]4f^2 \rightarrow [Xe]4f^2$ transitions of lower intensity are seen in the 450 to 800 nm wavelength spectral range. In this case, the LuASG sample with 3% B^{3+} has the most intense emission ($4f^15d^1 \rightarrow {}^3H_j, {}^3F_j$ transition).

It can be observed that in the case of $[Xe]4f^2 \rightarrow [Xe]4f^2$ transitions boron significantly improves the emission intensity. This may be most likely caused by the increase in particle size, which was induced by the use of B^{3+} as a flux.

Figure 45 (a) shows the excitation spectra of GdASG samples. In this case, electron transitions characteristic not only of praseodymium ions but also of gadolinium ions are observed [220,221]. At 242 nm and 285 nm Pr^{3+} ($^3H_4 \rightarrow [Xe]4f^15d^1$) and at 312 nm – Gd^{3+} ($^8S_{7/2} \rightarrow {}^6P_J$). In this case, the B^{3+} in the structure has a totally positive effect and all compounds containing boron have a stronger excitation, with the highest intensity sample being the one with doped 5% of B^{3+}. Interestingly, this sample has the highest amount of impurities, as such it is possible that they are in part responsible for the high-excitation intensity.

Since a large amount of scandium (especially in gadolinium garnet) quenches the $[Xe]4f^2 \rightarrow [Xe]4f^15d^1$ emission of praseodymium, no emission of these transitions is observed in Figure 45 (b) [85,86]. However, more intense $[Xe]4f^2 \rightarrow [Xe]4f^2$ emission is observed in this case (compared to LuAG and LuASG). Furthermore, the compound with 5% B^{3+} is also characterized by the most intense emission. As with excitation, the intensity is believed to be driven by the resulting impurities and changing particle size, as boron acts as a flux during synthesis [14,176].

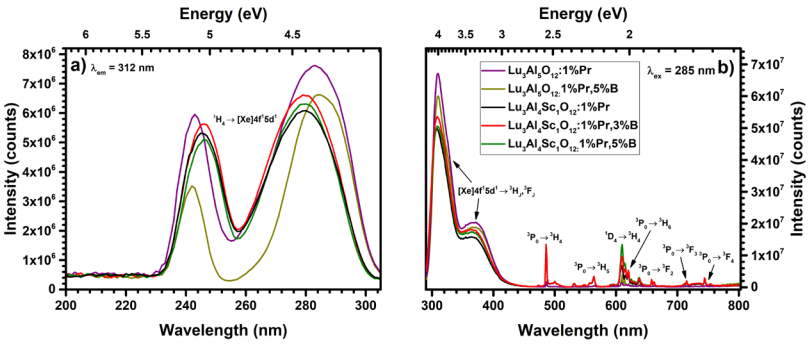

Figure 44. Excitation (a) and emission (b) spectra of 1% of praseodymium and different amounts of boron doped $Lu_3Al_5O_{12}$ and $Lu_3Al_4Sc_1O_{12}$.

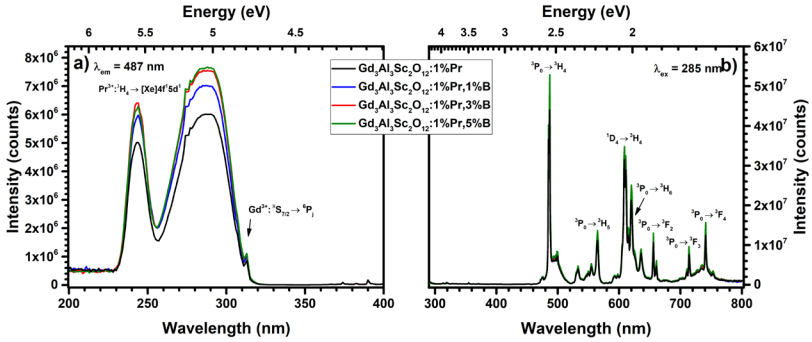

Figure 45. Excitation (a) and emission (b) spectra of 1% of praseodymium and different amounts of boron doped $Gd_3Al_3Sc_2O_{12}$.

The application of scintillators is based on the excitation of samples with high-energy radiation. Figures 46 and 47 show the emission spectra in conventional and heatmap forms with the integrated emission intensities of synthesized garnets under X-ray excitation at 50 kV and 1.8 mA.

The conventional spectra of LuAG and LuASG can be seen in Figure 46 left part. Both $[Xe]4f^2 \rightarrow [Xe]4f^15d^1$ and $[Xe]4f^2 \rightarrow [Xe]4f^2$ electron transitions characteristic of Pr^{3+} are observed under X-ray excitation. From the data, it can be seen that the introduction of scandium into the garnet lattice reduces the intensity of $[Xe]4f^2 \rightarrow [Xe]4f^15d^1$ electron transition but increases $[Xe]4f^2 \rightarrow [Xe]4f^2$ emission intensity. LuAG:1%Pr, as under UV excitation, exhibits the highest $[Xe]4f^2 \rightarrow [Xe]4f^15d^1$ emission intensity, as shown by the conventional emission spectrum (left) and heatmap (right).

Meanwhile, the most intense $[Xe]4f^2 \rightarrow [Xe]4f^2$ transitions are observed for LuASG:1%Pr,5%B sample. These differences are more clearly visible in the heatmap and in the graph of integrated intensity since the increase in intensity (red color) for this sample at 610 nm is readily observable. Similarly, under UV excitation, the increase in intensity may result from the increase in particle size upon the doping of B^{3+}.

Figure 47 left part shows the emission spectra of GdASG under X-ray excitation. The $[Xe]4f^2 \rightarrow [Xe]4f^15d^1$ electron transitions should be quenched by Sc^{3+} ions, but for the GdASG:1%Pr,3%B sample is visible in the 300 to 400 nm spectral range. Furthermore, the introduction of B^{3+} leads to an increase in the emission intensity for the $[Xe]4f^2 \rightarrow [Xe]4f^2$ transitions. The most intense emission was observed for the GdASG:1%Pr,3%B sample, which is even $1.2x10^5$ more intense than the sample without boron.

The discussed changes can be more clearly visible in the heat map (right side), which shows a yellow color at this sample and wavelength. These

observations are also confirmed by the graph of integrated intensities. Overall, B^{3+} has a positive effect on the emission intensity when X-ray excitation is used. Thus, indicating that such garnets could potentially be better scintillators than the boron-free samples.

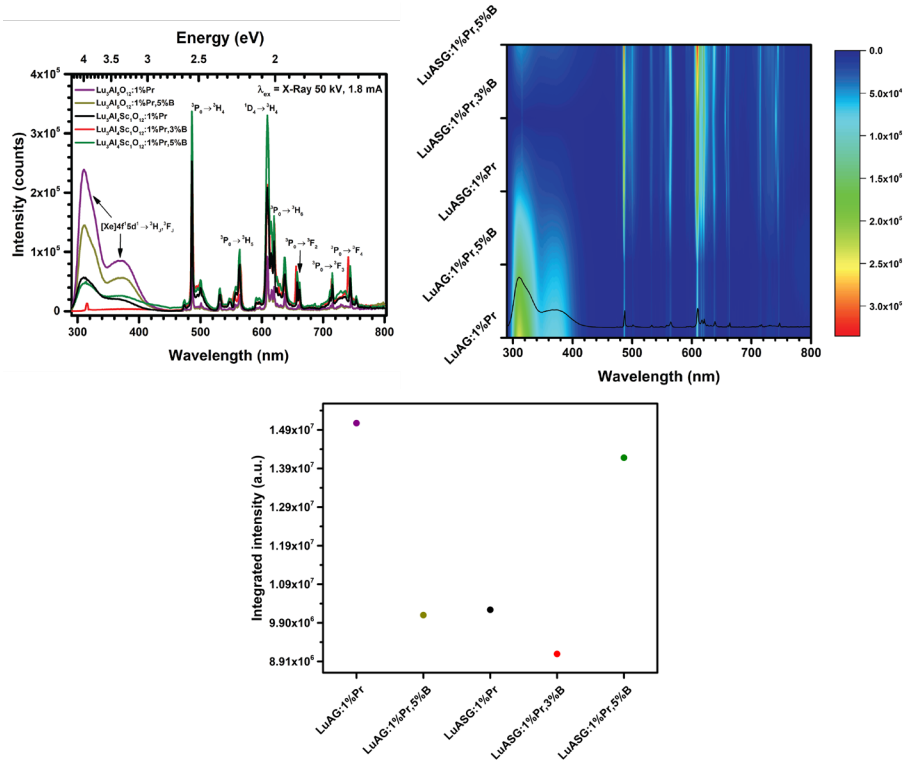

Figure 46. (Top) Emission spectra under X-Ray excitation (left), heatmap (right) of 1% of praseodymium and different amounts of boron doped $Lu_3Al_5O_{12}$ and $Lu_3Al_4Sc_1O_{12}$. (Bottom) Integrated intensities of samples emission spectra.

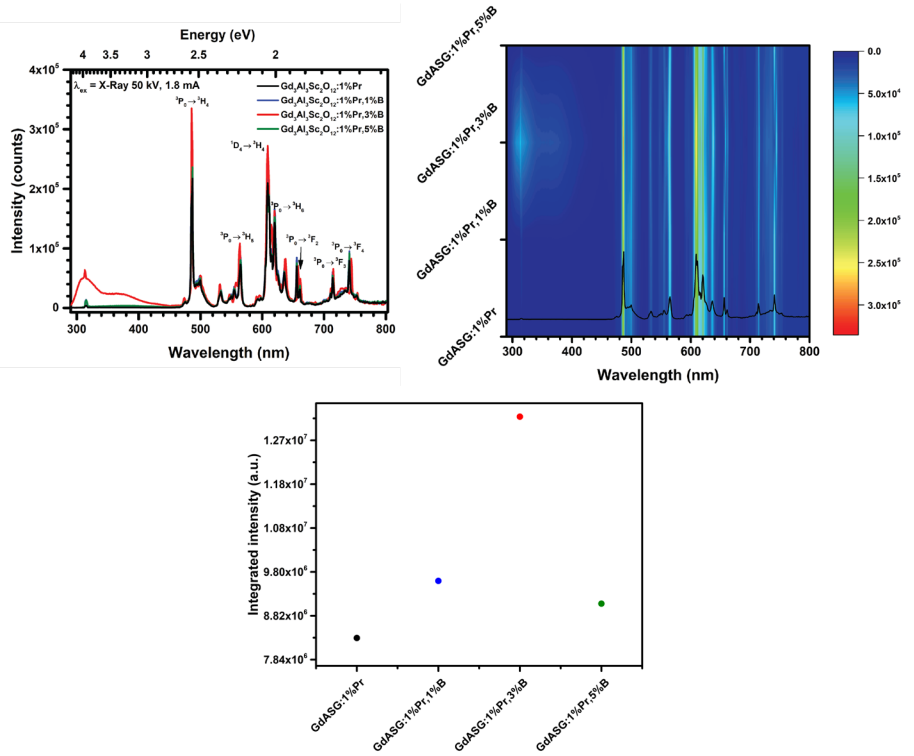

Figure 47. (Top) Emission spectra under X-ray excitation (left), heatmap (right) of 1% of praseodymium and varying amounts of boron doped $Gd_3Al_3Sc_2O_{12}$. (Bottom) Integrated intensities of samples emission spectra.

The measured decay times (excited at 265 nm for lutetium garnets and 285 nm for gadolinium garnets) and quantum efficiency values of the compounds at room temperature are given in Table 6.

The decay time of lutetium garnets is in the nanoseconds range, while that of gadolinium garnets is in microseconds. As there is energy migration through the Gd^{3+} sublattice, it acts as a slow component and the garnets' decay time becomes longer with Gd^{3+} than with Lu^{3+} ion [222]. The decay time of LuAG decreases as much as 3.6 ns when garnet is doped with boron. LuAG:1%Pr,5%B has the shortest decay time of all synthesized samples, and it is equal to 19.5 ns. The presence of boron in the garnet structure has a positive effect on the reduction of decay time values.

The decay times of the GdASG samples vary from 8.8 to 8.3 μm. As with LuAG and LuASG samples, values are reduced by doping compounds with B^{3+} ions. $Gd_3Al_3Sc_2O_{12}$:1%Pr,3%B has the lowest decay time. This reduction in value is due to the optimal amount of boron ions and the relatively low amount of impurities (just 0.64%). Further, increase in B^{3+} doping leads to an

increase in the amount of impurities (up to 1.73%), as a result the decay time may also increase.

In terms of quantum efficiency, $Lu_3Al_4Sc_1O_{12}$:1%Pr,5%B has the highest value of 87%. Meanwhile, the values of the other samples vary widely, although they tend to be greater than 50%. Table 6 shows that gadolinium garnets have lower EQE values than lutetium garnets. Interestingly, only in the LuAG case, a decrease in EQE was observed when boron was introduced. As in the LuASG and GdASG cases, a quite steady increase in the efficiency values was observed based on the B^{3+} content in the sample. The higher the doping content, the higher the values obtained, in LuASG ranging from 49% to 87%, and in GdASG values changed from 10% to 46%.

Table 6. Synthesized samples decay time and quantum efficiency.

Sample	Decay time	Quantum efficiency [%]
$Lu_3Al_5O_{12}$:1%Pr	23.1 ± 0.1 ns	70
$Lu_3Al_5O_{12}$:1%Pr,5%B	19.5 ± 0.1 ns	52
$Lu_3Al_4Sc_1O_{12}$:1% Pr	22.4 ± 0.1 ns	49
$Lu_3Al_4Sc_1O_{12}$:1% Pr,3%B	19.7 ± 0.1 ns	60
$Lu_3Al_4Sc_1O_{12}$:1% Pr,5%B	19.9 ± 0.1 ns	87
$Gd_3Al_3Sc_2O_{12}$:1% Pr	8.8 ± 0.2 µs	10
$Gd_3Al_3Sc_2O_{12}$:1% Pr,1%B	8.6 ± 0.2 µs	33
$Gd_3Al_3Sc_2O_{12}$:1% Pr,3%B	8.3 ± 0.2 µs	39
$Gd_3Al_3Sc_2O_{12}$:1% Pr,5%B	8.5 ± 0.2 µs	46

In conclusion, it can be said that lutetium aluminum garnet doped with 5% boron has the shortest decay time that managed to synthesize, which is 19.5 ns. Compounds of this value could already be used in commercial applications. However, in this case, coatings and ceramics of compounds with such a composition should be investigated.

CONCLUSIONS

1. Regardless of the fact that garnets doped with cerium ions (Ce^{3+}) are always heated in a reducing atmosphere, better luminescence properties (higher emission intensity, higher quantum efficiency and shorter decay time) are obtained when these compounds are doped with boron and heated in air.
2. The aqueous sol-gel synthesis method allows for the insertion of up to 5 mol% of boron ions into the garnet structure without the presence of extraneous phases. When compounds are doped with larger amounts of boron, the appearance of extraneous phases has already been observed. The exceptions are gotten in GdASG compounds, where an impurity phase is observed already with 3 mol% of boron.
3. The sol-gel spin-coating and dip-coating coating deposition techniques have been successfully used in the coating of garnet films on either quartz (SiO_2) or sapphire (Al_2O_3) substrates. A comparison of the two preparation techniques and the two substrates reveals that the optimal choice is a sapphire substrate and spin-coating technology for the production of films. In such conditions, the coating exhibits optimal properties, with a more uniform surface and the absence of cracks observed in other cases.
4. Yttrium, lutetium aluminum garnet ceramics doped with cerium and co-doped with boron and magnesium were successfully synthesized for the first time. Boron-doped ceramics exhibited enhanced emission and shorter decay times than garnets of similar elemental composition in literature sources.
5. The changes in morphology of garnets were observed, wherein the introduction of boron into the structure results in an increase in particle size. This is attributed to the role of boron as a flux. Larger particle size exerts a significant positive influence on the intensities of the reflection, emission, and excitation spectra of the compounds. Boron doped garnets (as long as pure garnet phase is observed) exhibit more intense spectral intensities than compounds lacking boron in their elemental composition. This phenomenon was observed in all garnets that were studied.
6. ICP-OES measurements revealed that the boron content of these compounds is in close agreement with theoretical values. It can be concluded that boron enters the garnet structure during synthesis and exerts a significant positive influence on the studied structural and luminescent properties.

7. Radioluminescence emission spectra, that most significantly describe scintillators, are also characterized by a positive effect resulting from the presence of boron in garnet composition. This positive effect is highlighted by the increase emission intensity. The summary of the data indicates that lutetium aluminum garnets doped with both cerium (Ce^{3+}) and praseodymium (Pr^{3+}) ions and co-doped with boron (B^{3+}) exhibits the highest radioluminescence emission intensity values.
8. Samples containing boron ions within the garnet crystal lattice exhibited shorter decay times than those without (particularly YAG:Ce and LuAG:Ce samples). This change can be attributed to the fact that boron ions possess a higher electronegativity than aluminum ions, which reduces polarization and therefore shortens the decay time. The described trend is observed not only in powder samples but also in synthesized coatings and ceramics.
9. Based on all of the obtained results, while taking into account the phase purity and the values of the decay times, the best compounds that could be used as a scintillator would be praseodymium and 5% of boron doped lutetium aluminum garnet. In particular it had the shortest overall decay time, which is equal to 19.5 ns. However, cerium and 5% of boron doped lutetium aluminum garnet also exhibited excellent properties. The decay time of this compound was one of the shortest amongst all cerium doped compounds for powder, coating, and ceramic forms.

LIST OF PUBLICATION AND CONFERENCES PARTICIPATION

List of Papers Related to the Dissertation

[P1] **G. Inkrataite,** M. Kemere, A. Sarakovskis, R. Skaudzius. Influence of Boron on the Essential Properties for New Generation Scintillators, Journal of Alloys and Compounds, 875, 160002, 2021. DOI: https://doi.org/10.1016/j.jallcom.2021.160002.

[P2] **G. Inkrataitė**, Ž. Stankevičiūtė, R. Skaudžius, Determination of different garnet films characteristics prepared via sol-gel spin or dip-coatings techniques, Journal of Luminescence, 244, 118751, 2022. DOI: 10.1016/j.jlumin.2022.118751.

[P3] **G. Inkrataite**, M. Skruodiene, R. Skaudzius. Synthesis and investigation of novel boron and magnesium doped YAG:Ce and LuAG:Ce phosphor ceramics. Luminescence. 391, 1, p. 4673, 2024. DOI: http://doi.org/10.1002/bio.4673.

[P4] **G. Inkrataite**, J.N. Keil, A. Zarkov, T. Jüstel, R. Skaudzius. The effect of boron and scandium doping on the luminescence of LuAG: Ce and GdAG: Ce for application as scintillators. Journal of Alloys and Compounds, 966, 171634, 2023. DOI: https://doi.org/10.1016/j.jallcom.2023.171634.

[P5] **G. Inkrataite**, J.N. Keil, A. Kizalaite, T. Jüstel, R. Skaudzius. Synthesis of Praseodymium Doped Lutetium and Gadolinium Aluminum Garnets Modified by Scandium and Boron to Improve Luminescence Properties. Ceramics International, 50, 11, 41879-41891, 2024. DOI: https://doi.org/10.1016/j.ceramint.2024.08.041

List of Conferences Related to the Dissertation

[C1] **Greta Inkrataitė**; Ramūnas Skaudžius. "Determination of different garnet films characteristics prepared using sol-gel and spin or dip-coatings techniques". NBCM 2020: Nanostructured Bioceramic Materials: International Conference. Vilnius, Lithuania, December 1-3, 2020;

[C2] **Greta Inkrataitė**; Ramūnas Skaudžius. "Coats of cerium, boron and/or magnesium doped garnets on different pallets and their luminescence properties for scintillators application". Functional Materials and Nanotechnologies: 13th international conference, FM&NT-2020. Vilnius, Lithuania, November 23-26, 2020;

[C3] **Greta Inkrataitė**; Ramūnas Skaudžius. "Synthesis and investigation of LuAG:Pr,B coatings on quartz substrate obtained by sol-gel spin coating technique". Open readings 2021: 64th International Conference for Students of Physics and Natural sciences. Vilnius, Lithuania, March 16-19, 2021 **(žodinis pranešimas)**;

[C4] **Greta Inkrataitė**; Ramūnas Skaudžius. "Characterization of Photoluminescence Garnet Coatings Derived by Sol-Gel Spin/Dip Coating Techniques" Advanced Materials and Technologies 2021: 23nd International Conference-School. Palanga, Lithuania, August 23-27, 2021;

[C5] **Greta Inkrataitė**; Ramūnas Skaudžius. "Investigation of cerium and boron doped yttrium and lutetium aluminum garnet ceramics". 16th International Conference of Lithuanian Chemistry Society "Chemistry and Chemical Technology". Vilnius, Lithuania, September 24, 2021;

[C6] **Greta Inkrataitė**; Ramūnas Skaudžius. "Influence of boron and magnesium ions on YAG:Ce and LuAG:Ce ceramics". 22nd International Scientific Conference „EcoBalt 2021", Riga, Latvia, October 21–23, 2021;

[C7] **Greta Inkrataitė**; Meldra Kemere; Anatolijs Sarakovskis; Ramūnas Skaudžius. "The effect of boron doping on luminescence of YAG and LuAG powder, ceramic and thin films", Open Readings 2022: 65th International Conference for Students of Physics and Natural Sciences. Vilnius, Lithuania, March 15-18, 2022 **(žodinis pranešimas)**;

[C8] **Greta Inkrataitė**; Ramūnas Skaudžius. "Synthesis and Investigation of Cerium and Boron and/or Magnesium doped YAG and LuAG for High Quality Scintillators Application", International Online Conference Multis2022. Krakow, Poland, June 27-30, 2022;

[C9] **Greta Inkrataitė**; Ramūnas Skaudžius. "Characterization of Photoluminescence Garnet Coatings Derived by Sol-Gel Spin/Dip Coating Techniques", International Congress Solgel2022. Lyon, France, July 24-29, 2022;

[C10] **Greta Inkrataitė**; Meldra Kemere; Anatolijs Sarakovskis; Ramūnas Skaudžius. "YAG and LuAG powder, ceramic and thin films. The effect of boron doping on compounds", Functional Inorganic Materials. Vilnius, Lithuania, October 6-8, 2022 **(žodinis pranešimas);**

[C11] **Greta Inkrataitė**; Ramūnas Skaudžius. "Synthesis and Investigation of Novel Boron and Magnesium Doped YAG:Ce and LuAG:Ce Phosphor Ceramics", CCT2022: International Conference Chemistry and Chemical Technology. Kaunas, Lithuania, October 14, 2022;

[C12] **Greta Inkrataitė**; Jan-Niklas Keil; Thomas Jüstel; Ramūnas Skaudžius. “Effect of Different Amounts of Cr^{3+} and B^{3+} Ions on the Luminescence Properties of LuAG”, CCT2023: International Conference Chemistry and Chemical Technology. Vilnius, Lithuania, March 10, 2023;

[C13] **Greta Inkrataitė**; Jan-Niklas Keil; Thomas Jüstel; Ramūnas Skaudžius. “Insights into the Effect of Boron Doping on the Luminescence Properties of Novel Lu/Gd And Al/Sc Based Garnets for Scintilation Application”, Open Readings 2023: 66th International Conference for Students of Physics and Natural Sciences. Vilnius, Lithuania, April 18-21, 2023 **(žodinis pranešimas)**;

[C14] **Greta Inkrataitė;** Jan-Niklas Keil; Thomas Jüstel; Ramūnas Skaudžius. “Improving the Luminescence Properties of Lutetium Aluminum Garnets by Doping Different Amounts of Boron”, International conference EcoBalt 2023. Tallinn, Estonia, October 9-11, 2023.

[C15] **Greta Inkrataitė;** Jan-Niklas Keil; Thomas Jüstel; Ramūnas Skaudžius. “Synthesis and Investigations of Boron and Cerium Doped Lutetium and Gadolinium Aluminum Garnets”, 1st National Conference Chemija ir Geomokslai. Vilnius, Lithuania, March 22, 2024.

[C16] **Greta Inkrataitė;** Jan-Niklas Keil; Thomas Jüstel; Ramūnas Skaudžius. “Synthesis of New Composition Praseodymium Doped Lutetium and Gadolinium Aluminum Garnets Modified by Scandium and Boron Elements to Improve Luminescence Properties”, Open readings 2024: 67th International Conference for Students of Physics and Natural Sciences. Vilnius, Lithuania, April 23-26, 2024.

[C17] **Greta Inkrataitė;** Jan-Niklas Keil; Thomas Jüstel; Ramūnas Skaudžius. “Effects of Boron Co-doping on the Luminescence Properties of Praseodymium doped Lutetium or Gadolinium Aluminum Garnets”, International Sol-Gel Conference. Berlin, Germany, September 1-6, 2024.

List of Papers not Related to the Dissertation

[P6] **G. Inkrataite,** A. Zabiliute-Karaliune, J. Aglinskaite, P. Vitta, K. Kristinaityte, A. Marsalka, R. Skaudzius, Study of YAG:Ce and polymer composite properties for application in LED devices, ChemPlusChem. 85, (7), 1504-1510, 2020.
DOI: https://doi.org/10.1002/cplu.202000318.

[P7] **G. Inkrataite,** G. Laurinavicius, D. Enseling, A. Zarkov, T. Jüstel, R. Skaudzius. Characterization of GAGG Doped with Extremely Low Levels of Chromium and Exhibiting Exceptional Intensity of Emission in NIR Region, Crystals, 11, (6), 673, 2021.
DOI: https://doi.org/10.3390/cryst11060673.

[P8] M. Skruodiene, R. Juodvalkyte, **G. Inkrataite**, A. Pakalniskis, R. Ramanauskas, A. Sarakovskis, R. Skaudzius. Sol-Gel Assisted Molten-Salt Synthesis of Novel Single Phase $Y_{3-2x}Ca_{2x}Ta_xAl_{5-x}O_{12}$:1%Eu Garnet Structure Phosphors, Journal of Alloys and Compounds, 890, 161889, 2021.
DOI: https://doi.org/10.1016/j.jallcom.2021.161889.

[P9] **G. Inkrataitė**, A. Pakalniškis, D. Vištorskaja, R. Skaudžius, A. Kareiva. A novel sol-gel synthesis of $Ca_3Nb_{1.775}Li_{0.275}Ga_{2.95}O_{12}$ garnet, Materials letters. 316, 131990, p. 111-113, 2022.
DOI: 10.1016/j.matlet.2022.131990.

[P10] **G. Inkrataitė**, A. Pakalniškis, S. Pazylbek, D. Vištorskaja, R. Skaudžius, A. Kareiva. Sol-gel synthesis and characterization of praseodymium-doped and calcium-, titanium-substituted yttrium aluminium garnets $Pr:Y_{3-x}Ca_xAl_{5-y}Ti_yO_{12}$, Materials science and engineering B: Solid-state materials for advanced technology. 285, 115963, 2022.
DOI: 10.1016/j.mseb.2022.115963.

[P11] M.Skruodienė, M. Kemere, **G. Inkrataitė**, M. Leimane, R. Ramanauskas, R. Skaudžius, A. Sarakovskis. Synthesis and investigation of novel optical active SiO_2 glasses with entrapped YAG:Ce synthesized via sol–gel method. Gels, 9(6), 488, 2023.
DOI: https://doi.org/10.3390/gels9060488.

List of Conferences not Related to the Dissertation

[C18] **Greta Inkrataitė**; Vytautas Klimavičius; Diana Vištorskaja; Aivaras Kareiva; Ramūnas Skaudžius. “A study on Endogenous Dynamic Nuclear Polarization (DNP) is being carried out using Garnet Structure

samples synthesized through Sol-Gel methods", International Online Conference Multis2023. Krakow, Poland, July 4-6, 2023;

[C19] **Greta Inkrataitė**; Vytautas Klimavičius; Vidmantas Kalendra; Aivaras Kareiva; Ramūnas Skaudžius. "Synthesis and Application of Garnet Structure Samples for the Study of Endogenous Dynamic Nuclear Polarization (DNP)", Advanced Materials and Technologies 2023: 25th International Conference-School. Palanga, Lithuania, August 21-25, 2023;

[C20] Monika Skruodienė; Rūta Juodvalkytė; **Greta Inkrataitė**; Anatolijs Sarakovskis; Ramūnas Skaudžius. "Sol-gel and molten salt synthesis of novel $Y_{3-2x}Ca_{2x}Ta_xAl_{5-X}O_{12}$ garnet structure phosphors", NBCM 2020: Nanostructured Bioceramic Materials, International Conference. Vilnius, Lithuania, December 1-3, 2020;

[C21] Monika Skruodiene; Medara Leimane; **Greta Inkrataitė**; Meldra Kemere; Anatolijs Sarakovskis. "Optically active yttrium aluminum garnet and silica glass system", FIM 2022: International Conference "Functional Inorganic Materials 2022". Vilnius, Lithuania, October 6-8, 2022;

[C22] **Greta Inkrataitė**; Andrius Pakalniškis; Sapargali Pazylbek; Diana Vištorskaja; Ramūnas Skaudžius; Aivaras Kareiva. "Different substitution effects on the formation and properties of yttrium aluminium garnet", Advanced Materials and Technologies 2022: 24th International Conference-School. Palanga, Lithuania, August 22-26, 2022.

CURRICULUM VITAE

Personal Information	
Name, Surname	Greta Inkrataitė
Date of birth	1995-03-25
E-mail	greta.inkrataite@chgf.vu.lt inkrataite.greta@gmail.com

Education	
2002–2014	Kudirkos Naumiestis Vincas Kudirka gymnasium
2014–2018	Bachelor of Science in Chemistry, Teacher qualification, Faculty of Chemistry and Geosciences, Vilnius University
2018–2020	Master of Science in Chemistry, Faculty of Chemistry and Geosciences, Vilnius University
2020–2024	PhD studies in Chemistry, Faculty of Chemistry and Geosciences, Vilnius University

Work experience	
August 2016 August 2017 Jul 2018–Sep 2018	Laboratory Specialist, Agrochema Ltd.
Aug 2019–May 2020 Dec 2020–Mar 2022	Project Administrator, Faculty of Chemistry and Geosciences, Vilnius University
Oct 2018–Jul 2020	Junior Specialist (Project), Project Management Division, Faculty of Chemistry and Geosciences, Vilnius University
Apr 2022–Aug 2023	Project Expert, Faculty of Philosophy, Vilnius University
Aug 2022–present	Specialist (Project), Project Management Division, Faculty of Chemistry and Geosciences, Vilnius University

Aug 2020–present	Junior Administrator, Faculty of Chemistry and Geosciences, Vilnius University
Sep 2021–present	Junior Assistant Professor, Institute of Chemistry, Faculty of Chemistry and Geosciences, Vilnius University

Internships

22nd May 2022–26th May 2022	Intern, Leipzig University, Leipzig, Germany
Sep 2022–Nov 2022	Intern, Münster University of Applied Science, Steinfurt, Germany
25th Nov 2023–29th Nov 2023	Intern, University of Wroclaw, Wroclaw, Poland

Awards

2018 2019 2020	CERN named scholarships for scientific works, The Lithuanian Academy of Sciences
Spring 2019 Autumn 2019 2020	Additional scholarship for academic trip, Faculty of Chemistry and Geosciences, Vilnius University
2022 2023	Additional doctoral scholarship for academic and scientific achievements, Research Council of Lithuania
2022 2023 2024	Additional doctoral scholarship for academic trip, Research Council of Lithuania
2020 2021	Incentive scholarships for academic achievements, Vilnius University
2022	DAAD named scholarships for scientific works, German Academic Exchange Service

SANTRAUKA

ĮVADAS

Viena iš sričių, kurioje stebima sparti technologijų pažanga, yra susijusi su elektromagnetinės spinduliuotės naudojimu, kitaip tariant, tai medžiagos ar sistemos, kurios sąveikauja su šviesa. Tokie junginiai gali būti naudojami baltos šviesos diodų (LED) gamybai, ar apsauginių rašalų, skirtų popierinių banknotų apsaugai nuo padirbinėjimo, kūrimui. Minėtos sistemos yra plačiai pritaikomos ir moksliniuose prietaisuose, pavyzdžiui, gaminant detektorius ar optinius jutiklius [1–3].

Šviesos technologijomis paremti detektoriai plačiausiai naudojami prietaisuose, skirtuose medicininiam žmogaus kūno vaizdavimui ir tyrimui, pavyzdžiui kompiuterinėje tomografijoje (CT) ar pozitronų emisijos tomografijoje (PET). Šiuose prietaisuose naudojamų detektorių veikimo principas yra pagrįstas didelės energijos, tokios kaip gama ar rentgeno spinduliai, konvertavimu į matomą šviesą. Medžiagos, kurios konvertuoja didelės energijos spinduliuotę į matomą šviesą, yra vadinamos scintiliatoriais [4,5]. Siekiant gaminti aukštos kokybės detektorius, pirmiausiai, reikia gerinti juose esančių scintiliatorių savybes. Detektorių, tiksliau, jų sudėtyje esančių scintiliatorių, tobulinimas, leistų gauti tikslesnę, kokybiškesnę ir patikimesnę informaciją analizės metu. Vienas iš pagrindinių būdų, kuris leistų pagerinti medžiagų savybes – susintetinti naujus junginius, kurie pasižymėtų visomis kokybiškiems scintiliatoriams reikalingomis savybėmis: aukštu šiluminiu stabilumu, dideliu tankiu, aukštu emisijos ir sužadinimo intensyvumu (ypač sužadinant junginius aukštos energijos spinduliuote) [6–8]. Be išvardintų savybių svarbu ir aukšta kvantinės išeigos vertė, tačiau daugiausiai mokslininkų dėmesio šiuo metu yra skiriama gesimo trukmės koregavimui.

Scintiliatoriams svarbi kiek įmanoma trumpesnė gesimo trukmė. Šiuo metu tai yra vienas iš scintiliatorių kokybę ribojančių parametrų, kuris itin aktualus. Kuo trumpesnė gesimo trukmė, tuo daugiau signalų gali būti užfiksuota per tą patį laiko tarpą. Dėl šios priežasties, atliekant tyrimus detektoriai galėtų sugeneruoti kokybiškesnį, patikimesnį ir didesnės skiriamosios gebos vaizdą [9,10].

Granato struktūrą turintys neorganiniai oksidai yra laikomi beveik idealia scintiliatorių matrica. Daug dėmesio skiriama itrio aliuminio ir lutecio aliuminio granatams, legiruotiems ceriu (YAG:Ce; LuAG:Ce). Minėti granatai pasižymi visomis, scintiliatoriams reikalingomis savybėmis, įskaitant ir didelį medžiagos tankį. Dėl itin trumpos gesimo trukmės, kurios vertės yra

nanosekundžių eilės, šios medžiagos yra plačiai naudojamos detektoriuose [8,11,12].

Nors granatuose, kurie yra legiruoti Ce^{3+} jonais, gesimo trukmė yra santykinai trumpa, tačiau šią savybę vis dar siekiama gerinti. Vienas iš būdų, kaip tą galima padaryti – pakeisti junginio elementinę sudėtį. Junginius galima legiruoti pakeičiant vienus jonus kitais, taip pakoreguojant struktūrines, morfologines ir liuminescencines savybes. Iki šiol buvo atlikta daug tyrimų junginius legiruojant skirtingais jonais (pavyzdžiui: Ga^{3+}, Ca^{2+} ar In^{3+}), tačiau remiantis gautais rezultatais, matyti, kad minėtas savybes vis dar galima tobulinti. Pastaruoju metu daugėja tyrimų, kuriais įrodoma, kad boro jonai turi teigiamą įtaką granato liuminescencinėms savybėms. Boro rūgštis, kuri yra naudojama kaip sintezės pirmtakas, turi žemą lydymosi temperatūrą (170 °C), todėl ji veikia ne tik kaip B^{3+} jonų šaltinis, bet tuo pačiu ir kaip fliusas. Ši dviguba boro rūgšties savybė leidžia ne tik pagerinti granatų emisijos ir sužadinimo intensyvumą, padidinti kvantinės išeigos vertes, tačiau tuo pačiu ir sumažinti junginių gesimo trukmę [9,13,14]. Dėl minėtų priežasčių boro jonai yra puikus komponentas, galintis pagerinti reikiamas scintiliatorių charakteristikas, ypač radioliuminescencijos, fotoliuminescencijos emisijos intensyvumą ir gesimo trukmę. Remiantis moksline literatūra galima teigti, kad B^{3+} jonai turi teigiamą poveikį, tačiau apie granatų legiravimą boro jonais informacijos vis dar yra labai mažai.

Norint gerinti granatų liuminescencines savybes, kartu su teigiamą poveikį turinčiu boru, junginiai gali būti papildomai legiruojami ir kitais jonais. Šiame darbe tirta, kokią įtaką skirtingoms savybėms turi ne tik populiariausių YAG:Ce ir LuAG:Ce granatų legiravimas boru, bet ir kokia B^{3+} įtaka kitiems granato struktūros junginiams. Buvo tirti mišrūs itrio ir lutecio aliuminio granatai, taip pat oksidai, kuriuose Y^{3+} arba Lu^{3+} yra pakeičiami gadolinio jonais. Be šių pakeitimų, tikintis optines savybes pagerinti dar labiau, minėti granatai buvo legiruoti magniu ir skandžiu [15]. Medžiagos, kurių sudėtyje yra trivalenčio prazeodimio jonų, pasižymi trumpesnėmis gesimo trukmėmis, lyginant medžiagas, legiruotas Ce^{3+} jonais. Dėl šios priežasties, junginiai su Pr^{3+} taip pat yra plačiai naudojami, kaip scintiliatoriai [16].

Šiame darbe, atsižvelgiant į gesimo trukmės vertes, buvo sintetinami ne tik ceriu, bet ir prazeodimiu legiruoti granatai, o visiems junginiams buvo tiriamos scintiliatoriams labai svarbios liuminescencinės, struktūrinės ir morfologinės savybės. Sintetinami miltelių formos mėginiai yra tinkamiausi tiriant įvairias savybes, tačiau tokios formos medžiagas sunku pritaikyti praktiškai. Dėl šios priežasties papildomai buvo sintetinamos analizuojamų granatų keramikos ir plonos dangos ant kvarco bei safyro padėklų.

Pagrindinis šios disertacijos tikslas – susintetinti ir charakterizuoti granato struktūrą turinčius neorganinius oksidus, kurie pasižymėtų optimaliomis scintiliatoriams reikalingomis savybėmis, pabrėžiant trumpą gesimo trukmę.

Darbo uždaviniai:

1. Vandeniniu zolių-gelių sintezės būdu susintetinti miltelių, dangų ir keramikos formos granato struktūrą turinčius junginius, kurių sudėtyje būtų Y^{3+} / Lu^{3+} / Gd^{3+} ir Al^{3+} jonų. Šiuos granatus papildomai legiruoti ceriu (Ce^{3+}) arba prazeodimiu (Pr^{3+}), boru (B^{3+}), magniu (Mg^{2+}) arba skandžiu (Sc^{3+});
2. Siekiant nustatyti susintetintų junginių grynumą, kristalinę struktūrą, elementinę sudėtį bei gautų dalelių formą ir dydį, ištirti struktūrines ir morfologines granatų savybes;
3. Ištirti granatų optines savybes, įskaitant gesimo trukmės vertes, siekiant nustatyti potencialų pritaikymą scintiliatoriams.

Darbo naujumas ir svarba:

Šio darbo tikslas – susintetinti skirtingos elementinės sudėties granatus, legiruotus ceriu ir prazeodimiu, siekiant pagerinti scintiliatoriams reikalingas liuminescencines savybes. Tam granatai papildomai buvo legiruoti boro, magnio ir / ar skandžio jonais.

Boru ir skandžiu legiruoti, granato struktūrą turintys, miltelių formos junginiai buvo susintetinti pirmą kartą. Dangos ir keramikos, kurių sudėtyje yra boro ir cerio jonų, taip pat buvo gautos ir ištirtos pirmą kartą. Susintetintos naujos elementinės sudėties medžiagos pasižymėjo geresnėmis liuminescencinėmis savybėmis lyginant su tais granatais, kurie struktūroje neturėjo boro jonų. Pagrindinis skirtumas buvo pastebėtas radioliuminescencijos, fotoliuminescencijos emisijos spektruose ir kvantinės išeigos bei gesimo trukmių vertėsse.

Ginamieji teiginiai:

1. Vandeniniu zolių-gelių sintezės metodu sėkmingai susintetinti vienfaziai, granato struktūrą turintys, junginiai, legiruoti Ce^{3+}, Pr^{3+}, B^{3+}, Sc^{3+}, Mg^{2+} jonais;
2. Legiravimas boro jonais pagerina granatų optines savybes. Struktūroje esantys B^{3+} jonai padidina radioliuminescencijos ir fotoliuminescencijos emisijos intensyvumą, kvantinės išeigos vertes ir sutrumpina junginių gesimo trukmes;
3. Granato junginių formos (milteliai, dangos ir keramikos) turi reikšmingą įtaką emisijos intensyvumui ir mėginių gesimo trukmių vertėms;

4. Lutecio aliuminio granatų, legiruotų prazeodimiu ir boru, gesimo trukmės yra trumpesnės nei itrio ar gadolinio aliuminio granatų, legiruotų cerio jonais.

REZULTATŲ APŽVALGA

Disertacija yra parašyta remiantis penkiomis mokslinėmis publikacijomis, išleistomis užsienyje leidžiamuos periodiniuose mokslo leidiniuose, turinčiuose cituojamumo rodiklį „Claritive“ duomenų bazėje „Web of Science“. Darbo rezultatų dalis yra sudaryta iš penkių skyrių, aptariant skirtingų serijų mėginių savybes.

Skirtingu boro kiekiu legiruotų YAG:Ce, YLuAG:Ce ir LuAG:Ce savybių tyrimas kaitinant junginius skirtingose atmosferose

Vandeniniu zolių-gelių sintezės metodu buvo sintetinami itrio, lutecio ir itrio / lutecio aliuminio granatai, legiruoti 0,5 % cerio ir skirtingais kiekiais boro (0 %, 1 %, 3 %, 5 %, 10 % ir 20 %). Yra žinoma, kad junginiai, kurių sudėtyje yra cerio jonų, siekiant išlaikyti krūvių balansą dažniausiai sintetinami juos kaitinant redukcinėje atmosferoje. Šiuo atveju, kadangi į granato matricą yra įterpiami ir boro jonai, nuspręsta papildomai ištirti, ar tiriamos savybės skiriasi junginį kaitinant ore.

Rentgeno spindulių difrakcinės analizės tyrimas parodė, kad visi junginiai, nepriklausomai nuo kaitinimo sąlygų, kurie savo sudėtyje turi 5 % ir mažiau boro, pasižymi gryna granato faze (YAG – PDF#96-152-9038, LuAG – PDF#00-056-1646) turinčia kubinės formos kristalinę gardelę ir pasižyminčia $Ia\bar{3}d$ erdvine grupe. Medžiagose, kurios buvo legiruotos didesniu boro kiekiu, nustatytos priemaišinės aliuminio borido fazės (PDF#96-231-0323). Siekiant nustatyti gautų granatų morfologines savybes, visi mėginiai buvo ištirti skenuojančiu elektronų mikroskopu (angl. SEM). SEM vaizdai parodė, kad didinant boro kiekį mėginiuose (nepriklausomai nuo kaitinimo atmosferos) dalelių dydis didėja. Granatuose, legiruotuose 1 % boro, nustatytas dalelių dydis – 300 nm, 5 % – 400 nm, 10 % – 600 nm, pridėjus 20 % boro stebimos net 800 nm dydžio dalelės. Šis pokytis įrodo, kad kaip ir tikėtasi, sintezės metu boras veikia kaip fliusas, dėl ko stebimas greitesnis aglomeratų formavimasis.

Atlikus fotoliuminescencijos emisijos ir sužadinimo tyrimus kambario temperatūroje buvo patvirtinta, kad visi sintetinti mėginiai pasižymi cerio (Ce^{3+}) jonams būdingais, leidžiamais elektronų perėjimais tarp $[Xe]5d^1$ ir $[Xe]4f^1$ orbitalių. Gauti duomenys rodo, kad mėginiai, kurie yra kaitinti ore ir yra legiruoti 1 % bei 5 % boro, pasižymi intensyviausia emisija. Panašūs rezultatai yra stebimi ir radioliuminescencijos emisijos spektruose. Tiesa, intensyviausia emisija pasižymėjo YAG:Ce mėginys, kaitintas ore, tačiau tik

šiek tiek mažesnio intensyvumo emisija pasižymi taip pat ore kaitintas YAG:Ce,5%B.

Vienas iš pagrindinių įvardintų uždavinių buvo granatų gesimo trukmės trumpinimas. Visiems susintetintiems junginiams buvo išmatuotos ir apskaičiuotos gesimo trukmės, kurios pateiktos ir 48 paveiksle. Gauti rezultatai leidžia teigti, kad B^{3+} jonų pridėjimas į struktūrą, minėtas vertes sutrumpina. Šis pokytis labai gerai matomas palyginant mišrių itrio ir lutecio aliuminio granatų gesimo trukmes: jos sutrumpėja net apie 15 ns. Gesimo vertės sumažėja ir esant didesniems boro kiekiams junginiuose (daugiau nei 5 %). Tačiau reikia atkreipti dėmesį į tai, kad tokie mėginiai, turi priemaišines fazes, kurios turi įtaką gesimo trumpėjimui. Teigiami legiravimo pokyčiai yra stebimi ir kvantinės išeigos (angl. QE) rezultatuose. Į junginius įterpiant B^{3+} jonų, QE vertės žymiai padidėja. Ore sintetinto YAG:Ce vertė nuo 58 % (esant 0 % B^{3+}) pakinta net iki 91 % (esant 5 % B^{3+}). Dar ryškesnis pokytis stebimas su redukcinėje atmosferoje kaitintu YAG:Ce. Šio mėginio kvantinės išeigos vertė padidėja nuo 22 % (esant 0 % B^{3+}) iki 93 % (esant 5 % B^{3+}). Apibendrinus gautus rezultatus galima teigti, kad boro jonai turi reikšmingą įtaką granato struktūrinėms, morfologinėms ir liuminescencinėms savybėms. Mėginiai, kurių sudėtyje yra boro, pasižymi intensyvesne fotoliuminescencijos, radioliuminescencijos emisija, akivaizdžiai trumpesnėmis gesimo trukmėmis ir aukštesnėmis kvantinės išeigos vertėmis. Sintezės metu naudojama kaitinimo atmosfera reikšmingos įtakos neturėjo, nors rezultatai leidžia teigti, kad boru legiruoti ir ore kaitinti granatai pasižymi kokybiškesnėmis liuminescencinėmis savybėmis. Remiantis gautais duomenimis, visi kiti tyrimai buvo atliekami kaitinant medžiagas tik ore ir pridedant 5 % boro.

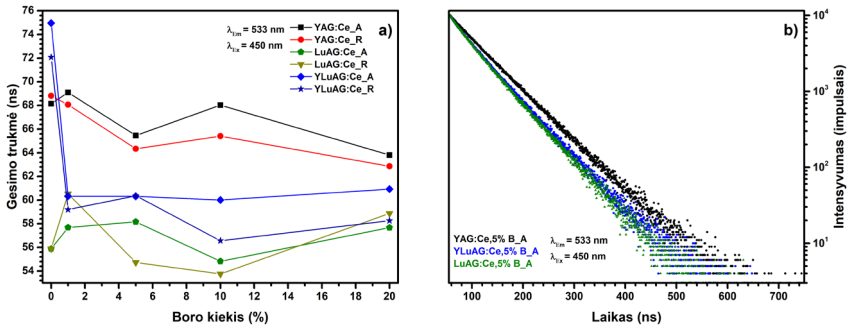

48 paveikslas. (a) Granatų gesimo trukmės; (b) granatų, legiruotų 5 % boro, gesimo kreivės.

Dėl platesnių praktinių pritaikymo galimybių buvo sintetinamos boru ir magniu legiruotos YAG:Ce ir LuAG:Ce dangos ant kvarco (SiO_2) ir safyro (Al_2O_3) padėklų. Remiantis ankstesniais mūsų bei kitų mokslininkų atliktais tyrimais nustatyta, kad optimaliausias boro kiekis granato matricoje yra 5 %, magnio – 0,03 %, dengiamų sluoksnių skaičius – 5, o kaitinimas turi būti vykdomas ore. Dėl šios priežasties atitinkamas B^{3+} ir Mg^{2+} jonų kiekis buvo pridedama į granato struktūrą. Visos dangos sintetintos naudojant zolių-gelių išsukimo ar įmerkimo metodus.

Rentgeno spindulių difrakcinė analizė buvo atliekama naudojant slystančio kampo metodiką. Šis metodas leido dalinai išvengti kvarco ir safyro įtakos difraktogramoms. Buvo gauti ne tik padėklo fono rezultatai, bet ir dangų difrakcines smailes. Difraktogramos patvirtina, kad visi susintetinti mėginiai pasižymi gryna granato faze. Priemaišinių fazių nepastebėta nei viename junginyje. Morfologijos tyrimo rezultatai matomi iš SEM vaizdų. Matoma, kad dangų morfologija skiriasi ir priklauso tiek nuo naudojamo padėklo, tiek nuo naudojamos dengimo technikos. Zolių-gelių įmerkimo metodu gautos dangos yra netolygios, atplyšusios ir sutrūkinėjusios. Tuo tarpu išsukimo metodu susintetintos plėvelės pasižymi akivaizdžiai tolygesniu paviršiumi, o granato sluoksnis yra pilnai padengęs visą padėklą. Tačiau šiuo atveju stebimi dangų kokybės skirtumai ant skirtingų padėklų. Ant safyro, kaip matyti 49 paveiksle, dangos yra lygios ir be trūkių, o ant kvarco – stebimi atsiradę įtrūkimai. Galima daryti išvadą, kad kokybiškiausios dangos buvo gautos ant Al_2O_3 padėklų naudojant zolių-gelių išsukimo metodiką.

Išmatuoti liuminescencijos emisijos ir sužadinimo spektrai, lyginant su miltelių mėginiais, pasižymi mažesniu intensyvumu. Visiems granatams yra matomi vykstantys $[Xe]5d^1$ ir $[Xe]4f^1$ Ce^{3+} jonų elektronų perėjimai. Deja, dėl itin mažo spektrų juostų intensyvumo, atskirų mėginių verčių lyginimas yra nekorektiškas. Gesimo trukmės yra apskaičiuojamos iš surinktų impulsų skaičiaus, todėl jos tarpusavyje gali būti lyginamos. Į struktūrą pridėjus boro ir magnio jonų, gesimo trukmės daugeliu atvejų sutrumpėja. Įmerkimo metodu ant kvarco padėklo sintetinto YAG:Ce vertė sumažėjo nuo 65,73 ns iki 49,44 ns, o LuAG:Ce nuo 47,07 ns iki 45,46 ns, kai junginys buvo legiruojamas B^{3+}. Panašus efektas stebimas ir dangų ant safyro padėklų. Pridėjus B^{3+} jonų LuAG:Ce gesimo trukmė pakinta nuo 66,37 ns iki 62,50 ns. Deja, tačiau ant Al_2O_3 padėklo YAG:Ce gesimo proceso vertė padidėja. Apibendrinant galima teigti, kad nors apskaičiuotos gesimo trukmių vertės

nekinta tolygiai, tačiau boro pridėjimas į struktūrą turi teigiamą poveikį jų sutrumpėjimui dangų mėginiuose.

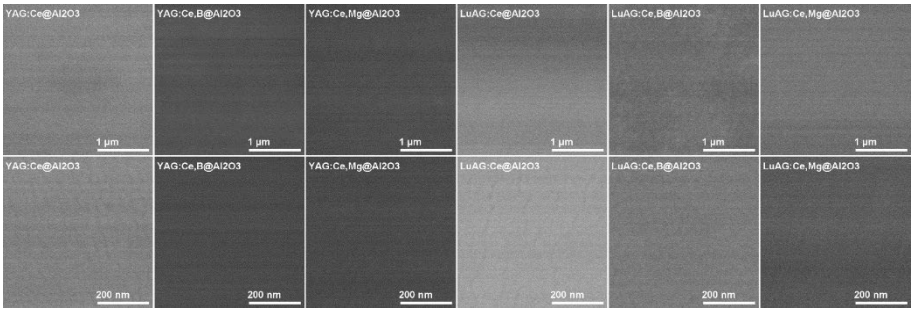

49 paveikslas. Granatų dangų, nusodintų ant safyro (Al_2O_3) padėklo naudojant išsukimo metodą ir kaitinant sluoksnius po kiekvieno dengimo, SEM paveikslai.

Pirmą kartą boru ir magniu legiruotų YAG:Ce ir LuAG:Ce keramikų sintezė ir savybių tyrimas

Aukštoje temperatūroje sintetinamos keramikos yra plačiai naudojamos kaip aukštos kokybės scintiliatoriai. Kadangi tokios formos medžiagos galėtų būti praktiškai pritaikytos, nuspręsta patikrinti, kokia legiravimo boru ir magniu įtaka YAG:Ce ir LuAG:Ce keramikos formos mėginiuose. Kaip ir plonų dangų sintezės metu, medžiagos buvo legiruojamos tik 5 % B^{3+}, 0,03 % Mg^{2+} ir kaitinamos ore. Granatų keramikos buvo gaunamos, kai susintetinti ir 600 °C temperatūroje iškaitinti milteliai, naudojant izostatinį presą, buvo suspaudžiami. Gautos tabletės formos medžiagos iškaitinamos 2 val. 1000 °C temperatūroje ir 5 val. 1500 °C temperatūroje.

Atlikus rentgeno difrakcinę analizę buvo nustatyta, kad visos gautos keramikos pasižymi gryna granato faze (YAG – PDF#96-152-9038, LuAG – PDF#00-056-1646). Priemaišinės fazės nebuvo užfiksuotos. Keramikų dangų morfologijos tyrimas parodė, kad keramikų paviršius yra tolygus, be akivaizdžių porų ir trūkių, o išmatuotas tabletės storis yra 749 µm. Paviršių sudarantys kristalitai didėja, kai į granatų struktūrą yra įterpiami boro jonai. Dalelių dydis kinta nuo ~1,5 µm iki ~3,2 µm tiek YAG:Ce, tiek LuAG:Ce mėginiuose. Galima teigti, kad B^{3+} jonų įtaka morfologijai yra stebima ne tik milteliuose, dangose, bet ir keramikose.

Nustatyta, kad visi susintetinti mėginiai pasižymi Ce^{3+} jonams būdingais $[Xe]5d^1$ ir $[Xe]4f^1$ elektronų perėjimais sužadinimo ir emisijos spektruose. Gauti spektrai patvirtina boro poveikį junginių liuminescencinėms savybėms.

50 paveiksle matyti, kad YAG:Ce, legiruotas 5 % boro, ir YAG:Ce, legiruotas 0,03 % magnio, pasižymi didžiausiais sužadinimo ir emisijos intensyvumais. Tuo tarpu LuAG:Ce intensyviausią emsiją turi mėginys, legiruotas tik 0,03 % magnio. Visi susintetinti granatai turi chromo jonų priemaišų, kurios spektruose yra matomos kaip papildomi $^2E \rightarrow {}^4A_2$ elektronų perėjimai bangos ilgiuose nuo 680 nm iki 730 nm. Apskaičiuotos gesimo trukmės patvirtina, kad B^{3+} jonai sumažina gesimo vertes apie 3 ns tiek YAG:Ce, tiek LuAG:Ce atveju. Nors granatų keramikose fiksuojami nedideli gesimo trukmių pokyčiai, tačiau yra stebima verčių mažėjimo tendencija. Apibendrinant gautus rezultatus galima patvirtinti, kad keramikų liuminescencinės savybės turi priklausomybę nuo junginių legiravimo boro ir magnio jonais, kurie lemia intensyvesnę emisiją ir trumpesnę gesimo trukmę.

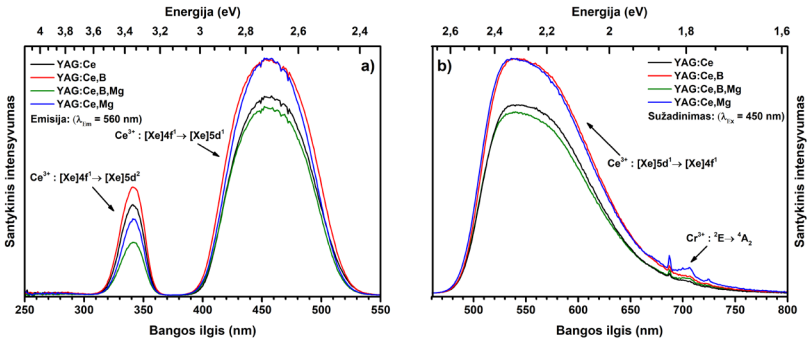

50 paveikslas. YAG keramikų sužadinimo (a) ir emisijos (b) spektrai.

Boro ir skandžio įtaka LuAG:Ce ir GdAG:Ce junginių liuminescencinėms savybėms

Remiantis ankstesniais rezultatais buvo nustatyta, kad boro jonai pagerina granatų liuminescencines savybes. Siekiant savybes tobulinti toliau LuAG:Ce ir GdAG:Ce granatai, be legiravimo B^{3+}, papildomai buvo keičiami ir Sc^{3+} jonais. Į struktūrą skandis buvo įterpiamas didesniais kiekiais nei boras ar ceris. Lutecio aliuminio granato atveju skandis pakeitė 1/5 aliuminio, o gadolinio aliuminio granato – 2/5 aliuminio jonų kiekio. Atitinkami kiekiai pasirinkti dėl to, kad būtų galima gauti stabilius, vienfazius junginius. Visi granatai sintetinti vandeniniu zolių-gelių sintezės metodu, o gauti milteliai iškaitinti 1200 °C temperatūroje. Mėginiai buvo gaunami legiruojant 1 % cerio ir keičiant boro kiekį junginiuose: 0 %, 1 %, 3 % ir 5 % B^{3+}. Mokslinėje

literatūroje nėra informacijos granatus, kurie sudėtyje turėtų cerio, boro ir skandžio jonų, todėl galima daryti išvadą, kad jie buvo sintetinti pirmą kartą.

Gautiems granatams buvo atliktas induktyviai susietos plazmos optinės emisijos spektrometrijos (angl. ICP-OES) tyrimas. Šis tyrimas leido nustatyti, koks tikrasis boro kiekis yra mėginio struktūroje. Remiantis gautais rezultatais buvo patvirtinta, kad B^{3+} jonai struktūroje yra, tačiau išmatuotas kiekis buvo šiek tiek mažesnis nei apskaičiuotas. Nustatyti kiekiai: apskaičiuotas kiekis – 0 % B^{3+} (išmatuotas kiekis yra 0 %); 1 % (0,9 %); 3 % (2,3 %); 5 % (3,5 %). Rentgeno difrakcinės analizės metu gautos difraktogramos rodo, kad $Lu_3Al_4Sc_1O_{12}$:1%Ce,5%B, $Gd_3Al_3Sc_2O_{12}$:1%Ce,3%B ir $Gd_3Al_3Sc_2O_{12}$:1%Ce,5%B turi priemaišines fazes. Be granato susidarė papildomos AlB_{10} ir Sc_2O_3 fazės. Boro jonų kiekio didėjimas turi reikšmingą įtaką ne tik junginio grynumui, bet ir jo morfologijai. Didinant B^{3+} jonų kiekį, dalelių dydis didėja. Šią tendenciją patvirtina morfologijos ir dalelių dydžio pasiskirstymo tyrimai.

Liuminescencinės savybės įrodo įvardintos granatų struktūros privalumus. 51 paveiksle matyti, kad susintetinti junginiai pasižymi aukšta optine kokybe, kadangi visų junginių atspindžio spektrų vertės yra arti 100 %. Kaip ir tikėtasi, fotoliuminescencijos atspindžio, sužadinimo bei emisijos spektruose stebimi cerio jonams būdingi elektronų perėjimai. Tiesa, gadolinio junginiuose atspindžio ir sužadinimo spektruose papildomai stebimi ir gadolinio jonams būdingi $^8S_{7/2} \rightarrow {}^6P_j$ elektronų perėjimai ties ~275 nm. Emisijos spektrai įrodo, kad legiravimas B^{3+} jonais padidina intensyvumą. Lyginant mėginius su Sc^{3+} jonais ir be jų, nustatyta, kad Sc^{3+} emisijos intensyvumą sumažina. Šie jonai taip pat yra atsakingi už spektro poslinkį į trumpesnių bangų pusę. Paveiksle 52 matoma, kad radioliuminescencijos emisijos spektrų intensyvumas didėja legiruojant granatus boro jonais. $Lu_3Al_5O_{12}$:1%Ce,5%B, $Gd_3Al_3Sc_2O_{12}$:1%Ce,3%B ir $Gd_3Al_3Sc_2O_{12}$:1%Ce,1%B pasižymi intensyviausia emisija. Gesimo trukmių vertės, kaip ir buvo siekta, sumažėja legiruojant junginius B^{3+} ir Sc^{3+} jonais. Lutecio aliuminio granato atveju vertės sumažėja nuo 60,6 ns iki 54,0 ns, gadolinio aliuminio skandžio granato atveju – nuo 50,8 ns iki 46,6 ns. Galima pastebėti, kad trumpiausiomis gesimo trukmėmis pasižymi priemaišinių fazių turintys junginiai. Išanalizavus gautus duomenis, galima patvirtinti, kad B^{3+} ir Sc^{3+} jonai turi teigiamą efektą tiriamoms fotoliuminescencinėms ir radioliuminescencinėms savybėms.

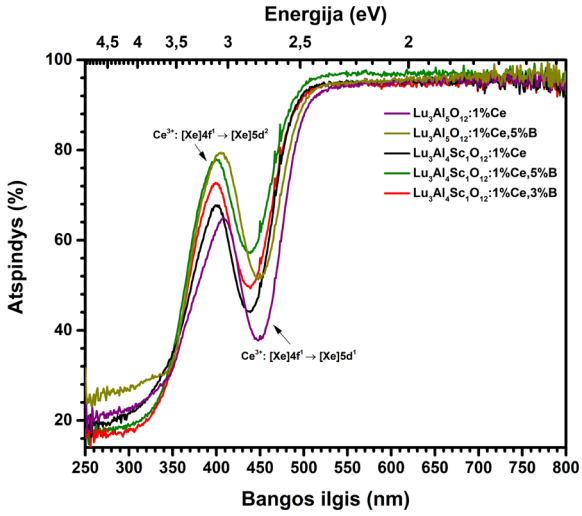

51 paveikslas. $Lu_3Al_5O_{12}$ ir $Lu_3Al_4Sc_1O_{12}$ granatų, legiruotų 1 % cerio ir skirtingais kiekiais boro atspindžio spektrai.

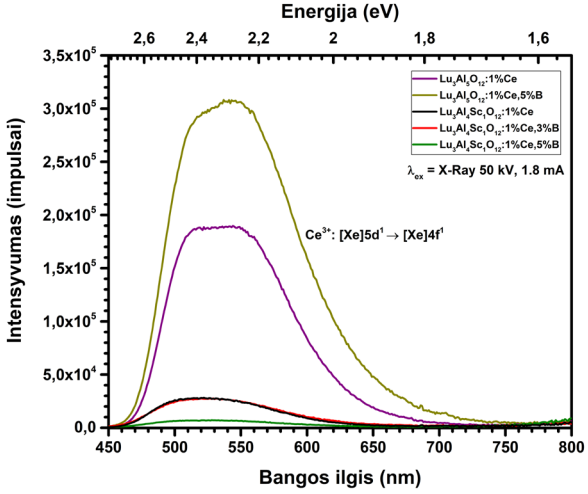

52 paveikslas. $Lu_3Al_5O_{12}$ ir $Lu_3Al_4Sc_1O_{12}$ granatų, legiruotų 1 % cerio ir skirtingais kiekiais boro radioliuminescencijos emisijos spektrai.

Boro ir skandžio įtaka LuAG:Pr ir GdAG:Pr junginių liuminescencinėms savybėms

Yra žinoma, kad Pr^{3+} jonais legiruoti granatai pasižymi trumpesnėmis gesimo trukmėmis, lyginant junginius su Ce^{3+}. Kadangi visi ankstesni tyrimai buvo

atliekami su cerio jonais, nuspręsta patikrinti boro įtaką naujos struktūros mėginiams. Keičiant aktyvatoriaus joną, siekiama dar labiau sutrumpinti gesimo trukmę. LuAG:Pr ir GdAG:Pr granatų milteliai buvo sintetinami vandeniniu zolių-gelių sintezės būdu, juos iškaitinant 1200 °C temperatūroje. Į struktūrą buvo įterpiama 1 % prazeodimio, 0 %, 1%, 3% arba 5 % boro, o skandžio buvo pridedama didesniu kiekiu nei B^{3+} ar Pr^{3+}. Lutecio aliuminio granato atveju skandis pakeitė 1/5 aliuminio, o gadolinio aliuminio granato – 2/5 aliuminio jonų kiekio. Kaip ir junginių su ceriu atveju, apie šią sintetinamą granato struktūrą ir jos tyrimus mokslinėje literatūroje informacijos nėra.

Gadolinio aliuminio skandžio granatams atlikus ICP-OES tyrimą buvo nustatyta, kad tiek boras, tiek prazeodimis yra struktūroje. Beveik visais atvejais Pr^{3+} užfiksuota ~0,2 % daugiau, o B^{3+} šiek tiek mažiau nei teigiama, kad buvo įterpta. Granato fazės grynumui mėginiuose nustatyti buvo atlikta Rentgeno difrakcinė analizė ir Rietveldo tikslinimas. Lutecio aliuminio granato atveju, visi sintetinti junginiai pasižymi gryna granato faze. 53 paveiksle matyti, kad gadolinio aliuminio skandžio granatai, legiruoti prazeodimiu ir 0 % bei 1 % boro, yra vienfaziai junginiai, turintys $Ia\bar{3}d$ erdvinę grupę. Į struktūrą pridedant didesnius kiekius boro, stebimos $GdAl_3(BO_3)_4$ (erdvinė grupė $R32$) ir Sc_2O_3 (erdvinė grupė: $I3\bar{a}$) priemaišos. 53 paveikslo dešinės pusės apatinėje dalyje matyti visų susintetintų junginių gardelės parametro *a* kitimas priklausomai nuo legiravimo boro jonais. Didinant boro kiekį, gardelės parametrai mažėja. GdASG:Pr junginiuose kristalinės gardelės parametras *a* kinta nuo 12.331 Å iki 12.328 Å, LuASG:Pr atveju nuo 12.068 Å iki 12.060 Å, o LuAG:Pr – nuo 11.914 Å iki 11.900 Å. Paveikslo dešinės pusės viršutinėje dalyje matoma sumaketuota kubinė GdASG:Pr granato kristalinė gardelė ir ją sudarantys poliedrai. Granatas yra sudarytas iš 8 kartus koordinuotų dodekaedrų, 6 kartus koordinuotų oktaedrų ir 4 kartus koordinuotų tetraedrų. Priklausomai nuo jonų dydžio (jie užima panašų spindulį turinčių elementų vietą), elementai struktūroje gali užimti skirtingas vietas. Šiuo atveju Sc^{3+}, Al^{3+} ir B^{3+} užima tetraedrines ir oktaedrines vietas, o Lu^{3+}, Gd^{3+} ir Pr^{3+} – dodekaedrines vietas. SEM tyrimo metu nustatyta, kad boras veikia kaip fliusas ir didinant jo kiekį junginyje, dalelių dydis didėja.

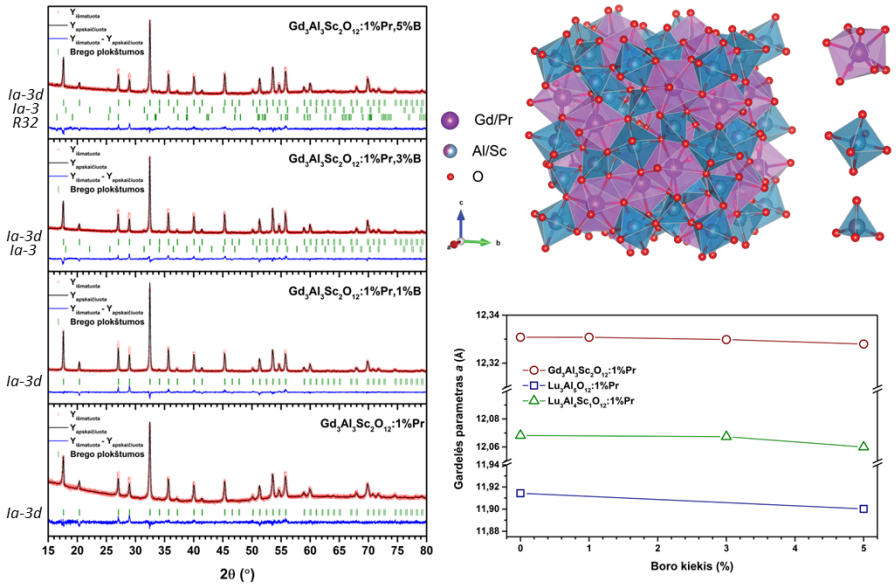

53 paveikslas. $Gd_3Al_3Sc_2O_{12}$ granatų, legiruotų Pr^{3+} and B^{3+} jonais, Rietveldo tikslinimo rezultatai, matuojant junginius kambario temperatūroje. Paveikslo dešinės pusės viršuje – granato struktūros kristalinė gardelė, gauta po Rietveldo tikslinimo. Dešinės pusės apačioje – po Rietveldo tikslinimo apskaičiuoti gardelės parametrai *a*.

Visiems mėginiams buvo atlikti liuminescenciniai tyrimai. Išmatuoti atspindžio spektrai leidžia teigti, kad susintetinti granatai, dėl pasiektos artimos 100 % atspindžio vertės, pasižymi itin aukšta optine kokybe. Lutecio aliuminio granatų fotoliuminescencijos emisijos spektruose matomi tiek leidžiami ($4f^15d^1 \rightarrow {}^3H_j, {}^3F_j$) , tiek draudžiami ($^3P_0 \rightarrow {}^3H_j$; $^1D_4 \rightarrow {}^3H_4$) prazeodimio jonų elektronų perėjimai. Intensyviausia leidžiamų perėjimų emisija pasižymi LuAG:Pr mėginys, kai tuo tarpu LuASG:Pr,3%B turi intensyviausią draudžiamų elektronų perėjimų emisiją. Gadolinio aliuminio skandžio granatuose nėra fiksuojama leidžiama Pr^{3+} emisija. Šį pokytį galima paaiškinti Gd^{3+} ir Sc^{3+} jonų nespinduliniu relaksacijos procesu iš 5d sužadintos būsenos į 4f pradinę būseną. Intensyviausia $[Xe]4f^2 \rightarrow [Xe]4f^2$ emisija pasižymi 5 % boro legiruotas junginys. Radioliuminescencijos emisijos intensyvumas buvo matuotas visiems susintetintiems junginiams. Priešingai nei fotoliuminescencijos tyrimo atveju, 54 paveiksle matyti, kad $[Xe]4f^2 \rightarrow [Xe]4f^2$ junginių emisija yra intensyvesnė nei fotoliuminescencijos atveju. Taip pat matoma, kad kitas junginys (LuASG:1%Pr,5%B) pasižymi intensyviausia emisija. GdASG:Pr mėginių spektruose matoma, kad pasikeitė

intensyviausią draudžiamą emisiją turintis granatas ir šiuo atveju yra mėginys, legiruotas 3 % boro. B^{3+} jonų įtaka granatų gesimo trukmių ir kvantinės išeigos vertėms yra akivaizdi. LuAG:Pr bandinio atveju, legiruojant boro jonais, gesimo trukmė pakinta nuo 23,1 ns iki 19,5 ns, o LuASG:Pr – nuo 22,4 ns iki 19.9 ns. Apskaičiavus matyti, kad kvantinė išeiga padidėja nuo 49 % iki 87 %.

Apibendrinant ištirtus rezultatus galima daryti išvadą, kad granatų legiravimas prazeodimio ir boro jonais pagerina liuminescencines savybes ir įvardintuose junginiuose gaunamas aukštas foto ir radioliuminescencijos intensyvumas. Lyginant visas, šiame darbe ištirtas, granatų struktūros modifikacijas, teigiama, kad būtent šios struktūros junginys (LuAG:Pr,5%B) pasižymi trumpiausia šiame darbe išmatuota gesimo trukme, kuri lygi 19,5 ns.

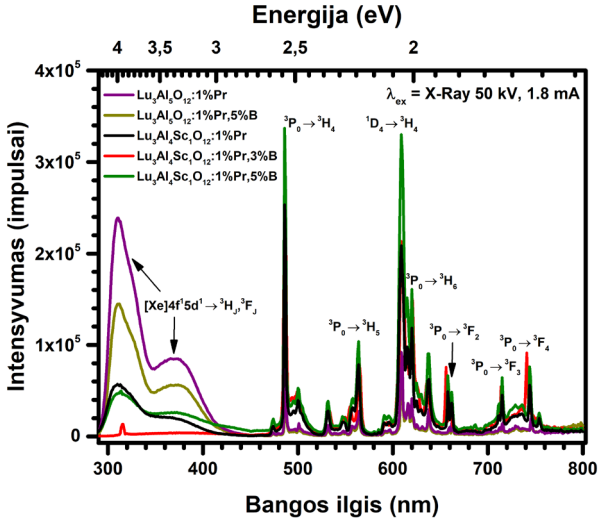

54 paveikslas. $Lu_3Al_5O_{12}$ ir $Lu_3Al_4Sc_1O_{12}$ granatų, legiruotų 1 % prazeodimio ir skirtingais kiekiais boro radioliuminescencijos emisijos spektrai.

IŠVADOS

1. Nepriklausomai nuo to, jog, dažniausiai, cerio (Ce^{3+}) jonais legiruoti granatai yra kaitinami redukcinėje atmosferoje, kolegiruojant junginius boru, geresnėmis liuminescencinėmis savybėmis (didesnis emisijos intensyvumas, aukštesnė kvantinės išeigos vertė ir trumpesnė gesimo trukmė) pasižymi ore kaitinti granatai.
2. Atliekant sintezę vandeniniu zolių-gelių sintezės metodu į granato struktūrą galima įterpti iki 5 mol% boro jonų. Legiruojant junginius didesniais boro kiekiais, stebimas pašalinių fazių atsiradimas. Išimtis stebima GdASG mėginiuose, kai priemaišos atsiranda pridėjus 3 mol% boro.
3. Granatų dangos ant kvarco (SiO_2) ir safyro (Al_2O_3) padėklų gali būti sėkmingai nusodintos naudojant zolių-gelių įmerkimo ir išsukimo sintezės metodus. Kokybiškiausios dangos buvo gautos zolių-gelių išsukimo sintezės metodu naudojant safyro padėklą. Taip gautos dangos pasižymi lygiu paviršiumi, kuriame nėra įtrūkimų.
4. Pirmą kartą sėkmingai susintetintos itrio aliuminio ir lutecio aliuminio granatų keramikos, legiruotos ceriu, boru ir / ar magniu. Keramikos, legiruotos boro jonais, pasižymi intensyvesne emisija ir trumpesne gesimo trukme nei panašios elementinės sudėties junginiai, kurių struktūroje B^{3+} nėra.
5. Atliktas skenuojančios elektronų mikroskopijos tyrimas įrodo, kad boro jonų pridėjimas į struktūrą didina dalelių dydį, kadangi B^{3+} veikia kaip fliusas. Didesnės granato dalelės, turi teigiamą įtaką junginių atspindžio, sužadinimo ir emisijos spektrų intensyvumams. Boru legiruoti granatai beveik visais atvejais (kol yra stebima gryna granato fazė) pasižymi intensyvesniais emisijos spektrais nei junginiai, kurių elementinėje sudėtyje nėra boro. Šis poveikis stebimas visuose tirtuose granatuose.
6. Atlikus ICP-OES matavimus, nustatyta, kad boro kiekis sintetintuose junginiuose yra gana artimas apskaičiuotoms reikšmėms. Galima teigti, kad sintezės metu B^{3+} jonai yra įterpiami į granato struktūrą ir turi teigiamą įtaką tirtoms struktūrinėms ir liuminescencinėms savybėms.
7. Scintiliatorių savybes apibūdinantys radioliuminescencijos emisijos spektrai pasižymi teigiamu efektu dėl granato sudėtyje esančių boro jonų. Emisijos intensyvumas padidėja, kai mėginiai yra legiruojami B^{3+} jonais. Stebima, kad aukščiausias radioliuminescencijos emisijos vertes turi borą (B^{3+}) struktūroje turintys lutecio aliuminio granatai, legiruoti tiek cerio (Ce^{3+}), tiek prazeodimio jonais (Pr^{3+}).

8. Granatai, kurių struktūroje yra boro jonų, apskaičiuotos gesimo trukmės yra trumpesnės lyginant junginius, kurių sudėtyje nėra B^{3+} (atkreipiant dėmesį į YAG:Ce ir LuAG:Ce). Verčių sumažėjimas aiškinamas tuo, kad boro jonai turi didesnį elektroneigiamumą nei aliuminio jonai. Dėl šios priežasties sumažėja poliarizacija, o dėl to sutrumpėja gesimo trukmė. Aprašyta tendencija stebima ne tik milteliuose, bet ir dangose bei keramikose.
9. Remiantis gautais rezultatais ir atkreipiant dėmesį į junginių grynumą ir gesimo trukmių vertes galima teigti, kad lutecio aliuminio granatas, legiruotas prazeodimiu ir 5 % boro, galėtų būti naudojamas kaip geriausiomis savybėmis pasižymintis scintiliatorius iš visų šiame darbe sintetintų junginių. Šis junginys turi pačią trumpiausią išmatuotą gesimo trukmę, lygią 19,5 ns. Kitas, labai geromis savybėmis pasižymintis junginys yra lutecio aliuminio granatas, legiruotas ceriu ir 5 % boro. Šio granato gesimo trukmė buvo viena iš trumpiausių visų formų (milteliai, dangos ir keramikos) junginiuose.

PADĖKA

Visų pirma norėčiau padėkoti doktorantūros studijų darbo vadovui profesoriui dr. Ramūnui Skaudžiui. Dar būdama trečio kurso bakalauro studentė nedrąsiai atėjau su prašymu pradėti dirbti Jūsų mokslinėje grupėje. Ačiū, kad tuo metu suteikėte galimybę pamatyti mokslo pasaulį atliekant sintezes ir tyrimus laboratorijoje. Ačiū už tai, kad visada galėjau kreiptis pagalbos, kad suteikėte begalo naudingas pamokas, patarimus ir, žinoma, pastabas. Jūsų dėka išmokau būti savarankiška ir turėjau plačias galimybes save realizuoti moksliniame darbe.

Ačiū norėčiau pasakyti ir profesoriui habil. dr. Aivarui Kareivai. Jūsų nuolatinis palaikymas ir skatinimas yra neatsiejamas nuo mano pasiekimų, sėkmingų mokslinių darbų ir galimybių tobulėti ateityje.

Dėkoju profesoriui dr. Artūrui Katelnikovui, profesoriui dr. Aleksej Žarkov ir docentei dr. Živilei Stankevičiūtei iš Vilniaus universiteto, profesoriui dr. Thomas Jüstel, docentui dr. David Enseling ir dr. Jan-Niklas Keil iš Miunsterio taikomųjų mokslų universiteto, profesoriui dr. Anatolijs Sarakovskis iš Latvijos universiteto, dr. Monikai Skruodienei iš Fizinių ir technologijos mokslų centro už pagalbą ir patarimus atliekant mokslinius tyrimus, juos suprantant bei aprašant.

Noriu padėkoti dr. Rūtai, kuri nuo pat bakalauro studijų buvo kartu ir palaikė kiekviename sunkiasniame ar lengvesniame žingsnyje. Labai džiaugiuosi, kad studijose sutikau artimą draugę! Ačiū dr. Aleksandrai ir Gintarei už pokalbius, palaikymą ir bendrą laiką kartu. Būtų sunku įsivaizduoti studijas ir darbą be Jūsų. Ačiū dr. Andriui už bendrą darbą laboratorijoje ir nuolatinį palaikymą studijų ir mokslo kelyje. Ačiū ir draugams dr. Dovydui, Viktorijai ir Lukui. Labai džiaugiuosi, kad visi kartu galėjome leisti laiką ne tik universitete, bet ir už jo ribų.

Atskirai padėkoti norėčiau visam Neorganinės chemijos katedros kolektyvui. Ačiū, kad esate kolegos, kurie niekada negailėjo patarimų ir palaikė visų studijų metu. Susitikimai ir pokalbiai katedroje buvo tai, kas skatino judėti pirmyn ir siekti užsibrėžtų tikslų.

Ačiū Chemijos ir geomokslų fakulteto administracijai už pagalbą ir operatyvų problemų sprendimą visais kylančiais klausimais.

Didelis ačiū Pauliui už kantrybę, rūpestį ir palaikymą visų ilgų studijų metu. Tėvams ir broliui, kad visuomet skatinote siekti ir nepamiršti savo svajonių. Ačiū už tai, jog kartu džiaugėtės kiekviena, nors ir nedidele mano pergale ir pasiekimu.

AČIŪ visiems, jog dabar esu ten, kur esu!

BIBLIOGRAPHY

[1] M. Teimoorisichani, V. Panin, H. Rothfuss, H. Sari, A. Rominger, M. Conti, A CT-less approach to quantitative PET imaging using the LSO intrinsic radiation for long-axial FOV PET scanners, Med. Phys. 49 (2022) 309–323. https://doi.org/10.1002/MP.15376.

[2] J.C.G. Bünzli, Rising Stars in Science and Technology: Luminescent Lanthanide Materials, Eur. J. Inorg. Chem. 2017 (2017) 5058–5063. https://doi.org/10.1002/EJIC.201701201.

[3] J. Ling, W. Xu, J. Yang, T. Mu, Y. Zhang, Y. Zhou, M. Hong, The effect of Lu^{3+} doping upon YAG:Ce phosphor ceramics for high-power white LEDs, J. Eur. Ceram. Soc. 41 (2021) 5967–5976. https://doi.org/10.1016/J.JEURCERAMSOC.2021.05.005.

[4] J.W. Cates, C.S. Levin, Evaluation of a clinical TOF-PET detector design that achieves 100 ps coincidence time resolution, Phys. Med. Biol. 63 (2018). https://doi.org/10.1088/1361-6560/aac504.

[5] X. Qiu, Z. Luo, J. Zhang, H. Jiang, J. Jiang, Mechanical properties and machinability of GYGAG:Ce ceramic scintillators, Ceram. Int. 46 (2020) 4550–4555. https://doi.org/10.1016/j.ceramint.2019.10.183.

[6] T.C. Wang, S.Y. Yao, S.P. Yan, J. Yu, Z.Y. Deng, A.N. Yakovlev, B. Meng, J.B. Qiu, X.H. Xu, High Thermal Stability of Copper-Based Perovskite Scintillators for High-Temperature X-ray Detection, ACS Appl. Mater. Interfaces. 15 (2023) 23421–23428.

[7] P. Schauer, O. Lalinský, M. Kučera, Overview of S(T)EM electron detectors with garnet scintillators: Some potentials and limits, Microsc. Res. Tech. 84 (2021) 753–770. https://doi.org/10.1002/JEMT.23634.

[8] D.S. McGregor, Materials for Gamma-Ray Spectrometers: Inorganic Scintillators, Annu. Rev. Mater. Res. 48 (2018) 245–277. https://doi.org/10.1146/annurev-matsci-070616-124247.

[9] C. Foster, M. Koschan, Y. Wu, C.L. Melcher, Boron codoping of Czochralski grown lutetium aluminum garnet and the effect on scintillation properties, J. Cryst. Growth. 486 (2018) 126–129. https://doi.org/10.1016/j.jcrysgro.2018.01.028.

[10] R. Baba, A. Yoneyama, M. Kawamoto, Quantitative analysis of the physical properties of CsI, GAGG, LuAG, CWO, YAG, BGO, and GOS scintillators using 10-, 20- and 34-keV monochromated synchrotron radiation, Opt. Mater. Express, Vol. 11, Issue 2, Pp. 398-411. 11 (2021) 398–411. https://doi.org/10.1364/OME.409161.

[11] W. Chewpraditkul, L. Swiderski, M. Moszynski, T. Szczesniak, A. Syntfeld-Kazuch, C. Wanarak, P. Limsuwan, Scintillation properties of LuAG:Ce, YAG:Ce and LYSO:Ce crystals for gamma-ray detection, in: IEEE Trans. Nucl. Sci., 2009: pp. 3800–3805. https://doi.org/10.1109/TNS.2009.2033994.

[12] L. Pan, B. Jiang, J. Fan, P. Zhang, X. Mao, L. Zhang, Co-precipitation synthesis of lutetium aluminum garnet (LuAG) powders: The influence of ethanol, Opt. Mater. (Amst). 71 (2017) 50–55.

https://doi.org/10.1016/j.optmat.2016.06.020.
[13] G. Inkrataite, M. Kemere, A. Sarakovskis, R. Skaudzius, Influence of boron on the essential properties for new generation scintillators, J. Alloys Compd. 875 (2021) 160002. https://doi.org/10.1016/j.jallcom.2021.160002.
[14] T. Yang, C.M.R. de Almeida, D. Han, L. Meng, J. Deng, E.L. da Silva, M.C. Santos, S. Shi, Hydrothermal synthesis and optimization of boron doped $LiZr_2(PO_4)_3$ Li-ion solid electrolyte, Appl. Surf. Sci. 474 (2019) 250–255. https://doi.org/10.1016/j.apsusc.2018.02.158.
[15] S. V. Kuznetsov, V.S. Sedov, A.K. Martyanov, S.C. Batygov, D.S. Vakalov, K.N. Boldyrev, I.A. Tiazhelov, A.F. Popovich, D.G. Pasternak, H. Bland, S. Mandal, O. Williams, M.S. Nikova, V.A. Tarala, Cerium-doped gadolinium-scandium-aluminum garnet powders: synthesis and use in X-ray luminescent diamond composites, Ceram. Int. 48 (2022) 12962–12970. https://doi.org/10.1016/J.CERAMINT.2022.01.169.
[16] L. Swiderski, K. Brylew, W. Drozdowski, M. Grodzicka-Kobylka, Ł. Janiak, M. Moszyński, LuAG:Pr, LuAG:Pr,Mo and LuYAG:Pr relative light yield measured at wide temperature range with MPPC readout, Nucl. Instruments Methods Phys. Res. Sect. A Accel. Spectrometers, Detect. Assoc. Equip. 1021 (2022) 165924. https://doi.org/10.1016/J.NIMA.2021.165924.
[17] K.V.R. Murthy, H.S. Virk, Luminescence phenomena: An introduction, Defect Diffus. Forum. 347 (2014) 1–34. https://doi.org/10.4028/www.scientific.net/DDF.347.1.
[18] B. Valeur, M.N. Berberan-Santos, A brief history of fluorescence and phosphorescence before the emergence of quantum theory, J. Chem. Educ. 88 (2011) 731–738.
[19] J. Xu, S. Tanabe, Persistent luminescence instead of phosphorescence: History, mechanism, and perspective, J. Lumin. 205 (2019) 581–620. https://doi.org/10.1016/j.jlumin.2018.09.047.
[20] X. Wang, M. Dong, Z. Li, Z. Wang, F.S. Liang, Recent advances of room temperature phosphorescence and long persistent luminescence by doping system of purely organic molecules, Dye. Pigment. 204 (2022) 110400. https://doi.org/10.1016/j.dyepig.2022.110400.
[21] V. Singh, A. Kumar, C.M. Mehare, H. Jeong, S.J. Dhoble, UV/VUV excited photoluminescence of Tb^{3+} doped $LaPO_4$ green emitting phosphors for PDP applications, Optik (Stuttg). 206 (2020) 163733. https://doi.org/10.1016/j.ijleo.2019.163733.
[22] P. Deshmukh, S. Satapathy, M.K. Singh, Y.P. Kumar, P.K. Gupta, Tb^{3+}/Yb^{3+} co-doped Y_2O_3 upconversion transparent ceramics: Fabrication and characterization for IR excited green emission, J. Eur. Ceram. Soc. 37 (2017) 239–242. https://doi.org/10.1016/j.jeurceramsoc.2016.07.031.
[23] D.A. Hora, A.B. Andrade, N.S. Ferreira, V.C. Teixeira, M.V.D.S. Rezende, X-ray excited optical luminescence of Eu-doped YAG nanophosphors produced via glucose sol-gel route, Ceram. Int. 42 (2016) 10516–10519. https://doi.org/10.1016/j.ceramint.2016.03.142.

[24] J. Lincoln, Phosphorescence as an exponential decay, Phys. Teach. 59 (2021) 220–221. https://doi.org/10.1119/10.0003675.

[25] L. Lin, X. Bi, Y. Gu, F. Wang, J. Ye, Surface-enhanced Raman scattering nanotags for bioimaging, J. Appl. Phys. 129 (2021). https://doi.org/10.1063/5.0047578/848955.

[26] D. Frackowiak, The Jablonski diagram, J. Photochem. Photobiol. B Biol. 2 (1988) 399. https://doi.org/10.1016/1011-1344(88)85060-7.

[27] H. Deng, F. Chen, C. Yang, al -, C.-C. Ting, Y.-C. Chien, W.-F. Sung, G. Naresh, J.P. Borah, C. Borgohain, N. Paul, Synthesis, characterization and effect of dopant on magnetic hyperthermic efficacy of Gd_2O_3 nanoparticles, Mater. Res. Express. 8 (2021) 115014. https://doi.org/10.1088/2053-1591/AC3B14.

[28] M.F. Ferreira, W.E. Willian, C. Falcony, L.A. Rocha, E.J. Nassar, Synthesis and characterization of gadolinium vanadate matrix triply doped with lanthanide ions (Eu^{3+}, Er^{3+}, and Yb^{3+}) by non-hydrolytic sol-gel, J. Lumin. 256 (2023) 119616. https://doi.org/10.1016/J.JLUMIN.2022.119616.

[29] A.F. Zatsepin, Y.A. Kuznetsova, M.A. Mashkovtsev, V.N. Rychkov, Er-doped gadolinium oxide nanoparticles for enhanced UV-VIS energy conversion: Structural features, optical properties and quantum efficiency, J. Lumin. 260 (2023) 119831. https://doi.org/10.1016/J.JLUMIN.2023.119831.

[30] K. Tang, Study on the influence of thermal treatments on the radio-luminescence in LiF:Mg,Cu,P (GR-200A), Radiat. Meas. 148 (2021) 106666. https://doi.org/10.1016/J.RADMEAS.2021.106666.

[31] W. Chewpraditkul, T. Horiai, A. Beitlerova, R. Kucerkova, V. Babin, A. Yoshikawa, W. Chewpraditkul, M. Nikl, Temperature dependence of photo- and radio-luminescence and scintillation properties of $Lu_2YAl_{2.5}Ga_{2.5}O_{12}$:Ce,Mg multicomponent garnet crystals, Opt. Mater. (Amst). 147 (2024) 114738. https://doi.org/10.1016/J.OPTMAT.2023.114738.

[32] T. Kirchartz, J.A. Márquez, M. Stolterfoht, T. Unold, Photoluminescence-Based Characterization of Halide Perovskites for Photovoltaics, Adv. Energy Mater. 10 (2020) 1904134. https://doi.org/10.1002/AENM.201904134.

[33] E.G. Yukihara, A.J.J. Bos, P. Bilski, S.W.S. McKeever, The quest for new thermoluminescence and optically stimulated luminescence materials: Needs, strategies and pitfalls, Radiat. Meas. 158 (2022) 106846. https://doi.org/10.1016/J.RADMEAS.2022.106846.

[34] K. Huang, N. Le, J.S. Wang, L. Huang, L. Zeng, W.-C. Xu, Z. Li, Y. Li, G. Han, K. Huang, N. Le, J.S. Wang, L. Huang, L. Zeng, G. Han, W.-C. Xu, Z. Li, Y. Li, Designing Next Generation of Persistent Luminescence: Recent Advances in Uniform Persistent Luminescence Nanoparticles, Adv. Mater. 34 (2022) 2107962. https://doi.org/10.1002/ADMA.202107962.

[35] J. Rodrigues, N. Ben Sedrine, M.R. Correia, T. Monteiro, Photoluminescence investigations of ZnO micro/nanostructures, Mater. Today Chem. 16 (2020) 100243. https://doi.org/10.1016/J.MTCHEM.2020.100243.

[36] D.S.M. Ravinson, M.E. Thompson, Thermally assisted delayed fluorescence

(TADF): fluorescence delayed is fluorescence denied, Mater. Horizons. 7 (2020) 1210–1217. https://doi.org/10.1039/D0MH00276C.

[37] A. Kotb, R.D. Abdel-Rahim, A.S. Ali, H. Gomaa, Smart nanomaterials based on metals and metal oxides for photocatalytic applications, Adv. Smart Nanomater. Their Appl. (2023) 351–421. https://doi.org/10.1016/B978-0-323-99546-7.00004-5.

[38] Z. Yang, C. Xu, W. Li, Z. Mao, X. Ge, Q. Huang, H. Deng, J. Zhao, F. Long Gu, Y. Zhang, Z. Chi, Z. Yang, W. Li, Z. Mao, X. Ge, Q. Huang, H. Deng, Y. Zhang, Z. Chi, C. Xu, F.L. Gu, J. Zhao, Boosting the Quantum Efficiency of Ultralong Organic Phosphorescence up to 52 % via Intramolecular Halogen Bonding, Angew. Chemie Int. Ed. 59 (2020) 17451–17455. https://doi.org/10.1002/ANIE.202007343.

[39] G. Schwendt, S.M. Borisov, Achieving simultaneous sensing of oxygen and temperature with metalloporphyrins featuring efficient thermally activated delayed fluorescence and phosphorescence, Sensors Actuators B Chem. 393 (2023) 134236. https://doi.org/10.1016/J.SNB.2023.134236.

[40] C. Zhu, J. Xin, J. Li, H. Li, X. Kang, Y. Pei, M. Zhu, C. Zhu, H. Li, X. Kang, M. Zhu, J. Xin, J. Li, Y. Pei, Fluorescence or Phosphorescence? The Metallic Composition of the Nanocluster Kernel Does Matter, Angew. Chemie. 134 (2022) e202205947. https://doi.org/10.1002/ANGE.202205947.

[41] H.T. Feng, J. Zeng, P.A. Yin, X.D. Wang, Q. Peng, Z. Zhao, J.W.Y. Lam, B.Z. Tang, Tuning molecular emission of organic emitters from fluorescence to phosphorescence through push-pull electronic effects, Nat. Commun. 2020 111. 11 (2020) 1–9. https://doi.org/10.1038/s41467-020-16412-4.

[42] H. Wang, X. Ji, Z.A. Page, J.L. Sessler, Fluorescent materials-based information storage, Mater. Chem. Front. 4 (2020) 1024–1039. https://doi.org/10.1039/C9QM00607A.

[43] J.G. Cadondon, J.P.D. Napal, S. Tatsuo, E.A. Vallar, M.C.D. Galvez, Pulsed LED light source for fluorescence spectroscopy applications, AIP Conf. Proc. 2319 (2021). https://doi.org/10.1063/5.0037374/642327.

[44] S. Sargazi, I. Fatima, M. Hassan Kiani, V. Mohammadzadeh, R. Arshad, M. Bilal, A. Rahdar, A.M. Díez-Pascual, R. Behzadmehr, Fluorescent-based nanosensors for selective detection of a wide range of biological macromolecules: A comprehensive review, Int. J. Biol. Macromol. 206 (2022) 115–147. https://doi.org/10.1016/J.IJBIOMAC.2022.02.137.

[45] P. She, J. Duan, J. Lu, Y. Qin, F. Li, C. Liu, S. Liu, Y. Ma, Q. Zhao, P. She, J. Duan, J. Lu, Y. Qin, F. Li, C. Liu, S. Liu, Y. Ma, Q. Zhao, Single-Component Molecular Dual Persistent Room Temperature Phosphorescence from Low- and High-Lying Triplet States, Adv. Opt. Mater. 10 (2022) 2102706. https://doi.org/10.1002/ADOM.202102706.

[46] F. Xiao, H. Gao, Y. Lei, W. Dai, M. Liu, X. Zheng, Z. Cai, X. Huang, H. Wu, D. Ding, Guest-host doped strategy for constructing ultralong-lifetime near-infrared organic phosphorescence materials for bioimaging, Nat. Commun. 2022 131. 13 (2022) 1–10. https://doi.org/10.1038/s41467-021-27914-0.

[47] N. Hussain, I. Ayoub, U. Mushtaq, R. Sehgal, S. Rubab, R. Sehgal, H.C. Swart, V. Kumar, Introduction to phosphors and luminescence, Rare-Earth-Activated Phosphors Chem. Appl. (2022) 3–41. https://doi.org/10.1016/B978-0-323-89856-0.00008-0.

[48] H.I.L. Jacobs, J.M. Riphagen, N.J. Ashton, S. Janelidze, R.A. Sperling, K.A. Johnson, H.-S. Yang, K. Blennow, O. Hansson, H. Zetterberg, M. Van Egroo, Plasma ptau231 predicts locus coeruleus integrity earlier in life than other Alzheimer's disease plasma markers: a 7T MRI study across the adult lifespan, Alzheimer's Dement. 18 (2022) e065878. https://doi.org/10.1002/ALZ.065878.

[49] P.S. Chelushkin, J.R. Shakirova, I.S. Kritchenkov, V.A. Baigildin, S.P. Tunik, Phosphorescent NIR emitters for biomedicine: applications, advances and challenges, Dalt. Trans. 51 (2022) 1257–1280. https://doi.org/10.1039/D1DT03077A.

[50] X. Ouyang, R. Lin, Y. Ding, Y. Liang, W. Zheng, L. Chen, X. Song, F. Huang, X. Ouyang, Efficient sky-blue radioluminescence of microcrystalline $Cs_3Cu_2I_5$ based large-scale eco-friendly composite scintillators for high-sensitive ionizing radiation detection, Mater. Chem. Front. 5 (2021) 4739–4745. https://doi.org/10.1039/D1QM00356A.

[51] G.W. Jeon, S. Cho, S. Park, W. Kim, A. Jana, D.H. Park, J. Kwak, H. Im, J.-W. Jang, G.W. Jeon, S. Cho, S. Park, D.W. Kim, A. Jana, H. Im, J.-W. Jang, D.H. Park, J. Kwak, Plasmonically-Enhanced Radioluminescence Induced by Energy Transfer in Colloidal $CsPbBr_3$ Nanocrystals via Hybridization of Silver Nanoparticles, Adv. Opt. Mater. 11 (2023) 2300221. https://doi.org/10.1002/ADOM.202300221.

[52] J.N. Demas, S.E. Demas, Luminescence, Ref. Modul. Chem. Mol. Sci. Chem. Eng. (2014). https://doi.org/10.1016/B978-0-12-409547-2.11000-5.

[53] F. Reading, Photon Activation, IUPAC Compend. Chem. Terminol. (2008) 20–27. https://doi.org/10.1351/goldbook.p04628.

[54] Y. Liu, K. Zhao, Y. Ren, S. Wan, C. Yang, J. Li, F. Wang, C. Chen, J. Su, D. Chen, Y. Zhao, K. Liu, H. Zhang, Highly Plasticized Lanthanide Luminescence for Information Storage and Encryption Applications, Adv. Sci. 9 (2022) 2105108. https://doi.org/10.1002/ADVS.202105108.

[55] D. Parker, J.D. Fradgley, K.L. Wong, The design of responsive luminescent lanthanide probes and sensors, Chem. Soc. Rev. 50 (2021) 8193–8213. https://doi.org/10.1039/D1CS00310K.

[56] D.M. Lyubov, A.N. Carneiro Neto, A. Fayoumi, K.A. Lyssenko, V.M. Korshunov, I. V. Taydakov, F. Salles, Y. Guari, J. Larionova, L.D. Carlos, J. Long, A.A. Trifonov, Employing three-blade propeller lanthanide complexes as molecular luminescent thermometers: study of temperature sensing through a concerted experimental/theory approach, J. Mater. Chem. C. 10 (2022) 7176–7188. https://doi.org/10.1039/D2TC01289H.

[57] S.K. Gupta, J.P. Zuniga, M. Abdou, M.P. Thomas, M. De Alwis Goonatilleke, B.S. Guiton, Y. Mao, Lanthanide-doped lanthanum hafnate nanoparticles as

multicolor phosphors for warm white lighting and scintillators, Chem. Eng. J. 379 (2020) 122314. https://doi.org/10.1016/J.CEJ.2019.122314.

[58] J.C.G. Bünzli, Lanthanide Luminescence: From a Mystery to Rationalization, Understanding, and Applications, Handb. Phys. Chem. Rare Earths. 50 (2016) 141–176. https://doi.org/10.1016/bs.hpcre.2016.08.003.

[59] T. Charytanowicz, B. Sieklucka, S. Chorazy, Lanthanide Hexacyanidoruthenate Frameworks for Multicolor to White-Light Emission Realized by the Combination of d-d, d-f, and f-f Electronic Transitions, Inorg. Chem. 62 (2023) 1611–1627.

[60] B.M. Van Der Ende, L. Aarts, A. Meijerink, Lanthanide ions as spectral converters for solar cells, Phys. Chem. Chem. Phys. 11 (2009) 11081–11095. https://doi.org/10.1039/B913877C.

[61] G.M. Martins, K.P.F. Siqueira, C. Fantini, R.L. Moreira, A. Dias, New insight on the use of diffuse reflectance spectroscopy for the optical characterization of $Ln_2Ge_2O_7$ (Ln = lanthanides) pyrogermanates, J. Lumin. 238 (2021) 118312. https://doi.org/10.1016/J.JLUMIN.2021.118312.

[62] G. López-Pacheco, I. Padilla-Rosales, A. Miguel-Eugenio, E. Barrera-Calva, R. Rosas, F. González, Insight into the optical absorption and luminescent properties due to the presence of Pr^{4+} in Pr-doped Y_2O_3, J. Lumin. 242 (2022) 118596. https://doi.org/10.1016/J.JLUMIN.2021.118596.

[63] T. Kornher, K. Xia, R. Kolesov, N. Kukharchyk, R. Reuter, P. Siyushev, R. Stöhr, M. Schreck, H.W. Becker, B. Villa, A.D. Wieck, J. Wrachtrup, Production yield of rare-earth ions implanted into an optical crystal, Appl. Phys. Lett. 108 (2016). https://doi.org/10.1063/1.4941403.

[64] C.M. Trindade, R.T. Alves, A.C.A. Silva, N.O. Dantas, A.S. Gouveia-Neto, Tunable greenish to reddish luminescence and two-way energy transfer in Ho^{3+} and Pr^{3+} doped TeO_2:ZnO glass, Opt. Mater. (Amst). 99 (2020) 109574. https://doi.org/10.1016/J.OPTMAT.2019.109574.

[65] L. Sun, C. Zhang, L. Yan, L. Gao, T. Ma, Praseodymium-doped triple-cation perovskite layer for enhanced photovoltaic performance, J. Solid State Chem. 307 (2022) 122826. https://doi.org/10.1016/J.JSSC.2021.122826.

[66] P. Ramakrishna, R.K. Padhi, S.K. Parida, D.K. Mohapatra, H. Jena, B.S. Panigrahi, Effect of U on the photoluminescence of Pr and structural properties of U/Pr doped and co-doped Li_2O–ZnO–SrO borophosphate glass, Opt. Mater. (Amst). 134 (2022) 113121. https://doi.org/10.1016/J.OPTMAT.2022.113121.

[67] A. Tuomela, M. Zhang, M. Huttula, S. Sakirzanovas, A. Kareiva, A.I. Popov, A.P. Kozlova, S.A. Aravindh, W. Cao, V. Pankratov, Luminescence and vacuum ultraviolet excitation spectroscopy of samarium doped SrB_4O_7, J. Alloys Compd. 826 (2020) 154205. https://doi.org/10.1016/J.JALLCOM.2020.154205.

[68] P. Vinodkumar, G. Jaiganesh, S. Panda, R.K. Padhi, U. Madhusoodanan, B.S. Panigrahi, Color tuning from green to orange-red in $SrBPO_5$:UO_2^{2+}/Pr^{3+} phosphor via energy transfer for solid-state lighting applications, Results Phys. 21 (2021) 103757. https://doi.org/10.1016/J.RINP.2020.103757.

[69] K.H. Mahmoud, A.S. Alsubaie, K.A. Elsayed, Modulation of optical

properties of PolyvinylPyrrolidone via doping with praseodymium (III) nitrate salt, Optik (Stuttg). 231 (2021) 166383. https://doi.org/10.1016/J.IJLEO.2021.166383.

[70] L. Nádherný, V. Doležal, D. Sedmidubský, J. Cajzl, R. Kučerková, M. Nikl, V. Jakeš, K. Rubešová, Optical and magnetic properties of nanostructured cerium-doped $LaMgAl_{11}O_{19}$, J. Mater. Res. 35 (2020) 1672–1679. https://doi.org/10.1557/JMR.2020.119/FIGURES/7.

[71] S. Yang, W. Sun, Q. Xu, C. Yang, S. Zhang, M. Jiao, Synthesis, structure, and luminescence properties of Europium/Cerium/Terbium doped strontium-anorthite-type green phosphor for solid state lighting, Spectrochim. Acta Part A Mol. Biomol. Spectrosc. 292 (2023) 122402. https://doi.org/10.1016/J.SAA.2023.122402.

[72] X. Li, H. Yu, F. Yao, H. Ni, R. Sun, J. Zhou, J. Ding, J. Li, Q. Zhang, Insight into site occupancy of cerium and manganese ions in $MgAl_2O_4$ and their energy transfer for dual-mode optical thermometry, J. Alloys Compd. 928 (2022) 166701. https://doi.org/10.1016/J.JALLCOM.2022.166701.

[73] P. Fang, J. Liu, H. Liu, G. Yu, P. Fu, B. Wang, J. Qu, Y. Huang, Z. Bian, Z. Liu, Delayed Doublet Emission in a Cerium(III) Complex, Angew. Chemie. 135 (2023) e202302192. https://doi.org/10.1002/ANGE.202302192.

[74] G. Inkrataite, J. Keil, A. Zarkov, T. Jüstel, R. Skaudzius, The effect of boron and scandium doping on the luminescence of LuAG:Ce and GdAG:Ce for application as scintillators, J. Alloys Compd. 966 (2023) 171634. https://doi.org/10.1016/j.jallcom.2023.171634.

[75] V. Bachmann, C. Ronda, A. Meijerink, Temperature quenching of yellow Ce^{3+} luminescence in YAG:Ce, Chem. Mater. 21 (2009) 2077–2084. https://doi.org/10.1021/cm8030768.

[76] A.M. Srivastava, C.R. Ronda, W.W. Beers, W.E. Cohen, The Influence of Optically Active Impurities on the Performance of Phosphors and Scintillators, ECS J. Solid State Sci. Technol. 12 (2023) 066009. https://doi.org/10.1149/2162-8777/ACDEA5.

[77] A.V. Dotsenko, L.B. Glebov, V.A. Tsekhomsky, Physics and Chemistry of Photochromic Glasses, 2020. https://doi.org/10.1201/9781003067986.

[78] D.Y. Kosyanov, X. Liu, A.A. Vornovskikh, A.P. Zavjalov, A.M. Zakharenko, A.A. Kosianova, A.N. Fedorets, O.O. Shichalin, A.A. Leonov, W. Li, J. Li, Al_2O_3–Ce:YAG composite ceramics for high brightness lighting: Cerium doping effect, J. Alloys Compd. 887 (2021) 161486. https://doi.org/10.1016/J.JALLCOM.2021.161486.

[79] R. Boddula, J. Tagare, K. Singh, S. Vaidyanathan, White light-emissive europium complexes and their versatile applications, Mater. Chem. Front. 5 (2021) 3159–3175. https://doi.org/10.1039/D1QM00083G.

[80] A.A. Nashivochnikov, A.I. Kostyukov, M.I. Rakhmanova, S. V. Cherepanova, V.N. Snytnikov, Photoluminescence and structure evolution of laser synthesized $ZrO_2:Eu^{3+}$ nanopowders depending on the dopant concentration, Ceram. Int. 49 (2023) 5049–5057.

https://doi.org/10.1016/J.CERAMINT.2022.10.018.
[81] A. Basaif, A. Oresegun, H.T. Zubair, H. Zin, K.Y. Choo, S.A. Ibrahim, T. Wang, J. Wen, D. Gang, E. Lewis, H.A. Abdul-Rashid, D.A. Bradley, Time-resolved radiation dosimetry using a cerium and terbium Co-doped YAG crystal scintillator, Radiat. Phys. Chem. 204 (2023) 110625. https://doi.org/10.1016/J.RADPHYSCHEM.2022.110625.
[82] R. Skaudzius, A. Katelnikovas, D. Enseling, A. Kareiva, T. Jüstel, Dependence of the 5D0→7F4 transitions of Eu^{3+} on the local environment in phosphates and garnets, J. Lumin. 147 (2014) 290–294. https://doi.org/10.1016/J.JLUMIN.2013.11.051.
[83] Y. Wei, P. Dang, Z. Dai, G. Li, J. Lin, Advances in Near-Infrared Luminescent Materials without Cr^{3+}: Crystal Structure Design, Luminescence Properties, and Applications, Chem. Mater. 33 (2021) 5496–5526.
[84] L. Xu, X. Jiang, K. Liang, M. Gao, B. Kong, Frontier luminous strategy of functional silica nanohybrids in sensing and bioimaging: From ACQ to AIE, Aggregate. 3 (2022) e121. https://doi.org/10.1002/AGT2.121.
[85] H.P. Labaki, F.H. Borges, F.J. Caixeta, R.R. Gonçalves, Widely dual tunable visible and near infrared emission in Pr^{3+}-doped yttrium tantalate: Pr^{3+} concentration dependence on radiative transitions from 3P0 to the 1D2, J. Lumin. 236 (2021) 118073. https://doi.org/10.1016/J.JLUMIN.2021.118073.
[86] X. Shi, Q. Wang, S. Song, X. Wang, J. Feng, H. Zhang, The influence of Pr^{3+} ions on the emission characteristics of Er^{3+}-doped YSGG single crystal fibers in the 1–3 μm wavelength range, Opt. Mater. (Amst). 145 (2023) 114468. https://doi.org/10.1016/J.OPTMAT.2023.114468.
[87] G. Yang, Y. Song, Q. Wang, L. Zhang, L. Deng, Review of ionic liquids containing, polymer/inorganic hybrid electrolytes for lithium metal batteries, Mater. Des. 190 (2020) 108563. https://doi.org/10.1016/J.MATDES.2020.108563.
[88] K. Yu, Y. Liu, Y. Yang, Review on form-stable inorganic hydrated salt phase change materials: Preparation, characterization and effect on the thermophysical properties, Appl. Energy. 292 (2021) 116845. https://doi.org/10.1016/J.APENERGY.2021.116845.
[89] H. Luo, W. Rao, P. Zhao, L. Wang, Y. Liu, C. Yu, An efficient organic/inorganic phosphorus–nitrogen–silicon flame retardant towards low-flammability epoxy resin, Polym. Degrad. Stab. 178 (2020) 109195. https://doi.org/10.1016/J.POLYMDEGRADSTAB.2020.109195.
[90] R.E. Rojas-Hernandez, F. Rubio-Marcos, J.F. Fernandez, I. Hussainova, Aluminate-Based Nanostructured Luminescent Materials: Design of Processing and Functional Properties, Mater. 2021, Vol. 14, Page 4591. 14 (2021) 4591. https://doi.org/10.3390/MA14164591.
[91] X. Zhou, J. Qiao, Z. Xia, Learning from Mineral Structures toward New Luminescence Materials for Light-Emitting Diode Applications, Chem. Mater. 33 (2021) 1083–1098.
[92] V. Kumar, Z. Luo, A Review on X-ray Excited Emission Decay Dynamics in

Inorganic Scintillator Materials, Photonics 2021, Vol. 8, Page 71. 8 (2021) 71. https://doi.org/10.3390/PHOTONICS8030071.

[93] L. Fernández-Rodríguez, A. Durán, M.J. Pascual, Silicate-based persistent phosphors, Open Ceram. 7 (2021) 100150. https://doi.org/10.1016/J.OCERAM.2021.100150.

[94] P. Kumar, S. Pachisia, R. Gupta, Turn-on detection of assorted phosphates by luminescent chemosensors, Inorg. Chem. Front. 8 (2021) 3587–3607. https://doi.org/10.1039/D1QI00032B.

[95] T. Famprikis, P. Canepa, J.A. Dawson, M.S. Islam, C. Masquelier, Fundamentals of inorganic solid-state electrolytes for batteries, Nat. Mater. 18 (2019) 1278–1291. https://doi.org/10.1038/s41563-019-0431-3.

[96] J. Cui, S. Yao, H. Khani, Solid Electrolytes for Lithium-Metal Batteries, Encycl. Mater. Electron. 1–3 (2023) 213–225. https://doi.org/10.1016/B978-0-12-819728-8.00024-3.

[97] E.A.D. White, Synthetic gemstones, Q. Rev. Chem. Soc. 15 (1961) 1–29. https://doi.org/10.1039/qr9611500001.

[98] Y. Liu, S. Hu, Y. Zhang, Z. Wang, G. Zhou, S. Wang, Crystal structure evolution and luminescence property of Ce^{3+}-doped Y_2O_3-Al_2O_3-Sc_2O_3 ternary ceramics, J. Eur. Ceram. Soc. 40 (2020) 840–846. https://doi.org/10.1016/j.jeurceramsoc.2019.10.022.

[99] R. Nakamoto, B. Xu, C. Xu, H. Xu, L. Bellaiche, Properties of rare-earth iron garnets from first principles, Phys. Rev. B. 95 (2017). https://doi.org/10.1103/PhysRevB.95.024434.

[100] K. Byrappa, M. Yoshimura, Hydrothermal Synthesis of Native Elements and Simple Oxides, Handb. Hydrothermal Technol. (2013) 569–614. https://doi.org/10.1016/B978-0-12-375090-7.00009-8.

[101] D. Navas, S. Fuentes, A. Castro-Alvarez, E. Chavez-Angel, Review on Sol-Gel Synthesis of Perovskite and Oxide Nanomaterials, Gels 2021, Vol. 7, Page 275. 7 (2021) 275. https://doi.org/10.3390/GELS7040275.

[102] M.H. El Makdah, M.H. El-Dakdouki, R. Mhanna, J. Al Boukhari, R. Awad, Effects of neodymium substitution on the structural, optical, and magnetic properties of yttrium iron garnet nanoparticles, Appl. Phys. A Mater. Sci. Process. 127 (2021) 1–15. https://doi.org/10.1007/S00339-021-04466-0/TABLES/5.

[103] A. Nurpeissov, S. Pazylbek, D. Karoblis, A. Katelnikovas, D. Vistorskaja, T. Nurakhmetov, A. Zarkov, A. Kareiva, Study on the formation of sol-gel derived calcium, lithium and lanthanide element (Ln - Ce, Eu, Tb) substituted yttrium gallium/aluminium garnets $Y_{3-x-y-z}Ca_xLi_yLn_zGa_{5-m}Al_mO_{12}$: Novel insight to high-entropy compounds, Opt. Mater. (Amst). 148 (2024) 114942. https://doi.org/10.1016/J.OPTMAT.2024.114942.

[104] Q. Liu, W. Wang, Z. Dai, V. Boiko, H. Chen, X. Liu, D. Zhu, J. Xu, D. Hreniak, J. Li, Fabrication and long persistent luminescence of Ce^{3+}-Cr^{3+} co-doped yttrium aluminum gallium garnet transparent ceramics, J. Rare Earths. 40 (2022) 1699–1705. https://doi.org/10.1016/J.JRE.2022.01.017.

[105] M. Vallés-Pelarda, R.S. Sanchez, E.M. Barea, I. Mora-Seró, B. Julián-López, Up-Converting Lanthanide-Doped YAG Nanospheres, Front. Mater. 7 (2020) 564043. https://doi.org/10.3389/FMATS.2020.00273/BIBTEX.

[106] A.A. Ansari, M.R. Muthumareeswaran, R. Lv, Coordination chemistry of the host matrices with dopant luminescent Ln^{3+} ion and their impact on luminescent properties, Coord. Chem. Rev. 466 (2022) 214584. https://doi.org/10.1016/J.CCR.2022.214584.

[107] G. Liu, B. Wang, J. Li, B. Cao, Y. Lu, Z. Liu, Research progress of gadolinium aluminum garnet based optical materials, Phys. B Condens. Matter. 603 (2021) 412775. https://doi.org/10.1016/J.PHYSB.2020.412775.

[108] G. Liu, T. Hu, M.S. Molokeev, Z. Xia, Li/Na substitution and $Yb_{3x}002B$; co-doping enabling tunable near-infrared emission in $LiIn_2SbO_6$:$Cr_{3x}002B$; phosphors for light-emitting diodes, (2021). https://doi.org/10.1016/j.isci.2021.102250.

[109] C.H. Lu, G. V. Biesold-Mcgee, Y. Liu, Z. Kang, Z. Lin, Doping and ion substitution in colloidal metal halide perovskite nanocrystals, Chem. Soc. Rev. 49 (2020) 4953–5007. https://doi.org/10.1039/C9CS00790C.

[110] L. Havlák, J. Bárta, M. Buryi, V. Jarý, E. Mihóková, V. Laguta, P. Boháček, M. Nikl, Eu^{2+} Stabilization in YAG Structure: Optical and Electron Paramagnetic Resonance Study, J. Phys. Chem. C. 120 (2016) 21751–21761. https://doi.org/10.1021/acs.jpcc.6b06397.

[111] I. Stenina, D. Golubenko, V. Nikonenko, A. Yaroslavtsev, Selectivity of Transport Processes in Ion-Exchange Membranes: Relationship with the Structure and Methods for Its Improvement, Int. J. Mol. Sci. 2020, Vol. 21, Page 5517. 21 (2020) 5517. https://doi.org/10.3390/IJMS21155517.

[112] J. Wang, Q. Zhang, J. Sheng, Z. Liang, J. Ma, Y. Chen, G. Zhou, H.M. Cheng, Direct and green repairing of degraded $LiCoO_2$ for reuse in lithium-ion batteries, Natl. Sci. Rev. 9 (2022). https://doi.org/10.1093/NSR/NWAC097.

[113] S. Kahl, A.M. Grishin, Evolution of properties of epitaxial bismuth iron garnet films with increasing thickness, J. Magn. Magn. Mater. 278 (2004) 244–255. https://doi.org/10.1016/j.jmmm.2003.12.1355.

[114] V.M. Goldschmidt, Die Gesetze der Krystallochemie, Naturwissenschaften. 14 (1926) 477–485. https://doi.org/10.1007/BF01507527/METRICS.

[115] Strengthening of metal alloys, Introd. to Aerosp. Mater. (2012) 57–90. https://doi.org/10.1533/9780857095152.57.

[116] K. Chu, Y.H. Cheng, Q.Q. Li, Y.P. Liu, Y. Tian, Fe-doping induced morphological changes, oxygen vacancies and Ce^{3+}–Ce^{3+} pairs in CeO_2 for promoting electrocatalytic nitrogen fixation, J. Mater. Chem. A. 8 (2020) 5865–5873. https://doi.org/10.1039/C9TA14260F.

[117] X. Li, W. Fan, Y. Bai, Y. Liu, F. Wang, H. Bai, W. Shi, Photoelectrochemical reduction of nitrate to ammonia over CuPc/CeO_2 heterostructure: Understanding the synergistic effect between oxygen vacancies and Ce sites, Chem. Eng. J. 433 (2022) 133225. https://doi.org/10.1016/J.CEJ.2021.133225.

[118] B. Sun, L. Zhang, L. Zhang, T. Zhou, C. Shao, Y. Ma, Q. Yao, Z. Jiang, F.A. Selim, H. Chen, Protected-annealing regulated defects to improve optical

properties and luminescence performance of Ce:YAG transparent ceramics for white LEDs, J. Mater. Chem. C. 7 (2019) 4057–4065. https://doi.org/10.1039/c8tc06600k.

[119] D. Kanakaraju, F.D. anak Kutiang, Y.C. Lim, P.S. Goh, Recent progress of Ag/TiO_2 photocatalyst for wastewater treatment: Doping, co-doping, and green materials functionalization, Appl. Mater. Today. 27 (2022) 101500. https://doi.org/10.1016/J.APMT.2022.101500.

[120] R. Ghorbali, G. Essalah, A. Ghoudi, H. Guermazi, S. Guermazi, A. El Hdiy, H. Benhayoune, B. Duponchel, A. Oueslati, G. Leroy, The effect of (In, Cu) doping and co-doping on physical properties and organic pollutant photodegradation efficiency of ZnO nanoparticles for wastewater remediation, Ceram. Int. 49 (2023) 33828–33841. https://doi.org/10.1016/J.CERAMINT.2023.08.076.

[121] D. Zhou, Z. Wang, Z. Song, F. Wang, S. Zhang, Q. Liu, Enhanced Persistence Properties through Modifying the Trap Depth and Density in $Y_3Al_2Ga_3O_{12}:Ce^{3+},Yb^{3+}$ Phosphor by Co-doping B^{3+}, Inorg. Chem. 58 (2019) 1684–1689. https://doi.org/10.1021/acs.inorgchem.8b03270.

[122] V. V. Bakhmetyev, T.S. Minakova, S. V. Mjakin, L.A. Lebedev, A.B. Vlasenko, A.A. Nikandrova, I.A. Ekimova, N.S. Eremina, M.M. Sychov, A. Ringuede, Synthesis and surface characterization of nanosized Y_2O_3:Eu and YAG:Eu luminescent phosphors which are useful in photodynamic therapy of cancer, Eur. J. Nanomedicine. 8 (2016) 173–184. https://doi.org/10.1515/ejnm-2016-0020.

[123] Y. Mei, W.C. Zheng, H.G. Liu, Insight into the thermal shifts of ten fluorescence peaks Y1–Y10 for Sm^{3+} ions in $Y_3Al_5O_{12}$ crystal, J. Phys. Chem. Solids. 135 (2019) 109101. https://doi.org/10.1016/j.jpcs.2019.109101.

[124] C. Ma, F. Tang, J. Zhu, Z. Wen, Y. Yu, K. Wang, M. Du, J. Zhang, J. Long, X. Yuan, W. Guo, Y. Cao, Cation diffusion at the interface of composite YAG/Re: LuAG (Re = Nd or Yb) transparent ceramics, J. Eur. Ceram. Soc. 36 (2016) 2555–2564. https://doi.org/10.1016/j.jeurceramsoc.2016.03.031.

[125] D. Nakauchi, T. Kato, N. Kawaguchi, T. Yanagida, Characterization of high dense $Pr:GdTaO_4$ crystal scintillators, Radiat. Phys. Chem. 182 (2021) 109390. https://doi.org/10.1016/J.RADPHYSCHEM.2021.109390.

[126] A. De Martinis, L. Montalto, L. Scalise, D. Rinaldi, P. Mengucci, C. Michail, G. Fountos, N. Martini, V. Koukou, I. Valais, A. Bakas, C. Fountzoula, I. Kandarakis, S. David, Luminescence and Structural Characterization of Gd_2O_2S Scintillators Doped with Tb^{3+}, Ce^{3+}, Pr^{3+} and F for Imaging Applications, Cryst. 2022, Vol. 12, Page 854. 12 (2022) 854. https://doi.org/10.3390/CRYST12060854.

[127] N. Ugemuge, Y.R. Parauha, S.J. Dhoble, Synthesis and luminescence study of silicate-based phosphors for energy-saving light-emitting diodes, Energy Mater. Fundam. to Appl. (2021) 445–480. https://doi.org/10.1016/B978-0-12-823710-6.00017-0.

[128] X. Li, C. Guo, H. Wang, Y. Chen, J. Zhou, J. Lin, Q. Zeng, Green emitting

$Ba_{1.5}Lu_{1.5}Al_{3.5}Si_{1.5}O_{12}:Ce^{3+}$ phosphor with high thermal emission stability for warm WLEDs and FEDs, Ceram. Int. 46 (2020) 5863–5870. https://doi.org/10.1016/j.ceramint.2019.11.037.

[129] D.S. McGregor, J.K. Shultis, Physical Sensors: Radiation Sensors, Encycl. Sensors Biosens. Vol. 1-4, First Ed. 1–4 (2023) 141–160. https://doi.org/10.1016/B978-0-12-822548-6.00157-6.

[130] F. Wilkinson, Scintillators, Emiss. Tomogr. Fundam. PET SPECT. (2004) 229–254. https://doi.org/10.1016/B978-012744482-6.50016-8.

[131] B. Collum, Radiometric instruments, Nucl. Facil. (2017) 349–368. https://doi.org/10.1016/B978-0-08-101938-2.00011-8.

[132] N. V. Klassen, V. V. Kedrov, V.N. Kurlov, Y.A. Ossipyan, S.Z. Shmurak, I.M. Shmyt'ko, G.K. Strakova, N.P. Kobelev, E.A. Kudrenko, O.A. Krivko, A.P. Kiselev, A. V. Bazhenov, T.N. Fursova, Advantages and problems of nanocrystalline scintillators, IEEE Trans. Nucl. Sci. 55 (2008) 1536–1541. https://doi.org/10.1109/TNS.2008.924050.

[133] C.L. Melcher, Perspectives on the future development of new scintillators, Nucl. Instruments Methods Phys. Res. Sect. A Accel. Spectrometers, Detect. Assoc. Equip. 537 (2005) 6–14. https://doi.org/10.1016/J.NIMA.2004.07.222.

[134] J.S. Neal, D.M. Devito, B.L. Armstrong, M. Hong, B. Kesanli, X. Yang, N.C. Giles, J.Y. Howe, J.O. Ramey, D.J. Wisniewski, M. Wisniewska, Z.A. Munir, L.A. Boatner, Investigation of ZnO-based polycrystalline ceramic scintillators for use as α -particle detectors, IEEE Trans. Nucl. Sci. 56 (2009) 892–898. https://doi.org/10.1109/TNS.2008.2004702.

[135] L. Fiserova, J. Janda, Scintillation powders for the detection of neutrons, IEEE Trans. Nucl. Sci. 65 (2018) 2140–2146. https://doi.org/10.1109/TNS.2018.2818299.

[136] Z. Wang, C. Dujardin, M.S. Freeman, A.E. Gehring, J.F. Hunter, P. Lecoq, W. Liu, C.L. Melcher, C.L. Morris, M. Nikl, G. Pilania, R. Pokharel, D.G. Robertson, D.J. Rutstrom, S.K. Sjue, A.S. Tremsin, S.A. Watson, B.W. Wiggins, N.M. Winch, M. Zhuravleva, Needs, Trends, and Advances in Scintillators for Radiographic Imaging and Tomography, IEEE Trans. Nucl. Sci. 70 (2023) 1244–1280. https://doi.org/10.1109/TNS.2023.3290826.

[137] M.S.J. Marshall, J. Wang, S. Miller, B. Singh, V. Nagarkar, Developing Perovskite Halide Scintillator thin Films for Fast-Timing Applications, 2020 IEEE Nucl. Sci. Symp. Med. Imaging Conf. NSS/MIC 2020. (2020). https://doi.org/10.1109/NSS/MIC42677.2020.9508006.

[138] V.S. Shevelev, A. V. Ishchenko, A.S. Vanetsev, V. Nagirnyi, S.I. Omelkov, Ultrafast hybrid nanocomposite scintillators: A review, J. Lumin. 242 (2022) 118534. https://doi.org/10.1016/J.JLUMIN.2021.118534.

[139] P. Aim-O, S. Klinkhieo, M. Sophon, N. Sumano, W. Phacheerak, M. Phanak, A. Ruangvittayanon, Performance of CsI (Tl) photodiode with optic fiber wire for Gamma-rays and X-rays detection, J. Phys. Conf. Ser. 2175 (2022) 012013. https://doi.org/10.1088/1742-6596/2175/1/012013.

[140] K. Watanabe, Applications of scintillators in optical-fiber-based detectors, Jpn. J. Appl. Phys. 62 (2022) 010507. https://doi.org/10.35848/1347-

4065/AC90A5.
[141] M.J. Weber, Inorganic scintillators: today and tomorrow, J. Lumin. 100 (2002) 35–45. https://doi.org/10.1016/S0022-2313(02)00423-4.
[142] J.T.M. De Haas, P. Dorenbos, C.W.E. Van Eijk, Measuring the absolute light yield of scintillators, Nucl. Instruments Methods Phys. Res. Sect. A Accel. Spectrometers, Detect. Assoc. Equip. 537 (2005) 97–100. https://doi.org/10.1016/J.NIMA.2004.07.243.
[143] X. Zhao, G. Niu, J. Zhu, B. Yang, J.H. Yuan, S. Li, W. Gao, Q. Hu, L. Yin, K.H. Xue, E. Lifshitz, X. Miao, J. Tang, All-Inorganic Copper Halide as a Stable and Self-Absorption-Free X-ray Scintillator, J. Phys. Chem. Lett. 11 (2020) 1873–1880.
[144] J. Xu, L. Cao, Y. Feng, Y. Huang, Y. Wang, L. Qin, H.J. Seo, Improved scintillation luminescence and thermal stability of $In_2Si_2O_7$ ceramic phosphor, J. Lumin. 183 (2017) 166–172. https://doi.org/10.1016/J.JLUMIN.2016.11.021.
[145] D. Poda, Scintillation in Low-Temperature Particle Detectors, Phys. 2021, Vol. 3, Pages 473-535. 3 (2021) 473–535. https://doi.org/10.3390/PHYSICS3030032.
[146] P. Lecoq, Scintillation Detectors for Charged Particles and Photons, Part. Phys. Ref. Libr. Vol. 2 Detect. Part. Radiat. 2 (2020) 45–89. https://doi.org/10.1007/978-3-030-35318-6_3/TABLES/2.
[147] L. Lu, M. Sun, Q. Lu, T. Wu, B. Huang, High energy X-ray radiation sensitive scintillating materials for medical imaging, cancer diagnosis and therapy, Nano Energy. 79 (2021) 105437. https://doi.org/10.1016/J.NANOEN.2020.105437.
[148] J.-M. Regis, Fast Timing with $LaBr_3$(Ce) Scintillators and the Mirror Symmetric Centroid Difference Method, Phd Thesis. 3 (2011).
[149] Z. Lin, S. Lv, Z. Yang, J. Qiu, S. Zhou, Structured Scintillators for Efficient Radiation Detection, Adv. Sci. 9 (2022) 2102439. https://doi.org/10.1002/ADVS.202102439.
[150] Z. Xie, Y. Sui, J. Buckeridge, C.R.A. Catlow, T.W. Keal, P. Sherwood, A. Walsh, M.R. Farrow, D.O. Scanlon, S.M. Woodley, A.A. Sokol, Donor and Acceptor Characteristics of Native Point Defects in GaN, (2018). https://doi.org/10.1088/1361-6463/ab2033.
[151] A. Faanu, J.H. Ephraim, E.O. Darko, Assessment of public exposure to naturally occurring radioactive materials from mining and mineral processing activities of Tarkwa Goldmine in Ghana, Environ. Monit. Assess. 180 (2011) 15–29. https://doi.org/10.1007/S10661-010-1769-9.
[152] J. 1966- Haus, Optical Sensors Basics and Applications, (n.d.). https://books.google.com/books/about/Optical_Sensors.html?hl=lt&id=n7Eu-T-xy14C (accessed February 19, 2024).
[153] T. Pöschl, D. Greenwald, M.J. Losekamm, S. Paul, Measurement of ionization quenching in plastic scintillators, Nucl. Instruments Methods Phys. Res. Sect. A Accel. Spectrometers, Detect. Assoc. Equip. 988 (2021) 164865. https://doi.org/10.1016/J.NIMA.2020.164865.
[154] Y. Zhang, Y. Liu, Z. Xu, H. Ye, Z. Yang, J. You, M. Liu, Y. He, M.G. Kanatzidis, S. (Frank) Liu, Nucleation-controlled growth of superior lead-free

perovskite $Cs_3Bi_2I_9$ single-crystals for high-performance X-ray detection, Nat. Commun. 2020 111. 11 (2020) 1–11. https://doi.org/10.1038/s41467-020-16034-w.

[155] M. Chen, L. Sun, Z. Hong, H. Wang, Y. Xia, S. Liu, X. Ren, X. Zhang, D. Chi, H. Yang, W. Hu, Anthracene Single-Crystal Scintillators for Computer Tomography Scanning, ACS Appl. Mater. Interfaces. 14 (2022) 41275–41282.

[156] Z. Wang, R. Sun, N. Liu, H. Fan, X. Hu, D. Shen, Y. Zhang, H. Liu, X-Ray imager of 26-μm resolution achieved by perovskite assembly, Nano Res. 15 (2022) 2399–2404. https://doi.org/10.1007/S12274-021-3808-Y/METRICS.

[157] R. Masełek, K. Sakurai, Prospects for detecting long-lived particles at the Large Hadron Collider, (2023). https://arxiv.org/abs/2310.13748v1 (accessed February 21, 2024).

[158] R.V.V. Petrescu, F.I.T. Petrescu, Contributions to the Hydrogen Fusion, Am. J. Eng. Appl. Sci. 13 (2020) 477–486. https://doi.org/10.3844/AJEASSP.2020.477.486.

[159] D. Buttazzo, R. Franceschini, A. Wulzer, Two paths towards precision at a very high energy lepton collider, J. High Energy Phys. 2021 (2021) 1–39. https://doi.org/10.1007/JHEP05(2021)219/METRICS.

[160] P. Albicocco, J. Alexander, F. Bossi, P. Branchini, B. Buonomo, C. Capoccia, E. Capitolo, G. Chiodini, A.P. Caricato, R. de Sangro, C. Di Giulio, D. Domenici, F. Ferrarotto, G. Finocchiaro, S. Fiore, L.G. Foggetta, A. Frankenthal, G. Georgiev, A. Ghigo, F. Giacchino, P. Gianotti, S. Ivanov, V. Kozhuharov, E. Leonardi, B. Liberti, E. Long, M. Martino, I. Oceano, F. Oliva, G.C. Organtini, G. Piperno, M. Raggi, F. Safai Tehrani, I. Sarra, B. Sciascia, R. Simeonov, A. Saputi, T. Spadaro, S. Spagnolo, E. Spiriti, D. Tagnani, C. Taruggi, L. Tsankov, P. Valente, E. Vilucchi, Characterisation and performance of the PADME electromagnetic calorimeter, J. Instrum. 15 (2020) T10003. https://doi.org/10.1088/1748-0221/15/10/T10003.

[161] C. Kim, W. Lee, A. Melis, A. Elmughrabi, K. Lee, C. Park, J.Y. Yeom, A Review of Inorganic Scintillation Crystals for Extreme Environments, Cryst. 2021, Vol. 11, Page 669. 11 (2021) 669. https://doi.org/10.3390/CRYST11060669.

[162] F. Consoli, V.T. Tikhonchuk, M. Bardon, P. Bradford, D.C. Carroll, J. Cikhardt, M. Cipriani, R.J. Clarke, T.E. Cowan, C.N. Danson, R. De Angelis, M. De Marco, J.L. Dubois, B. Etchessahar, A.L. Garcia, D.I. Hillier, A. Honsa, W. Jiang, V. Kmetik, J. Krasa, Y. Li, F. Lubrano, P. McKenna, J. Metzkes-Ng, A. Poye, I. Prencipe, P. Raczka, R.A. Smith, R. Vrana, N.C. Woolsey, E. Zemaityte, Y. Zhang, Z. Zhang, B. Zielbauer, D. Neely, Laser produced electromagnetic pulses: generation, detection and mitigation, High Power Laser Sci. Eng. 8 (2020) e22. https://doi.org/10.1017/HPL.2020.13.

[163] E. Snider, N. Dasenbrock-Gammon, R. McBride, X. Wang, N. Meyers, K. V. Lawler, E. Zurek, A. Salamat, R.P. Dias, Synthesis of Yttrium Superhydride Superconductor with a Transition Temperature up to 262 K by Catalytic Hydrogenation at High Pressures, Phys. Rev. Lett. 126 (2021) 117003.

https://doi.org/10.1103/PHYSREVLETT.126.117003/FIGURES/4/MEDIUM.

[164] T. Horn, V. V. Berdnikov, S. Ali, A. Asaturyan, M. Carmignotto, J. Crafts, A. Demarque, R. Ent, G. Hull, H.S. Ko, M. Mostafavi, C. Munoz-Camacho, A. Mkrtchyan, H. Mkrtchyan, T. Nguyen Trung, I.L. Pegg, E. Rindel, A. Somov, V. Tadevosyan, R. Trotta, S. Zhamkochyan, R. Wang, S.A. Wood, Scintillating crystals for the Neutral Particle Spectrometer in Hall C at JLab, Nucl. Instruments Methods Phys. Res. Sect. A Accel. Spectrometers, Detect. Assoc. Equip. 956 (2020) 163375. https://doi.org/10.1016/J.NIMA.2019.163375.

[165] H. Fukushima, D. Nakauchi, T. Kato, N. Kawaguchi, T. Yanagida, Photoluminescence and Scintillation Properties of Ce-doped $(Mg_xCa_{1-x})HfO_3$ Single Crystals, Sensors Mater. 35 (2023) 429–437. https://doi.org/10.18494/SAM4139.

[166] O. Sidletskiy, K. Lebbou, D. Kofanov, Micro-pulling-down growth of long YAG- and LuAG-based garnet fibres: advances and bottlenecks, CrystEngComm. 23 (2021) 2633–2643. https://doi.org/10.1039/D1CE00091H.

[167] M. Skruodiene, M. Misevicius, M. Sakalauskaite, A. Katelnikovas, R. Skaudzius, Doping effect of Tb^{3+} ions on luminescence properties of $Y_3Al_5O_{12}:Cr^{3+}$ phosphor, J. Lumin. 179 (2016) 355–360. https://doi.org/10.1016/j.jlumin.2016.07.041.

[168] G. Inkrataite, A. Zabiliute-Karaliune, J. Aglinskaite, P. Vitta, K. Kristinaityte, A. Marsalka, R. Skaudzius, Study of YAG:Ce and Polymer Composite Properties for Application in LED Devices, Chempluschem. 85 (2020) 1504–1510. https://doi.org/10.1002/cplu.202000318.

[169] E. Garskaite, M. Lindgren, M.A. Einarsrud, T. Grande, Luminescent properties of rare earth (Er, Yb) doped yttrium aluminium garnet thin films and bulk samples synthesised by an aqueous sol-gel technique, J. Eur. Ceram. Soc. 30 (2010) 1707–1715. https://doi.org/10.1016/j.jeurceramsoc.2010.01.001.

[170] G. Inkrataitė, Ž. Stankevičiūtė, R. Skaudžius, Determination of different garnet films characteristics prepared via sol-gel spin or dip-coatings techniques, J. Lumin. 244 (2022) 118751. https://doi.org/10.1016/J.JLUMIN.2022.118751.

[171] M.T. Lucchini, V. Babin, P. Bohacek, S. Gundacker, K. Kamada, M. Nikl, A. Petrosyan, A. Yoshikawa, E. Auffray, Effect of Mg^{2+} ions co-doping on timing performance and radiation tolerance of Cerium doped $Gd_3Al_2Ga_3O_{12}$ crystals, Nucl. Instruments Methods Phys. Res. Sect. A Accel. Spectrometers, Detect. Assoc. Equip. 816 (2016) 176–183. https://doi.org/10.1016/j.nima.2016.02.004.

[172] J. Grigorjevaite, A. Katelnikovas, Luminescence and luminescence quenching of $K_2Bi(PO_4)(MoO_4):Eu^{3+}$ phosphors with efficiencies close to unity, ACS Appl. Mater. Interfaces. 8 (2016) 31772–31782. https://doi.org/10.1021/acsami.6b11766.

[173] W. Zhou, Z. Ma, Y. Cai, X. Bi, T. Li, W. Niu, X. Sun, Q. Lu, The Synthesis

Temperature Selection of Cerium Doped Lutetium Yttrium Oxyorthosilicate Single Crystal Powder, in: Atlantis Press, 2018. https://doi.org/10.2991/aetr-17.2018.44.

[174] S. Feng, H. Qin, G. Wu, H. Jiang, J. Zhao, Y. Liu, Z. Luo, J. Qiao, J. Jiang, Spectrum regulation of YAG:Ce transparent ceramics with Pr, Cr doping for white light emitting diodes application, J. Eur. Ceram. Soc. 37 (2017) 3403–3409. https://doi.org/10.1016/j.jeurceramsoc.2017.03.061.

[175] L.M. Chepyga, G. Jovicic, A. Vetter, A. Osvet, C.J. Brabec, M. Batentschuk, Photoluminescence properties of thermographic phosphors YAG:Dy and YAG:Dy, Er doped with boron and nitrogen, Appl. Phys. B Lasers Opt. 122 (2016) 1–10. https://doi.org/10.1007/s00340-016-6487-8.

[176] S. Cho, C. Yun, Y.S. Kim, H. Wang, J. Jian, W. Zhang, J. Huang, X. Wang, H. Wang, J.L. MacManus-Driscoll, Strongly enhanced dielectric and energy storage properties in lead-free perovskite titanate thin films by alloying, Nano Energy. 45 (2018) 398–406. https://doi.org/10.1016/j.nanoen.2018.01.003.

[177] M. Xu, J. Song, R. Wang, S. Li, N. Wang, S. Yu, H. Yan, T. Xia, F. Chen, Effect of sintering AIDS on the properties of porous YAG ceramics, Key Eng. Mater. 697 (2016) 178–181. https://doi.org/10.4028/www.scientific.net/KEM.697.178.

[178] L. Chen, X. Chen, F. Liu, H. Chen, H. Wang, E. Zhao, Y. Jiang, T.S. Chan, C.H. Wang, W. Zhang, Y. Wang, S. Chen, Charge deformation and orbital hybridization: Intrinsic mechanisms on tunable chromaticity of $Y_3Al_5O_{12}:Ce^{3+}$ luminescence by doping Gd^{3+} for warm white LEDs, Sci. Rep. 5 (2015) 1–17. https://doi.org/10.1038/srep11514.

[179] M.G. Brik, Fully relativistic analysis of the covalence effects for the isoelectronic 3d3 ions (Cr^{3+}, Mn^{4+}, Fe^{5+}) in $SrTiO_3$, J. Phys. Chem. Solids. 67 (2006) 856–861. https://doi.org/10.1016/j.jpcs.2005.12.006.

[180] Y. Shen, D.R. Clarke, Effects of reducing atmosphere on the luminescence of Eu^{3+}-doped yttria-stabilized zirconia sensor layers in thermal barrier coatings, J. Am. Ceram. Soc. 92 (2009) 125–129. https://doi.org/10.1111/j.1551-2916.2008.02866.x.

[181] E. Zych, A. Walasek, A. Szemik-Hojniak, Variation of emission color of $Y_3Al_5O_{12}$:Ce induced by thermal treatment at reducing atmosphere, J. Alloys Compd. 451 (2008) 582–585. https://doi.org/10.1016/j.jallcom.2007.04.116.

[182] Y. Kim, S. Kang, Effect of particle size on photoluminescence emission intensity in ZnO, Acta Mater. 59 (2011) 3024–3031. https://doi.org/10.1016/j.actamat.2011.01.042.

[183] T. Gavrilović, J. Periša, J. Papan, K. Vuković, K. Smits, D.J. Jovanović, M.D. Dramićanin, Particle size effects on the structure and emission of Eu^{3+}:$LaPO_4$ and $EuPO_4$ phosphors, J. Lumin. 195 (2018) 420–429. https://doi.org/10.1016/j.jlumin.2017.12.002.

[184] E.P. Jahrman, G.T. Seidler, J.R. Sieber, Determination of Hexavalent Chromium Fractions in Plastics Using Laboratory-Based, High-Resolution X-ray Emission Spectroscopy, Anal. Chem. 90 (2018) 6587–6593. https://doi.org/10.1021/acs.analchem.8b00302.

[185] S. Kurumada, S. Takamori, M. Yamashita, An alkyl-substituted aluminium anion with strong basicity and nucleophilicity, Nat. Chem. 12 (2020) 36–39. https://doi.org/10.1038/s41557-019-0365-z.

[186] T. Yanagida, Y. Fujimoto, A. Yamaji, N. Kawaguchi, K. Kamada, D. Totsuka, K. Fukuda, K. Yamanoi, R. Nishi, S. Kurosawa, T. Shimizu, N. Sarukura, Study of the correlation of scintillation decay and emission wavelength, in: Radiat. Meas., Pergamon, 2013: pp. 99–102. https://doi.org/10.1016/j.radmeas.2012.05.014.

[187] K. Lin, J. Xing, L.N. Quan, F.P.G. de Arquer, X. Gong, J. Lu, L. Xie, W. Zhao, D. Zhang, C. Yan, W. Li, X. Liu, Y. Lu, J. Kirman, E.H. Sargent, Q. Xiong, Z. Wei, Perovskite light-emitting diodes with external quantum efficiency exceeding 20 per cent, Nature. 562 (2018) 245–248. https://doi.org/10.1038/s41586-018-0575-3.

[188] H.-S. Zhang, L. Shi, X.-B. Yang, Y.-J. Zhao, K. Xu, L.-W. Wang, First-Principles Calculations of Quantum Efficiency for Point Defects in Semiconductors: The Example of Yellow Luminance by GaN:C_N+O_N and GaN:C_N, Adv. Opt. Mater. 5 (2017) 1700404. https://doi.org/10.1002/adom.201700404.

[189] J. Sun, Z. Xu, W. Li, X. Shen, Effect of Nano-SiO_2 on the Early Hydration of Alite-Sulphoaluminate Cement, Nanomaterials. 7 (2017) 102. https://doi.org/10.3390/nano7050102.

[190] M. Malakauskaite-Petruleviciene, Z. Stankeviciute, A. Beganskiene, A. Kareiva, Sol-gel synthesis of calcium hydroxyapatite thin films on quartz substrate using dip-coating and spin-coating techniques, J. Sol-Gel Sci. Technol. 71 (2014) 437–446. https://doi.org/10.1007/s10971-014-3394-5.

[191] A. Antonio, R. Botero, E.A. Ramírez, G. Gordillo, S. Ilican, Y. Caglar, M. Caglar, Preparation and Characterization of Semiconductor Thin Films View project Preparation and characterization of ZnO thin films deposited by sol-gel spin coating method, 2008. https://www.researchgate.net/publication/280492099 (accessed April 15, 2020).

[192] Properties: Supplier Data - Sapphire Single Crystal (Alumina 99.9%) - (Goodfellow), (n.d.). https://www.azom.com/properties.aspx?ArticleID=1721 (accessed April 20, 2020).

[193] Silica - Silicon Dioxide (SiO_2), (n.d.). https://www.azom.com/article.aspx?ArticleID=1114 (accessed April 20, 2020).

[194] M. Shimizu, M. Koshimizu, Y. Fujimoto, T. Yanagida, S. Ono, K. Asai, Luminescence and scintillation properties of Cs_3BiC_{l6} crystals, Opt. Mater. (Amst). 61 (2016) 115–118. https://doi.org/10.1016/J.OPTMAT.2016.05.057.

[195] M. Rathaiah, M. Kucera, P. Prusa, A. Beitlerova, M. Nikl, M. Rathaiah, M. Kucera, P. Prusa, A. Beitlerova, M. Nikl, Effect of Si^{4+} co-doping on luminescence and scintillation properties of $Lu_3Al_5O_{12}$:Ce,Ca epitaxial garnet films, OptMa. 91 (2019) 321–325. https://doi.org/10.1016/J.OPTMAT.2019.03.038.

[196] D. Nakauchi, G. Okada, N. Kawano, N. Kawaguchi, T. Yanagida,

Luminescent and scintillation properties of Ce-doped $Tb_3Al_5O_{12}$ crystal grown from Al-rich composition, Appl. Phys. Express. 10 (2017). https://doi.org/10.7567/APEX.10.072601.

[197] O. Sidletskiy, K. Lebbou, D. Kofanov, V. Kononets, I. Gerasymov, R. Bouaita, V. Jary, R. Kucerkova, M. Nikl, A. Polesel, K. Pauwels, E. Auffray, Progress in fabrication of long transparent YAG:Ce and YAG:Ce,Mg single crystalline fibers for HEP applications, CrystEngComm. 21 (2019) 1728–1733. https://doi.org/10.1039/C8CE01781F.

[198] M. Norkus, R. Skaudžius, Enhanced NIR region emission of chromium by changing the chromium concentration in yttrium aluminum garnet (YAG) host matrix, J. Alloys Compd. 908 (2022) 164601. https://doi.org/10.1016/J.JALLCOM.2022.164601.

[199] M. Zeyrek Ongun, Investigation of brightness and decay characteristics of YAG:Ce^{3+}, Ca-α-Sialon:Eu^{2+} and $CaAl_{12}O_{19}$:Mn^{4+} phosphors incorporated with Ni-doped SnO_2 particles, J. Lumin. 240 (2021) 118405. https://doi.org/10.1016/J.JLUMIN.2021.118405.

[200] C. Hu, J. Li, F. Yang, B. Jiang, L. Zhang, R.Y. Zhu, LuAG ceramic scintillators for future HEP experiments, Nucl. Instruments Methods Phys. Res. Sect. A Accel. Spectrometers, Detect. Assoc. Equip. 954 (2020) 161723. https://doi.org/10.1016/J.NIMA.2018.12.038.

[201] Z.T. Karipbayev, V.M. Lisitsyn, D.A. Mussakhanov, G.K. Alpyssova, A.I. Popov, E.F. Polisadova, E. Elsts, A.T. Akilbekov, A.B. Kukenova, M. Kemere, A. Sarakovskis, A. Lushchik, Time-resolved luminescence of YAG:Ce and YAGG:Ce ceramics prepared by electron beam assisted synthesis, Nucl. Instruments Methods Phys. Res. Sect. B Beam Interact. with Mater. Atoms. 479 (2020) 222–228. https://doi.org/10.1016/J.NIMB.2020.06.046.

[202] W. Ma, B. Jiang, X. Feng, X. Huang, W. Wang, K. Sreebunpeng, L. Zhang, On fast LuAG:Ce scintillation ceramics with Ca^{2+} co-dopants, J. Am. Ceram. Soc. 104 (2021) 966–973. https://doi.org/10.1111/JACE.17506.

[203] N.I. Matskevich, T. Wolf, M.Y. Matskevich, Energetic characteristics of barium cerates doped by yttrium, gadolinium and luthetium oxides, J. Chem. Thermodyn. 118 (2018) 188–192. https://doi.org/10.1016/J.JCT.2017.11.010.

[204] J. Chan, L. Cao, W. Li, N. Ma, Z. Xu, X. Huang, Highly Efficient Broad-Band Green-Emitting Cerium(III)-Activated Garnet Phosphor Allows the Fabrication of Blue-Chip-Based Warm-White LED Device with a Superior Color Rendering Index, Inorg. Chem. 2022 (2022) 6963.

[205] Y. Zorenko, V. Gorbenko, M. Nikl, J.A. Mares, T. Martin, P.A. Douissard, Development of novel UV emitting single crystalline film scintillators, IEEE Trans. Nucl. Sci. 57 (2010) 1335–1342. https://doi.org/10.1109/TNS.2009.2037150.

[206] A. Bala, S. Rani, UV excited emission spectra of gadolinium aluminium garnet, J. Opt. (2022). https://doi.org/10.1007/s12596-022-01052-2.

[207] V. Singh, S. Kaur, A.S. Rao, N. Singh, M.S. Pathak, J.L. Rao, An Electron Paramagnetic Resonance and Photoluminescence Investigation of UVB

Radiation Emitting Gadolinium-Activated $CaY_2Al_4SiO_{12}$ Garnet Compound, J. Electron. Mater. 48 (2019) 4092–4098. https://doi.org/10.1007/s11664-019-07175-w.

[208] A. Of, S. Based, O.N. Lu, A.O. Ce, Preparation, Luminescence Properties, and Application of Scintillators Based On $Lu_3Al_5O_{12}$:Ce Single-Crystal Films, Appl. Phys. 69 (2002) 665–670.

[209] R.D. Shannon, IUCr, Revised effective ionic radii and systematic studies of interatomic distances in halides and chalcogenides, Urn:Issn:0567-7394. 32 (1976) 751–767. https://doi.org/10.1107/S0567739476001551.

[210] L. Ding, Q. Zhang, J. Luo, W. Liu, W. Zhou, S. Yin, Preparation, structure and photoluminescence of nanoscaled-Nd: $Lu_3Al_5O_{12}$, J. Alloys Compd. 509 (2011) 10167–10171. https://doi.org/10.1016/J.JALLCOM.2011.07.083.

[211] K. Momma, F. Izumi, VESTA: a three-dimensional visualization system for electronic and structural analysis, Urn:Issn:0021-8898. 41 (2008) 653–658. https://doi.org/10.1107/S0021889808012016.

[212] J. Ueda, S. Tanabe, Review of luminescent properties of Ce^{3+}-doped garnet phosphors: New insight into the effect of crystal and electronic structure, Opt. Mater. X. 1 (2019). https://doi.org/10.1016/J.OMX.2019.100018.

[213] G. He, Y. Liu, H. Zhou, X. Chen, Sintering behavior, phase composition, microstructure, and dielectric characteristics of garnet-type $Ca_3Fe_2Ge_3O_{12}$ microwave ceramics, J. Mater. 9 (2023) 472–481. https://doi.org/10.1016/J.JMAT.2022.12.005.

[214] P. Maurya, R.C. Kamath, V. Gaddale Srinivas, Experimental investigation of suspension-type abrasive water jet machining of nitrile rubber for positive displacement motor applications, Int. J. Light. Mater. Manuf. 6 (2023) 367–378. https://doi.org/10.1016/J.IJLMM.2023.03.002.

[215] Y. Guo, H. Li, S. Li, L. Chen, Z. Li, Study on the Structure, Magnetic Properties and Mechanism of Zn-Doped Yttrium Iron Garnet Nanomaterial Prepared by the Sol-gel Method, Gels 2022, Vol. 8, Page 325. 8 (2022) 325. https://doi.org/10.3390/GELS8050325.

[216] M. Dioktyanto, A. Noviyanto, A.H. Yuwono, Influence of Mechanical Activation on the Formation of Yttrium Aluminum Garnet (YAG) at Lower Temperature, Solid State Phenom. 339 (2022) 69–75. https://doi.org/10.4028/P-98UO37.

[217] M. Laube, T. Jüstel, On the temperature and time dependent photoluminescence of $Lu_3Al_5O_{12}$:Gd^{3+}, J. Lumin. 216 (2019) 116729. https://doi.org/10.1016/J.JLUMIN.2019.116729.

[218] N.S. M Viswanath, J. Hyeong In, H. Jun Kim, al -, V. Hugo López-Lugo, M. Judith Rivera-Medina, J. Carlos Alonso-, G. Seon Park, K. Min Kim, S. Wook Mhin, First-Principles Analysis of the Effects of Covalency and Ionicity on the 4f–5d Transition Energy of Ce^{3+} in Garnet-Type Oxides, ECS J. Solid State Sci. Technol. 12 (2023) 076013. https://doi.org/10.1149/2162-8777/ACE84A.

[219] A. Pakalniskis, A. Marsalka, R. Raudonis, V. Balevicius, A. Zarkov, R.

Skaudzius, A. Kareiva, Sol-gel synthesis and study of praseodymium substitution effects in yttrium aluminium garnet $Y_{3-x}Pr_xAl_5O_{12}$, Opt. Mater. (Amst). 111 (2021) 110586.

[220] L. Rößmann, F. Schröder, T. Jüstel, Effect of Gd^{3+} doping on the luminescence and up-conversion of Pr^{3+} activated $Ca_2(Lu_{0.99-x}Gd_xPr_{0.01})Hf_2Al_3O_{12}$, J. Lumin. 263 (2023) 120033. https://doi.org/10.1016/J.JLUMIN.2023.120033.

[221] G. Inkrataite, G. Laurinavicius, D. Enseling, A. Zarkov, T. Jüstel, R. Skaudzius, Characterization of GAGG Doped with Extremely Low Levels of Chromium and Exhibiting Exceptional Intensity of Emission in NIR Region, Cryst. 2021, Vol. 11, Page 673. 11 (2021) 673. https://doi.org/10.3390/CRYST11060673.

[222] N.J. Cherepy, Z.M. Seeley, S.A. Payne, P.R. Beck, O.B. Drury, S.P. O'Neal, K.M. Figueroa, S. Hunter, L. Ahle, P.A. Thelin, T. Stefanik, J. Kindem, Development of transparent ceramic Ce-doped gadolinium garnet gamma spectrometers, IEEE Trans. Nucl. Sci. 60 (2013) 2330–2335. https://doi.org/10.1109/TNS.2013.2261826.

Journal of Alloys and Compounds 875 (2021) 160002

Contents lists available at ScienceDirect

Journal of Alloys and Compounds

journal homepage: www.elsevier.com/locate/jalcom

Influence of boron on the essential properties for new generation scintillators

Greta Inkrataite[a,*], Meldra Kemere[b], Anatolijs Sarakovskis[b], Ramunas Skaudzius[a]

[a] Institute of Chemistry, Faculty of Chemistry and Geosciences, Vilnius University, Naugarduko 24, LT-03225 Vilnius, Lithuania
[b] Institute of Solid State Physics, University of Latvia, 8 Kengaraga street, LV-1063 Riga, Latvia

ARTICLE INFO

Article history:
Received 25 November 2020
Received in revised form 9 March 2021
Accepted 15 April 2021
Available online 20 April 2021

Keywords:
Inorganic materials
Luminescence
Sol-gel processes

ABSTRACT

Cerium doped yttrium aluminum (YAG:Ce) and lutetium aluminum garnets (LuAG:Ce) are some of the most popular materials used as scintillators. While the scintillators themselves are materials that absorb and convert high-energy radiation into light. The decay time in YAG:Ce and LuAG:Ce is about 60 ns, therefore the essential task for their improvement would be to shorten it as much as possible. For this reason, in this work, the aforementioned garnets were doped with different amounts of boron. B^{3+} ion has a suitable neutron capture cross section and can therefore absorb gamma radiation. Because of the extremely strong absorption of thermal neutrons and the weak interaction with MeV gamma rays the material is an exciting new inorganic scintillator candidate for the detection thermal and epithermal neutrons. B^{3+} stimulates and improves the absorption of such radiation. In the study, 0.05% of cerium and different amounts of boron doped YAG, YLuAG ($Y_{1.5}Lu_{1.5}Al_5O_{12}$) and LuAG were synthesized by the sol-gel method. To investigate the influence of the annealing atmosphere, all samples in powder form were heated either under air or reducing atmospheres. XRD, SEM characterization techniques were performed on the synthesized samples. Luminescent properties were measured and analyzed. The main results that have been observed from this research were that boron does indeed shorten decay time, while also increasing emission intensity. The most intensive emission was of those powder compounds containing 1% and 5% of boron, regardless of the annealing atmosphere. While pure samples doped with 5% of boron have the shortest decay times.

1. Introduction

Technologies based on fluorescent materials are exceptionally popular and are constantly being improved. Scintillators are one of the key compounds in the development of light science today. Such materials are used in computed tomography (CT) and positron emission tomography (PET) devices [1,2]. In addition, these compounds can be applied in devices used for the measuring of radioactive contamination. Since the above-mentioned fields of application of scintillators are related to human health, it is especially important that the produced materials are of the highest possible quality [3,4].

YAG and LuAG compounds doped with Ce^{3+} ions are excellent scintillating materials. They have nearly perfect physical and chemical properties that are required for scintillators: high density (for YAG:Ce – 4.55 g/cm^3; for LuAG:Ce – 6.72 g/cm^3), high thermal stability, high emission intensity and excellent quantum efficiency. However, as already mentioned some of the properties of the scintillator compounds need to be improved upon. The most essential being the decay time. It needs to be shortened as much as possible. Cerium doped yttrium and lutetium garnets respectively have 88 ns and 55 ns lifetimes, with 660 ps and 583 ps rise times [5,6]. This is particularly important because the shorter the decay, the less likely it is that the incoming signals will overlap with the existing one when being received by device, resulting in more of the required information being obtained and thus making the device more reliable [7].

However, not all fluorescent materials can be used as scintillators. The other core parameter required for this type of material is the ability to induce emissions when being excited by high energy radiation. As already mentioned, such compounds in most cases have a high density and high thermal stability. Various garnets are known to have these properties [5,6]. Due to this reason the study on cerium and other lanthanide doped gadolinium gallium aluminum garnets is of immense popularity. Although the main application of cerium doped yttrium aluminum and lutetium aluminum garnets is

* Corresponding author.
E-mail address: greta.inkrataite@chgf.vu.lt (G. Inkrataite).

https://doi.org/10.1016/j.jallcom.2021.160002
0925-8388/

in white light LED's, due to the good conformity to of the aforementioned characteristics they are also in quite the demand in the field of scintillators as well [8,9].

In this work, cerium doped yttrium aluminum garnet (YAG:Ce), cerium doped yttrium lutetium aluminum garnet (YLuAG:Ce), cerium doped lutetium aluminum garnet (LuAG:Ce) powder samples with different amounts of boron were synthesized. All samples were also annealed under either air or reducing atmospheres. Boron, was used as dopant ion to cause defects in the system, as well as to increase the absorption of high energy radiation. The defects were introduced into the garnet systems in an attempt to shorten the decay time, without any substantial reduction in emission intensity. Therefore, such compounds are likely to be in more demand for the development of high quality and widely used scintillators.

The main purpose of this work is to synthesize garnets with the shortest possible decay times, without compromising other luminescent properties.

2. Experimental

2.1. Synthesis procedure

Yttrium and lutetium aluminum garnets powders were synthesized by the sol-gel method. Cerium concentration was kept at 0.5 mol% of the dodecahedral coordinated yttrium for all of the samples. Two different atmospheres were chosen for sample calcination. One of them was the air (in compounds name titled _A), which helps maintain normal garnet-receiving conditions. The other is a reducing atmosphere (in compounds name titled _R). This atmosphere is used to maintain the cerium in its Ce^{3+} oxidation state by reducing any Ce^{4+} that form during the preparation procedure. All of the synthesized powder compounds are listed in Table 1.

Nominal formulas of the synthesized samples are as follows: $Y_{2985}Al_2Al_{3-x}O_{12}:Ce_{0015}:B_x$, $Lu_{2985}Al_2Al_{3-x}O_{12}:Ce_{0015}:B_x$ and $Y(Lu)_{2985}Al_2Al_{3-x}O_{12}:Ce_{0015}:B_x$. For these compounds, Y_2O_3, Lu_2O_3, $Al(NO_3)_3 \cdot 9H_2O$, $(NH_4)_2Ce(NO_3)_6$, H_3BO_3 were used as precursors. Firstly, Y_2O_3 and/or Lu_2O_3 were dissolved in an excess of concentrated nitric acid at 50 °C. Then, the excess of nitric acid was evaporated and the remaining gel was washed with distilled water 3 times, followed by further evaporation of added water each time. An additional 200 ml of water were added, after the washing, and $Al(NO_3)_3 \cdot 9H_2O$, $(NH_4)_2Ce(NO_3)_6$, H_3BO_3 were then dissolved. The solution was left under magnetic stirring for 2 h at around 50 °C. After that, citric acid was added to the solution with a ratio of 1:1 to metal ions and was left to stir overnight. The solution was evaporated at the same temperature, and obtained gels were dried at 140 °C for 24 h in the a drying furnace. The obtained powders were then ground and heated firstly at 1000 °C for 2 h in the air, with 5°/min heating rate. After which the same powders were then annealed at 1200 °C for 4 h under air or reducing atmosphere, with 5°/min heating rate [10,11]. The synthesis scheme is shown in Fig. 1.

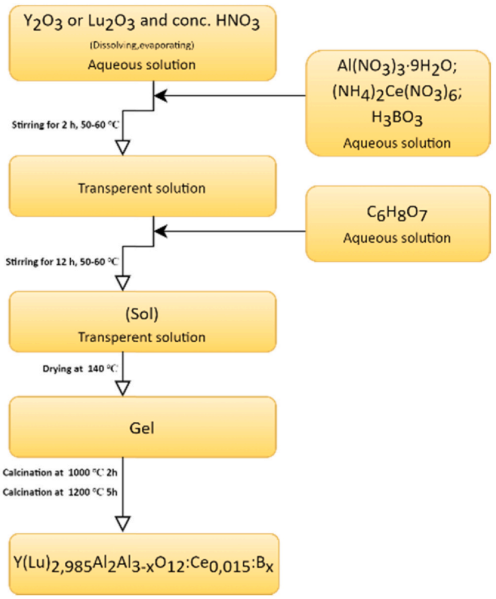

Fig. 1. Scheme of garnet sol-gel synthesis.

2.2. Characterization

X-ray diffraction (XRD): XRD measurements of powders were performed using the Rigaku MiniFlex II X-ray diffractometer. Powders used for analysis were evenly dispersed on the glass sample holder using ethanol. Then diffraction patterns were recorded in the range of 2θ angles from 15° to 80° for all compounds. CuKα radiation (λ = 1.5418740 Å) was used for the analysis. The measurement parameters were set as follows: current was 15 mA, voltage – 30 kV, x-ray detector movement step was 0.010° and dwell time of 5.0 s.

Electron scanning microscopy measurements (SEM): SEM analysis was performed using a Hitachi SU-70 scanning electron microscope. Powder samples were deposited on a double-sided carbon tape, which was then applied to alumina sample holder.

Measurements of emission and excitation: Edinburgh Instruments FLS980 spectrometer equipped with double excitation and emission monochromators and 450 W Xe arc lamp, a cooled (−20 °C) single-photon counting photomultiplier (Hamamatsu R928) and mirror optics for powder samples were used for measuring the excitation and emission of the prepared samples. Obtained photoluminescence emission spectra were corrected using correction file obtained from a tungsten incandescent lamp certified by NPL (National Physics Laboratory, UK). Excitation spectra were corrected by a reference detector.

Calculation of Quantum Efficiency: External quantum efficiencies were calculated by comparing the emission spectrum of the $BaSO_4$ sample (99% Merck) and the desired compounds that were measured in Teflon coated integration sphere. The EQE values were obtained employing the following formula (1) [12]:

Table 1
Synthesized powder samples.

$Y_3Al_5O_{12}$ (YAG)	$Lu_3Al_5O_{12}$ (LuAG)	$Y_{1.5}Lu_{1.5}Al_5O_{12}$ (YLuAG)
YAG:Ce (A and R)	LuAG:Ce (A and R)	YLuAG:Ce (A and R)
YAG:Ce,1%B (A and R)	LuAG:Ce,1%B (A and R)	YLuAG:Ce,1%B (A and R)
YAG:Ce,5%B (A and R)	LuAG:Ce,5%B (A and R)	YLuAG:Ce,5%B (A and R)
YAG:Ce,10%B (A and R)	LuAG:Ce,10%B (A and R)	YLuAG:Ce,10%B (A and R)
YAG:Ce,20%B (A and R)	LuAG:Ce,20%B (A and R)	YLuAG:Ce,20%B (A and R)

$$EQE = \frac{\int I_{em,sample} - \int I_{em,BaSO_4}}{\int I_{ref,BaSO_4} - \int I_{ref,sample}} \times 100\% = \frac{N_{em}}{N_{abs}} \times 100\% \quad (1)$$

where $\int I_{em,sample}$ and $\int I_{em,BaSO4}$ are integrated emission intensities of the phosphor sample and $BaSO_4$, respectively. $\int I_{ref,sample}$ and $\int I_{ref,Baso4}$ are the integrated reflectances of the phosphor sample and $BaSO_4$, respectively. N_{em} and N_{abs} stand for the number of emitted and absorbed photons.

Temperature Dependency Measurements: In order to evaluate the temperature dependency of luminescence properties a cryostat "MicrostatN" from the Oxford Instruments was added to the already described spectrometer. Liquid nitrogen was used to decrease the temperature. Overall, properties were measured at 10 different temperatures, starting at 77 K, then from 100 K at intervals of 50 K up to 500 K. Stabilization duration for each temperature point was kept at 90 s while the allowed temperature tolerance interval was chosen as ±5 K. Also, to prevent the water from condensing on the cryostat window dried nitrogen was being flushed during the procedure on its surface. From the temperature dependency measurements the activation energy was calculated using Arrhenius function (Eq. 2) [13]:

$$I(T) = \frac{I(0)}{1 + B(\exp -\Delta E/kT)} \quad (2)$$

where, T is the absolute temperature, B is the quenching frequency factor, $I(0)$ corresponds to the intensity of the luminescence at T = 0 K, ΔE is the activation energy for the thermal quenching process, and k is the Boltzmann constant ($8.617342 \cdot 10^{-5}$ eV/K). Also, thermal quenching value $-TQ_{1/2,}$ has been calculated following the (3) equation. B value in this formula is the quenching frequency factor [14]:

$$TQ_{1/2} = \frac{-E_a}{k \times \ln(1/B)} \quad (3)$$

Decay Time Measurements: The photoluminescence decay kinetics were studied for powders and thin films using the FLS980 spectrometer. 450 nm laser was used for these measurements.

Radioluminescence Measurements: X-ray lamp (W anode, 40 kV, 30 mA) was used for the excitation of the radioluminescence. Radioluminescence spectra were measured by Andor iSTAR DH734_18 mm CCD camera coupled to Andor SR-303i-B spectrometer.

3. Results and discussion

3.1. X-ray diffraction

In order to determine the purity of the garnet powder samples X-ray diffraction analysis was performed. All samples, which contain 5 or less % of boron, independently of the atmosphere under which they were heated, exhibit pure garnets phase (Powder Diffraction File, (PDF) #96-152-9038). Compounds with 10% and 20% of boron also contain aluminum borate (AlB_{10}) impurity phase. This secondary phase displays peaks at 20.1, 27.1, 34.0, 47.9 and 49.9 2θ degrees. These reflections are marked with * sign in the given diffraction patterns. From the given diffractograms (Fig. 2 and Supplementary 1) it could be said that increasing the amount of boron, causes an increase of the volume fraction of the impurity phase as well as to a larger intensity of its specific reflections. Also, it is noticeable that the introduction of lutetium into the garnet structure, from YAG, to LuAG with intermediate YLuAG stage, causes shifting of peaks towards larger angle values. This trend can be attributed to the fact that yttrium and lutetium have different atomic radii, 1.16 Å and 0.98 Å respectively [15]. Due to the relatively low doping concentration of cerium and boron, this lattice modification does not affect peak position to a noticeable degree. Boron is a light element, for this reason it is complicated to determine its occupancy by the XRD method. Based on the literature it occupies a tetrahedral position in the garnet matrix [16,17]. However, when comparing peaks of PDF cards to that of the measured samples, no shift can be noticed for yttrium and lutetium aluminum garnets, but yttrium/lutetium aluminum garnet shows a small displacement from pdf card peaks. This can be explained by the fact that for identification of YLuAG samples, YAG PDF card was used as no phase transitions occur and only the cell parameters are affected by the substitution. In summary from the measured data, it can be argued that garnets could be doped with no more than 5% of boron with no additional impurity phase formation.

3.2. Scanning electron microscopy analysis

Scanning electron microscopy (SEM) analysis was performed in order to determine the morphology and particle size of the synthesized materials. All samples were measured using two different magnifications (2.5 k and 20 k). The smaller magnification (2.5 k) was used to see the larger aggregation of the particles, while the larger (20 k), to get a clearer vision of the individual particles. SEM images are shown in Figs. 3 and 4. It is clearly seen that the size of garnet particles as well as porosity increases, when garnets are doped with more boron ions and annealed under air. Size of particles varies around 180 nm when no boron is introduced and increased up to 300 nm when sample is doped with 1% of B, 400 nm when doped with 5% of boron, 600 nm – 10% of B and lastly, up to 800 nm when boron amount reaches 20% B. It can also be observed that when compound is heated under reducing atmosphere, the particle size, especially LuAG:Ce,5%B sample, is larger than its equivalent which was annealed under air. From these images, it is clear that a higher boron content gives a larger particle size with an almost uniform increase in diameter. This change is likely due to a lower melting point of boron doped garnet phase as compared to pure garnet. The lower melting point may be influenced by the fact that the melting point of the boric acid is 170 °C. Therefore, in this case, the acid may also act as a flux. As a result, the particles agglomerate faster, resulting in larger and more discrete particles [18]. Similarly, to particle size the addition of boron causes increased formation of pores. Samples without boron show only small and sparse pores, while the samples with 20% show an abundant amount of larger pores. One of the most likely explanations for this difference is that at sintering temperature of 1200 °C, the inner pores are transferred to the surface of the sample where they form open pores. By increasing the amount of boron in the sample, the melting point of the compound potentially decreases, which results in quicker sintering and a faster transfer of pores. The results of the mentioned process are then seen in the SEM images [19]. The effect of the different heating atmospheres and the introduction of lutetium ions on particle size and morphology was also investigated. However, the SEM images show neither the sintering atmosphere nor the introduction of lutetium induced any significant changes to the particle size or morphology.

3.3. Luminescence properties

Luminescence properties are the most important characteristic of all of the samples synthesized in this work. These are caused by the doping of garnet with a rare earth element and in this case cerium. Cerium distinguishes itself from the other lanthanides because of the allowed nature of its electron transitions from $5d^1$ to $4f^1$ orbitals and vice versa. During these jumps, energy is either radiated or absorbed, which gives the garnet its optical properties. For the practical application of scintillators, it is essential to produce devices with the best optical properties, and thus important to find the most appropriate modifications to the material structure.

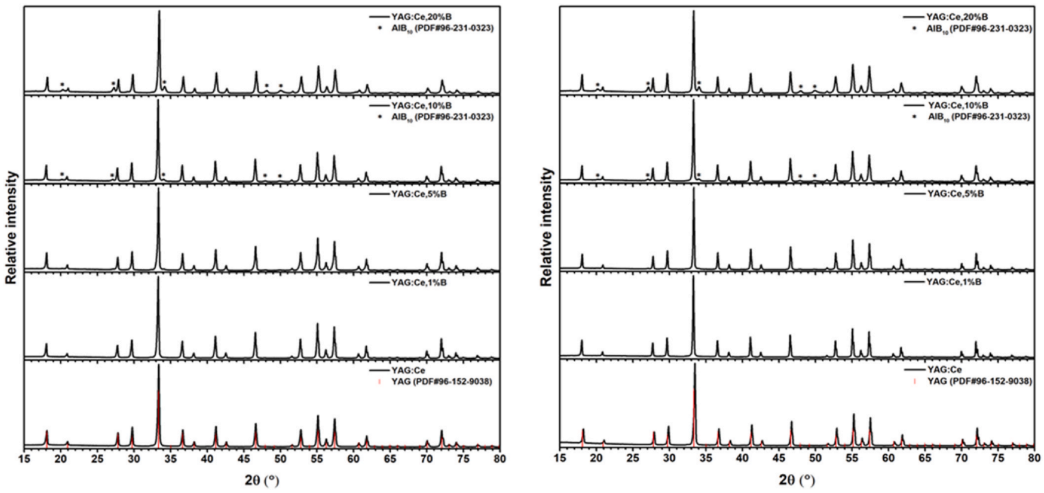

Fig. 2. YAG:Ce powder samples diffractions patterns heated under different atmospheres: left – air atmosphere; right – reducing atmosphere (*–phase of AlB_{10}).

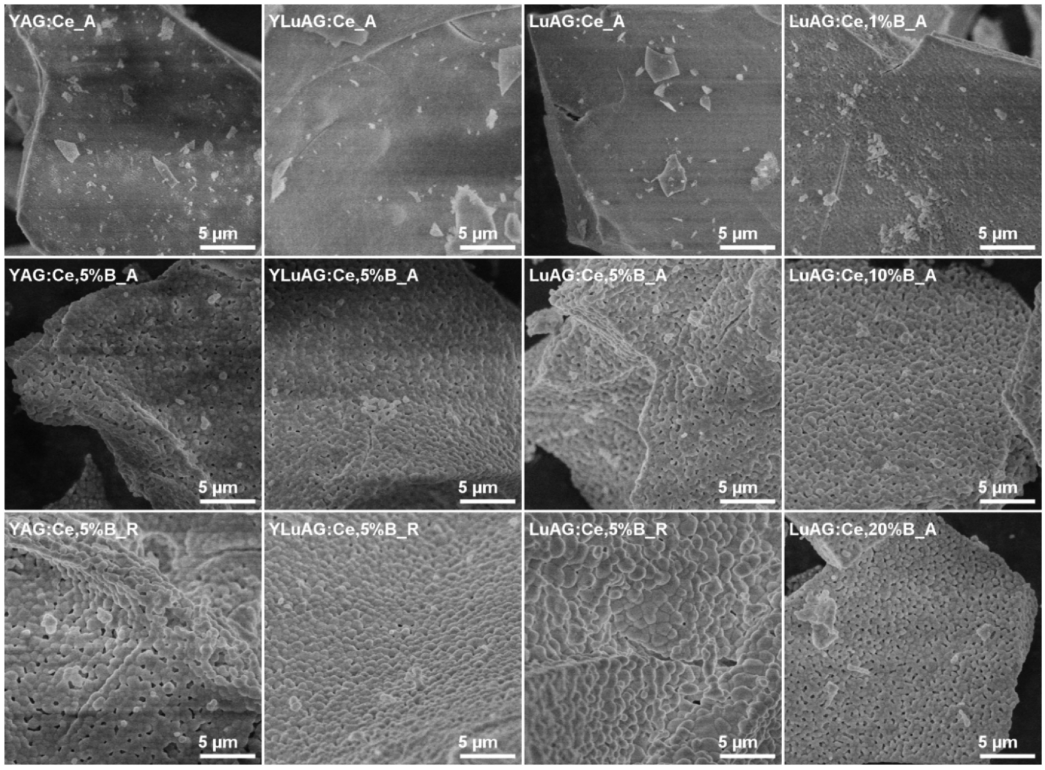

Fig. 3. SEM images of garnet powder samples made under 2.5 k magnification.

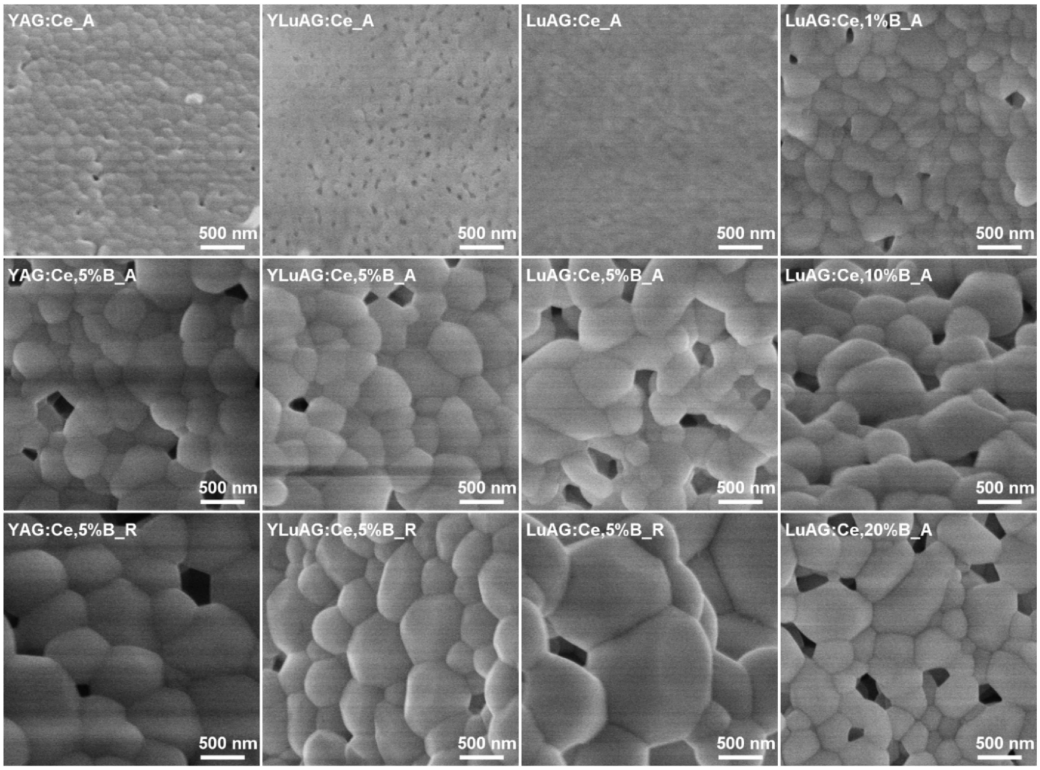

Fig. 4. SEM images of garnet powder samples made under 20 k magnification.

Figs. 5, 6 and 7 show excitation and emission spectra of different compounds measured at room temperature. From these graphs, it can be noted that, all YAG, YLuAG, and LuAG garnet samples, are characterized by wide excitation and emission bands. It was already mentioned that this is caused by electron transitions from $4f^1$ to $5d^1$ in the excitation process and from $5d^1$ to $4f^1$ orbitals in emission process [20]. These transitions are allowed therefore, figures show neat single-jump spectra. It was decided to excite all different

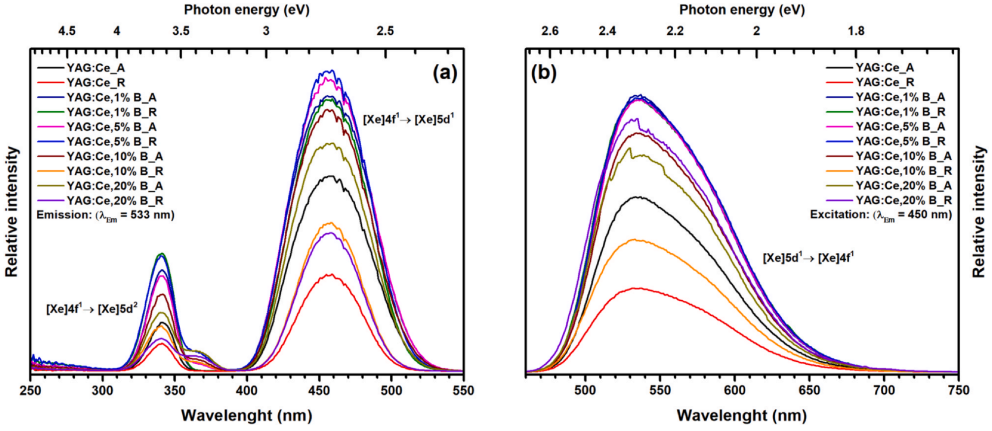

Fig. 5. Yttrium aluminum garnet samples excitation (a) and emission (b) spectra.

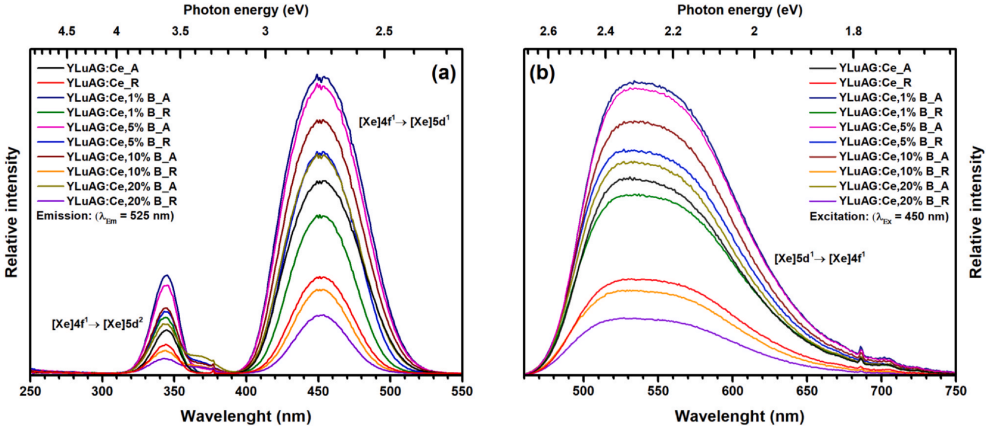

Fig. 6. Yttrium-lutetium aluminum garnet samples excitation (a) and emission (b) spectra.

garnets with the same wavelength light that would give the best emission intensity. From the excitation spectra given in Figs. 5a, 6a and 7a it was concluded that the best choice for excitation is the 450 nm wavelength light. Apart from the basic excitation intensities, an additional peak at 368 nm can be seen for several of the samples. This additional peak increases in intensity when increasing the amount of boron in the samples. Third excitation peak at 340 nm in YAG phase, 342 nm in YLuAG phase and 345 nm in LuAG phase is attributed to the electron transition from $4f^1$ to $5d^2$ orbitals [21].

According to Figs. 5b, 6b and 7b, all the samples exhibit band emission in green region. YAG has emission maximum at $\lambda = 533$ nm, YLuAG – $\lambda = 525$ nm and LuAG has the greatest shift towards higher energy when compared with yttrium aluminum garnet with emission maximum at $\lambda = 514$ nm. This shift can be explained by the difference in the covalence of the compounds, this is the due different electronegativity of the bond. The higher the covalence of the bond, the greater the shift to longer waves. In this case, the electronegativity of lutetium is 1.27 and that of yttrium is 1.22. Although small, the difference is what influences the shift of the emission maximum of lutetium compounds towards the higher energy range [22]. From the figures it can also be noticed that the samples demonstrating the highest luminescence intensity were all annealed under air and not under reducing atmosphere. This effect of the heating atmosphere has been previously observed by other scientists, but it is still not fully understood as to what may be the cause of it [23,24]. Other important difference of all synthesized garnets is the boron amount inside the garnet structure. This difference gives obvious emission intensity changes. It could be said, that compounds when the boron amount is the highest, whilst no secondary phase has formed, have the highest luminescence intensity. The addition of boron causes an increase of particle size. And since particles with bigger size have a relatively larger amount of dopant ions in bulk as compared to the surface resulting in higher emission intensity [25,26]. When AlB_{10} phase is formed, the emission weakens. One of the possible explanations why boron ions affect the luminescent properties, could be, that boron can create extra defects in Y/LuAG phosphors. While, equivalent substitution between boron and aluminum occurs in the $Y_3Al_5O_{12}$ matrix, the defects in order to compensate for charge difference, cannot form since the charge is equal. However, since the radius of B^{3+} ions is much smaller in comparison

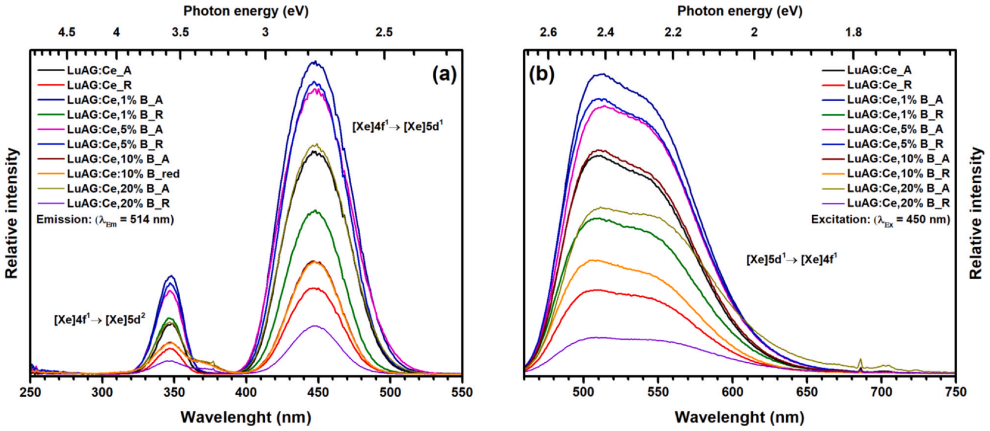

Fig. 7. Lutetium aluminum garnet samples excitation (a) and emission (b) spectra.

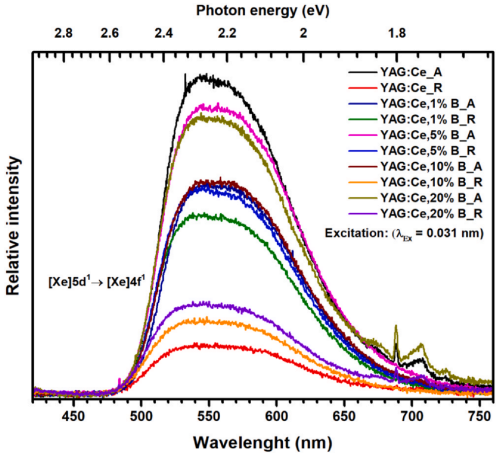

Fig. 8. Yttrium aluminum garnets sample emission spectra, excited with X-rays.

to that of Al^{3+} ions, the irregularity of the coordination polyhedron of the dopant site can increase, which causes an exceptionally large increase in local strain. This strain could be partially reduced by the formation trigonal planar units of BO_3, which tends to then form oxygen vacancies and thus finally decreases the emission intensity [27]. For YAG samples, the compounds with 1% of boron that were annealed under air atmosphere show the most intensive luminescence. Samples that were doped with 5% of boron show slightly lower emission intensities. Compounds, of which the dodecahedral position partially occupied by Y^{3+} and Lu^{3+} ions, have emission intensities similar to that of YAG powders. The highest luminescence intensity is seen for sample doped 1% of boron and the second highest – doped with 5% of boron, all of these samples were annealed under air atmosphere. LuAG sample emission spectra are shown in Fig. 7b. Similarly, to the aforementioned YAG and YLuAG, in LuAG spectra, the most intensive emission was detected for compound calcinated under air atmosphere with 1% of boron. Second and third most intensive luminescence having compounds are samples doped with 5% of boron. From all emission spectra it can be clearly seen that samples doped 20% of boron and heated under reducing atmosphere exhibit the weakest emission. To sum up, from Figs. 5, 6 and 7, it could be said, that all of the synthesized garnet powders have almost the same excitation and emission intensities independently of which element occupied the dodecahedral structure position. So in turn, the majority differences are caused by addition of different B^{3+} amounts into the structure.

For materials that could be used as scintillators, in this case all of the synthesized compounds: YAG, YLuAG and LuAG, it is important to measure the emission when using shorter excitation wavelengths than the blue laser light. Devices incorporating such materials operate on the principle that compounds emit light when they are excited by X-rays. Therefore, one of the most important studies that can gauge the value of garnets synthesized in this work as potential scintillating materials is the measurement of the emission spectrum when X-rays are used for excitation. However, due to the fact that such procedure is not readily available, only yttrium aluminum garnets samples were measured. From Fig. 8 it is clear that, as in the usual emission spectrum, one broad band, attributed permissible $[Xe]5d^1 \rightarrow [Xe]4f^1$ transitions is visible. The emission maxima were located at $\lambda = 535$ nm, overall, the sample that was without boron and was heated under air atmosphere showed the highest luminescence intensity. The second most intensive emission is almost identical to that of the first compound was measured for sample also heated under air atmosphere, but doped with 5% of boron. Note that at about 700 nm several additional peaks for several of the samples were observed. These extra peaks may be attributed Cr^{3+} emission, which may be incorporated to the compound during synthesis from precursor impurities. The emission of these ions is very strong under X-ray excitation, even if the amount is negligible. This can be confirmed because in Fig. 5b, in the measured spectrum of the same samples, no additional peaks are observed [28]. To conclude this measurement, it is obvious that the compounds that are heated under air atmosphere are better suited to be used as scintillators, due to higher emission intensity. Therefore, other more significant studies will be conducted on the boron-containing compound with the highest emission – YAG:Ce,5%B_A.

As already mentioned, probably the most important compound from this work is cerium and 5% of boron co-doped yttrium aluminum garnet heated under air atmosphere, so the temperature dependency measurements were performed on it. As it is known, cerium ion emission drastically changes at different temperatures. At

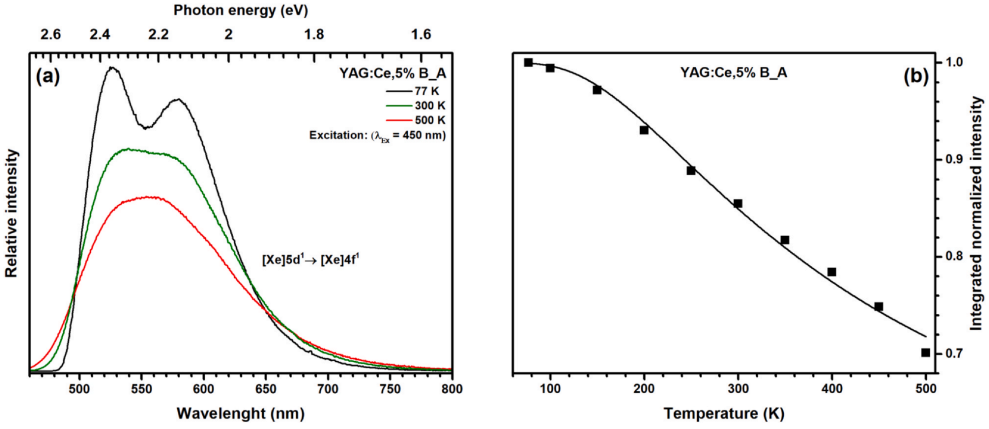

Fig. 9. Yttrium aluminum garnet sample (a) emission spectra at different temperatures and (b) process fitted curve.

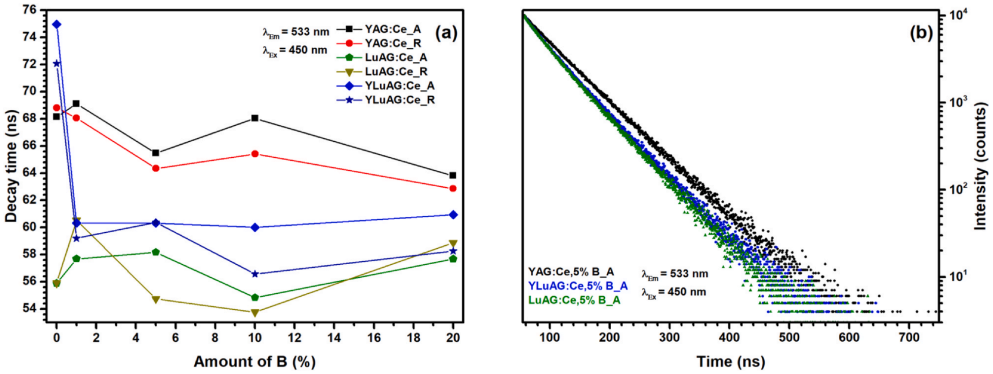

Fig. 10. (a) Different garnet decay times at room temperature; (b) 5% of boron doped garnet decay lines.

low temperature, exactly 77 K, the spectra showed a double band structure of the Ce^{3+} emission (Fig. 9a). When the temperature is raised, the split emission band, attributed to transitions from 5d level to ground $^2F_{5/2}$ and $^2F_{7/2}$ configurations, respectively, starts to broaden and overlap. Then it eventually turns into one broad emission band at 500 K. At temperatures below that point fine structure is observed [20]. Also, it could be mentioned that luminescence intensity decreases when the temperature is raised. From the graph it is clearly visible that emission intensity peak maxima are at 525 nm and 580 nm when the temperature is 77 K, 539 nm and 576 nm at room temperature, and to 554 nm at highest – 500 K temperature point.

From the temperature dependent emission spectra integration is possible which then allows for the calculation of the activation energy of the processes. The calculated activation energy of this system was $E_a = 0.152 \pm 0.003$ eV. In this system, activation energy describes the non-radiative recombination process. Taking into account the activation energies of other similar systems found by other scientists, $E_a = 0.136$ eV or $E_a = 0.83$ eV, clearly it can be seen that this value for our system is lower in comparison [13,29]. Other value, which has been calculated is temperature at which phosphor loses half of its efficiency – $TQ_{1/2}$. For the characterized system, calculated $TQ_{1/2} = 625.317$ K. Other scientists have obtained similar thermal quenching values in their research, which are ranging from 500 K to 700 K and more [30,31]. Consequently, the developed system not only gives better luminescent properties such as emission intensity, quantum yield and decay time but also reduces energy loss in the form of heat, making for a more effective phosphor overall.

The main idea of all work is to synthesize such compounds, that have shorter decay times, as this is the most important characteristic of the samples. As mentioned in introduction part, the improvement of this property would give scintillators of a much better quality in different devices. Garnets, such as cerium doped YAG, YLuAG and LuAG have fast decay times, which are in nanosecond scale. Of course, this property could be still be improved upon and by shortening decay time as a result of co-doping. In this case materials are co-doped with boron ions. The influence of B^{3+} ions on the decay times is visible in Fig. 10a. Garnets with an appropriate amount of boron exhibit a decay time that is shorter than that of the samples doped with only cerium, except YAG:Ce_A and LuAG:Ce. Surely, it is necessary to emphasize that only samples with 1% and 5% boron have a pure garnet phase. Larger alloying may reduce the duration due to the resulting AlB_{10} phase. As expected, yttrium garnets exhibit longer decay times by more than 10 ns as compared to lutetium garnets [16]. If talking about pure garnets, then the shortest decay time was observed for cerium and 5% of boron co-doped lutetium aluminum garnet heated under reducing atmosphere, which is 54.7 ns. Of course, the decay times of all garnets were affected by the

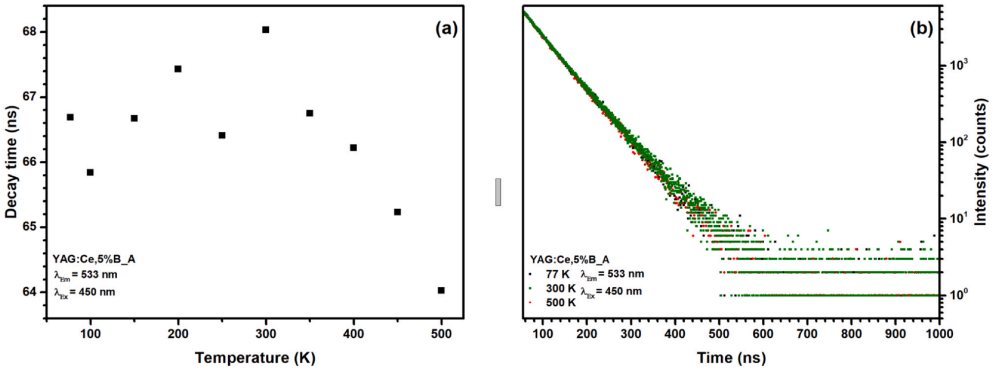

Fig. 11. Yttrium aluminum garnet sample (a) decay time values at different temperatures (b) decay times lines at different temperatures.

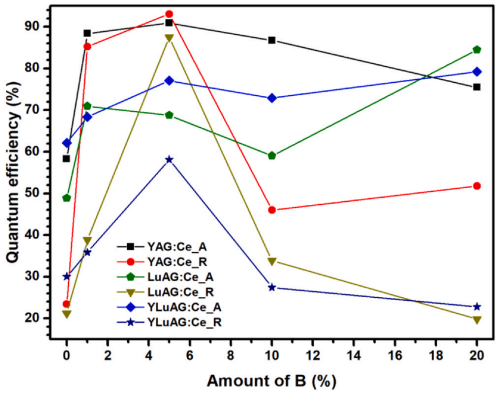

Fig. 12. Quantum efficiency of different garnet samples.

addition of the appropriate amount of boron. However, no clear dependency was observed since the decay times of other samples change rather unevenly. Of course, the shortening of the decay times themselves can be based on the fact that the boron has a higher electronegativity than that of aluminum. The shortened decay time again could be associated with the polarization of the local activator ion environment. Therefore, when the ions electronegativity increases, then the polarization decreases and the decay time becomes shorter. Different electronegativity of boron as compared to aluminum can cause the decrease photoluminescence decay time which also correlated with blue wavelength shift of emission [32]. The reason why the decay time decreases less when the samples are heated under a reducing atmosphere, may be due to the fact that boron incorporates in the structure less well in such a case and thus does not create the desired effect. Although scintillation decay has not been measured for some samples, it should be noted that there have been previous reports drawing a direct correlation between luminescence and scintillation decays, which are very similar in most cases [33].

Sample decay times, similarly to emission intensities, change at different temperatures, and it can be seen in Fig. 11. Although the profile of the decay lines does not change and the shift does not occur, but slight variation of decay times was observed. At room temperature, the decay time is the highest and is 68.0 ns, meanwhile, it is the shortest at 500 K at 64.0 ns. A general trend cannot be discerned, as durations change unevenly.

All materials capable of luminescence exhibit one or another value of quantum efficiency (QE). This property demonstrates the quality of the synthesized phosphor. Of course, quality is indicated by the approximation of the yield in percentages up to one hundred [34]. Materials, prepared in this work have broadly distributed efficiency values which are shown in Fig. 12. Ranging from 19.8% - LuAG:Ce_R to 93.0% - YAG:Ce,5%B_R. From further inspection of the graph, it can be seen that the optimum content of boron in the compounds is 5%, since this is the amount that gives the highest QE value. While yttrium aluminum garnets have a higher initial quantum efficiency as compared to lutetium ones, addition of boron increases the QE value for each matrix. This effect is much more pronounced for LuAG compounds, especially for LuAG:Ce_R Also, most compounds doped with more than 5% boron have lower quantum efficiency as compared to the ones doped with 5%, except for LuAG:Ce_A sample. This can be explained by the presence of an impurity phase in all of these garnets, which results in a darker (greyish) color from the yellowish or greenish tones. Furthermore impurity phase compound contains number of defects, which can absorb part of the photons falling on the sample, thus reducing the amount of absorbed and emitted by the desired phase [35]. Another point is that in this case, although the decay time of the compounds with doped boron is reduced. The quantum efficiency is not that which is due to the collarability of these properties ($QE = 1/\tau$), but rather increases, especially in the case of garnets doped with 5% boron. Based on these studies, it is clear that boron has a positive effect on all scintillation-specific characteristics. That is, increasing the emission intensity, shortening the decay time, and improving the quantum yield in most cases. These changes are particularly pronounced for YAG:Ce_A, YAG:Ce_R and LuAG:Ce_R sample series. Summarizing the results obtained, it is obvious that the addition of boron has a positive effect on the required optical properties.

If in terms of luminescent properties, they would preferably be expressed in color, for this reason a CIE chromaticity diagram can be used. Ce^{3+} emits light in the green region. From Fig. 13 it is obvious that regardless of which garnets is being measured, its emission is in this particular region. This is also shown in Fig. 13 when YAG:Ce emitted light is illuminating the products in the picture. Of course, the shades and CIE coordinates slightly vary. The most monochromatic and closest to the graph edge is YAG sample, while LuAG is closest to the middle of the graph. Other properties from this diagram for all these samples were also found. Although the main idea

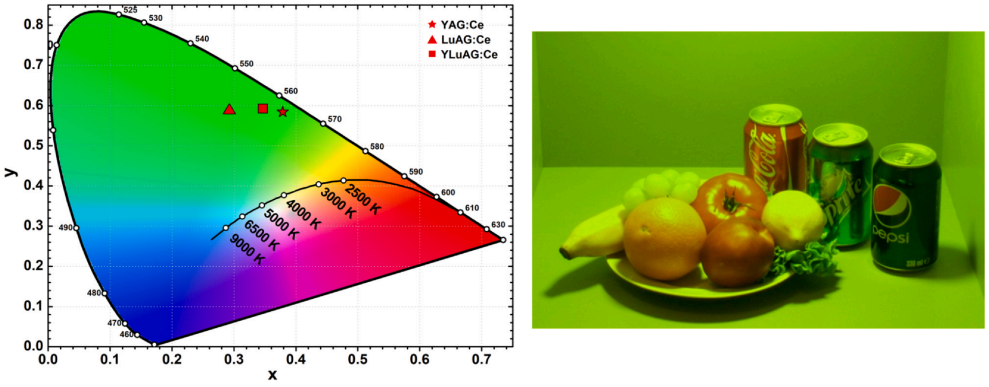

Fig. 13. CIE chromaticity diagram of garnets and the image (Image - @apsvietimas.net) when YAG:Ce emitted light is used.

of this work is not about black-body radiation of light, but the CCT factors were still calculated. This parameter changes from 5000 K for YAG:Ce, 5325 K for YLuAG:Ce to 6182 K to LuAG:Ce. Another characteristic, which shows how realistically color could be rendered is CRI index. This index changes from 18.8 for YAG:Ce, 18.7 for YLuAG:Ce, to 16.6 to LuAG:Ce. From these results, it can be said that the more monochromatic light and the lower the temperature, the more accurately true colors are reproduced. This obtained trend is also confirmed by the study conducted by Jargus et al. and other scientists on the change of these parameters [36]. Taking into account the data obtained from the chromaticity diagram, it can be confirmed that if these materials would be used to produce an LED light, such a garnet alone would not be a sufficient phosphor as it would produce a green light. If the ambition would be to produce white daylight it would be needed to additionally insert other compounds. This material must emit in the red area of the visible light spectrum. Red phosphor with the green guarantor would emit white light when excited by the blue light emitted by the InGaN chip [37].

4. Conclusions

Yttrium, yttrium/lutetium and lutetium aluminum garnets doped with 0.5% of cerium and 1% or 5% of boron were synthesized by the sol-gel method, without the impurity phase of AlB_{10}. If the boron concentration exceeds 5%, impurities are then formed. The influence of boron on the morphology of garnets was observed by scanning electron microscopy. The introduction of boron into the structure causes the increase in particle size, because boron source acts as a flux. In addition to that, the porosity becomes much more prevalent in the compounds with larger dopant concentrations. Investigated of luminescent properties showed that samples containing 1% or 5% of boron, due to the larger particle size s caused by introduction of boron in compounds were found to have the highest emission intensities. This trend was noticed for all prepared compounds independent of the matrix even if compared to non-codoped phosphors. The YAG compound with 5% of boron and annealed under air atmosphere was revealed to have the almost the same emission intensity under X-ray excitation as compared to compound without boron and one of the highest quantum efficiencies out of all samples. Additionally, this yttrium aluminum garnet had the shortest decay time of the entire YAG:Ce_A samples series. Most samples with boron ions inserted into the garnet crystal lattice had shorter decay times as compared to the ones without. This change can be explained by the fact that boron ions have a higher electronegativity than aluminum ions, which reduces polarization and therefore shortens the decay time. It can be concluded that LuAG:Ce,5%B_R and YAG:Ce,5%B_A samples have the best properties that are required in high quality scintillators. The aforementioned lutetium garnet sample had the shortest decay time found in the entire study. While the YAG compound had a short decay time and a high quantum efficiency coupled with high emission intensity.

CRediT authorship contribution statement

Greta Inkrataite: Investigation, Visualization, Writing - review & editing, Writing - original draft, Validation, Formal analysis. **Meldra Kemere:** Investigation, Writing - review & editing. **Anatolijs Sarakovskis:** Investigation, Writing - review & editing, Visualization. **Ramūnas Skaudžius:** Supervision, Writing - review & editing, Writing - original draft, Formal analysis, Conceptualization.

Declaration of Competing Interest

The authors declare that they have no known competing financial interests or personal relationships that could have appeared to influence the work reported in this paper.

Acknowledgements

Scholarship from Experimental nuclear and particle physics center of the Faculty of Physics of Vilnius University.

Appendix A. Supporting information

Supplementary data associated with this article can be found in the online version at doi:10.1016/j.jallcom.2021.160002.

References

[1] J.W. Cates, C.S. Levin, Evaluation of a clinical TOF-PET detector design that achieves ⩽100 ps coincidence time resolution, Phys. Med. Biol. 63 (2018) 115011, https://doi.org/10.1088/1361-6560/aac504
[2] X. Qiu, Z. Luo, J. Zhang, H. Jiang, J. Jiang, Mechanical properties and machinability of GYGAG:Ce ceramic scintillators, Ceram. Int. 46 (2020) 4550–4555, https://doi.org/10.1016/j.ceramint.2019.10.183
[3] E. Matioli, C. Weisbuch, Internal quantum efficiency in LEDs, Top. Appl. Phys. 126 (2013) 121–152, https://doi.org/10.1007/978-94-007-5863-6_6
[4] X. Li, C. Guo, H. Wang, Y. Chen, J. Zhou, J. Lin, Q. Zeng, Green emitting Ba1.5Lu1.5Al3.5Si1.5O12: Ce3+ phosphor with high thermal emission stability for warm WLEDs and FEDs, Ceram. Int. 46 (2020) 5863–5870, https://doi.org/10.1016/j.ceramint.2019.11.037
[5] W. Chewpraditkul, L. Swiderski, M. Moszynski, T. Szczesniak, A. Syntfeld-Kazuch, C. Wanarak, P. Limsuwan, Scintillation properties of LuAG:Ce, YAG:Ce and LYSO:Ce crystals for gamma-ray detection, IEEE Trans. Nucl. Sci. 56 (2009) 3800–3805, https://doi.org/10.1109/TNS.2009.2033994
[6] L. Pan, B. Jiang, J. Fan, P. Zhang, X. Mao, L. Zhang, Co-precipitation synthesis of lutetium aluminum garnet (LuAG) powders: the influence of ethanol, Opt. Mater. 71 (2017) 50–55, https://doi.org/10.1016/j.optmat.2016.06.020
[7] C. Foster, M. Koschan, Y. Wu, C.L. Melcher, Boron codoping of Czochralski grown lutetium aluminum garnet and the effect on scintillation properties, J. Cryst. Growth 486 (2018) 126–129, https://doi.org/10.1016/j.jcrysgro.2018.01.028
[8] D.S. McGregor, Materials for gamma-ray spectrometers: inorganic scintillators, Annu. Rev. Mater. Res. 48 (2018) 245–277, https://doi.org/10.1146/annurev-matsci-070616-124247
[9] R. Zhang, H. Lin, Y. Yu, D. Chen, J. Xu, Y. Wang, A new-generation color converter for high-power white LED: transparent Ce3+: YAG phosphor-in-glass, Laser Photonics Rev. 8 (2014) 158–164, https://doi.org/10.1002/lpor.201300140
[10] M. Skruodiene, M. Misevicius, M. Sakalauskaite, A. Katelnikovas, R. Skaudzius, Doping effect of Tb3+ ions on luminescence properties of Y3Al5O12:Cr3+ phosphor, J. Lumin. 179 (2016) 355–360, https://doi.org/10.1016/j.jlumin.2016.07.041
[11] G. Inkrataite, A. Zabiliute-Karaliune, J. Aglinskaite, P. Vitta, K. Kristinaityte, A. Marsalka, R. Skaudzius, Study of YAG: Ce and polymer composite properties for application in LED devices, Chempluschem 85 (2020) 1504–1510, https://doi.org/10.1002/cplu.202000318
[12] J. Grigorjevaite, A. Katelnikovas, Luminescence and luminescence quenching of K2Bi(PO4)(MoO4):Eu3+ phosphors with efficiencies close to unity, ACS Appl. Mater. Interfaces 8 (2016) 31772–31782, https://doi.org/10.1021/acsami.6b11766
[13] Y. Zhang, L. Li, X. Zhang, Q. Xi, Temperature effects on photoluminescence of YAG:Ce3+ phosphor and performance in white light-emitting diodes, J. Rare Earths 26 (2008) 446–449, https://doi.org/10.1016/S1002-0721(08)60115-5
[14] A. Kruopyte, R. Giraitis, R. Juskenas, D. Enseling, T. Jüstel, A. Katelnikovas, Luminescence and luminescence quenching of efficient GdB5O9:Eu3+ red phosphors, J. Lumin. 192 (2017) 520–526, https://doi.org/10.1016/j.jlumin.2017.07.038
[15] W. Zhou, Z. Ma, Y. Cai, X. Bi, T. Li, W. Niu, X. Sun, Q. Lu, The Synthesis Temperature Selection of Cerium Doped Lutetium Yttrium Oxyorthosilicate Single Crystal Powder, 153 Atlantis Press, 2018, pp. 230–234, https://doi.org/10.2991/aetr-17.2018.44
[16] S. Feng, H. Qin, G. Wu, H. Jiang, J. Zhao, Y. Liu, Z. Luo, J. Qiao, J. Jiang, Spectrum regulation of YAG:Ce transparent ceramics with Pr, Cr doping for white light emitting diodes application, J. Eur. Ceram. Soc. 37 (2017) 3403–3409, https://doi.org/10.1016/j.jeurceramsoc.2017.03.061
[17] L.M. Chepyga, G. Jovicic, A. Vetter, A. Osvet, C.J. Brabec, M. Batentschuk, Photoluminescence properties of thermographic phosphors YAG:Dy and YAG:Dy, Er doped with boron and nitrogen, Appl. Phys. B Lasers Opt. 122 (2016) 1–10, https://doi.org/10.1007/s00340-016-6487-8

[18] S. Cho, C. Yun, Y.S. Kim, H. Wang, J. Jian, W. Zhang, J. Huang, X. Wang, H. Wang, J.L. MacManus-Driscoll, Strongly enhanced dielectric and energy storage properties in lead-free perovskite titanate thin films by alloying, Nano Energy 45 (2018) 398–406, https://doi.org/10.1016/j.nanoen.2018.01.003
[19] M. Xu, J. Song, R. Wang, S. Li, N. Wang, S. Yu, H. Yan, T. Xia, F. Chen, Effect of sintering AIDS on the properties of porous YAG ceramics, Key Eng. Mater. 697 (2016) 178–181, https://doi.org/10.4028/www.scientific.net/KEM.697.178
[20] V. Bachmann, C. Ronda, A. Meijerink, Temperature quenching of yellow Ce3+ luminescence in YAG:Ce, Chem. Mater. 21 (2009) 2077–2084, https://doi.org/10.1021/cm8030768
[21] L. Chen, X. Chen, F. Liu, H. Chen, H. Wang, E. Zhao, Y. Jiang, T.S. Chan, C.H. Wang, W. Zhang, Y. Wang, S. Chen, Charge deformation and orbital hybridization: intrinsic mechanisms on tunable chromaticity of Y3Al5O12:Ce3+ luminescence by doping Gd3+ for warm white LEDs, Sci. Rep. 5 (2015) 1–17, https://doi.org/10.1038/srep11514
[22] M.G. Brik, Fully relativistic analysis of the covalence effects for the isoelectronic 3d3 ions (Cr3+, Mn4+, Fe5+) in SrTiO3, J. Phys. Chem. Solids 67 (2006) 856–861, https://doi.org/10.1016/j.jpcs.2005.12.006
[23] Y. Shen, D.R. Clarke, Effects of reducing atmosphere on the luminescence of Eu3+-doped yttria-stabilized zirconia sensor layers in thermal barrier coatings, J. Am. Ceram. Soc. 92 (2009) 125–129, https://doi.org/10.1111/j.1551-2916.2008.02866.x
[24] E. Zych, A. Walasek, A. Szemik-Hojniak, Variation of emission color of Y3Al5O12:Ce induced by thermal treatment at reducing atmosphere, J. Alloy. Compd. 451 (2008) 582–585, https://doi.org/10.1016/j.jallcom.2007.04.116
[25] Y. Kim, S. Kang, Effect of particle size on photoluminescence emission intensity in ZnO, Acta Mater. 59 (2011) 3024–3031, https://doi.org/10.1016/j.actamat.2011.01.042
[26] T. Gavrilović, J. Periša, J. Papan, K. Vuković, K. Smits, D.J. Jovanović, M.D. Dramićanin, Particle size effects on the structure and emission of Eu3+:LaPO4 and EuPO4 phosphors, J. Lumin. 195 (2018) 420–429, https://doi.org/10.1016/j.jlumin.2017.12.002
[27] D. Zhou, Z. Wang, Z. Song, F. Wang, S. Zhang, Q. Liu, Enhanced persistence properties through modifying the trap depth and density in $Y_3Al_2Ga_3O_{12}$:Ce $^{3+}$,Yb $^{3+}$ phosphor by Co-doping B^{3+}, Inorg. Chem. 58 (2019) 1684–1689, https://doi.org/10.1021/acs.inorgchem.8b03270
[28] E.P. Jahrman, G.T. Seidler, J.R. Sieber, Determination of hexavalent chromium fractions in plastics using laboratory-based, high-resolution X-ray emission spectroscopy, Anal. Chem. 90 (2018) 6587–6593, https://doi.org/10.1021/acs.analchem.8b00302
[29] M. Rejman, V. Babin, R. Kucerková, M. Nikl, Temperature dependence of CIE-x,y color coordinates in YAG:Ce single crystal phosphor, J. Lumin. 187 (2017) 20–25, https://doi.org/10.1016/j.jlumin.2017.02.047
[30] A. Lakshmanan, S. Kumar, V. Sivakumar, P.C. Thomas, M.T. Jose, Synthesis, photoluminescence and thermal quenching of YAG:Ce phosphor for white light emitting diodes, Indian J. Pure Appl. Phys. 49 (2011) 303–307.
[31] K.V. Ivanovskikh, J.M. Ogiegło, A. Zych, C.R. Ronda, A. Meijerink, Luminescence temperature quenching for Ce $^{3+}$ and Pr $^{3+}$ *d-f* emission in YAG and LuAG, ECS J. Solid State Sci. Technol. 2 (2013) R3148–R3152, https://doi.org/10.1149/2.011302jss
[32] S. Kurumada, S. Takamori, M. Yamashita, An alkyl-substituted aluminium anion with strong basicity and nucleophilicity, Nat. Chem. 12 (2020) 36–39, https://doi.org/10.1038/s41557-019-0365-z
[33] T. Yanagida, Y. Fujimoto, A. Yamaji, N. Kawaguchi, K. Kamada, D. Totsuka, K. Fukuda, K. Yamanoi, R. Nishi, S. Kurosawa, T. Shimizu, N. Sarukura, Study of the correlation of scintillation decay and emission wavelength, Radiat. Meas. 55 (2013) 99–102, https://doi.org/10.1016/j.radmeas.2012.05.014
[34] K. Lin, J. Xing, L.N. Quan, F.P.G. de Arquer, X. Gong, J. Lu, L. Xie, W. Zhao, D. Zhang, C. Yan, W. Li, X. Liu, Y. Lu, J. Kirman, E.H. Sargent, Q. Xiong, Z. Wei, Perovskite light-emitting diodes with external quantum efficiency exceeding 20 per cent, Nature 562 (2018) 245–248, https://doi.org/10.1038/s41586-018-0575-3
[35] H.-S. Zhang, L. Shi, X.-B. Yang, Y.-J. Zhao, K. Xu, L.-W. Wang, First-principles calculations of quantum efficiency for point defects in semiconductors: the example of yellow luminance by GaN: C_N +O_N and GaN:C_N, Adv. Opt. Mater. 5 (2017) 1700404, https://doi.org/10.1002/adom.201700404
[36] J. Jargus, J. Nedoma, R. Martinek, Dependence of CCT and CRI on the variable excitation wavelength and on the weight ratio of the phosphor in polydimethylsiloxane, J. Optoelectron. Adv. Mater. 21 (2019) 320–326.
[37] A. Zabiliūtė-Karaliūnė, H. Dapkus, R.P. Petrauskas, S. Butkutė, A. Žukauskas, A. Kareiva, Cr 3+ doped yttrium gallium garnet for phosphor-conversion light emitting diodes, Lith. J. Phys. 55 (2015), https://doi.org/10.3952/physics.v55i3.3149

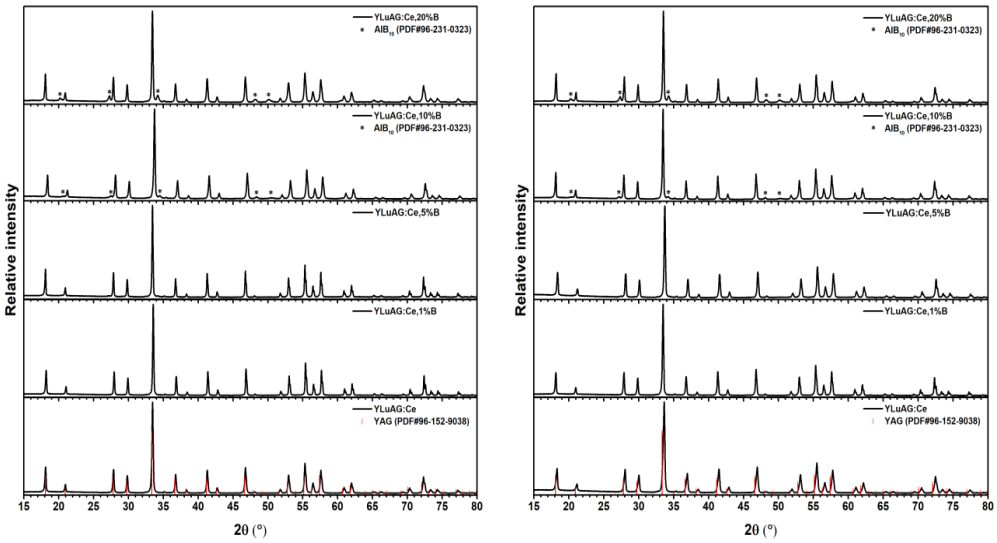

Figure S1. YLuAG:Ce powder samples diffractions patterns heated under different atmospheres: left – air atmosphere; right – reducing atmosphere (*– phase of AlB_{10}).

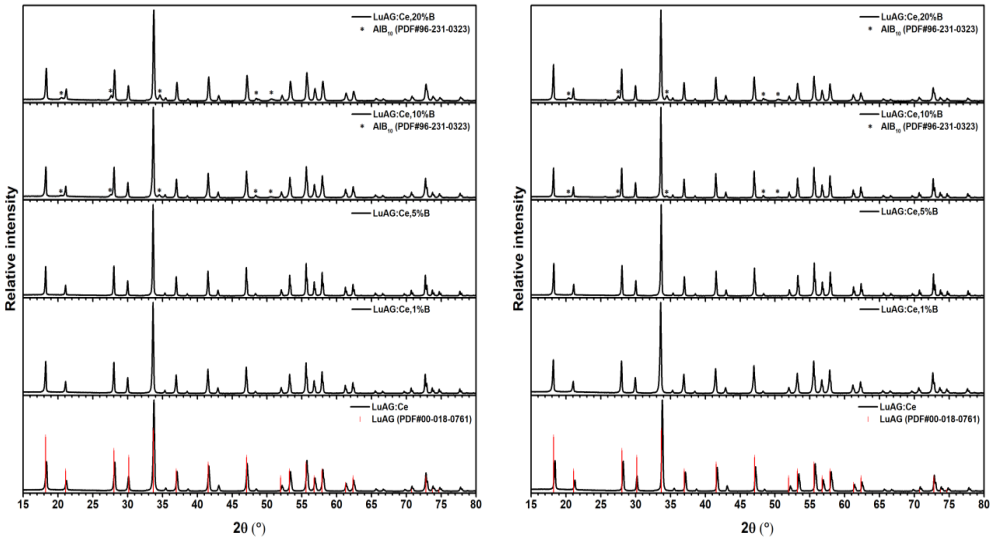

Figure S2. LuAG:Ce powder samples diffractions patterns heated under different atmospheres: left – air atmosphere; right – reducing atmosphere (*– phase of AlB_{10}).

Journal of Luminescence 244 (2022) 118751

Contents lists available at ScienceDirect

Journal of Luminescence

journal homepage: www.elsevier.com/locate/jlumin

Determination of different garnet films characteristics prepared via sol-gel spin or dip-coatings techniques

Greta Inkrataitė *, Živilė Stankevičiūtė, Ramūnas Skaudžius

Institute of Chemistry, Faculty of Chemistry and Geosciences, Vilnius University, Naugarduko 24, LT-03225, Vilnius, Lithuania

ARTICLE INFO

Keywords:
Coatings
Garnets
Luminescence
Sol-gel processes

ABSTRACT

In order to convert high-energy radiation, such as gamma or X-rays, into a visible light, a certain type of material is needed. Such compounds are usually referred to as scintillators. Over the years many different candidates to fit the requirements were examined. However, compounds with garnet structure have attracted a particularly large amount of attention. Cerium doped yttrium and lutetium aluminum garnets (YAG:Ce, LuAG:Ce), have high density, high thermal stability, a rather intensive emission/excitation and high quantum efficiency which are needed for a good scintillator. However, further optimization and improvement is still needed especially on the shortening of the decay time. One way to approach this problem is to alloy the aforementioned compounds with different elements, such as boron or magnesium.

1. Introduction

The compounds used as scintillators can be synthesized by various methods such as solid state, microwave and combustion just to name a few [1]. However, one of the simplest, most convenient and cheapest is the sol-gel synthesis route. Coatings can also be easily synthesized using the sol-gel spin-coating or dip-coating techniques, which is quite difficult or even impossible using other synthesis methods [2,3]. Despite the similarities between the aforementioned deposition techniques, one advantage of using a spin-coating technique should be mentioned. A smoother layer of coating throughout the substrate is prepared, which allows the entire surface to be coated relatively uniformly [4,5]. The usage of coatings opens up new areas of practical application that would be otherwise inaccessible for powders obtained by other methods. As the actual incorporation of the powder into devices requires extra attention, while the coatings do not as they retain their shape no matter how they are placed. The most commonly synthesized compounds either in powder form or coatings and used as scintillators are different lanthanide doped yttrium or lutetium aluminum garnets [5]. These materials are also important in that their coatings are transparent, which opens up even more additional practical and research avenues [6]. Transparent coatings coupled with transparent substrates are required to study high-quality luminescence characteristics. For this reason, sapphire and quartz wafers are usually used [7]. By synthesizing such compounds on the aforementioned substrates, they are well suited for all necessary studies. YAG:Ce and LuAG:Ce compounds, in addition to the above mentioned transparency in the case of coatings, have other properties that are very important for scintillators: high quantum efficiency, intense luminescent emission and excitation, high density (for YAG:Ce – 4.55 g/cm^3; for LuAG:Ce - 6.72 g/cm^3) and high thermal and chemical stability [8,9]. It is also very important to note that these compounds have some of the shortest decay times in nanometer scale [10]. Although this alone is not a sufficient indication for practical suitability. Currently, one of the goals for the majority of scintillator research is to shorten the decay time [11]. One way to do this is to dope the compounds with additional elements. It has been reported that in some cases both boron B^{3+} and magnesium Mg^{2+} ions may shorten the decay time [12,13]. It should be noted that boron is additionally used as an X-ray absorber [14]. Therefore, its use in the compound will not only shorten the decay time, but help also absorb X-rays, resulting in a higher amount of light that will be converted in the scintillator.

In this work we describe the synthesized YAG and LuAG garnets that are doped with 0.5% of cerium that are additionally doped with 5% of boron and/or 0.03% of magnesium. In order to evaluate the compounds in a more practical applicable setting, coatings were synthesized. Coatings of these compounds were synthesized by sol-gel spin and dip-coating methods on different sapphire and quartz substrates. Boron and additional doping by magnesium are expected to reduced decay time of garnets. Selected sol-gel method determines the homogeneity of compounds and low temperatures of synthesis. Phosphor coatings were

* Corresponding author.
E-mail address: greta.inkrataite@chgf.vu.lt (G. Inkrataitė).

https://doi.org/10.1016/j.jlumin.2022.118751
Received 20 September 2021; Received in revised form 11 January 2022; Accepted 16 January 2022
Available online 20 January 2022

Table 1
Synthesized thin film samples.

Samples	Synthesis conditions			
YAG:Ce **YAG:Ce:B** **YAG:Ce:Mg** **LuAG:Ce** **LuAG:Ce:B** **LuAG:Ce:Mg**	•Dip-coating •Quartz, SiO_2 •Coatings together	•Dip-coating •Quartz, SiO_2 •Coatings 1by1	•Spin-coating •Quartz, SiO_2 •Coatings 1by1	•Spin-coating •Sapphire, Al_2O_3 •Coatings 1by1

analyzed by X-ray diffraction analysis, atomic force and scanning electron microscopies. Emission, excitation spectra and decay times have been investigated as well. The main novelty and result of this research is that boron does indeed shorten the decay time, while also increasing emission intensity.

2. Experimental

2.1. Synthesis procedure

All coatings on different substrates were synthesized by either sol-gel dip-coating or spin-coating methods. In this work both quartz and sapphire were used as substrates. On these substrates thin films of $Y_{2,985-y}Al_2Al_{3-x}O_{12}:Ce_{0,015}:B_x:Mg_y$ or $Lu_{2,985-y}Al_2Al_{3-x}O_{12}:Ce_{0,015}:B_x:Mg_y$ were deposited. Based on previous research, it was determined that YAG dope with 5% of boron showed the best luminescence properties, hence this amount was chosen in this for the prepared samples [15]. The magnesium content was chosen based results obtained by M.T. Lucchini in their research [13]. All garnets are doped with 5% of boron or 0.03% of magnesium. From the literature it is known that doping compounds with magnesium or boron similarly results in shorter decay times of the emission process [12,16]. In this study, boron was also used as a flux and dopant, resulting in larger particles that could affect the higher luminescence intensity [15]. As more research is being carried on the doping effect with these elements, it was decided to additionally use coatings in order to compare the effects of different elements on decay times and other studied properties. The list of all synthesized samples is shown in Table 1.

Synthesis of thin films consist of three steps. First, synthesis of sol using sol-gel method. Secondly, follows the making of aqueous solution with 3% polyvinyl alcohol (PVA) and substrate preparation. The last step is coating deposition on substrates.

2.2. Sol synthesis

For the sol Y_2O_3, Lu_2O_3, $Al(NO_3)_3{\cdot}9H_2O$, $(NH_4)_2Ce(NO_3)_6$, H_3BO_3 and $Mg(NO_3)_2{\cdot}6H_2O$ were used as precursors. Firstly, Y_2O_3 or Lu_2O_3 were dissolved in an excess of concentrated nitric acid at 50–60 °C. Then, the excess of nitric acid was evaporated and the remaining gel was washed with distilled water 3 times, followed by further evaporation of added water each time. An additional 200 ml of water were added, after the washing, and $Al(NO_3)_3{\cdot}9H_2O$, $(NH_4)_2Ce(NO_3)_6$, H_3BO_3 and Mg $(NO_3)_2{\cdot}6H_2O$ were then dissolved. The solution was left under magnetic stirring for 2 h at around 50–60 °C. After that, citric acid was added to the solution with a ratio of 1:1 to metal ions and was left to stir overnight [17,18].

2.3. PVA and sol solution

When the sol was prepared, the 3% PVA solution was introduced into the already prepared sol in order to improve the wettability of the substrate. The volume ratio of the PVA and precursor solutions was kept at a 1:1. The final concentration in the solution was left at 0.1 M for all samples. The substrates were washed for about 30 min in boiling acidic piranha solution, after that they were soaked in distilled water and then washed in an ultrasonic bath for 3 min.

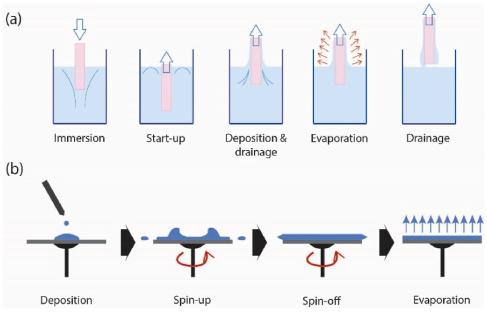

Fig. 1. Examples of different coating processes: (a) dip-coating; (b) spin-coating.

2.4. Coating procedure

When the coating solution was ready and the substrates were washed, the coating processes were started. First, sol-gel dip-coating technique was used. For dip-coating procedure a KSV Dip Coater device was used. For Y2,985-yAl2Al3-xO12:Ce0,015,Bx, Mgy or Lu2,985-yAl2Al3-xO12:Ce0,015,Bx, Mgy films, five layers were deposited by a single-dipping process. During the process, the immersion time of the substrate is 85 mm/min and holding time in the solution is 20 s. Withdrawal from the solution takes place at a speed of 40 mm/min, with support for 30 s after withdrawal. During a single dipping process (marked - 1by1), each deposited layer is calcined for 2 h at 900 °C in air, with heating pace of 1°/min. Then the second layer is deposited using the same procedure as before. After final deposition, films were annealed once again at 900 °C for 2 h in air, with 1°/min heating pace, and lastly at 1000 °C for 2 h in air, with the same heating rate as before [19]. Samples (marked - together) are that of which the layers were coated one after the other, with brief annealing of each layer at a temperature of 200 °C ant then all five layers are calcinated as mentioned earlier.

Secondly, sol-gel spin-coating technique was used for thin film synthesis. For it a "Spincoater model P6700" device was used. The substrate is placed on the head of the device, and then is attached to it by the forming vacuum. Several drops of coating solution are placed on the substrate using a membrane syringe. Using spin-coating method (spin rate = 2000 rpm for 60 s), the excess solution is eliminated because of centrifugal forces, resulting in a smooth coating throughout the surface of the substrate. One layer is applied at one time and is calcined at 900 °C for 2 h in air, with 1°/min heating pace. After final deposition, the films were annealed for the first time at 900 °C for 2 h in air, with 1°/min heating pace, and the second time at 1000 °C for 2 h in the air, with 1°/min heating pace. The heating rates were all the same as in the dip-coating procedure. Both spin and dip-coating processes are shown in Fig. 1.

2.5. Characterization

X-ray diffraction (XRD): XRD measurements of thin films were performed using Bruker D8 Advance X-ray diffractometer. Monochromatic CuKα_1 radiation (λ = 1.541 Å) was used for analysis. Substrates with thin films were placed in sample holder, dwell time was 1.0 s. Measurements were performed under glancing angle conditions.

Electron scanning microscopy measurements (SEM): SEM analysis

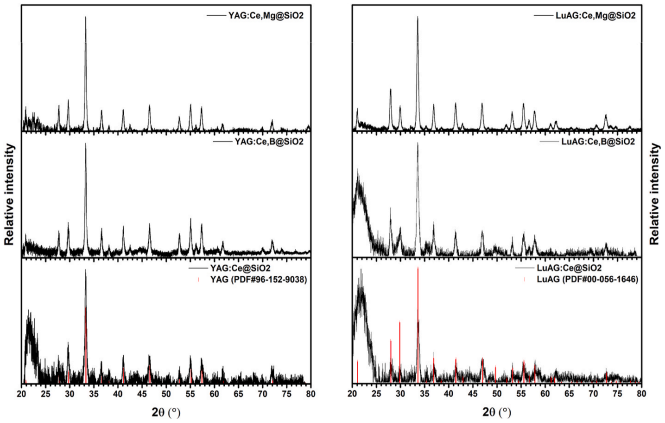

Fig. 2. Thin film diffractograms of YAG and LuAG garnets on quartz (SiO_2) substrate using dip-coating technique when all layers were coated without intermittent heating.

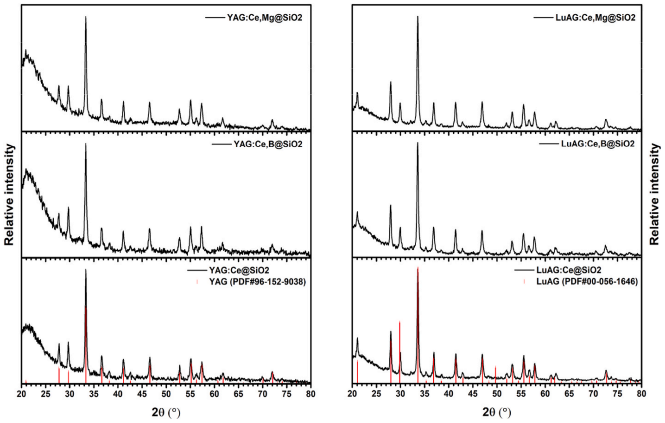

Fig. 3. Thin film diffractograms of YAG and LuAG garnets on quartz (SiO_2) substrate using spin-coating technique when each layer is heated separately.

was performed using a Hitachi SU-70 scanning electron microscope. Coating substrates were held onto the alumina sample holder by copper bars.

Atomic force microscopy (AFM) measurements: AFM Catalyst (Bruker) with SiN-needle at k = 0.06 N/m stiffness at F = 18 kHz and with a tip diameter of 20 nm.

Measurements of emission and excitation: Edinburgh Instruments FLS980 spectrometer equipped with double excitation and emission monochromators and 450 W Xe lamp, a cooled (−20 °C) single-photon counting photomultiplier (Hamamatsu R928). Obtained photoluminescence emission spectra were corrected using correction file obtained from a tungsten incandescent lamp certified by NPL (National Physics Laboratory, UK). Excitation spectra were corrected by a reference detector [15].

Decay Time Measurements: The photoluminescence decay kinetics were studied for thin films using the FLS980 spectrometer. 450 nm laser was used for these measurements.

3. Results and discussion

3.1. X-ray diffraction

When performing X-ray diffraction analysis of the as prepared thin films, samples must be measured using the glancing angle method. This method is necessary because the quartz substrate is highly amorphous, as seen from increased background intensity visible from 20 to 25 2θ degrees [20]. When recording diffraction patterns by the conventional method only this high-intensity amorphousness remains visible, the phase peaks merge with the background due to the relatively low intensity. This low intensity of the peaks is due to the thinness of the coating, as only five layers were deposited. Figs. 2 and 3 show diffractograms of two out of four series of prepared coatings of YAG and LuAG on quartz substrates. From these Figures, it can be said that all samples have pure garnets phase with cubic symmetry and Ia-3d (#230) space group. It can also be observed that the most intense peaks, remain narrow. They also have a slight shift to larger angles in the case of LuAG

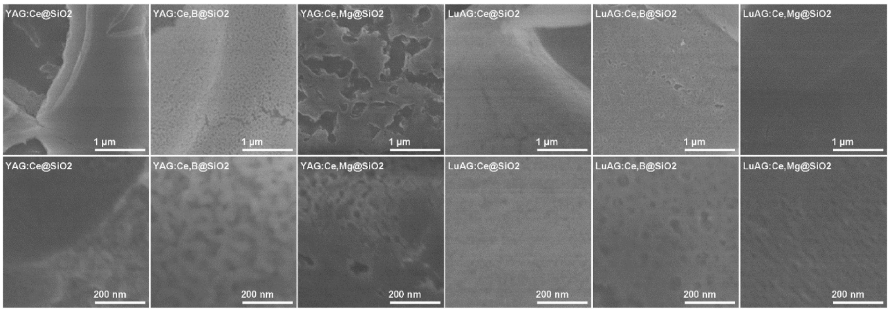

Fig. 4. SEM images of garnet coatings on quartz (SiO_2) substrate using dip-coating technique when all layers were coated without intermittent heating.

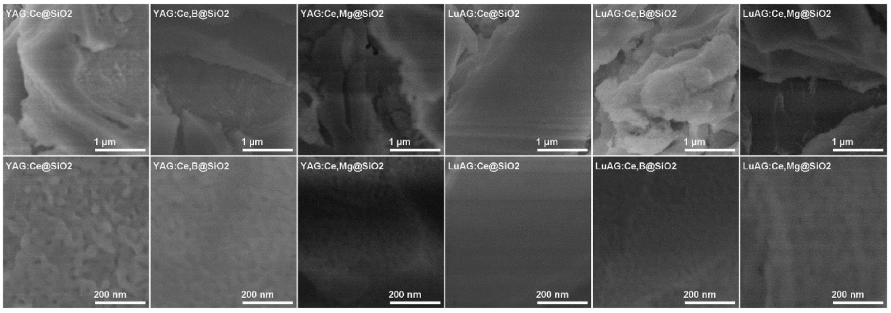

Fig. 5. SEM images of garnet coatings on quartz (SiO_2) substrate using dip-coating technique when each layer is heated separately.

samples due to the replaced element in the dodecahedral positions, since yttrium ions are larger (1.16 Å) as compared to lutetium (0.98 Å) [21]. From the results of this measurement, it can be stated that all coatings independently of the doping still retain their pure garnet phase structures.

3.2. Scanning electron microscopy analysis

Scanning electron microscopy, revealed the fact that different coating methods and substrates resulted in different morphologies of thin films [22]. From the micrographs it can be observed that using the dip-coating technique (Figs. 4 and 5) the coatings are uneven, split and layered. In principle, it can be argued that such coatings do not have the same properties over their entire area, as different parts of them have different material thickness and are inhomogeneous. Of course, when analyzing SEM data, the two different ways of deposition can be compared in case of the dip-coating methodology. Fig. 4 shows the samples of which the layers were coated one after the other, with brief annealing of each layer at a temperature of 200 °C, this method was referred to as coating all the layers without intermittent heating, in micrograph titles. Meanwhile, in Fig. 5, each layer was calcinated at 900 °C with the 1°/min pace. It can be seen that in the first case, the coatings are less layered, but they have many more cracks and voids on the substrate. This difference in morphology can be explained by the fact

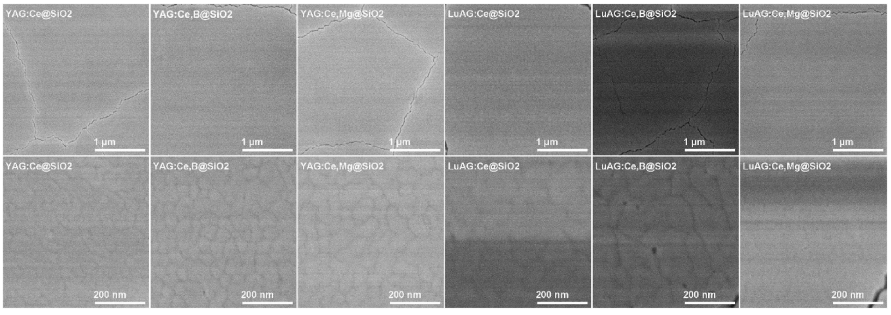

Fig. 6. SEM images of garnet coatings on quartz (SiO_2) substrate using spin-coating technique when each layer is heated separately.

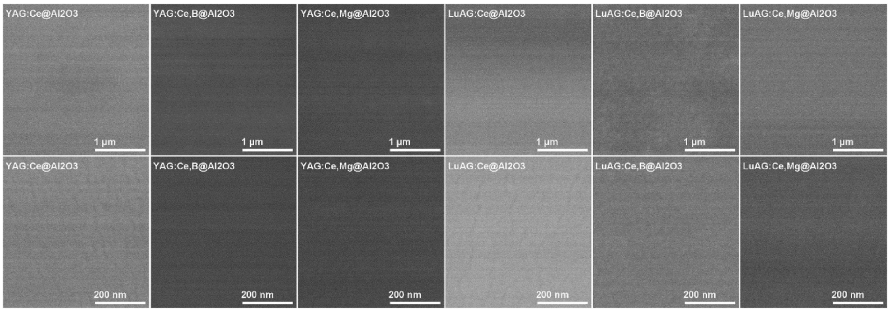

Fig. 7. SEM images of garnet coatings on sapphire (Al_2O_3) substrate using spin-coating technique when each layer is heated separately.

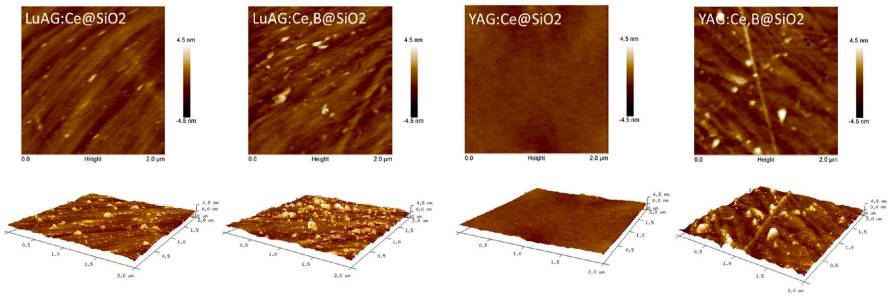

Fig. 8. Photographs of surface topography and 3D images of different coatings synthesized by sol-gel spin-coating method obtained by AFM analysis.

that with short annealing time, the sample is already placed on a heated hot plate, so that heating and the release of organic impurities and the evaporation of the remaining water take place rapidly. This causes cracks and tears in the coatings [23]. Also, looking at the images with higher magnification, it can be seen that coating the layers together results in less smooth coatings and formation of more cracks and empty, uncovered gaps. In this case, it can be said that the coating with annealing at a higher temperature gives, albeit layered, but less cracked thin films.

Thin films were much tidier, smoother and less cracked when spin-coating technique was used for their preparation. Figs. 6 and 7 show that the coatings are evenly distributed over the entire substrate, with no protrusions and empty, uncovered gaps. Fig. 6 shows that on the quartz substrates cracks in the thin films that may have been caused by the shrinkage of the substrate during heating. While the higher magnification figures show individual particles in the garnet layer that are about 50 nm in size. The essential difference with using different, sapphire substrate, is only that there are no visible cracks in the coatings on it. This retention of the smooth surface of the coatings may have been influenced by a high coefficient of thermal expansion of Al_2O_3 which is

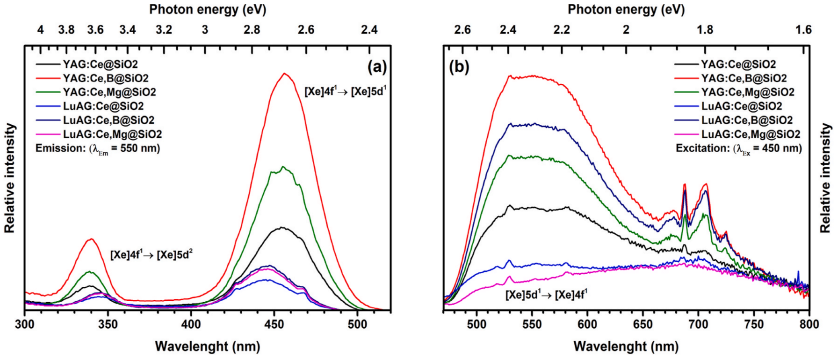

Fig. 9. Excitation (a) and emission (b) spectra of garnet coatings on quartz (SiO_2) substrate using dip-coating technique when all layers were coated without intermittent heating.

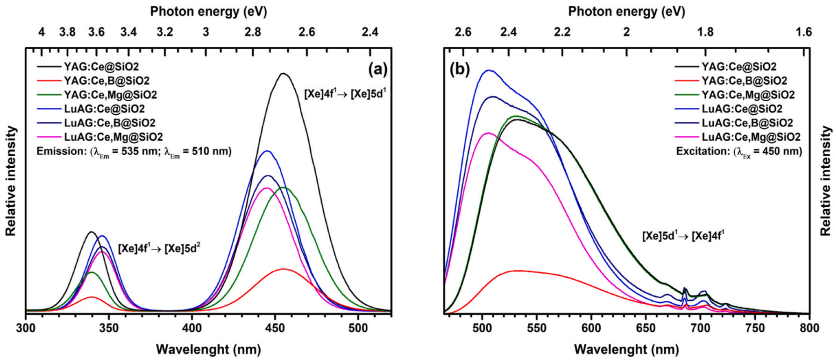

Fig. 10. Excitation (a) and emission (b) spectra of garnet coatings on quartz (SiO_2) substrate using dip-coating technique when each layer is heated separately.

equals from 4.5 to 5.8 × 10^{-6} K^{-1}. Meanwhile, the coefficient of thermal expansion of quartz is almost 10 times lower and can be from 0.55 to 0.75 × 10^{-6} K^{-1}. It is obvious that in order for the sapphire to start to expand the same distance as sapphire, a higher temperature is required, so when heated at the same temperature, the coating on this substrate remains unbroken [24,25].

Summarizing the obtained data, it can be stated that in order to obtain better quality thin films, it is essential to use the spin-coating technique. This method helps to avoid unnecessary layering of coatings, which affects the inhomogeneity of the coating at different locations on the substrate.

3.3. Atomic force microscopy

Atomic force microscopy was performed to determine the topography of the coatings and their roughness. From Fig. 8 we can see that the materials are completely covered by the substrate. This fact can be confirmed by linking the data obtained from the SEM analysis. We can observe that all the roughness of the samples is in the nm range. Consequently, we can say that such coatings are smooth, without sharp protrusions of the coating. The 3D images of the samples show that the available coating irregularities are evenly distributed and are very insignificant. Furthermore, it is clear that sample the YAG sample without boron shows the smoothest surface, without almost no uneven regions. While the most uneven sample was the LuAG doped with cerium and boron, showing many uneven locations, though as mentioned previously the roughness is in nanometer scale.

Table 2
Decay times of different garnets thin films.

Sample	Decay time (ns)			
	Dip-coating, SiO_2, Together	Dip-coating, SiO_2, 1by1	Spin-coating, SiO_2, 1by1	Spin-coating, Al_2O_3, 1by1
YAG:Ce	59.64	65.73	67.67	68.83
YAG:Ce, B	59.13	49.44	64.97	77.46
YAG:Ce, Mg	59.54	48.69	71.22	74.22
LuAG:Ce	53.47	47.07	63.31	66.37
LuAG: Ce,B	50.60	45.46	65.74	62.50
LuAG: Ce,Mg	61.88	46.65	60.52	72.93

3.4. Luminescence properties

The luminescence of the compounds and its efficiency are highly dependent on the active centers in the sample. Since for preparation of films a much diluted solution is used, only a thin layer is deposited on the substrate. Moreover, the number of active emission centers is much smaller if compared to that of powders or ceramics. This disparity leads to the much more reduced emission and excitation intensity [15]. Nevertheless, Fig. 9 – 12 show that the coatings have luminescent properties. Note, a self-made sample holder was used for the luminescent measurement of the thin films. For this reason, emission intensity is very sensitive and not comparable parameter, because even the smallest displacement in the coating can have a huge effect on the emission and excitation strength.

Despite the fact that the luminescence intensity cannot be compared between different compounds samples, the properties of YAG and LuAG garnets can be seen in Figs. 9–12. The excitation spectra (Figures a) show two intense peaks, which, are assigned to the transitions characteristic to Ce^{3+} ions. These peaks occur during the electron transitions from $4f^1$ to 5 d^1 and from $4f^1$ to 5 d^2 orbitals. Obviously, all samples are best excited with a wavelength of about 450 nm. Also, for lutetium garnets, a shift towards shorter wavelengths is observed due to covalence effect of this element. The effect of covalence is the influence of different ions electronegativity. The transition to longer wavelengths is observed when there is greater covalence. In the case of yttrium and lutetium, the electronegativity of yttrium is 1.22 and that of lutetium is 1.27. Although the difference is not large, the effect is observed and the lutetium garnet peaks shift towards the higher energy [26].

From the emission spectra (images b in all of the figures) one main emission band characteristic to Ce^{3+} ions is observed and is attributed to the 5 d^1 → $4f^1$ electron transitions. Its maximum varies from 505 nm to 550 nm depending on the composition of the garnet. The Figures also show extraneous peaks of different intensities located in the region from 660 nm to 740 nm. All of these peaks are attributed to Cr^{3+} ion emission [27]. Given the composition of the materials and substrates used, it can be stated that the influence of chromium ions seen in the spectrum may be caused by the impurities in used substrates. All substrates seem to contain appropriate amounts of chromium impurities. In Fig. 10b this area particularly stands out. This can be explained by the fact that sapphire contains about 10% of other elements, including chromium, impurities. A different quartz substrate has also been used for dip-coating (Fig. 9b) where all layers were coated without intermittent heating. It can be seen that higher levels of chromium ions impurities are also observed in this substrate. The substrates used in the synthesis of the other two compounds have the lowest amount of parasitic phase. These quartz substrates, and impurities are the smallest and less than 8%. From

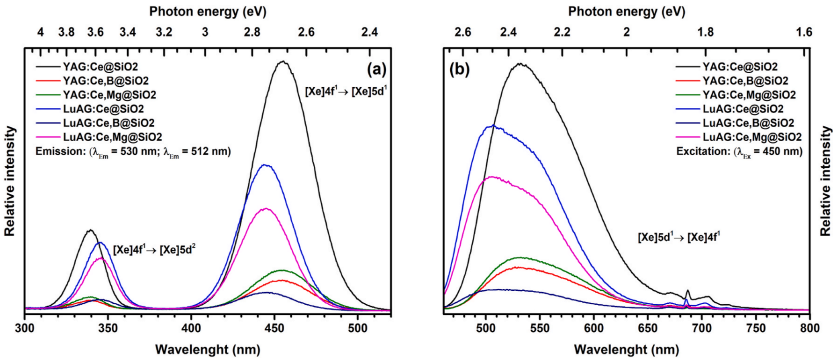

Fig. 11. Excitation (a) and emission (b) spectra of garnet coatings on quartz (SiO_2) substrate using spin-coating technique when each layer is heated separately.

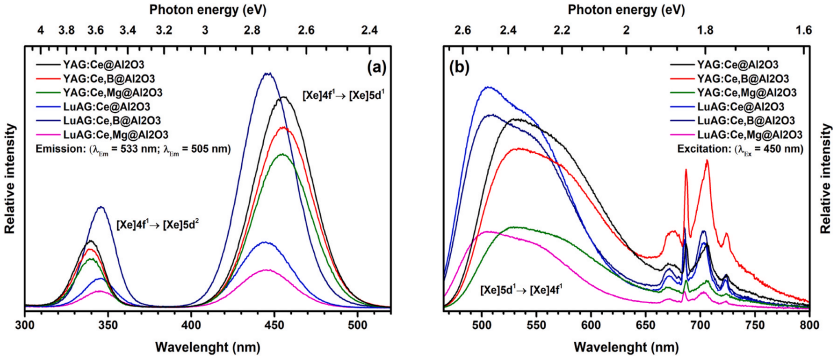

Fig. 12. Excitation (a) and emission (b) spectra of garnet coatings on sapphire (Al_2O_3) substrate using spin-coating technique when each layer is heated separately.

the obtained spectra for the thin films, it can be said that regardless of the coating technique and the substrate used, the optical properties that are characteristic of synthesized garnets are observed. This confirms that these coating deposition methods retain their characteristic luminescent properties.

While the fact that the emission and excitation intensities of the garnet coatings cannot be compared between each other stands, the decay times can be compared because the same number of counts were used for all samples. Depending on the intensity of the emission, only the duration of the measurement itself varied. The luminescence decay time was also measured for the prepared compounds. According to the literature, the specific trends and values applicable for luminescence decay times (decreases and increases) corelate well with ones obtained during scintillation decay [28–31]. The basic idea is that the added boron and magnesium shortens the decay time. Indeed, as seen from Table 2, both YAG and LuAG samples show a decrease in decay times when adding boron and magnesium with only slight reduction for some samples. In some cases the reduction even up to 6 ns (YAG:Ce,B – dip-coating, SiO_2, 1by1). Determination of the sample decay times shows that in this case the introduction of boron to the structure gives more of an advantage as compared to magnesium, although there are more literature sources on magnesium doping [32]. This suggests that boron is the element that has the potential to adjust and improve the required luminescent properties, especially in the reducing of the decay time. The decrease in this parameter can be explained by the fact that

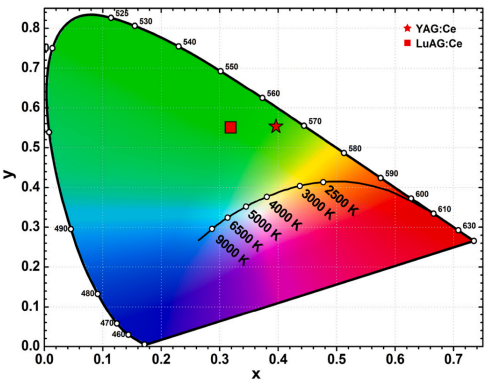

Fig. 13. CIE chromaticity diagram of garnet thin films on quartz (SiO_2) substrate using dip-coating technique when all layers were coated without intermittent heating.

Table 3
Parameters from CIE diagram from thin films of garnet using different synthesis conditions.

Thin film conditions of synthesis	YAG:Ce				LuAG:Ce			
	CIE x	CIE y	CRI	CCT	CIE x	CIE y	CRI	CCT
Dip-coating, SiO_2, together	0.3116	0.5624	31.3	5888 K	0.3145	0.5812	25.3	5823 K
Dip-coating, SiO_2, 1by1	0.3963	0.5530	37.5	5000 K	0.3188	0.5505	32.3	5771 K
Spin-coating, SiO_2, 1by1	0.4001	0.5430	45.5	5000 K	0.3425	0.5315	45.9	5354 K
Spin-coating, Al_2O_3, 1by1	0.4029	0.5497	39.2	5000 K	0.3158	0.5497	33.0	5825 K

aluminum ions have a lower electronegativity than boron ions. As a result, the polarization decreases and the decay time was been shorten accordingly [15,33]. As expected and mentioned in literature LuAG garnets have shorter decay times than YAG compounds [34]. In principle, different coating methods do not affect the decay times, they remain similar. Maybe, slightly longer durations are observed on sapphire substrate, but this can be affected by the replacement of the substrate itself. Looking at all the obtained data, it can be seen that the shortest extinction time is for LuAG:Ce,B sample, which is coated by dip-coating method, when each layer is heated separately 900 °C. Summarizing the measured decay times, it can be concluded that the attempt to dope the samples with appropriate elements is useful. This is justified in the synthesis of coatings, which have a wider practical application, especially in terms as scintillators.

Using data obtained from emission spectra, CIE diagrams of different thin films were determined. For the samples coated by the dip-coating method, where each layer is annealed separately, the CIE diagram is shown in Fig. 13. The corresponding data for other thin films using different coating conditions are shown in Table 3. The Figure shows that the compounds emit light in the green region of the visible light spectrum. All other samples also demonstrate the emission in the green area, according to the x:y coordinates. These are fairly distant coordinates from the white light that is normal to the human eye, which can be seen in the Planck locus, so the color rendering index (CRI) indices are small. If they are small, then the reproducibility of the true color is low. Also, samples prepared by spin-coating technique on quartz have the highest CRI values. The one sample that stands out the rest was coated by the dip-coating technique, where the layers are coated together, while all others are relatively similar. Due to the broad emission band shown in Fig. 9b, the x:y coordinates for the YAG and LuAG samples are almost indistinguishable and they emit at the same location on the color chart. Unlike other cases where the color change of these garnets is observed. In general, it can be said that all prepared samples have similar characteristics that were obtained from the CIE chromaticity diagram. They remain characteristic to YAG:Ce and LuAG:Ce garnets that were studied to date by other scientists [35,36].

4. Conclusions

Sol-gel spin-coating and dip-coating coating deposition techniques have been successfully used in coating garnet film on either quartz (SiO_2) or sapphire (Al_2O_3) substrates. From XRD patterns could be said that, pure yttrium and lutetium aluminum garnets doped with 0.5% of cerium and/or 5% of boron, 0.03% of magnesium were synthesized. Overall, the used methods allows for a rather simple route of preparing single phase compounds. When comparing both preparation techniques and used substrates, it can be stated that it is better to use a sapphire substrate and spin-coating technology to obtain better films resulting even surface of coatings without cracks that exist in other cases. AFM and SEM analyzes confirm the low roughness of the coatings. Most compounds containing boron or magnesium ions have a shorter decay time, which can be explained by the different electronegativity between boron and aluminum elements. Although, it can be observed that different coating technologies have an effect on the decay time characteristic and vary depending on how the layers were coated. With the lowest decay time of 45.46 ns being obtained for LuAG:Ce,B compound prepared by Dip-coating 1by1 methodology on SiO_2 substrate.

Declaration of competing interest

The authors declare that they have no known competing financial interests or personal relationships that could have appeared to influence the work reported in this paper.

References

[1] I.P. Machado, V.C. Teixeira, C.C.S. Pedroso, H.F. Brito, L.C.V. Rodrigues, X-ray scintillator Gd2O2S:Tb3+ materials obtained by a rapid and cost-effective microwave-assisted solid-state synthesis, J. Alloys Compd. 777 (2019) 638–645, https://doi.org/10.1016/j.jallcom.2018.10.348.

[2] D. Wang, G.P. Bierwagen, Sol-gel coatings on metals for corrosion protection, Prog. Org. Coating 64 (2009) 327–338, https://doi.org/10.1016/j.porgcoat.2008.08.010.

[3] M.E. Cruz, J. Li, G. Gorni, A. Durán, G.C. Mather, R. Balda, J. Fernández, Y. Castro, Crystallization process and site-selective excitation of Nd3+ in LaF3/NaLaF4 sol–gel-synthesized transparent glass-ceramics, Crystals 11 (2021) 464, https://doi.org/10.3390/cryst11050464.

[4] Y. Liu, J. Zou, M. Shi, B. Yang, Y. Han, W. Li, Z. Wang, H. Zhou, M. Li, N. Jiang, Effect of gallium ion content on thermal stability and reliability of YAG: Ce phosphor films for white LEDs, Ceram. Int. 44 (2018) 1091–1098, https://doi.org/10.1016/j.ceramint.2017.10.056.

[5] A. Boukerika, L. Guerbous, H. Chelef, L. Benharrat, Preparation and characterization of bright high quality YAG: Eu3+ thin films grown by sol–gel dip-coating technique, Thin Solid Films 683 (2019) 74–81, https://doi.org/10.1016/j.tsf.2019.05.017.

[6] R. Zhang, H. Lin, Y. Yu, D. Chen, J. Xu, Y. Wang, A new-generation color converter for high-power white LED: transparent Ce $^{3+}$:YAG phosphor-in-glass, Laser Photon. Rev. 8 (2014) 158–164, https://doi.org/10.1002/lpor.201300140.

[7] J.J. Bauer, E.R. Rosenberg, C.A. Ross, Perpendicular magnetic anisotropy and spin mixing conductance in polycrystalline europium iron garnet thin films, Appl. Phys. Lett. 114 (2019), 052403, https://doi.org/10.1063/1.5074166.

[8] W. Chewpraditkul, L. Swiderski, M. Moszynski, T. Szczesniak, A. Syntfeld-Kazuch, C. Wanarak, P. Limsuwan, Scintillation properties of LuAG:Ce, YAG:Ce and LYSO: Ce crystals for gamma-ray detection, IEEE Trans. Nucl. Sci. (2009) 3800–3805, https://doi.org/10.1109/TNS.2009.2033994.

[9] L. Pan, B. Jiang, J. Fan, P. Zhang, X. Mao, L. Zhang, Co-precipitation synthesis of lutetium aluminum garnet (LuAG) powders: the influence of ethanol, Opt. Mater. 71 (2017) 50–55, https://doi.org/10.1016/j.optmat.2016.06.020.

[10] V. Bachmann, C. Ronda, A. Meijerink, Temperature quenching of yellow Ce3+ luminescence in YAG:Ce, Chem. Mater. 21 (2009) 2077–2084, https://doi.org/10.1021/cm8030768.

[11] D.S. McGregor, Materials for gamma-ray spectrometers: inorganic scintillators, Annu. Rev. Mater. Res. 48 (2018) 245–277, https://doi.org/10.1146/annurev-matsci-070616-124247.

[12] C. Foster, M. Koschan, Y. Wu, C.L. Melcher, Boron codoping of Czochralski grown lutetium aluminum garnet and the effect on scintillation properties, J. Cryst. Growth 486 (2018) 126–129, https://doi.org/10.1016/j.jcrysgro.2018.01.028.

[13] M.T. Lucchini, O. Buganov, E. Auffray, P. Bohacek, M. Korjik, D. Kozlov, S. Nargelas, M. Nikl, S. Tikhomirov, G. Tamulaitis, A. Vaitkevicius, K. Kamada, A. Yoshikawa, Measurement of non-equilibrium carriers dynamics in Ce-doped YAG, LuAG and GAGG crystals with and without Mg-codoping, J. Lumin. 194 (2018) 1–7, https://doi.org/10.1016/j.jlumin.2017.10.005.

[14] I. Jiménez, L.J. Terminello, F.J. Himpsel, M. Grush, T.A. Callcott, Photoemission, X-ray absorption and X-ray emission study of boron carbides, J. Electron. Spectrosc. Relat. Phenom. 101–103 (1999) 611–615, https://doi.org/10.1016/s0368-2048(98)00342-9.

[15] G. Inkrataite, M. Kemere, A. Sarakovskis, R. Skaudzius, Influence of boron on the essential properties for new generation scintillators, J. Alloys Compd. 875 (2021) 160002, https://doi.org/10.1016/j.jallcom.2021.160002.

[16] A. Belsky, K. Lebbou, V. Kononets, O. Sidletskiy, A. Gektin, E. Auffray, D. Spassky, A.N. Vasil'ev, Mechanisms of luminescence decay in YAG-Ce,Mg fibers excited by

γ- and X-rays, Opt. Mater. 92 (2019) 341–346, https://doi.org/10.1016/j.optmat.2019.04.054.
[17] M. Skruodiene, M. Misevicius, M. Sakalauskaite, A. Katelnikovas, R. Skaudzius, Doping effect of Tb3+ ions on luminescence properties of Y3Al5O12:Cr3+ phosphor, J. Lumin. 179 (2016) 355–360, https://doi.org/10.1016/j.jlumin.2016.07.041.
[18] G. Inkrataite, A. Zabiliute-Karaliune, J. Aglinskaite, P. Vitta, K. Kristinaityte, A. Marsalka, R. Skaudzius, Study of YAG:ceand polymer composite properties for application in LED devices, Chempluschem 85 (2020) 1504–1510, https://doi.org/10.1002/cplu.202000318.
[19] E. Garskaite, M. Lindgren, M.A. Einarsrud, T. Grande, Luminescent properties of rare earth (Er, Yb) doped yttrium aluminium garnet thin films and bulk samples synthesised by an aqueous sol-gel technique, J. Eur. Ceram. Soc. 30 (2010) 1707–1715, https://doi.org/10.1016/j.jeurceramsoc.2010.01.001.
[20] J. Sun, Z. Xu, W. Li, X. Shen, Effect of nano-SiO2 on the early hydration of alite-sulphoaluminate cement, Nanomaterials 7 (2017) 102, https://doi.org/10.3390/nano7050102.
[21] W. Zhou, Z. Ma, Y. Cai, X. Bi, T. Li, W. Niu, X. Sun, Q. Lu, The Synthesis Temperature Selection of Cerium Doped Lutetium Yttrium Oxyorthosilicate Single Crystal Powder, Atlantis Press, 2018, https://doi.org/10.2991/aetr-17.2018.44.
[22] M. Malakauskaite-Petruleviciene, Z. Stankeviciute, A. Beganskiene, A. Kareiva, Sol-gel synthesis of calcium hydroxyapatite thin films on quartz substrate using dip-coating and spin-coating techniques, J. Sol. Gel Sci. Technol. 71 (2014) 437–446, https://doi.org/10.1007/s10971-014-3394-5.
[23] A. Antonio, R. Botero, E.A. Ramírez, G. Gordillo, S. Ilican, Y. Caglar, M. Caglar, Preparation and Characterization of Semiconductor Thin Films View Project Preparation and Characterization of ZnO Thin Films Deposited by Sol-Gel Spin Coating Method, 2008. https://www.researchgate.net/publication/280492099. (Accessed 15 April 2020).
[24] Properties: Supplier Data - Sapphire Single Crystal (Alumina 99.9%) - (Goodfellow), (n.d.). https://www.azom.com/properties.aspx?ArticleID=1721 (accessed April 20, 2020).
[25] Silica - Silicon Dioxide (SiO2), (n.d.). https://www.azom.com/article.aspx?ArticleID=1114 (accessed April 20, 2020).
[26] M.G. Brik, Fully relativistic analysis of the covalence effects for the isoelectronic 3d3 ions (Cr3+, Mn4+, Fe5+) in SrTiO3, J. Phys. Chem. Solid. 67 (2006) 856–861, https://doi.org/10.1016/j.jpcs.2005.12.006.
[27] E.P. Jahrman, G.T. Seidler, J.R. Sieber, Determination of hexavalent chromium fractions in plastics using laboratory-based, high-resolution X-ray emission spectroscopy, Anal. Chem. 90 (2018) 6587–6593, https://doi.org/10.1021/acs.analchem.8b00302.
[28] M. Shimizu, M. Koshimizu, Y. Fujimoto, T. Yanagida, S. Ono, K. Asai, Luminescence and scintillation properties of Cs3BiCl6 crystals, Opt. Mater. 61 (2016) 115–118, https://doi.org/10.1016/J.OPTMAT.2016.05.057.
[29] M. Rathaiah, M. Kucera, P. Prusa, A. Beitlerova, M. Nikl, M. Rathaiah, M. Kucera, P. Prusa, A. Beitlerova, M. Nikl, Effect of Si^{4+} co-doping on luminescence and scintillation properties of $Lu_3Al_5O_{12}$:Ce,Ca epitaxial garnet films, OptMa 91 (2019) 321–325, https://doi.org/10.1016/J.OPTMAT.2019.03.038.
[30] D. Nakauchi, G. Okada, N. Kawano, N. Kawaguchi, T. Yanagida, Luminescent and scintillation properties of Ce-doped Tb3Al5O12 crystal grown from Al-rich composition, APEX 10 (2017), https://doi.org/10.7567/APEX.10.072601.
[31] T. Yanagida, Y. Fujimoto, A. Yamaji, N. Kawaguchi, K. Kamada, D. Totsuka, K. Fukuda, K. Yamanoi, R. Nishi, S. Kurosawa, T. Shimizu, N. Sarukura, Study of the correlation of scintillation decay and emission wavelength, in: Radiat. Meas, Pergamon, 2013, pp. 99–102, https://doi.org/10.1016/j.radmeas.2012.05.014.
[32] O. Sidletskiy, K. Lebbou, D. Kofanov, V. Kononets, I. Gerasymov, R. Bouaita, V. Jary, R. Kucerkova, M. Nikl, A. Polesel, K. Pauwels, E. Auffray, Progress in fabrication of long transparent YAG:Ce and YAG:Ce,Mg single crystalline fibers for HEP applications, CrystEngComm 21 (2019) 1728–1733, https://doi.org/10.1039/C8CE01781F.
[33] S. Kurumada, S. Takamori, M. Yamashita, An alkyl-substituted aluminium anion with strong basicity and nucleophilicity, Nat. Chem. 12 (2020) 36–39, https://doi.org/10.1038/s41557-019-0365-z.
[34] S. Feng, H. Qin, G. Wu, H. Jiang, J. Zhao, Y. Liu, Z. Luo, J. Qiao, J. Jiang, Spectrum regulation of YAG:Ce transparent ceramics with Pr, Cr doping for white light emitting diodes application, J. Eur. Ceram. Soc. 37 (2017) 3403–3409, https://doi.org/10.1016/j.jeurceramsoc.2017.03.061.
[35] S. Hu, C. Lu, G. Zhou, X. Liu, X. Qin, G. Liu, S. Wang, Z. Xu, Transparent YAG:Ce ceramics for WLEDs with high CRI: Ce3+ concentration and sample thickness effects, Ceram. Int. 42 (2016) 6935–6941, https://doi.org/10.1016/j.ceramint.2016.01.079.
[36] Z. Wang, J. Zou, C. Zhang, M. Shi, B. Yang, Y. Li, H. Zhou, Y. Liu, M. Li, X. Qian, High color rendering index of warm WLED based on LuAG: Ce3+ PiG coated CaAlSiN3: Eu2+ phosphor film for residential lighting applications, J. Mater. Sci. Mater. Electron. 29 (2018) 8767–8773, https://doi.org/10.1007/s10854-018-8893-7.

Received: 20 September 2023 | Revised: 15 November 2023 | Accepted: 19 December 2023
DOI: 10.1002/bio.4673

RESEARCH ARTICLE

LUMINESCENCE The Journal of Biological and Chemical Luminescence WILEY

Synthesis and investigation of novel boron- and magnesium-doped YAG:Ce and LuAG:Ce phosphor ceramics

Greta Inkrataite[1] | Monika Skruodiene[2] | Ramunas Skaudzius[1]

[1]Institute of Chemistry, Faculty of Chemistry and Geosciences, Vilnius University, Vilnius, Lithuania

[2]Institute of Solid State Physics, University of Latvia, Riga, Latvia

Correspondence
Greta Inkrataite, Institute of Chemistry, Faculty of Chemistry and Geosciences, Vilnius University, LT-03225 Vilnius, Lithuania.
Email: greta.inkrataite@chgf.vu.lt

Funding information
ERDF PostDoc, Grant/Award Number: 1.1.1.2/VIAA/3/19/480; European Union's Horizon 2020 Framework Programme H2020-WIDESPREAD-01-2016-2017-TeamingPhase2 project CAMART, Grant/Award Number: 739508

Abstract

YAG:Ce and LuAG:Ce ceramics are widely used as scintillator materials that convert high-energy radiation into visible light. For the practical application of such compounds, short decay times are a necessity. One way of shortening the existing decay times even more is to change the local environment of emitting ions by means of doping the matrix with additional elements, for example, boron or magnesium. Furthermore, boron ions also can help absorb gamma rays more efficiently, therefore improving overall applicability. Due to the aforementioned reasons, YAG and LuAG ceramics doped with cerium, boron, and magnesium were synthesized. Initial amorphous powders have been obtained by means of sol–gel synthesis and pressed into pellets under isostatic pressure and finally calcinated to form crystalline ceramics. The effects of boron and magnesium doping on the morphological, structural, and luminescence properties were investigated. The key results showed that doping with boron has indeed shortened the decay times of the garnet pellets. Overall, boron doping of ceramics is a relatively new research area; however, it is rather promising as it helps both to improve the luminescence properties and to increase particle growth rate.

KEYWORDS
ceramics, garnets, luminescence, scintillators

1 | INTRODUCTION

Cerium-doped yttrium and lutetium aluminium garnets (YAG:Ce, LuAG:Ce) are well known scintillators, but are also commonly used in light-emitting diodes (LEDs). Transparent ceramic phosphors have a particularly high potential in this field, especially in terms of their practical application [1]. Cerium ions (Ce^{3+}) are characterized using electron transitions between the f and d orbital (more specifically between the $5d^1$ and $4f^1$ orbitals). During these transitions, when electrons return from the excited state ($5d^1$ level) to the ground state ($4f^1$ level) they emit energy in the form of visible light, which we describe as fluorescence [2, 3]. However, for compounds to be applied as scintillators not only an element emitting light is needed but also a suitable matrix with very specific properties. The aforementioned garnets have high chemical and thermal stability, radiation resistance, high quantum efficiency (when doped with Ce^{3+}), intense emission and excitation, and relatively high density (YAG:Ce 4.55 g/cm^3; LuAG:Ce 6.72 g/cm^3), and as such are quite suitable compounds and used as scintillators [4–6].

It should also be emphasized that the decay time of such compounds is in the nano-second range, which is also very important for high-quality materials required in scintillating devices. While in theory garnets that are doped with other lanthanides such as europium (Eu^{3+}) or ytterbium (Yb^{3+}), could be used as scintillators, in reality the decay time will be longer and such compounds will be less relevant for practical applications [3, 7]. Although the decay time of cerium ions in the garnet structure is short, it is still a point of interest for scientists to reduce it even further. This is important because devices [such as computed tomography (CT) or positron emission tomography (PET)] that use scintillators are required to obtain the highest possible

image quality [8, 9]. To achieve this a decay time that is as short as possible is needed. The shorter the decay time, the more signals the device will be able to capture one after the other without overlap, resulting in more points and a better and higher quality image at the same time [10]. This can be achieved by additionally doping the compounds with other elements. There have been some reports that the doping of garnets with both boron and magnesium has the ability to shorten the decay times [10, 11].

In addition to the scintillation properties themselves, applicability is an important factor as well. For this reason, materials synthesized in the form of monocrystals, coatings, or ceramics are much more viable to fashion into actual devices compared with powders that are impractical in this case [12, 13]. In view of this, boron- and/or magnesium-doped YAG:Ce and LuAG:Ce ceramics were synthesized in this work. The resulting ceramics were durable and have a suitable tablet shape. Both B^{3+} and Mg^{2+} ions are introduced into the crystal lattice to shorten the decay time while also increasing the emission intensity.

2 | EXPERIMENTAL

2.1 | Synthesis procedure

Yttrium and lutetium aluminium garnet ceramics were obtained using an isostatic press. The ceramics consisted of a garnet powder synthesized using the sol–gel method. For the synthesis of powders Y_2O_3, Lu_2O_3, $Al(NO_3)_3{\cdot}9H_2O$, $(NH_4)_2Ce(NO_3)_6$, H_3BO_3, and $Mg(NO_3)_2{\cdot}6H_2O$ were used as precursors. The synthesis scheme of powders is shown in Figure 1. First, Y_2O_3 or Lu_2O_3 was dissolved in an excess of concentrated nitric acid at 50°C. Then, the acid was evaporated, and the remaining gel was washed with distilled water two or three times, followed by further evaporation of added water. An additional 50 ml of water was added, after washing $Al(NO_3)_3{\cdot}9H_2O$, $(NH_4)_2Ce(NO_3)_6$, H_3BO_3, and $Mg(NO_3)_2{\cdot}6H_2O$ were dissolved. The solution was left under magnetic stirring for 2 h at 50–60°C. After that, citric acid was added to the solution with a ratio of 1:1 to metal ions and the solution was left to stir overnight. The solution was evaporated at the same temperature, and the obtained gels were dried at 140°C for 24 h in the drying furnace. To remove the organic residue and for all powders to remain amorphous, the compounds were heated at 600°C for 2 h under air [14–16].

The resulting white powders were ground in a 'Retsch Emax' ball mill with ZrO_2 balls (5 mm diameter) at 1200 rpm for 10 min to reduce and homogenize the size of the synthesized powders resulting in stronger ceramics later on. After that 0.1 g of the fine powder was initially compressed into a 10 mm diameter tablet using 'Perkin Elmer Hydraulic press' under a force of 4 kN for 10 min. Then the tablet was embedded between two 10 mm diameter metal plates, vacuum sealed in a plastic container and placed in a 'P/O/Weber' isostatic press for 30 min under a force of 400 kN. The obtained tablet was heated at 1000°C for 2 h in air and then further calcined at 1500°C for 4 h in air.

While synthesizing ceramics, various different tablet pressing times (from 30 s to 30 min) and pressures (from 0.5 to 4 kN) were tested. Attempts were also made to make ceramics from different amounts of materials (from 0.05 to 1 g). The obtained ceramics were also heated in different conditions, changing the temperature (from 800 to 1700°C) and the heating time (from 1 to 6 h) to adjust the most appropriate heating temperature and time. It was

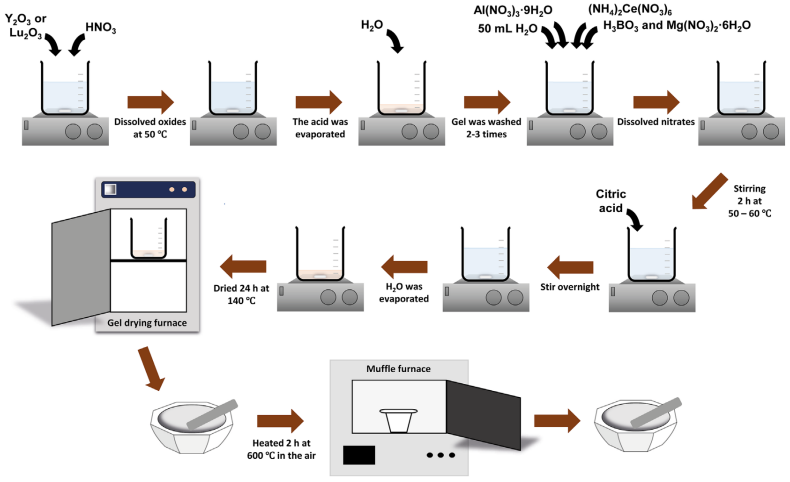

FIGURE 1 Sol–gel synthesis scheme of powders.

only after testing many different parameters that the best were selected.

Nominal formulas of the synthesized samples are the following: $Y_{2.985-y}Al_2Al_{3-x}O_{12}:Ce_{0.015},B_x,Mg_y$, $Lu_{2.98-y5}Al_2Al_{3-x}O_{12}:Ce_{0.015}B_x,Mg_y$. According to our previous studies, YAG and LuAG ceramics were doped with 5% or 0% of boron and/or with 0.03 or 0% of magnesium [16–18]. A list of all ceramics is presented in Table 1, in addition Figure 2 shows the images of synthesized garnets ceramics. It can be seen that the YAG samples exhibit a yellow colour in daylight, while the LuAG samples have a greenish colour. This feature is particularly well revealed when illuminated using light with a wavelength of 365 nm. Yttrium garnets emit yellow, while lutetium ones emit in the green part of the spectral region. It is very clear from the photographs taken (this is confirmed by the emission spectra in Figure 9b) that YAG:Ce,B shines the brightest from yttrium garnets. Due to the unevenness of the edges of the obtained ceramics, colour changes are visible in some samples when excited by 365 nm light. All obtained samples are not transparent, as confirmed in the supporting information Figure S1.

2.2 | Characterization

2.2.1 | X-ray diffraction (XRD)

XRD measurements of ceramics were performed using a 'Rigaku MiniFlex II' X-ray diffractometer. Then diffraction patterns were recorded in the range 2θ angles from 15° to 80° for all compounds. CuKα radiation (λ = 1.542 Å) was used for the analysis. The measurement parameters were set as follows: Current was 15 mA, voltage—30 kV, X-ray detector movement step was 0.010°, and dwell time 5.0 s.

TABLE 1 The list of synthesized ceramic samples.

YAG	LuAG
YAG:Ce	LuAG:Ce
YAG:Ce,5%B (YAG:Ce,B)	LuAG:Ce,5%B (LuAG:Ce,B)
YAG:Ce,5%B,0.03%Mg (YAG:Ce,B,Mg)	LuAG:Ce,5%B,0.03%Mg (LuAG:Ce,B,Mg)
YAG:Ce,0.03%Mg (YAG:Ce,Mg)	LuAG:Ce,0.03%Mg (LuAG:Ce,Mg)

2.2.2 | Scanning electron microscopy (SEM) measurements

SEM analysis was performed using a 'Hitachi SU-70' scanning electron microscope. Ceramics were fixed onto the alumina sample holder by copper holders. Particle sizes were measured using ImageJ software.

2.2.3 | Measurements of emission and excitation

Edinburgh Instruments FLS980 spectrometer equipped with double excitation and emission monochromators and 450 W Xe lamp, a cooled (−20°C) single-photon counting photomultiplier (Hamamatsu R928). Obtained photoluminescence emission spectra were corrected using a correction file obtained from a tungsten incandescent lamp certified by the National Physics Laboratory (NPL, UK). Excitation spectra were corrected using a reference detector.

2.2.4 | Decay time measurements

The photoluminescence decay kinetics were studied for ceramics using the FLS980 spectrometer. A 400 nm laser was used for these measurements [16, 17].

3 | RESULTS AND DISCUSSION

3.1 | X-ray diffraction analysis

XRD analysis was performed to determine the purity of the synthesized ceramics. The diffraction patterns of the garnet samples are shown in Figure 3. Every peak corresponds to the garnet phase according to the reference data (YAG: PDF#96-152-9038 and LuAG: PDF#00-056-1646). No additional and unassigned reflections were observed that could be attributed to any impurity phases. Therefore, from the given results it can be clearly seen that all of the obtained yttrium aluminium (Part a) and lutetium aluminium (Part b) garnet ceramics exhibit a single-phase structure. A cubic garnet crystal lattice was observed with an *Ia3d* (#230) space group for all compounds. This

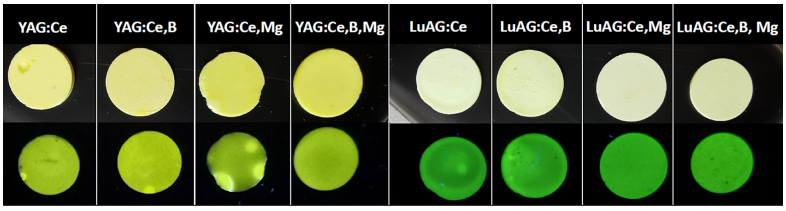

FIGURE 2 Different garnet ceramics in daylight (upper) and under 365 nm excitation (lower).

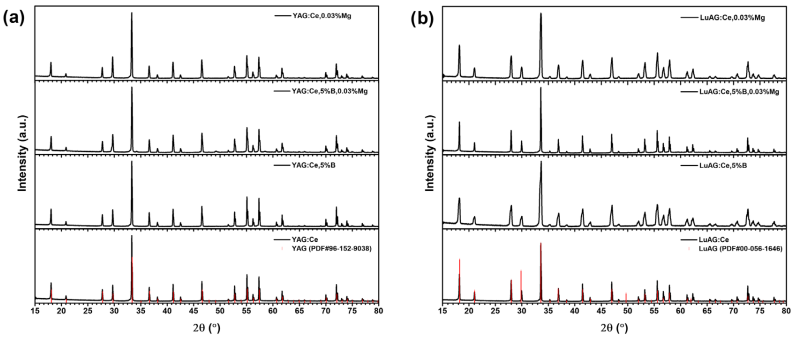

FIGURE 3 Diffractions patterns of YAG (a) and LuAG (b) ceramics.

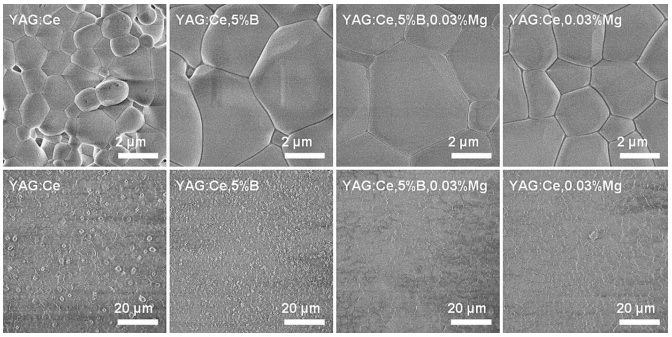

FIGURE 4 Scanning electron microscopy (SEM) images of YAG ceramic samples.

crystal structure is characterized by three different cation positions with different coordination numbers and can be expressed as $A_3B_2C_3O_{12}$. A is the 12-fold coordinated dodecahedral position, B is the six-fold coordinated octahedral position and C is the four-fold coordinated tetrahedral position. LuAG and YAG Al^{3+} occupies both octahedral and tetrahedral positions. Furthermore, from the diffraction patterns it can be seen that the reflections in the LuAG samples are slightly shifted towards larger 2θ angle values (YAG:Ce peak maxima at 33.30° and LuAG:Ce at 33.60°) even though the same crystal structure is observed for both sample series. This shift can be explained by the change (decrease) in the ionic radius of the atom in the dodecahedral position: the atomic radius of yttrium is 1.16 Å and for lutetium it is 0.98 Å [19]. Slight peak shifts are observed in the diffraction patterns, which may have occurred due to the doping effect.

3.2 | SEM analysis

SEM analysis was performed to determine the surface morphology of the ceramics as well as to estimate the particle size. Figures 4 and 5 show the surfaces of YAG and LuAG ceramics under different magnifications. This was done to investigate both the broader surface of the ceramics as well as the individual particles that make up the ceramics. It can be clearly seen from the figures that the incorporation of boron into the garnet structure has a significant influence on the morphology of the ceramics. This was expressed mostly in the fact that the particle size increased drastically when comparing the samples doped with boron to the ones doped with cerium only (in both LuAG and YAG cases). This can be explained by a couple of reasons. First, in some cases when compounds are alloyed with other elements their melting point decreases and, as such, the particle growth increases due to a more rapid mass transport. Second, as boron can also act as a flux, not just dopant in this case, which also drastically increases grain growth, this results in larger individual particles [20].

Particle size distribution histograms obtained from the SEM images are shown in Figures 6 and 7. The size of all particles varies from 0.6 to 8 μm. The histograms more clearly depict the information provided by the SEM images. The particle size distribution of YAG:Ce is between 1 to 2 μm with the average size being 1.43 μm. In the presence of boron (B^{3+}) the particle size changes and is between 1 and 6 μm with the average size being 3.51 μm. For LuAG:Ce samples the particle size is between 0.3 to 1.8 μm with the average size

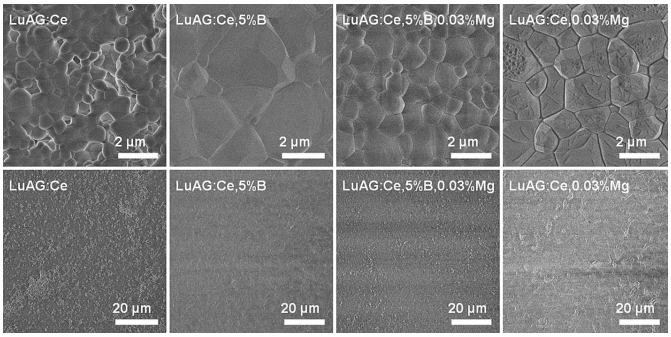

FIGURE 5 Scanning electron microscopy (SEM) images of LuAG ceramic samples.

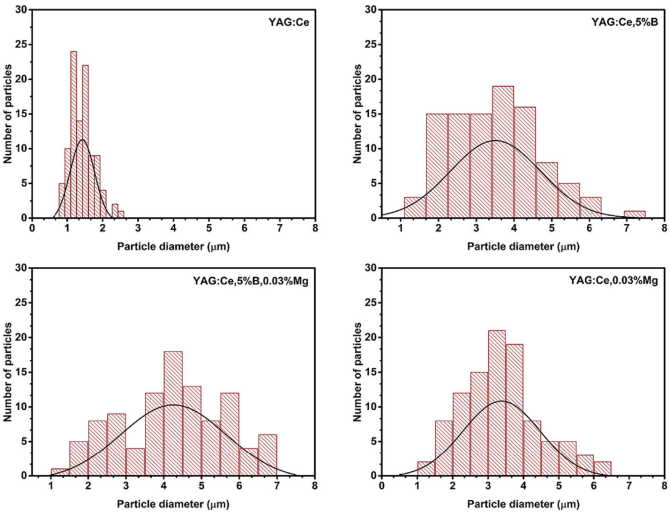

FIGURE 6 Particle size histograms of YAG ceramic samples.

being 0.98 μm and for LuAG:Ce,5%B between 1 and 5 μm with the average size being 2.88 μm. It is also worthy to mention that for magnesium or co-doping with both elements a similar increase in particle size was observed. Only some slight deviation can be seen for LuAG that is doped with both boron and magnesium as the particle size increased only slightly compared with the undoped sample. As already mentioned, this change in particle size may have occurred due to the fact that boron/magnesium acts as a flux. Furthermore, Figures 6 and 7 show that the yttrium aluminium garnets have larger particles than lutetium aluminium garnets. This trend can be attributed to the fact that YAG has a melting point of ~1970°C and LuAG has a melting point of ~2060°C. This means that the mass transport during yttrium aluminium garnet preparation happens slightly faster compared with the lutetium garnet and as such larger particles are obtained [21, 22].

In addition to surface morphology, the thickness of ceramics was determined using SEM. During the synthesis, the aim was to obtain ceramics as thin as possible. Figure 8 shows a side view of YAG:Ce,5%B ceramic. It can be seen that the thickness of the ceramic is ~749 μm. It is therefore clear that a sufficiently thin ceramic was obtained during the synthesis.

3.3 | Luminescence properties

Photoluminescence emission and excitation spectra were measured for all samples and are shown in Figures 9 and 10. For all ceramics, electron transitions between $4f^1$, $5d^1$ and $5d^2$ levels are observed. These electron transitions are characteristic of the Ce^{3+} ions and are

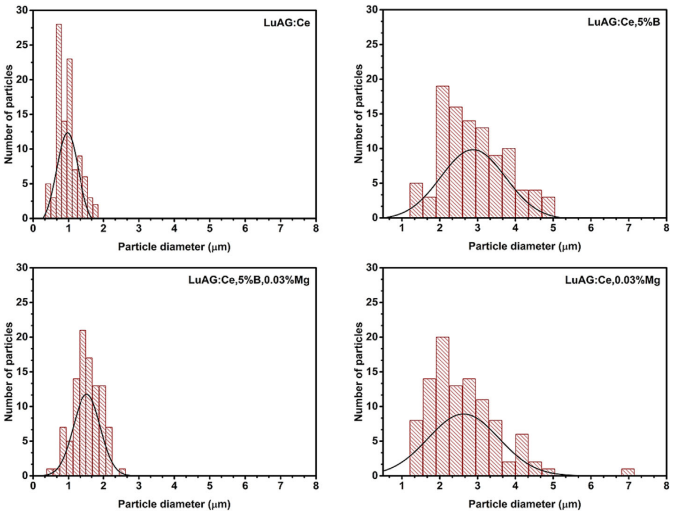

FIGURE 7 Particle size histograms of LuAG ceramic samples.

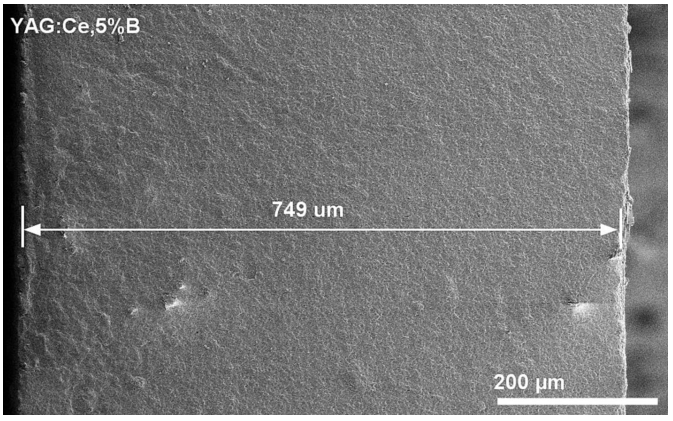

FIGURE 8 Scanning electron microscopy (SEM) images of YAG:Ce,5%B ceramic sample side view.

exhibited as broad emission and excitation bands [23]. The excitation spectra (Part a) consist of two broad bands. These bands are located at 342 and 457 nm for yttrium aluminium garnet and at 347 and 450 nm for lutetium aluminium garnet. The first (less intensive) band is attributed to the electron transition that occurs between $4f^1$ and $5d^2$ levels, and the second band is between $4f^1$ and $5d^1$ levels [24]. It can be observed that the YAG:Ce,B and LuAG:Ce,Mg compounds have the most intense bands in the excitation spectra.

Figures 9b and 10b show a broad band emission spectra of the Ce^{3+} ions. Similarly as before this band appears due to the electron transition from the $5d^1$ to the $4f^1$ orbital [23]. The emission was measured by exciting the compounds with 450 nm wavelength light. The emission maxima are seen at 545 and 512 nm for YAG and LuAG ceramics, respectively. The lutetium aluminium garnet samples have their emission maxima shifted towards the higher energy side. This blue shift can be explained using the different covalency of the samples that originated from the different electronegativity of the (Lu^{3+} and Y^{3+}) bonds inside the matrix. The higher the covalency of the bond, the greater the shift towards shorter wavelengths. Yttrium ions are known to have an electronegativity of 1.22 and lutetium of 1.27. It can be seen that although the difference in electronegativity is small, the covalency of the compounds changes, resulting in a shift of the spectra towards shorter wavelengths [25]. Similarly to the excitation spectra, the emission spectra show that the YAG:Ce,B and LuAG:

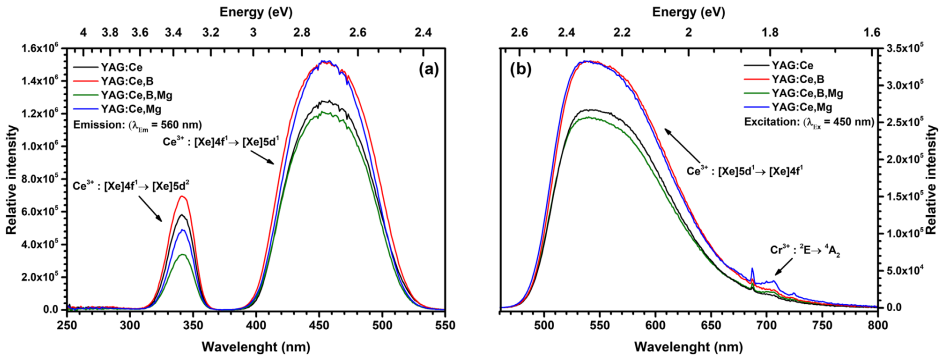

FIGURE 9 YAG ceramics excitation (a) and emission (b) spectra.

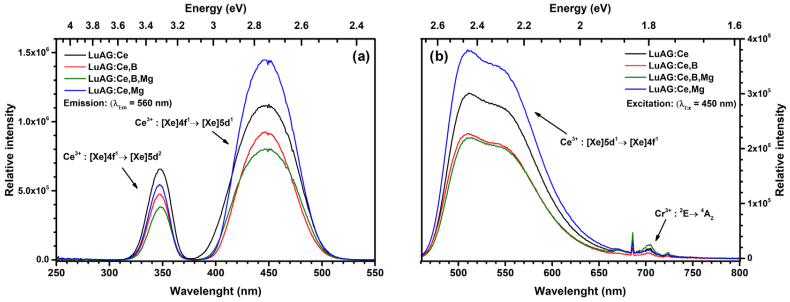

FIGURE 10 LuAG ceramics excitation (a) and emission (b) spectra.

Ce,Mg samples have the highest emission intensity. The increase in emission intensity can be explained by the change in particle size (from SEM data). Both YAG:Ce,B and LuAG:Ce,Mg have the largest particles, and larger particles in most cases have higher emission intensity due to relatively small surface area to volume ratio. This occurs because most luminescence quenching defects exist on the surface of the particles, therefore less surface area compared with volume means that less of these defects are present [26, 27].

In addition to Ce^{3+} emissions, Cr^{3+} ion emission is also observed in the emission spectra at ~700 nm. The emission of chromium ions originates from the $^2E \rightarrow {}^4A_2$ electron transitions [28]. The chromium ions are most likely to be introduced as impurities from the precursors used during synthesis as even extremely small amounts have been reported to show reasonably intensive emission [17].

The main idea behind the boron and/or magnesium doping was to reduce the decay times. As such they were measured for all of the obtained samples. The decay curves of YAG and LuAG ceramics with and without boron and magnesium doping are also shown in Figure 11. From decay curves, it was determined that a two-component process is happening. Bi-exponential decay occurred due to doping of YAG:Ce and LuAG:Ce with boron and magnesium ions. As a result of this doping, defects appear in the samples that trap electrons and delay recombination and, as such, cause the bi-exponential decay profile [29]. It can be seen that samples doped with magnesium exhibit decay curves with a similar profile as boron-doped ones, but with different intensities. The intensity of these curves decreases fairly uniformly for all samples. No sharp difference in the angle of incidence of the curves is observed, as in the samples without magnesium. Observing the curves of decay times of all samples, it is obvious that garnets containing B^{3+} have the highest count intensity. Furthermore, it is clear that samples containing boron have shorter decay times than those without boron.

For more clarity the decay times of all synthesized samples are displayed in Table 2. Due to the two-component nature of the process average decay times were calculated. The obtained results suggest that the doping of ceramics with boron was successful and as a result the decay times of the compounds decreased. For YAG:Ce that was not doped with boron the decay time is 55.79 ns, and after

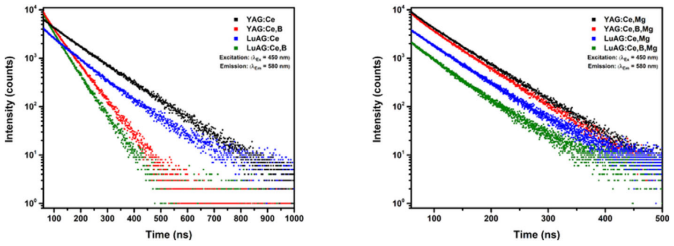

FIGURE 11 Decay curves of the obtained ceramics.

TABLE 2 Decay times of YAG and LuAG ceramics.

Sample	Decay time (ns)		
	τ_1	τ_2	τ_{Av}
YAG:Ce	18.59 ± 0.77	58.48 ± 0.77	55.79 ± 0.97
YAG:Ce,5%B	16.04 ± 0.37	56.44 ± 0.37	52.74 ± 0.75
YAG:Ce,5%B,0.03%Mg	18.41 ± 0.50	67.84 ± 0.50	66.51 ± 0.79
YAG:Ce,0.03%Mg	21.44 ± 0.39	60.06 ± 0.39	60.16 ± 0.78
LuAG:Ce	21.24 ± 0.92	51.97 ± 0.92	52.17 ± 1.10
LuAG:Ce,5%B	21.32 ± 0.89	52.68 ± 0.89	48.86 ± 1.14
LuAG:Ce,5%B,0.03%Mg	17.55 ± 0.93	51.92 ± 0.93	48.67 ± 1.17
LuAG:Ce,0.03%Mg	32.24 ± 0.37	57.47 ± 0.37	54.86 ± 1.09

doping it decreased to 52.74 ns. For lutetium aluminium garnets, this change is even more visible and the decay times decrease from 52.17 to 48.86 ns. The reduction in decay times of ceramics by doping compounds with boron is based on the polarization of a local activator in an ionic environment. Because boron has a higher electronegativity than aluminium, polarization decreases and decay time becomes shorter [16, 30]. However, for magnesium and combination doping the decay times have increased, in most cases. This may potentially show that magnesium doping is not suitable for ceramics, at least for YAG and LuAG. Comparing the results seen from the emission spectra (Figures 9 and 10) it can be observed that magnesium improves the emission intensity, which may be caused by increased particle size and changes in the morphology of the compounds. However, the decay time depends on the electronegativity difference of the different ions [26, 30]. Based on the obtained results, it can be concluded that boron-doped ceramics have a shorter decay time, which is required for scintillators. The decay times of this synthesized ceramic are one of the shortest compared with the work of other scientists (for YAG:Ce this varies from 58 to 60 ns, for LuAG this is from 54 to 50 ns) [31–33]. Although scintillation decay times have not been measured in this work, it can be argued from the literature that for both photoluminescence and scintillation decay times (decreases and increases), specific trends and values correlate [17, 34–36].

Commission Internationale de l'éclairage (CIE) chromaticity diagrams are plotted using coordinates derived from emission spectra of the ceramics. The diagram is shown in Figure 12. Cerium (Ce^{3+}) ions are known to emit light in the green region, as also evidenced by the

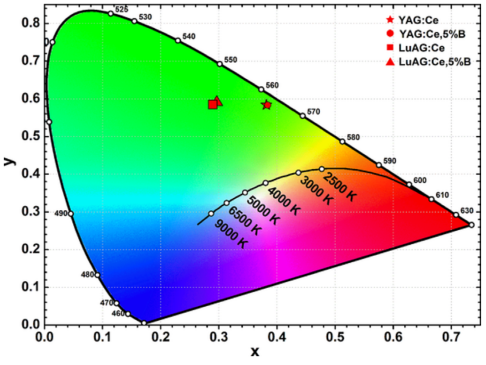

FIGURE 12 Commission Internationale de l'éclairage (CIE) chromaticity diagram of synthesized garnet ceramic samples.

diagram [37]. It can be seen that the emission colour of the yttrium aluminium garnet is more monochromatic because it is closer to the edge of the CIE diagram chart [38]. In addition, lutetium aluminium garnets are closer to the middle of the graph. The more monochromatic light, the better the quality of the samples because they emit light over a narrower range. Only four sample points are shown in Figure 12, as the others overlapped due to a small coordinate difference and no large difference between them was visible.

4 | CONCLUSION

Yttrium and lutetium aluminium garnet ceramics doped with boron and/or magnesium were obtained using an isostatic press. The XRD patterns showed that all the synthesized ceramics had a pure garnet phase. While the doping did not affect the purity of the phases, its effect was observed in the analysis of particle morphology. Samples containing boron/magnesium ions contained larger particles on the surface due to the flux properties of the elements. In terms of luminescence, all ceramics had emission characteristics for cerium ions, and samples with boron and magnesium had a higher emission intensity than that of pure YAG:Ce. The measured decay times confirmed that, at least, boron doping was successful as the decay times of the compounds decreased for YAG from 55.79 ± 0.97 to 52.74 ± 0.75 ns and for LuAG from 52.17 ± 1.10 to 48.86 ± 1.14 ns. Overall, the decay times of the compounds were successfully reduced and were one of the shortest reported in the literature. Furthermore, the emission intensity also increased, therefore indicating that boron doping could be applied potentially in the scintillator field of research for ceramics samples.

AUTHOR CONTRIBUTIONS

Greta Inkrataite: Conceptualization; methodology; software; validation; formal analysis; investigation; resources; data curation; writing—original draft preparation; visualization. **Monika Skruodiene:** Formal analysis; data curation; writing—review and editing; project administration; funding acquisition. **Ramunas Skaudzius:** Conceptualization; validation; formal analysis; data curation; writing—review and editing; supervision.

ACKNOWLEDGEMENTS

The work of Monika Skruodiene is supported by the ERDF PostDoctorate project no. 1.1.1.2/VIAA/3/19/480. Institute of Solid State Physics, University of Latvia has received funding from the European Union's Horizon 2020 Framework Programme H2020-WIDESPREAD-01-2016-2017-TeamingPhase2 under grant agreement no. 739508, project CAMART^2.

CONFLICT OF INTEREST STATEMENT

The authors declare no conflict of interest.

DATA AVAILABILITY STATEMENT

Author elects to not share data.

ORCID

Greta Inkrataite https://orcid.org/0000-0001-7173-7454

REFERENCES

[1] Q. Yao, P. Hu, P. Sun, M. Liu, R. Dong, K. Chao, Y. Liu, J. Jiang, H. Q. Jiang Yao, P. Hu, P. Sun, R. Dong, Y. Liu, J. Jiang, H. Jiang, Q. Yao, M. Liu, *Adv. Mater.* **2020**, *32*, 1907888. https://doi.org/10.1002/ADMA.201907888

[2] V. Ţucureanu, D. Munteanu, *Ceram. Int.* **2019**, *45*, 7641. https://doi.org/10.1016/j.ceramint.2019.01.061

[3] A. Boukerika, L. Guerbous, H. Chelef, L. Benharrat, *Thin Solid Films* **2019**, *683*, 74. https://doi.org/10.1016/j.tsf.2019.05.017

[4] W. Chewpraditkul, L. Swiderski, M. Moszynski, T. Szczesniak, A. Syntfeld-Kazuch, C. Wanarak, P. Limsuwan, *IEEE Trans. Nucl. Sci.* **2009**, *56*, 3800. https://doi.org/10.1109/TNS.2009.2033994

[5] L. Pan, B. Jiang, J. Fan, P. Zhang, X. Mao, L. Zhang, *Opt. Mater. (Amst).* **2017**, *71*, 50. https://doi.org/10.1016/j.optmat.2016.06.020

[6] D. S. McGregor, *Annu. Rev. Mater. Res.* **2018**, *48*, 245. https://doi.org/10.1146/annurev-matsci-070616-124247

[7] M. Chaika, R. Tomala, W. Strek, *J. Alloys Compd.* **2021**, *865*, 158957. https://doi.org/10.1016/J.JALLCOM.2021.158957

[8] S. Chen, B. Jiang, Q. Zhu, W. Ma, G. Zhang, Y. Jiang, W. Chewpraditkul, L. Zhang, *Nucl. Instruments Methods Phys. Res. Sect. A Accel. Spectrometers, Detect. Assoc. Equip.* **2019**, *942*, 162360. https://doi.org/10.1016/J.NIMA.2019.162360

[9] S. Yamamoto, H. Nitta, *Nucl. Instruments Methods Phys. Res. Sect. A Accel. Spectrometers, Detect. Assoc. Equip.* **2018**, *900*, 25. https://doi.org/10.1016/J.NIMA.2018.05.029

[10] C. Foster, M. Koschan, Y. Wu, C. L. Melcher, *J. Cryst. Growth* **2018**, *486*, 126. https://doi.org/10.1016/j.jcrysgro.2018.01.028

[11] A. Belsky, K. Lebbou, V. Kononets, O. Sidletskiy, A. Gektin, E. Auffray, D. Spassky, A. N. Vasil'ev, *Opt. Mater. (Amst).* **2019**, *92*, 341. https://doi.org/10.1016/J.OPTMAT.2019.04.054

[12] S. Chen, B. Jiang, Y. Wang, Q. Zhu, Q. Yang, W. Ma, G. Zhang, L. Zhang, *J. Rare Earths* **2019**, *37*, 978. https://doi.org/10.1016/J.JRE.2019.01.001

[13] Z. Lin, S. Lv, Z. Yang, J. Qiu, S. Zhou, *Adv. Sci.* **2022**, *9*, 2102439. https://doi.org/10.1002/ADVS.202102439

[14] M. Skruodiene, M. Misevicius, M. Sakalauskaite, A. Katelnikovas, R. Skaudzius, *J. Lumin.* **2016**, *179*, 355. https://doi.org/10.1016/j.jlumin.2016.07.041

[15] G. Inkrataite, A. Zabiliute-Karaliune, J. Aglinskaite, P. Vitta, K. Kristinaityte, A. Marsalka, R. Skaudzius, *ChemPlusChem* **2020**, *85*, 1504. https://doi.org/10.1002/cplu.202000318

[16] G. Inkrataite, M. Kemere, A. Sarakovskis, R. Skaudzius, *J. Alloys Compd.* **2021**, *875*, 160002. https://doi.org/10.1016/j.jallcom.2021.160002

[17] G. Inkrataitė, Ž. Stankevičiūtė, R. Skaudžius, *J. Lumin.* **2022**, *244*, 118751. https://doi.org/10.1016/J.JLUMIN.2022.118751

[18] M. T. Lucchini, V. Babin, P. Bohacek, S. Gundacker, K. Kamada, M. Nikl, A. Petrosyan, A. Yoshikawa, E. Auffray, *Nucl. Instruments Methods Phys. Res. Sect. A Accel. Spectrometers, Detect. Assoc. Equip.* **2016**, *816*, 176. https://doi.org/10.1016/j.nima.2016.02.004

[19] W. Zhou, Z. Ma, Y. Cai, X. Bi, T. Li, W. Niu, X. Sun, Q. Lu, *2017 International Conference Advanced Engineering and Technology Research (AETR 2017)*, Atlantis Press, The Netherlands **2018**, 230. https://doi.org/10.2991/aetr-17.2018.44

[20] S. Cho, C. Yun, Y. S. Kim, H. Wang, J. Jian, W. Zhang, J. Huang, X. Wang, H. Wang, J. L. MacManus-Driscoll, *Nano Energy* **2018**, *45*, 398. https://doi.org/10.1016/j.nanoen.2018.01.003

[21] Y. Kurashima, S. Kurosawa, R. Murakami, A. Yamaji, S. Ishikawa, J. Pejchal, K. Kamada, M. Yoshino, S. Toyoda, H. Sato, Y. Yokota, Y. Ohashi, A. Yoshikawa, *Cryst. Growth Des.* **2021**, *21*, 572. https://doi.org/10.1021/ACS.CGD.0C01396/ASSET/IMAGES/LARGE/CG0C01396_0012.JPEG

[22] A. G. Petrosyan, K. L. Ovanesyan, R. V. Sargsyan, G. O. Shirinyan, D. Abler, E. Auffray, P. Lecoq, C. Dujardin, C. Pedrini, *J. Cryst. Growth* **2010**, *312*, 3136. https://doi.org/10.1016/J.JCRYSGRO.2010.07.042

[23] J. Ling, W. Xu, J. Yang, T. Mu, Y. Zhang, Y. Zhou, M. Hong, *J. Eur. Ceram. Soc.* **2021**, *41*, 5967. https://doi.org/10.1016/J.JEURCERAMSOC.2021.05.005

[24] L. Chen, X. Chen, F. Liu, H. Chen, H. Wang, E. Zhao, Y. Jiang, T. S. Chan, C. H. Wang, W. Zhang, Y. Wang, S. Chen, *Sci. Rep.* **2015**, *5*, 11514. https://doi.org/10.1038/srep11514
[25] M. G. Brik, *J. Phys. Chem. Solids* **2006**, *67*, 856. https://doi.org/10.1016/j.jpcs.2005.12.006
[26] Y. Shen, D. R. Clarke, *J. Am. Ceram. Soc.* **2009**, *92*, 125. https://doi.org/10.1111/j.1551-2916.2008.02866.x
[27] E. Zych, A. Walasek, A. Szemik-Hojniak, *J. Alloys Compd.* **2008**, *451*, 582. https://doi.org/10.1016/j.jallcom.2007.04.116
[28] M. Norkus, R. Skaudžius, *J. Alloys Compd.* **2022**, *908*, 164601. https://doi.org/10.1016/J.JALLCOM.2022.164601
[29] M. Zeyrek Ongun, *J. Lumin.* **2021**, *240*, 118405. https://doi.org/10.1016/J.JLUMIN.2021.118405
[30] S. Kurumada, S. Takamori, M. Yamashita, *Nat. Chem.* **2020**, *12*, 36. https://doi.org/10.1038/s41557-019-0365-z
[31] C. Hu, J. Li, F. Yang, B. Jiang, L. Zhang, R. Y. Zhu, *Nucl. Instruments Methods Phys. Res. Sect. A Accel. Spectrometers, Detect. Assoc. Equip.* **2020**, *954*, 161723. https://doi.org/10.1016/J.NIMA.2018.12.038
[32] Z. T. Karipbayev, V. M. Lisitsyn, D. A. Mussakhanov, G. K. Alpyssova, A. I. Popov, E. F. Polisadova, E. Elsts, A. T. Akilbekov, A. B. Kukenova, M. Kemere, A. Sarakovskis, A. Lushchik, *Nucl. Instruments Methods Phys. Res. Sect. B Beam Interact. Mater. Atoms* **2020**, *479*, 222. https://doi.org/10.1016/J.NIMB.2020.06.046
[33] W. Ma, B. Jiang, X. Feng, X. Huang, W. Wang, K. Sreebunpeng, L. Zhang, *J. Am. Ceram. Soc.* **2021**, *104*, 966. https://doi.org/10.1111/JACE.17506
[34] T. Yanagida, Y. Fujimoto, A. Yamaji, N. Kawaguchi, K. Kamada, D. Totsuka, K. Fukuda, K. Yamanoi, R. Nishi, S. Kurosawa, T. Shimizu, N. Sarukura, *Radiat. Meas.* **2013**, *55*, 99. https://doi.org/10.1016/j.radmeas.2012.05.014
[35] D. Nakauchi, G. Okada, N. Kawano, N. Kawaguchi, T. Yanagida, *Appl. Phys. Express* **2017**, *10*, 072601. https://doi.org/10.7567/APEX.10.072601
[36] M. Shimizu, M. Koshimizu, Y. Fujimoto, T. Yanagida, S. Ono, K. Asai, *Opt. Mater. (Amst).* **2016**, *61*, 115. https://doi.org/10.1016/J.OPTMAT.2016.05.057
[37] X. Yi, S. Zhou, C. Chen, H. Lin, Y. Feng, K. Wang, Y. Ni, *Ceram. Int.* **2014**, *40*, 7043. https://doi.org/10.1016/J.CERAMINT.2013.12.034
[38] I. S. Park, M. Yang, H. Shibata, N. Amanokura, T. Yasuda, I. S. Park, M. Yang, T. Yasuda, H. Shibata, N. Amanokura, *Adv. Mater.* **2022**, *34*, 2107951. https://doi.org/10.1002/ADMA.202107951

SUPPORTING INFORMATION

Additional supporting information can be found online in the Supporting Information section at the end of this article.

How to cite this article: G. Inkrataite, M. Skruodiene, R. Skaudzius, *Luminescence* **2024**, *39*(1), e4673. https://doi.org/10.1002/bio.4673

Journal of Alloys and Compounds 966 (2023) 171634

Contents lists available at ScienceDirect

Journal of Alloys and Compounds

journal homepage: www.elsevier.com/locate/jalcom

The effect of boron and scandium doping on the luminescence of LuAG:Ce and GdAG:Ce for application as scintillators

Greta Inkrataite [a,*], Jan-Niklas Keil [b], Aleksej Zarkov [a], Thomas Jüstel [b], Ramunas Skaudzius [a]

[a] Institute of Chemistry, Faculty of Chemistry and Geosciences, Vilnius University, Naugarduko 24, Vilnius LT-03225, Lithuania
[b] Department of Chemical Engineering, Münster University of Applied Sciences, Stegerwaldstrasse 39, Steinfurt D-48565, Germany

ARTICLE INFO

Keywords:
Boron co-doping
Ce^{3+} activated garnets
LuAG:Ce
GdAG, photo- and radioluminescences
Scintillator

ABSTRACT

This study concerns cerium and boron doped $Lu_3Al_4Sc_1O_{12}$ and $Gd_3Al_3Sc_2O_{12}$ garnet μ-crystalline powders, which were synthesized for the first time. Rare earth ion, particularly Ce^{3+} activated garnets, due to their high density and efficient Ce^{3+} luminescence upon blue, UV, or x-ray excitation, can be used as scintillators that convert high-energy radiation into visible light. The incorporation of B^{3+} and Sc^{3+} ions into the garnet matrix corresponds to the improvement of the scintillating properties. Boron in these compounds could act like a flux and thus modulate particle morphology, while scandium solely changes the physical and luminescent properties of these garnets. From the measured radioluminescence emission spectra, it could be concluded that boron doping results in a higher emission intensity when the compounds are excited by high-energy radiation. The most striking effect is that the decay time is reduced, and the quantum efficiency of the compounds increases. After improving the kinetic properties of these compounds, it is possible to discuss a wider application of the synthesized materials. In addition to the aforementioned properties, room temperature as well as temperature dependent photoluminescence emission, excitation, and decay times at different temperatures were taken for all samples. The elemental composition of the samples was determined by using the ICP-OES technique. The crystal structure was analyzed by means of powder XRD. Particle morphology and size distribution were also investigated.

The main idea of this research is to synthesize new and adjusted garnet type compounds that show better luminescent properties, which are required for scintillator materials.

1. Introduction

One of the key areas where a lot of advances in technology are achieved is related to the use of electromagnetic radiation, in other words in materials or technical systems that interact with light. Such materials range from light emitting diodes (LEDs) for general and special lighting purposes, security inks, for example for anti-couterfeiting of valuables such as banknotes, to more scientific ones in detector equipment or optical sensors [1–3]. For example, computer-aided detection devices, such as CT (computed tomography) or PET (positron emission tomography) are based on the conversion of gamma radiation or X-rays into visible light. Materials that convert high-energy radiation into visible light are commonly called scintillators [4,5]. Garnets such as lutetium aluminum garnet (LuAG) and gadolinium aluminum garnet (GdAG) that are doped with lanthanides such as cerium (Ce^{3+}) show excellent scintillation properties. Doped LuAG and GdAG are characterized by high thermal stability, high energy resolution, and body density. Of course, LuAG:Ce and GdAG:Ce present the required luminescent properties as well, i.e. high light yield and quantum efficiency as well as a sufficiently short decay time [6–8]. For scintillators, the shortest possible decay time is especially important. The shorter the decay time value is, the more signals the device can capture during the same period, which will result in a much better image quality and energy resolution, which makes the detector system more reliable [9,10].

A development goal concerning these compounds is to improve their physical properties, in this case, the luminescent properties, especially to shorten the decay time. One way to improve the desired properties is the use of boron. B^{3+} ions, act as a flux and improve the emission intensity while at the same time due to their dual nature also acting as a dopant they shorten the decay time of scintillator compounds [9,11,12]. Another chemical element that may potentially lead to the improvement of optical properties of garnets is scandium. This trivalent ion may also

* Corresponding author.
E-mail address: greta.inkrataite@chgf.vu.lt (G. Inkrataite).

https://doi.org/10.1016/j.jallcom.2023.171634
Received 14 June 2023; Received in revised form 27 July 2023; Accepted 2 August 2023
Available online 3 August 2023

Table 1
Synthesized powder sample list.

$Lu_3Al_5O_{12}$ (LuAG)	$Lu_3Al_4Sc_1O_{12}$ (LuASG)	$Gd_3Al_3Sc_2O_{12}$ (GdASG)
LuAG:1 %Ce	LuASG:1 %Ce	GdASG:1 %Ce
LuAG:1 %Ce,5 %B	LuASG:1 %Ce,3 %B	GdASG:1 %Ce,1 %B
	LuASG:1 %Ce,5 %B	GdASG:1 %Ce,3 %B
		GdASG:1 %Ce,5 %B

shorten the decay time, increase emission intensity, and improve the physical properties of garnets. This is especially important in gadolinium aluminum garnets since this garnet type is not very stable and is often accompanied by impurity phases. It will only be obtained as single phase if the composition is modified in such a way that Al^{3+} is partially replaced by Sc or other trivalent ions [13–15].

The main goal of the present work was to synthesize garnets with a new composition, which would exhibit a shorter decay time than the base compounds, while maintaining excellent luminescent properties. As such in this work Ce^{3+} and different amount of B^{3+} doped $Lu_3Al_5O_{12}$, $Lu_3Al_4Sc_1O_{12}$ and $Gd_3Al_3Sc_2O_{12}$ garnet powders were synthesized. All samples were calcinated under air atmosphere at a temperature of 1200 ℃ to avoid impurity phases. Phase purity and luminescent properties were investigated in detail.

2. Experimental section

2.1. Synthesis procedure

Lutetium or gadolinium aluminum scandium garnet powders were synthesized by the aqueous sol-gel method. Cerium concentration was kept at 1 % for all samples. While boron ions were introduced into the garnet lattice at different contents. All synthesized powder compounds are listed in the Table 1.

Nominal formulas of synthesized samples are as follows: $Lu_{2,97}Al_{5-x}O_{12}:Ce_{0,03},B_x$, $Lu_{2,97}Al_{4-x}Sc_1O_{12}:Ce_{0,03},B_x$, $Gd_{2,97}Al_{3-x}Sc_2O_{12}:Ce_{0,03},B_x$. For these compounds Lu_2O_3 (99.9 % Alfa Aesar) or Gd_2O_3 (99.9 % Aldrich), Sc_2O_3 (99.9 % ThermoFisher), $Al(NO_3)_3{\cdot}9\ H_2O$ (99.999 % Alfa Aesar), $(NH_4)_2Ce(NO_3)_6$ (99.5 % Roth), H_3BO_3 (99.5 % Chempur) were used as precursors. Firstly, Gd_2O_3 or Lu_2O_3 and Sc_2O_3 were dissolved in an excess of concentrated nitric acid at 50 ℃. Then, acid was evaporated, and the remaining gel was washed with distilled water 2–3 times, followed by further evaporation of added water. An additional 50 ml of H_2O was added and $Al(NO_3)_3{\cdot}9\ H_2O$, $(NH_4)_2Ce(NO_3)_6$, H_3BO_3 were dissolved. The solution was left under magnetic stirring for 2 h at 50 – 60 ℃. After that, citric acid was added to the solution, and it was left to stir overnight. The solution was then evaporated and obtained gels were dried at 140 ℃ for 24 h in a drying furnace. The obtained powders were ground and firstly calcinated at 1000 ℃ for 2 h in air, with a 5 K/min heating pace, secondly the same powders were heated in a muffle furnace at 1200 ℃ for 4 h under air with 5 K/min heating pace [11,16]. The synthesis scheme is shown in Fig. 1.

2.2. Characterization

X-ray diffraction (XRD) analysis: A Rigaku MiniFlex II X-ray diffractometer was used for the analysis of the powder samples. Powders were pressed into a glass sample holder. Diffraction patterns were recorded in the 2θ range from 15° to 80° for all compounds. Cu-$K_{\alpha 1}$ radiation (λ = 1.5418740 Å) was used for analysis. Measurement parameters: current was 15 mA, voltage – 30 kV, X-ray detector movement step – 0.010°, dwell time – 5.0 s

Quantification of B in the synthesized species was performed by inductively coupled plasma optical emission spectrometry (ICP-OES) using Perkin-Elmer Optima 7000 DV spectrometer (Perkin-Elmer, Walthman, MA, USA). The powders were dissolved in concentrated nitric acid (HNO_3, Rotipuran® Supra 69 %, Roth) in a beaker and diluted to an appropriate volume with deionized water. Calibration solutions were prepared by dilution of the stock standard solution (single-element ICP standard, 1000 mg/L, Roth).

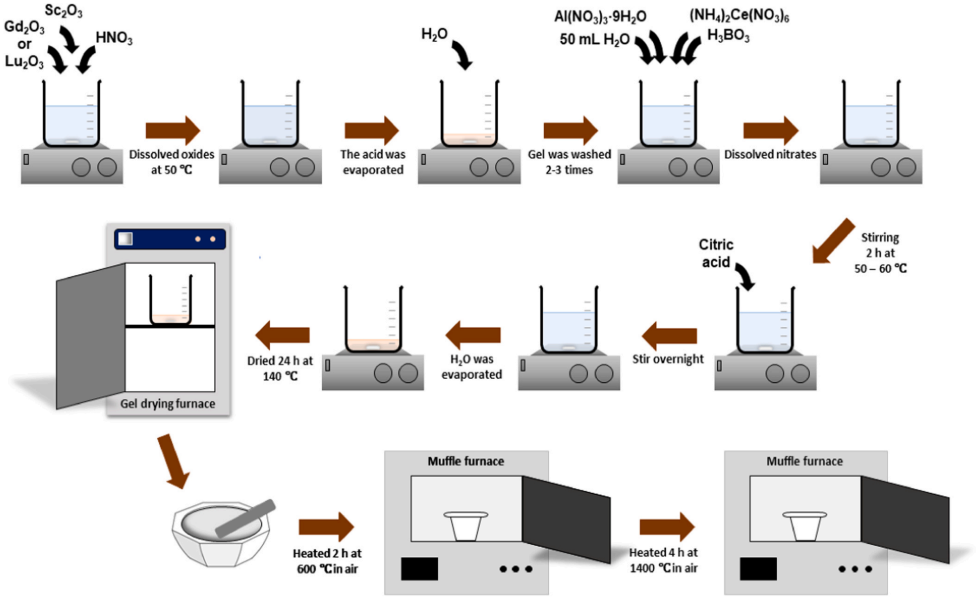

Fig. 1. Scheme of sol-gel synthesis of the respective garnets.

Table 2
Boron content in % in GdASG samples measured by ICP-OES.

Sample	Amount of boron (weighed in)	Amount of boron (determined)
$Gd_3Al_3Sc_2O_{12}$:1 %Ce	0 %	0 %
$Gd_3Al_3Sc_2O_{12}$:1 %Ce,1 %B	1 %	0.9 %
$Gd_3Al_3Sc_2O_{12}$:1 %Ce,3 %B	3 %	2.3 %
$Gd_3Al_3Sc_2O_{12}$:1 %Ce,5 %B	5 %	3.5 %

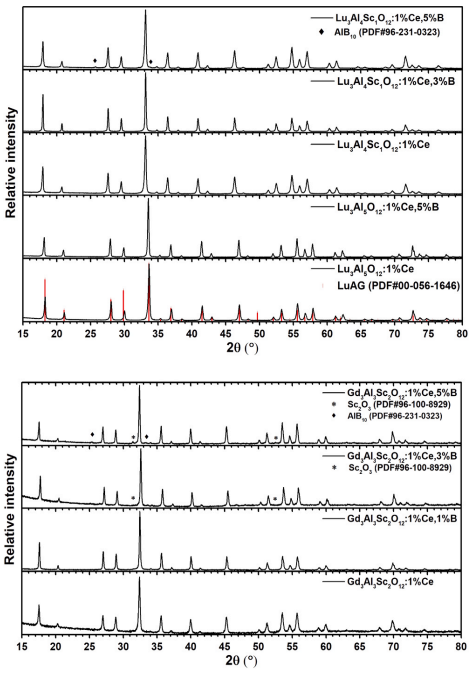

Fig. 2. Diffraction patterns of $Lu_3Al_5O_{12}$, $Lu_3Al_4Sc_1O_{12}$ (above) and $Gd_3Al_3Sc_2O_{12}$ (below) doped with 1 % of cerium and different concentrations of boron.

Particle morphology measurements: For the investigation of the particle shape, a scanning electron microscope was used. Respective photographs were taken using a Hitachi SU-70 scanning electron microscope. The particle sizes of the prepared materials were measured using the dynamic light scattering method with Horiba LA-950-V2 organic device.

Reflection spectroscopy: Edinburgh Instruments FL920 spectrometer was used for these measurements. Spectrometer was equipped with an integration sphere, which was coated by the white polymer Spectralon®. An ozone free 450 W xenon arc lamp was using as light source. Two S300 monochromators (Czerny-Turner Optics) with 1800 F/mm gratings and a photomultiplier tube R928 (Hamamatsu) were used in the spectrometer in synchronous scan mode The photomultiplier tube was cooled to −20 °C by using Peltier elements. Reflection spectra were measured between 250 and 800 nm. $BaSO_4$ (99.99 %, Sigma-Aldrich) was used as a standard.

Photoluminescence spectroscopy Edinburgh Instruments FLS980 spectrometer equipped with excitation and emission monochromators and 450 W Xe arc lamp, and single-photon counting photomultiplier tube (Hamamatsu R928P) which was cooled to −20 °C. Obtained photoluminescence emission spectra were corrected using a correction file obtained from a tungsten incandescent lamp certified by NPL (National Physics Laboratory, UK). Excitation spectra were corrected by a reference detector.

Determination of the quantum efficiency: Quantum yield like reflection spectra were measured by using an Edinburgh Instruments FL920 spectrometer with an integration sphere coated by the white polymer Spectralon®. External quantum efficiencies (EQE) were calculated by comparing the emission spectrum of the $BaSO_4$ sample (99.99 %, Sigma-Aldrich). The EQE values were obtained calculated with the following formula 1 [11,17]:

$$EQE = \frac{\int I_{em,sample} - \int I_{em,BaSO_4}}{\int I_{ref,BaSO_4} - \int I_{ref,sample}} \times 100\% = \frac{N_{em}}{N_{abs}} \times 100\% \quad (1)$$

where $\int I_{em,sample}$ and $\int I_{em,BaSo4}$ are integrated emission intensities of the phosphor sample and $BaSO_4$, respectively. $\int I_{ref}$, and $\int I_{ref,4}$ are the integrated reflectance of the phosphor sample and $BaSO_4$, respectively. N_{em} and N_{abs} stand for the number of emitted and absorbed photons.

Temperature resolved spectroscopy: Measurements were performed using Edinburgh Instruments FLS920 spectrometer, with an ozone generating 450 W Xe lamp (Osram AG) and a single-photon counting photomultiplier tube (Hamamatsu R928) which was cooled to −20 °C. Analysis in the temperature range from 77 to 500 K was used and recorded by using a liquid nitrogen cooled cryostat (Oxford Instruments MicrostatN2).

Time resolved spectroscopy: Decay kinetics of the powder samples were measured using the same Edinburgh Instruments FLS920 spectrometer. For photoluminescence decay time measurements, a 450 nm

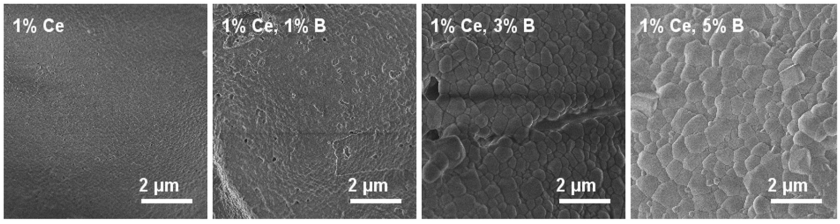

Fig. 3. SEM images of 1 % Ce^{3+} and different amounts of B^{3+} doped $Gd_3Al_3Sc_2O_{12}$ garnet powder samples (magnification = 2.5 k.).

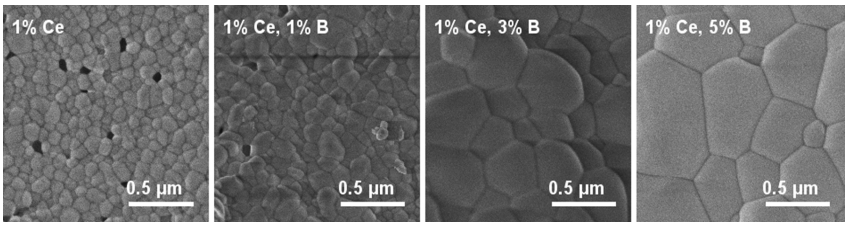

Fig. 4. SEM images of 1 % Ce^{3+} and different amounts of B^{3+} doped $Gd_3Al_3Sc_2O_{12}$ garnet powder samples (magnification = 20 k.).

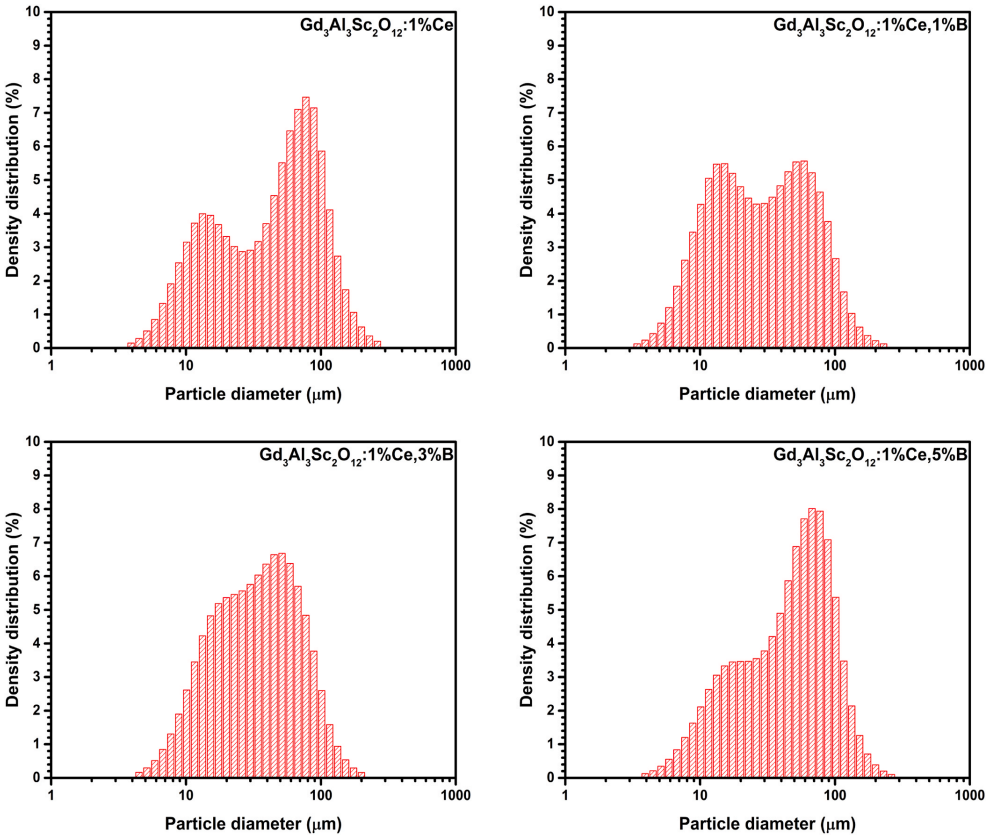

Fig. 5. Particle size histograms of 1 % Ce^{3+} and different amounts of B^{3+} doped $Gd_3Al_3Sc_2O_{12}$ garnet powder samples.

laser was used as an excitation source.

Radioluminescence spectroscopy: An Edinburgh Instruments FLS980 spectrometer equipped with a photomultiplier tube (PMT, Hamamatsu R928P) which is cooled to −20 °C by Peltier elements was used. X-ray analysis Oxford Instruments Neptune 5200 tube was used as an X-ray radiation source.

3. Results and discussion

3.1. ICP-OES analysis

The boron content in gadolinium aluminum scandium garnets was determined by using ICP-OES and the results are listed in Table 2. In all samples, the measured boron amount was slightly smaller than the calculated amounts used for the synthesis. This trend is expressed more

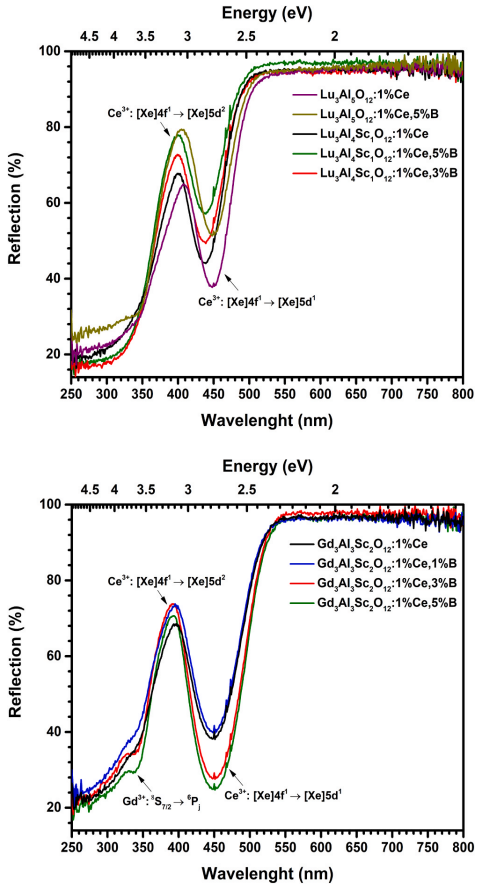

Fig. 6. Reflection spectra of 1 % cerium and different amounts of boron doped $Lu_3Al_5O_{12}$, $Lu_3Al_4Sc_1O_{12}$ (above) and $Gd_3Al_3Sc_2O_{12}$ (below).

in the compounds with higher total boron amount values (samples with 3 % and 5 % of Boron).

3.2. X-ray diffraction

To determine the phase purity of powder garnet samples X-ray diffraction analysis was performed. Lutetium aluminum garnet sample purity was checked based on Powder Diffraction File, (PDF) #00–056–1646. The purity of gadolinium aluminum scandium garnet is checked based on the same structure since no material PDF card of this garnet was found. The diffraction patterns show (Fig. 2) that garnets containing less than 3 % of boron (except LuAG) have a pure garnet phase, regardless of whether doped with Ce^{3+} ions or not. Lutetium or gadolinium aluminum scandium garnet compounds with more boron contain aluminum borate AlB_{10} ((PDF) #96–231–0323) impurities. The reflections attributed to these impurities are marked with a ◆ sign in the XRD patterns. When increasing the boron amount in gadolinium aluminum scandium garnets, impurities of scandium oxide Sc_2O_3 ((PDF) #96–100–8929) are also observed in the samples. Sc_2O_3 phase is marked with a * sign. From the given diffraction patterns, it could be said that the increasing amount of boron, leads to a rise in intensity and number of reflections that are ascribed to the impurities phase. As is commonly know the ionic radius of Gd^{3+} (1.08 Å) is larger than that of Lu^{3+} (0.98 Å) ions [18]. We can also observe this difference in ionic size in the diffractograms, as they show a shift to smaller angle values when gadolinium ions are present in the garnet lattice. Low amounts of cerium and boron ions do not significantly affect the peak position [19]. In summary from the measured data, it can be said that synthesized garnets could be doped with no additional impurity phase formation in LuAG with up to 5 % of boron. In lutetium or gadolinium aluminum scandium garnets the single-phase compounds are only obtained up to 3 % of boron.

3.3. Particles morphology analysis

Scanning electron microscopy (SEM) images were taken to determine the morphology of the garnet powders. All samples were imaged at different magnifications (2.5 k and 20 k). Lower magnification images show the overall size of the particles, while the higher magnification images reveal individual particles, porosity, arrangement, and shape. While analyzing the obtained results, all samples, regardless of the composition have similar morphological characteristics. This is mainly reflected in the particle shape, porosity, and particle arrangement, while in the case of particle size, significant differences were observed. These characteristics were most likely determined by chemical composition, synthesis procedure, and doping with B^{3+} ions. Fig. 3 displays images of cerium and different amount of boron doped gadolinium aluminum scandium garnet. All compounds have irregularly shaped interconnected particles, between which no significant porosity is observed. However, the particle size changes when compounds are co-doped with boron. The higher the boron content is used during the garnet synthesis, the larger the particle size is observed. These changes can be explained by the fact that boron can act as a flux. Since the melting point of boric acid used in the synthesis is 170 °C. Furthermore, boron most likely lowers the melting point of garnet. As a result, when heated at the same temperatures, garnets doped with a higher amount of boron show accelerated grain growth. For these reasons, larger garnet particles are obtained [20]. As can be seen from Fig. 4 as the boron content in the compounds increases, the porosity of the samples decreases. In boron-free garnets, relatively high porosity is observed, which disappears when samples are doped with 5 % of boron. This change can also be explained by boron acting as a flux and thus increasing grain growth.

The particle size distribution of the garnet samples was recorded by using the "Horiba LA-950-V2 organic" device. Histograms of particle size distribution are depicted in Fig. 5 and the supplementary material (Figure SM1). From the presented data, particle size correlates with the data obtained from the SEM images. Increasing the amount of boron in the samples increases the particle size. While the particle size of the samples with 1 % of boron changes only slightly. The average particle size of garnet containing 5 % B^{3+} increases much more to 60 μm, while the particle size of garnet without boron is about 50 μm. The same trend regards to particle sizes is observed in other histograms in the supplementary file.

3.4. Luminescence properties

The operation mechanism of scintillators is based on the high energy conversion to visible light in the form of luminescence. In this case, the photo and radio luminescent properties are determined by the presence of cerium ions in the composition of garnets. Ce^{3+} ions are characterized by interconfigurational electron transitions between the $[Xe]5d^1$ and $[Xe]4\ f^1$ configuration with light emitted in the green to yellow spectral range [21]. The luminescence properties were the main indicator which was sought to be modified, by adjusting the materials in such a way that they could be most applicable as scintillators.

Cerium doped garnets are among the most popular materials used in

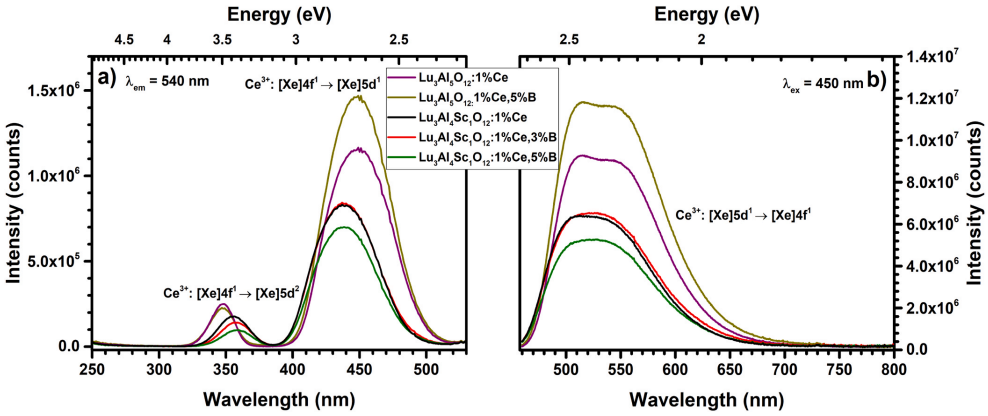

Fig. 7. a) Excitation and b) emission spectra of 1 % cerium and different amounts of boron doped $Lu_3Al_5O_{12}$ and $Lu_3Al_4Sc_1O_{12}$.

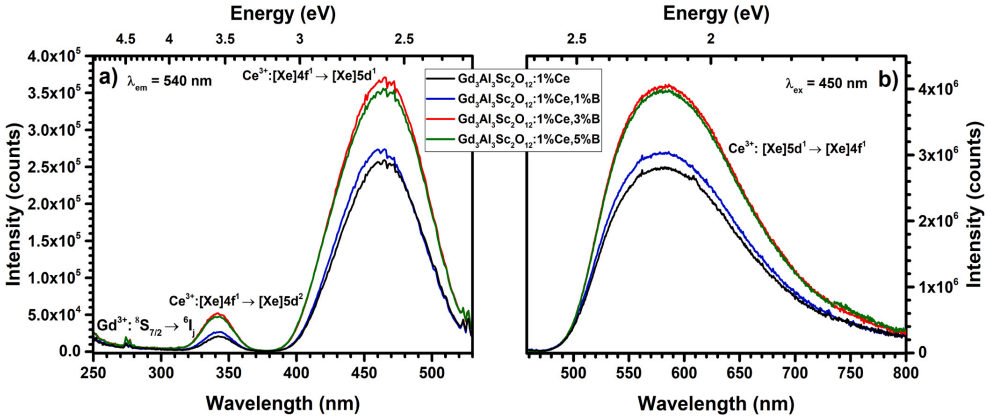

Fig. 8. a) Excitation and b) emission spectra of 1 % cerium and different amounts of boron doped $Gd_3Al_3Sc_2O_{12}$.

scintillation physics [22]. The reflection spectra of the synthesized lutetium aluminum and gadolinium aluminum garnets doped with scandium, cerium, and boron are shown in Fig. 6. It can be also noted that doping with other ions affects absorption strength, this is also observed when doping with B^{3+} and Sc^{3+} ions. However, scandium also causes the absorption band to red shift from 430 to 450 nm [23]. Similar trends are observed for the gadolinium garnets. In this case, it is not possible to estimate the shift due to scandium ions, since the compound without scandium is not stable in bulk form. However, B^{3+} influences the absorption strength. As the boron content increases, absorption becomes stronger. Electron transitions characteristic of Ce^{3+} can be observed, however, additionally, characteristic transitions of Gd^{3+} can also be observed at 340 nm and are identified as the intraconfigurational transitions $^8S_{7/2} \rightarrow {}^6P_j$. These transitions are not present in Lu based garnet samples because of the lack of Gd^{3+} [24].

Figs. 7 and 8 show excitation and emission spectra of different compounds measured at room temperature. Emission spectra were measured using 450 nm exciting wavelength. From these graphs, it can be seen that 5d^1 and 4 f^1 electron transitions are observed in both the excitation and emission spectra [25]. As was already observed from the reflection spectra, LuAG samples (Fig. 7) show the same tendency, when garnet was doped with Sc^{3+} the emission and excitation spectra shifted to lower energy waves and the intensity of the spectra decreased [23]. In this case, boron does not have a significant effect on the emission intensity, but a small amount of it does not reduce the intensity as well. However, a larger amount reduces the intensity. XRD showed that the compounds with higher boron content show AlB_{10} impurities that could be responsible for the reduction in intensity. Other possible explanation for effect of boron on luminescence intensity is that B^{3+} can cause additional defects in lutetium or gadolinium phosphors. Although equivalent substitution of Al^{3+} and B^{3+} ions occur in matrix, defects that appear to compensate for the ionic charge cannot form because the ionic charges are the same and equal to 3 + . However, the B^{3+} radius is much smaller than the Al^{3+} ion in tetrahedral and octahedral coordination and the irregularity of the coordination polyhedron of the dopant site can increase, which causes an exceptionally large increase in local strain. This strain could be partially reduced by the formation of trigonal-planar moieties of [BO_3], which tend to then form oxygen vacancies and thus finally decreases the emission intensity [26]. The emission spectra also show two peaks, which are specific to cerium doped garnets, as they

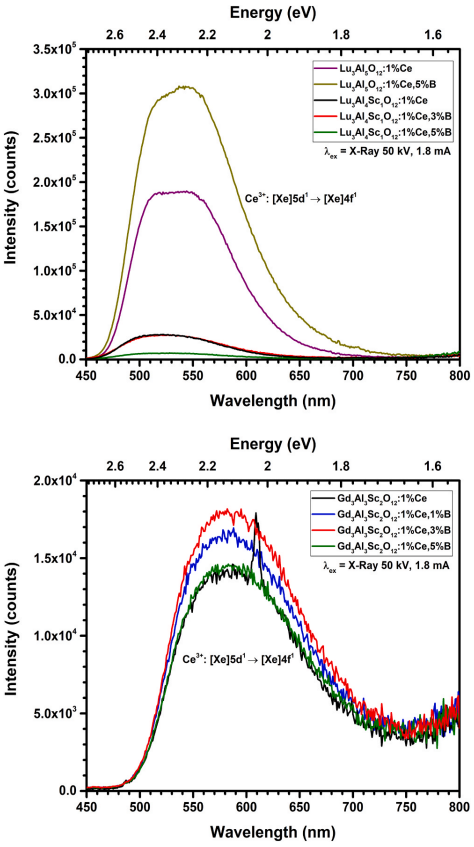

Fig. 9. Emission spectra of 1 % cerium and different amounts of boron doped $Lu_3Al_5O_{12}$, $Lu_3Al_4Sc_1O_{12}$ (above) and $Gd_3Al_3Sc_2O_{12}$ (below) under X-ray excitation.

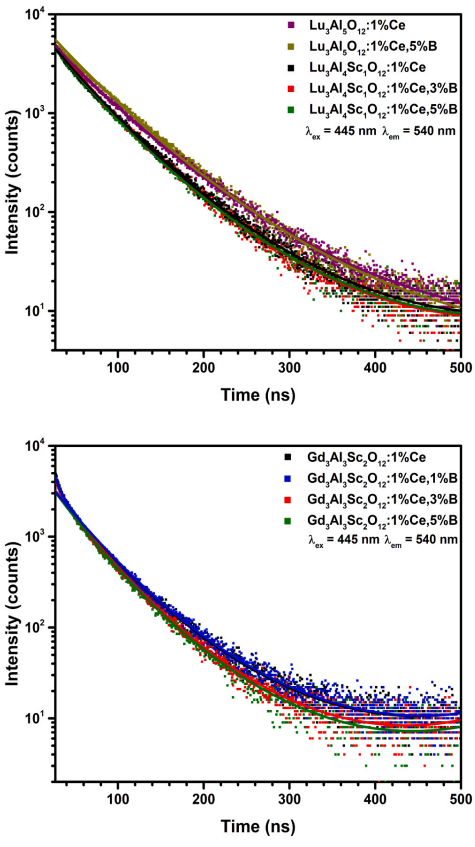

Fig. 10. Decay curves of 1 % cerium and different amounts of boron doped $Lu_3Al_5O_{12}$, $Lu_3Al_4Sc_1O_{12}$ (above) and $Gd_3Al_3Sc_2O_{12}$ (below).

Table 3
Synthesized samples decay time and quantum efficiency.

Sample	Decay time [ns]	Chi^2 values	Quantum efficiency [%]
$Lu_3Al_5O_{12}$:1 %Ce	60.6 ± 0.1	1.242	39
$Lu_3Al_5O_{12}$:1 %Ce,5 %B	58.8 ± 0.1	1.106	59
$Lu_3Al_4Sc_1O_{12}$:1 %Ce	54.9 ± 0.1	1.172	31
$Lu_3Al_4Sc_1O_{12}$:1 %Ce,3 %B	53.1 ± 0.1	1.245	35
$Lu_3Al_4Sc_1O_{12}$:1 %Ce,5 %B	54.0 ± 0.1	1.142	33
$Gd_3Al_3Sc_2O_{12}$:1 %Ce	50.8 ± 0.2	1.170	12
$Gd_3Al_3Sc_2O_{12}$:1 %Ce,1 %B	49.6 ± 0.2	1.168	13
$Gd_3Al_3Sc_2O_{12}$:1 %Ce,3 %B	46.8 ± 0.2	1.127	15
$Gd_3Al_3Sc_2O_{12}$:1 %Ce,5 %B	46.6 ± 0.2	1.137	14

indicate two different electronic transitions, which are the inter-configurational transitions $^5D \rightarrow {}^4F_{5/2}$ at higher energy and $^5D \rightarrow {}^4F_{7/2}$ at lower energy [25].

Emission and excitation spectra of gadolinium aluminum scandium garnet samples are plotted in Fig. 8. An $^8S_{7/2} \rightarrow {}^6I_j$ electron transition at 260 nm, which is attributed to Gd^{3+}, is additionally visible in the excitation spectra [27]. In contrast to LuAG, boron has an obvious influence on the intensity of these luminescence spectra. From the emission and excitation spectra, it can be derived that compounds doped with 5 % and especially 3 % B^{3+} show the highest intensities, while the boron free compound shows the lowest. From the SEM data, it is known that compounds with more boron have larger particles. The particle growth was likely responsible for the increase in intensity, due to the lower surface area to volume ratio resulting in less surface quenching and thus

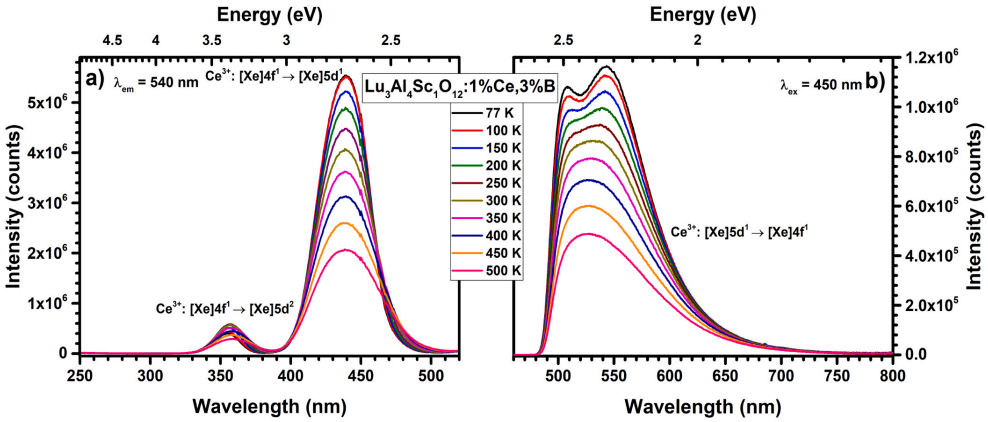

Fig. 11. Temperature dependent excitation (left) and emission (right) of 1 % cerium and 3 % boron doped $Lu_3Al_4Sc_1O_{12}$.

higher PL intensity [28,29]. In this case, it can also be observed that the emission maximum is red-shifted towards 580 nm. This shift can be explained by the different covalency of these compounds, which results from the different electronegativity of constituent atoms [30].

To find out how effective the synthesized materials are as scintillators, radioluminescence emission measurements were also performed for all samples. All cerium and boron doped lutetium and gadolinium aluminum scandium garnets were excited with X-rays (50 kV, 1.8 mA). From the above part of Fig. 9, lutetium garnets without scandium have a more intense emission. This was to be expected since the scandium extinguishes the intensity of the emission [31]. However, garnet doped with 5 % of boron has the most intense emission characteristic of cerium ions [Xe]5d^1 → [Xe]4 f^1 with maxima at a wavelength of 550 nm. The emission intensity of this sample is as much as 1.5 times higher than that of the boron-free sample. This, as in the case of photoluminescence, can be explained by the different particle sizes [28,29]. An additional peak at around 685 nm can be attributed to the photoluminescence of a Cr^{3+} impurity, which was most likely caused due to the use of chromium containing aluminum nitrate as a starting material. The emission of these ions when excited by X-rays is relatively strong, so impurity is very clearly visible even at extremely low content. This is quite a common occurrence and the low content of impurities can be confirmed due to the fact that these emission peaks are not observed under regular excitation conditions (Fig. 7) [32]. The bottom graph of Fig. 9 shows the emission spectra of cerium and boron doped gadolinium aluminum scandium garnets. From these spectra, it can be seen that boron increases the intensity of the emission like in LuAG samples. The most intense emission was observed for garnet doped with 3 % of boron, and the least intense emission for the boron-free garnet. This garnet indeed has an additional peak at approximately 608 nm, however, this is an artifact stemming from the measurement procedure and not a property of the sample. From the results of the radioluminescence emission spectra, it can be concluded that the addition of boron has a large and important influence on the compounds that are used for excitation with X-rays. In this case, boron ions increase the intensity of radioluminescence emission.

Ce^{3+} activated garnets have a decay time in the ns range [25]. In this case, the same trend is obtained. The measured decay times of the compounds and the B^{3+} influence of these values are shown in Table 3. The decay times of the synthesized samples range from 60 to 46 ns. It should be noted that in this synthesized series, the decay times of lutetium aluminum garnet are slightly shorter than the usual ones mentioned in other sources, where they equal to 68 ns [33]. In this case, lutetium aluminum garnet doped only with cerium boron has the longest decay time, which is 60.6 ns. Increasing the boron content and adding scandium shortens the decay time. Lutetium garnet doped with scandium and 3 % boron, most likely due to the formation recombination centers has the shortest decay, equaling 53.1 ns [31]. As expected, the decay time of gadolinium aluminum scandium garnets is shorter than that of lutetium garnets [34]. It can be seen from Table 3 that increasing the amount of boron in the compounds decreases the decay time. The decay time is even 4.2 ns shorter for the compound doped with 5 % of boron compared to the compound without boron. This decrease in decay when doping compound with boron can be also explained by the fact that boron has a higher electronegativity than aluminum. The decrease in decay time may be related to the polarization of the local activator ion environment. Therefore, when the electronegativity of the activator ions increases, the polarization decreases and the decay times become shorter [25]. Fig. 10 and supplementary material (Figs. SM5, SM6) shows the decay curves of the samples. It is clear from the figure that all the compounds exhibit decay curves that are characteristic of cerium-doped garnets.

Table 3 also shows the quantum efficiency values of the compounds. Lutetium aluminum garnets exhibit higher EQE values than gadolinium aluminum scandium garnets. A significant difference can again be seen due to the addition of boron to the compounds. Boron increases the quantum efficiency of the compounds. For LuAG, the EQE increases by more than 19 %. The corresponding change is also seen in gadolinium garnets, although it is smaller. However, it can be observed that garnets containing scandium doped with 5 % of boron have a lower EQE value. This can be explained by the appearance of impurities, which are confirmed by X-ray diffraction analysis. Additionally, the color of the sample with impurities is greyer as compared to materials without impurities. Furthermore, compounds doped with larger amounts of B^{3+} have more defects that absorb part of the photons falling on the sample. This is reducing in the amount of photons absorbed and emitted by the desired phase [35]. Nevertheless, it can be said that boron has a significant positive effect on the quantum yield.

The photoluminescence emission and excitation spectra of the synthesized samples were also recorded at different temperatures between 77 and 500 K. Measurements at different temperatures were performed for the following four samples: $Lu_3Al_5O_{12}$:1 %Ce; $Lu_3Al_5O_{12}$:1 %Ce,5 % B; $Lu_3Al_4Sc_1O_{12}$:1 %Ce, and $Lu_3Al_4Sc_1O_{12}$:1 %Ce,3 %B. Fig. 11 shows the spectra of the $Lu_3Al_4Sc_1O_{12}$:1 %Ce,3 %B compound. Spectra of other samples are shown in the supplementary material, viz. by figures SM2 and SM3. Fig. 11 shows that the sample, regardless of temperature,

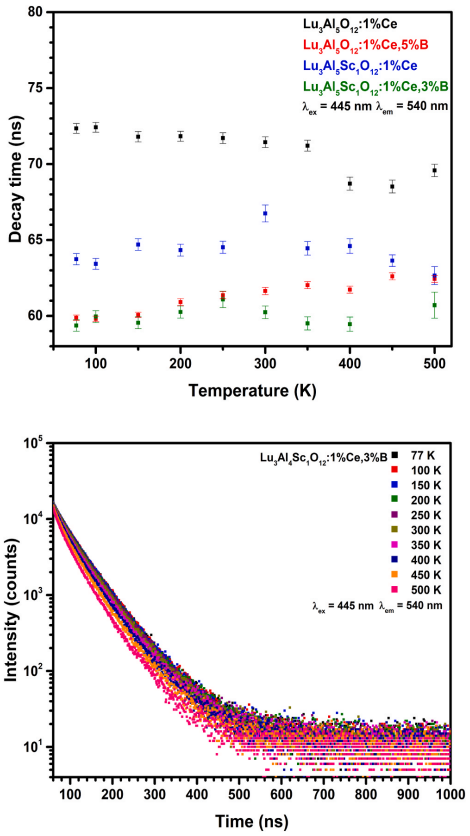

Fig. 12. Temperature dependent decay time values of 1 % cerium and different amounts of boron doped $Lu_3Al_5O_{12}$ and $Lu_3Al_4Sc_1O_{12}$ samples (above) and the decay curves of $Lu_3Al_4Sc_1O_{12}$:1 %Ce, 3 %B (below).

contains electron transitions characteristic to that of cerium ions. The intensities of both emission and excitation peaks decrease with increasing temperature. From Fig. 11 (left), all samples have electron transitions from 4 f^1 to 5d^1 (at 353 nm) and 5d^2 (at 438 nm) orbitals. From Fig. 11 (right), the emission of cerium ions varies with temperature. At low temperatures, especially at 77 K, Ce^{3+} shows a double band structure emission at 517 and 541 nm. These two bands are attributed to interconfigurational transitions between states of the [Xe]5d^1 and the [Xe]4 f^1 configuration, while the latter is composed of the spin-obit split $^2F_{5/2}$ and $^2F_{7/2}$ ground state terms. As the temperature increases, the splitting between the two emission bands decreases and they finally merge. Such emission band peaks at 520 nm, which was already observed for room temperature measurements [25]. The same trend of variation in the intensities of the excitation and emission spectra of cerium ions is observed in the supplementary material for other samples as well. As the temperature increases, the intensity of the spectra decreases, and the emission spectrum bands merge into one.

Decay times at different temperatures were also recorded for all four samples. Fig. 12 shows the profiles of the decay curves of $Lu_3Al_4Sc_1O_{12}$:1 %Ce,3 %B (decay curves of the three other samples are presented in the supplementary material) and the temperature dependent values of the decay times. It turns out that the curves are single exponential and follow the profiles typical of Ce^{3+} ions [36]. From Fig. 12 decay times values of compounds with B^{3+} (red and green) are shorter as compared to ones without boron. Furthermore, the decay time values are almost not affected by different temperatures. However, in the case when inspecting different temperatures, a discrete trend cannot be observed, as in some cases it leads to a reduction in others it shows an increase. The results are thus rather scattered and show no clear trend, unfortunately.

4. Conclusions

Cerium doped lutetium/gadolinium aluminum garnets co-doped by scandium and different amounts of boron were synthesized by a wet-chemical sol-gel method. Samples containing up to 3 % of boron (except for LuAG) do not show impurity phases. From the ICP-OES measurements, it was determined that the amount of boron in these compounds is quite close to the theoretical values. SEM and particle size analyses confirm that boron acts also as a flux, i.e. if the boron content is increased the particle size increases. This is especially predominant in the gadolinium-based garnets with larger particles, a higher efficiency of photoluminescence is observed and as such it could be concluded that boron has a positive effect on the emission intensity. The most intense radioluminescence emission was obtained for the LuAG:1 %Ce,5 %B sample. Furthermore, the introduction of boron into the samples, led to an overall decrease in decay times and most cases to an increase in EQE. Only noticeable exceptions were observed for $Lu_3Al_4Sc_1O_{12}$:1 %Ce,5 %B wherein decay time increased and EQE decreased as compared to sample doped with just 3 % of boron, and $Gd_3Al_3Sc_2O_{12}$:1 %Ce,5 %B EQE also decreased as compared to the sample with just 3 % of boron. The observed decay time changes could be explained by the fact that B^{3+} has higher electronegativity than aluminum ions and such a stronger polarization effect induces a higher polarized local environment. If the samples comprise scandium in the garnet structure, the decay times become shorter as well. However, the quantum efficiency is only slightly reduced.

CRediT authorship contribution statement

Greta Inkrataite – Conceptualization, Methodology, Software, Formal analysis, Investigation, Resources, Data Curation, Writing – Original Draft, Visualization. **Jan-Niklas Keil** – Conceptualization, Validation, Methodology, Software, Writing – Review & Editing. **Aleksej Zarkov** – Data Curation, Resources, Writing – Review & Editing. **Thomas Jüstel –** Conceptualization, Software, Resources, Data Curation, Writing – Review & Editing, Supervision. **Ramunas Skaudzius** – Conceptualization, Methodology, Software, Investigation, Resources, Data Curation, Writing – Review & Editing, Supervision.

Declaration of Competing Interest

The authors declare that they have no known competing financial interests or personal relationships that could have appeared to influence the work reported in this paper.

Data Availability

The data that has been used is confidential.

Appendix A. Supporting information

Supplementary data associated with this article can be found in the online version at doi:10.1016/j.jallcom.2023.171634.

References

[1] M. Teimoorisichani, V. Panin, H. Rothfuss, H. Sari, A. Rominger, M. Conti, A CT-less approach to quantitative PET imaging using the LSO intrinsic radiation for long-axial FOV PET scanners, Med. Phys. 49 (2022) 309–323, https://doi.org/10.1002/MP.15376.

[2] J.C.G. Bünzli, Rising stars in science and technology: luminescent lanthanide materials, Eur. J. Inorg. Chem. 2017 (2017) 5058–5063, https://doi.org/10.1002/EJIC.201701201.

[3] J. Ling, W. Xu, J. Yang, T. Mu, Y. Zhang, Y. Zhou, M. Hong, The effect of Lu^{3+} doping upon YAG:Ce phosphor ceramics for high-power white LEDs, J. Eur. Ceram. Soc. 41 (2021) 5967–5976, https://doi.org/10.1016/J.JEURCERAMSOC.2021.05.005.

[4] J.W. Cates, C.S. Levin, Evaluation of a clinical TOF-PET detector design that achieves 100 ps coincidence time resolution, Phys. Med. Biol. 63 (2018), https://doi.org/10.1088/1361-6560/aac504.

[5] X. Qiu, Z. Luo, J. Zhang, H. Jiang, J. Jiang, Mechanical properties and machinability of GYGAG:Ce ceramic scintillators, Ceram. Int. 46 (2020) 4550–4555, https://doi.org/10.1016/j.ceramint.2019.10.183.

[6] W. Chewpraditkul, L. Swiderski, M. Moszynski, T. Szczesniak, A. Syntfeld-Kazuch, C. Wanarak, P. Limsuwan, Scintillation properties of LuAG:Ce, YAG:Ce and LYSO:Ce crystals for gamma-ray detection, : IEEE Trans. Nucl. Sci. 56 (2009) 3800–3805, https://doi.org/10.1109/TNS.2009.2033994.

[7] L. Pan, B. Jiang, J. Fan, P. Zhang, X. Mao, L. Zhang, Co-precipitation synthesis of lutetium aluminum garnet (LuAG) powders: The influence of ethanol, Opt. Mater. (Amst.). 71 (2017) 50–55, https://doi.org/10.1016/j.optmat.2016.06.020.

[8] P. Schauer, O. Lalinský, M. Kučera, Overview of S(T)EM electron detectors with garnet scintillators: some potentials and limits, Microsc. Res. Tech. 84 (2021) 753–770, https://doi.org/10.1002/JEMT.23634.

[9] C. Foster, M. Koschan, Y. Wu, C.L. Melcher, Boron codoping of Czochralski grown lutetium aluminum garnet and the effect on scintillation properties, J. Cryst. Growth 486 (2018) 126–129, https://doi.org/10.1016/j.jcrysgro.2018.01.028.

[10] R. Baba, A. Yoneyama, M. Kawamoto, Quantitative analysis of the physical properties of CsI, GAGG, LuAG, CWO, YAG, BGO, and GOS scintillators using 10-, 20- and 34-keV monochromated synchrotron radiation, Opt. Mater. Express 11 (2021) 398–411, https://doi.org/10.1364/OME.409161.

[11] G. Inkrataite, M. Kemere, A. Sarakovskis, R. Skaudzius, Influence of boron on the essential properties for new generation scintillators, J. Alloys Compd. 875 (2021), 160002, https://doi.org/10.1016/j.jallcom.2021.160002.

[12] T. Yang, C.M.R. de Almeida, D. Han, L. Meng, J. Deng, E.L. da Silva, M.C. Santos, S. Shi, Hydrothermal synthesis and optimization of boron doped $LiZr_2(PO_4)_3$ Li-ion solid electrolyte, Appl. Surf. Sci. 474 (2019) 250–255, https://doi.org/10.1016/j.apsusc.2018.02.158.

[13] S.V. Kuznetsov, V.S. Sedov, A.K. Martyanov, S.C. Batygov, D.S. Vakalov, K. N. Boldyrev, I.A. Tiazhelov, A.F. Popovich, D.G. Pasternak, H. Bland, S. Mandal, O. Williams, M.S. Nikova, V.A. Tarala, Cerium-doped gadolinium-scandium-aluminum garnet powders: synthesis and use in X-ray luminescent diamond composites, Ceram. Int. 48 (2022) 12962–12970, https://doi.org/10.1016/J.CERAMINT.2022.01.169.

[14] K. Wantong, W. Chewpraditkul, W. Chewpraditkul, M. Rathaiah, M. Kucera, S. Danis, A. Beitlerova, R. Kucerkova, M. Nikl, Optical, luminescence and scintillation characteristics of $Gd_3Sc_2(Al_{3-x}Ga_x)O_{12}$: Ce,Mg (x = 0, 1, 2) single crystalline films, Opt. Mater. (Amst.). 134 (2022), 113240, https://doi.org/10.1016/J.OPTMAT.2022.113240.

[15] J. Li, J.G. Li, Z. Zhang, X. Wu, S. Liu, X. Li, X. Sun, Y. Sakka, Gadolinium aluminate garnet ($Gd_3Al_5O_{12}$): Crystal structure stabilization via lutetium doping and properties of the $(Gd_{1-x}Lu_x)_3Al_5O_{12}$ solid solutions (x = 0-0.5), J. Am. Ceram. Soc. 95 (2012) 931–936, https://doi.org/10.1111/J.1551-2916.2011.04991.X.

[16] G. Inkrataite, A. Zabiliute-Karaliune, J. Aglinskaite, P. Vitta, K. Kristinaityte, A. Marsalka, R. Skaudzius, Study of YAG: Ce and polymer composite properties for application in LED devices, Chempluschem 85 (2020) 1504–1510, https://doi.org/10.1002/cplu.202000318.

[17] J. Grigorjevaite, A. Katelnikovas, Luminescence and luminescence quenching of $K_2Bi(PO_4)(MoO_4):Eu^{3+}$ phosphors with efficiencies close to unity, ACS Appl. Mater. Interfaces 8 (2016) 31772–31782, https://doi.org/10.1021/acsami.6b11766.

[18] N.I. Matskevich, T. Wolf, M.Y. Matskevich, Energetic characteristics of barium cerates doped by yttrium, gadolinium and luthetium oxides, J. Chem. Thermodyn. 118 (2018) 188–192, https://doi.org/10.1016/J.JCT.2017.11.010.

[19] S. Feng, H. Qin, G. Wu, H. Jiang, J. Zhao, Y. Liu, Z. Luo, J. Qiao, J. Jiang, Spectrum regulation of YAG:Ce transparent ceramics with Pr, Cr doping for white light emitting diodes application, J. Eur. Ceram. Soc. 37 (2017) 3403–3409, https://doi.org/10.1016/j.jeurceramsoc.2017.03.061.

[20] S. Cho, C. Yun, Y.S. Kim, H. Wang, J. Jian, W. Zhang, J. Huang, X. Wang, H. Wang, J.L. MacManus-Driscoll, Strongly enhanced dielectric and energy storage properties in lead-free perovskite titanate thin films by alloying, Nano Energy 45 (2018) 398–406, https://doi.org/10.1016/j.nanoen.2018.01.003.

[21] J. Chan, L. Cao, W. Li, N. Ma, Z. Xu, X. Huang, Highly efficient broad-band green-emitting cerium(III)-activated garnet phosphor allows the fabrication of blue-chip-based warm-white LED device with a superior color rendering index, Inorg. Chem. 61 (2022) 6953–6963.

[22] A. Belsky, K. Lebbou, V. Kononets, O. Sidletskiy, A. Gektin, E. Auffray, D. Spassky, A.N. Vasil'ev, Mechanisms of luminescence decay in YAG-Ce,Mg fibers excited by γ- and X-rays, Opt. Mater. (Amst.). 92 (2019) 341–346, https://doi.org/10.1016/J.OPTMAT.2019.04.054.

[23] Y. Zorenko, V. Gorbenko, M. Nikl, J.A. Mares, T. Martin, P.A. Douissard, Development of novel UV emitting single crystalline film scintillators, IEEE Trans. Nucl. Sci. 57 (2010) 1335–1342, https://doi.org/10.1109/TNS.2009.2037150.

[24] A. Bala, S. Rani, UV excited emission spectra of gadolinium aluminium garnet, J. Opt. 52 (2022) 868–874, https://doi.org/10.1007/s12596-022-01052-2.

[25] V. Bachmann, C. Ronda, A. Meijerink, Temperature quenching of yellow Ce^{3+} luminescence in YAG:Ce, Chem. Mater. 21 (2009) 2077–2084, https://doi.org/10.1021/cm8030768.

[26] D. Zhou, Z. Wang, Z. Song, F. Wang, S. Zhang, Q. Liu, Enhanced persistence properties through modifying the trap depth and density in $Y_3Al_2Ga_3O_{12}:Ce^{3+},Yb^{3+}$ phosphor by co-doping B^{3+}, Inorg. Chem. 58 (2019) 1684–1689, https://doi.org/10.1021/acs.inorgchem.8b03270.

[27] V. Singh, S. Kaur, A.S. Rao, N. Singh, M.S. Pathak, J.L. Rao, An electron paramagnetic resonance and photoluminescence investigation of UVB radiation emitting gadolinium-activated $CaY_2Al_4SiO_{12}$ garnet compound, J. Electron. Mater. 48 (2019) 4092–4098, https://doi.org/10.1007/s11664-019-07175-w.

[28] Y. Kim, S. Kang, Effect of particle size on photoluminescence emission intensity in ZnO, Acta Mater. 59 (2011) 3024–3031, https://doi.org/10.1016/j.actamat.2011.01.042.

[29] T. Gavrilović, J. Periša, J. Papan, K. Vuković, K. Smits, D.J. Jovanović, M. D. Dramićanin, Particle size effects on the structure and emission of Eu^{3+}:$LaPO_4$ and $EuPO_4$ phosphors, J. Lumin. 195 (2018) 420–429, https://doi.org/10.1016/j.jlumin.2017.12.002.

[30] M.G. Brik, Fully relativistic analysis of the covalence effects for the isoelectronic 3d3 ions (Cr^{3+}, Mn^{4+}, Fe^{5+}) in $SrTiO_3$, J. Phys. Chem. Solids 67 (2006) 856–861, https://doi.org/10.1016/j.jpcs.2005.12.006.

[31] A. Of, S. Based, O.N. Lu, A.O. Ce, Preparation, luminescence properties, and application of scintillators based On $Lu_3Al_5O_{12}$:Ce single-crystal films, Appl. Phys. 69 (2002) 665–670.

[32] E.P. Jahrman, G.T. Seidler, J.R. Sieber, Determination of hexavalent chromium fractions in plastics using laboratory-based, high-resolution X-ray emission spectroscopy, Anal. Chem. 90 (2018) 6587–6593, https://doi.org/10.1021/acs.analchem.8b00302.

[33] W. Chewpraditkul, L. Swiderski, M. Moszynski, T. Szczesniak, C. Wanarak, P. Limsuwan, Scintillation properties of LuAG: Ce, YAG: Ce and LYSO, Ce Cryst. Gamma-Ray Detect. 56 (2009) 3800–3805.

[34] G. Liu, B. Wang, J. Li, B. Cao, Y. Lu, Z. Liu, Research progress of gadolinium aluminum garnet based optical materials, Phys. B Condens. Matter 603 (2021), 412775, https://doi.org/10.1016/J.PHYSB.2020.412775.

[35] H.-S. Zhang, L. Shi, X.-B. Yang, Y.-J. Zhao, K. Xu, L.-W. Wang, First-principles calculations of quantum efficiency for point defects in semiconductors: the example of yellow luminance by GaN: $C_N + O_N$ and GaN:C_N, Adv. Opt. Mater. 5 (2017), 1700404, https://doi.org/10.1002/adom.201700404.

[36] J.A. Mares, S. Witkiewicz-Lukaszek, V. Gorbenko, T. Zorenko, R. Kucerkova, A. Beitlerova, C. D'ambrosio, J. Dlouhy, M. Nikl, Y. Zorenko, Alpha and gamma spectroscopy of composite scintillators based on the LuAG:Pr crystals and single crystalline films of LuAG:Ce and (Lu,Gd, Tb)AG:Ce garnets 96 (2019), 109268, https://doi.org/10.1016/j.optmat.2019.109268.

The Effect of Boron and Scandium Doping on the Luminescence of LuAG:Ce and GdAG:Ce for Application as Scintillators

Greta Inkrataite[1], Jan-Niklas Keil[2], Aleksej Zarkov[1], Thomas Jüstel[2], Ramunas Skaudzius[1]

[1] Institute of Chemistry, Faculty of Chemistry and Geosciences, Vilnius University, Naugarduko 24, LT-03225 Vilnius, Lithuania
[2]Department of Chemical Engineering, Münster University of Applied Sciences, Stegerwaldstrasse 39, D-48565 Steinfurt, Germany

SUPPLEMENTARY MATERIAL

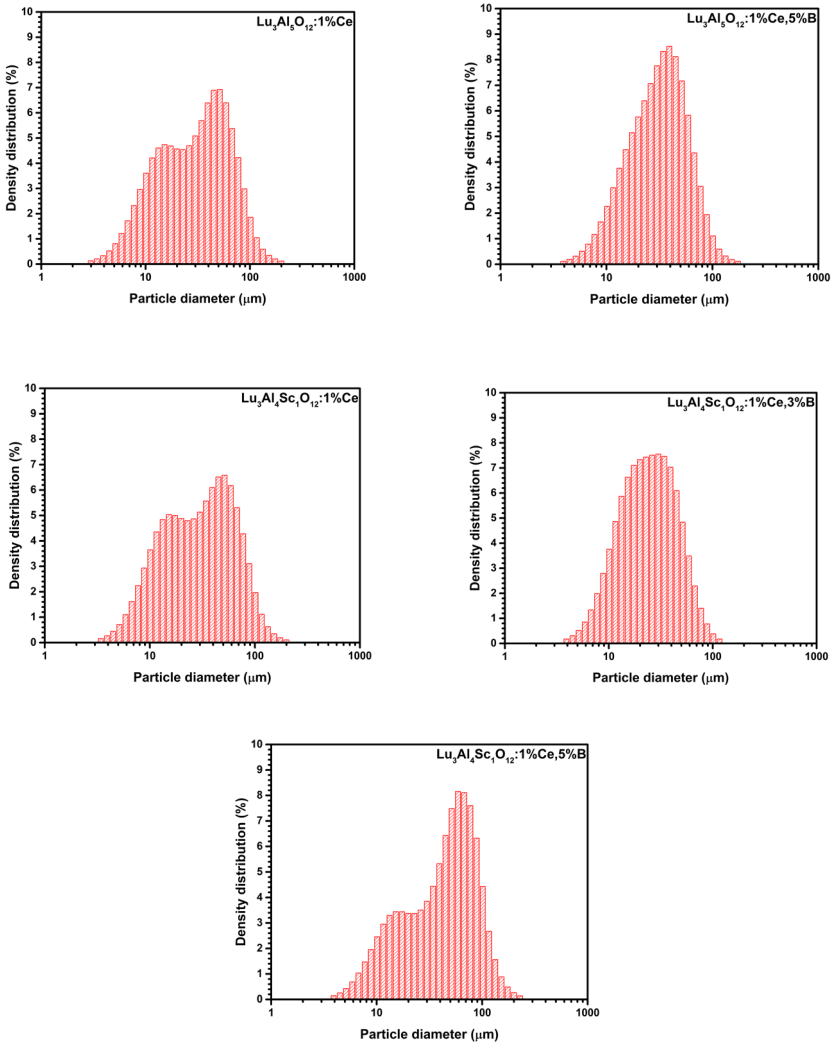

Figure SM1. Particles size histograms of 1% Ce^{+3} and different amount of B^{+3} doped $Lu_3Al_5O_{12}$ and $Lu_3Al_4Sc_1O_{12}$ garnet powder samples.

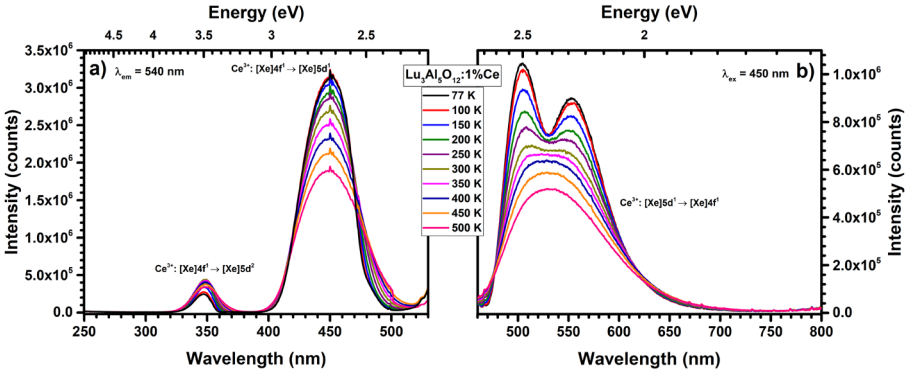

Figure SM2. Temperature dependency emission (b) and excitation (a) of 1% cerium doped $Lu_3Al_5O_{12}$.

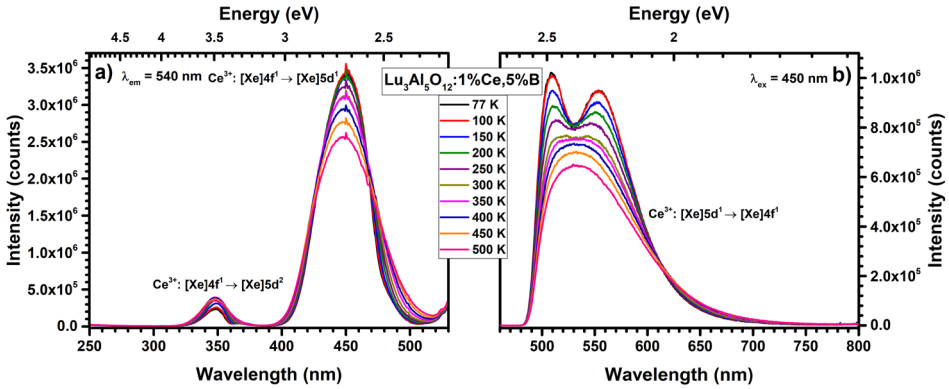

Figure SM3. Temperature dependency emission (b) and excitation (a) of 1% cerium and 5% boron doped $Lu_3Al_5O_{12}$.

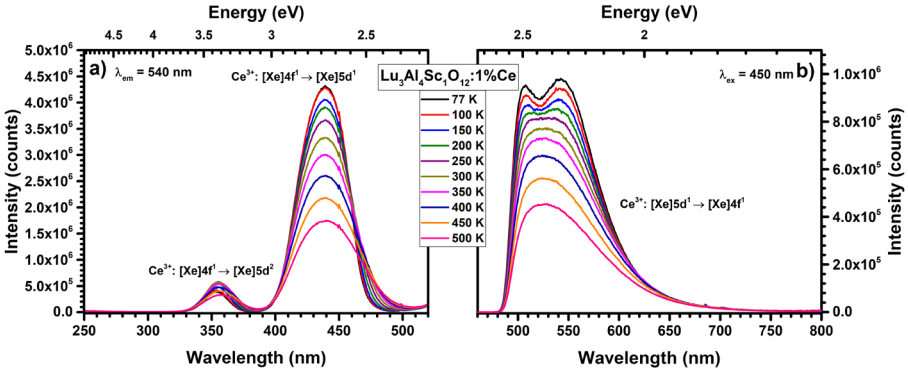

Figure SM4. Temperature dependency emission (b) and excitation (a) of 1% cerium doped $Lu_3Al_4Sc_1O_{12}$.

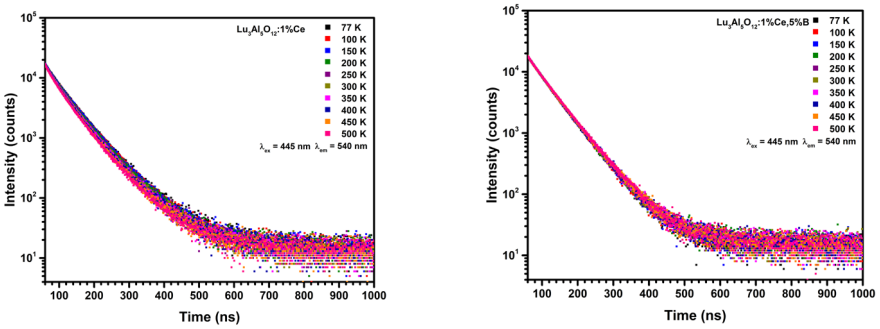

Figure SM5. Temperature dependency decay curves of 1% cerium and different amounts of boron doped $Lu_3Al_5O_{12}$.

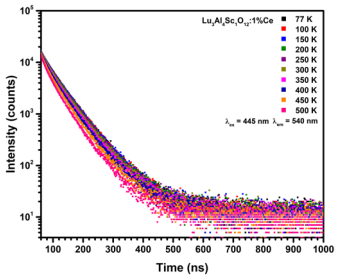

Figure SM6. Temperature dependency decay curves of 1% cerium doped $Lu_3Al_4Sc_1O_{12}$.

Ceramics International 50 (2024) 41879–41891

Contents lists available at ScienceDirect

Ceramics International

journal homepage: www.elsevier.com/locate/ceramint

Synthesis of praseodymium doped lutetium and gadolinium aluminum garnets modified by scandium and boron to improve luminescence properties

Greta Inkrataite [a,*], Jan-Niklas Keil [b], Agne Kizalaite [a], Thomas Jüstel [b], Ramunas Skaudzius [a]

[a] Institute of Chemistry, Faculty of Chemistry and Geosciences, Vilnius University, Naugarduko 24, LT-03225, Vilnius, Lithuania
[b] Department of Chemical Engineering, FH Münster University of Applied Sciences, Stegerwaldstrasse 39, D-48565, Steinfurt, Germany

ARTICLE INFO

Handling Editor: Dr P. Vincenzini

Keywords:
Boron doping
Garnet
Luminescence
Scintillators
Sol-gel synthesis

ABSTRACT

The structural and luminescence properties of the $Lu_3Al_4Sc_1O_{12}$:Pr and $Gd_3Al_3Sc_2O_{12}$:Pr garnet scintillators co-doped with boron (B^{3+}) ions were investigated. The addition of B^{3+} and Sc^{3+} to the structure has a positive effect on the luminescence properties, especially on the photo, radio emission intensities, quantum efficiency, and results in a reduction of the decay time, which is necessary for high-quality scintillators. Structural properties of garnets have been determined after X-ray diffraction analysis coupled with Rietveld refinement. Surface morphology analysis was performed using a scanning electron microscope and particle size was also determined. Elemental composition was confirmed by the ICP-OES technique. Reflection, excitation (in the UV and VUV range), emission (upon excitation by UV or X-rays), decay time, and quantum efficiency at room temperature were measured. Furthermore, the influence of temperature on excitation, emission, and decay curves was also analyzed. The obtained luminescence properties indicated positive effect caused by doping.

1. Introduction

Although a lot of research has been devoted to luminescent materials and their applications for more than 100 years, the scientific field itself remains relevant for many modern technical devices. Especially when it comes to scintillators and their improvements in their quality. High quality compounds are essential for various and important applications [1,2]. In order to improve the quality of scintillators, it is vital to discover new compounds that fit all the relevant requirements raised for these materials: high thermal stability, high density, high emission intensity, and good excitation properties (especially when it comes to excitation with high-energy radiation) [3–5]. A high quantum efficiency value is also important. However, one of the most important characteristics of scintillators, is the decay time. A short decay time is essential, so more signals could be recorded during the same timeframe. As a result a much higher quality and higher resolution image, for example in computed tomography (CT), single photon emission computed tomography (SPECT), or positron emission tomography (PET) is obtained [6–9]. All of the listed characteristics can be obtained, at least to a certain extent, in compounds with garnet structure. LuAG ($Lu_3Al_5O_{12}$) and GdASG ($Gd_3Al_3Sc_2O_{12}$) hosts are for many reasons excellent materials for the use as scintillators [10–12]. In particular, garnets doped with trivalent praseodymium are often used in this field. However, compounds doped with Pr^{3+} don't show sufficient quality for continuous use. For this reason, a lot of research was done on the improvement of such compounds [13–15]. From the data present in the literature, it was decided to synthesized praseodymium doped garnets. However, in this paper Sc^{3+} ions were used to modify the original LuAG and GdASG lattices by replacing part of the Al^{3+} ions. It is particularly important for gadolinium garnets, since only $Gd_3Al_5O_{12}$ cannot be synthesized as single phase compound without substitution [16,17]. As described in the literature, scandium may be able to influence the luminescence properties (increased emission intensity and shorter decay time) [12,18]. Furthermore, replacing Al^{3+} with B^{3+} could also improve the luminescence properties, especially the photo/radio emission intensity, and shorten the decay time [8,19]. Boric acid, which was used for the synthesis has a low melting/decomposition point (170 °C), therefore it was not only used as a boron source, but also as a flux. The use of boric acid, results in larger particles, which has a positive effect on the luminescence properties [20].

As such, based on the aforementioned problems and potential solutions a new and as scarcely investigated set of $Lu_{2.97}Al_{5-x}O_{12}$:$Pr_{0.03}$,B_x (x

* Corresponding author.
E-mail address: greta.inkrataite@chgf.vu.lt (G. Inkrataite).

https://doi.org/10.1016/j.ceramint.2024.08.041
Received 12 March 2024; Received in revised form 29 July 2024; Accepted 2 August 2024
Available online 3 August 2024

= 0, 0.15), $Lu_{2.97}Al_{4-x}Sc_1O_{12}:Pr_{0.03},B_x$ (x = 0, 0.09, 0.15),and $Gd_{2.97}Al_{3-x}Sc_2O_{12}:Pr_{0.03},B_x$ (X=0, 0.03 0.09, 0.15), garnets was synthesized. These are new samples have been studied by both structural and luminescence properties. X-ray diffraction analysis (XRD) with Rietveld refinement, scanning electron microscope (SEM), particle size distribution analysis, and inductively coupled plasma optical emission spectrometry (ICP-OES) were performed for structural and elemental investigation. Reflection, excitation in the UV and VUV region, emission upon excitation by UV and X-rays, decay time, and quantum efficiency were also measured. Temperature dependent analysis of emission, excitation, and decay times was performed. The main purpose of this work was to synthesize garnets with new compositions that would demonstrate the shortest possible decay times and improved luminescence properties.

2. Experimental Section

2.1. Synthesis procedure

An aqueous sol-gel method was used for the lutetium and gadolinium aluminum scandium garnet synthesis. For all samples, the same praseodymium amount (1 mol%) was used, while the amount of boron is 0, 1, 3 and 5 mol%. All samples are listed in Table 1.

Nominal formulas of synthesized samples are as follows: $Lu_{2.97}Al_{5-x}O_{12}:Pr_{0.03},B_x$ (LuAG), $Lu_{2.97}Al_{4-x}Sc_1O_{12}:Pr_{0.03},B_x$ (LuASG) and $Gd_{2.97}Al_{3-x}Sc_2O_{12}:Pr_{0.03},B_x$ (GdASG). Lu_2O_3 (99.9 % Alfa Aesar), Gd_2O_3 (99.9 % Aldrich), Sc_2O_3 (99.9 % ThermoFisher), $Al(NO_3)_3{\cdot}9H_2O$ (99.999 % Alfa Aesar), $Pr(NO_3)_3{\cdot}5H_2O$ (99.9 % Aldrich), H_3BO_3 (99.5 % Chempur) were used as precursor materials. Firstly, Gd_2O_3 or Lu_2O_3 and Sc_2O_3 were dissolved in a small amount (about 5 ml) of concentrated nitric acid at a temperature of 50 °C. Then, the acid was evaporated, and the remaining gel was washed with distilled water 3 times by evaporating the added water. After the washing process, an additional 50 ml of H_2O was added, along with the dissolution of $Al(NO_3)_3{\cdot}9H_2O$, $Pr(NO_3)_3{\cdot}6H_2O$, and H_3BO_3. The solution was left under magnetic stirring for 2 h at a temperature of 50 °C. Subsequently, citric acid was introduced to the solution, and it was left to stir overnight. The solution was then evaporated at a temperature of 50 °C, and the obtained gels were dried in a drying furnace at 140 °C for 24 h. Finally, the obtained powders were ground and subjected to two heating processes: firstly, heating at 1000 °C for 2 h in air with a heating pace of 5 °C/min, after which the powders were ground and further calcined at 1200 °C for 4 h under air with a heating pace of 5 °C/min [19,21]. The synthesis scheme is shown in Fig. 1.

2.2. Characterization

X-ray diffraction analysis (XRD) were performed using a Rigaku MiniFlex II X-ray diffractometer. Before analysis 0.05 g of samples were dispersed using 0.1 ml of ethanol on a glass sample holder and left to dry for 5 min in the air. Then diffraction patterns were recorded in the range of 2θ angles from 15° to 80° for all compounds. For analysis, Cu K_α radiation (λ = 1.5418 Å) was used. Other parameters of measurement: current – 15 mA, voltage – 30 kV, dwell time – 5.0 s, X-ray detector movement step – 0.010°. The FullProf program for Rietveld refinement was used.

Inductively coupled plasma optical emission spectroscopy (ICP-OES), for elemental composition of the synthesized materials was determined using PerkinElmer Optima 7000 DV spectrometer. For calibration standard stock solutions of Pr^{3+} (single-element ICP standard, 1000 mg/L, Roth) and B (multi-element ICP standard, 1000 mg/L, Roth) were diluted accordingly.

Table 1
List of the synthesized samples.

$Lu_3Al_5O_{12}$ (LuAG)	$Lu_3Al_4Sc_1O_{12}$ (LuASG)	$Gd_3Al_3Sc_2O_{12}$ (GdASG)
LuAG:1%Pr	LuASG:1%Pr	GdASG:1%Pr
LuAG:1%Pr,5%B	LuASG:1%Pr,3%B	GdASG:1%Pr,1%B
	LuASG:1%Pr,5%B	GdASG:1%Pr,3%B
		GdASG:1%Pr,5%B

Scanning electron microscopy (SEM)) was done, using a Hitachi SU-70 scanning electron microscope was used for the determination of particle morphology. For the measurement samples were prepared by dispersing them on a conductive double-sided carbon tape, that was attached to an aluminum sample holder.

The particle size distributions were measured using a Horiba LA-950-V2 organic device employing dynamic light scattering.

Diffuse reflection measurements between were recorded on an Edinburgh Instruments FL920 spectrometer equipped with an integration sphere coated by the white polymer Spectralon®. As a radiation source an ozone free 450 W xenon arc lamp was employed. The spectrometer contains two TMS300 monochromators (Czerny-Turner Optics) with 1800 F/mm gratings and a photomultiplier tube R928 (Hamamatsu), which were driven in the so-called synchronous scan mode. The photomultiplier tube is cooled to −20 °C by using Peltier elements. BaSO4 (99.99 %, Sigma-Aldrich) was used as a white standard for the reflection measurements.

Quantum Efficiency: The quantum yield, was measured using the diffuse reflection setup. External quantum efficiencies (EQE) were calculated by comparing the emission spectrum of the $BaSO_4$ sample (99.99 %, Sigma-Aldrich). The EQE values were obtained and calculated with the following formula 1, where $\int I_{em,sample}$ – integrated emission intensities of the phosphor sample, $\int I_{em,BaSO4}$ – integrated emission intensities of $BaSO_4$. $\int I_{ref}$ – integrated reflectance of the phosphor sample, $\int I_{ref,\ BaSO4}$ – integrated reflectance of $BaSO_4$. N_{em} and N_{abs} stand for the number of emitted and absorbed photons [19,22].

$$EQE = \frac{\int I_{em,sample} - \int I_{em,BaSO_4}}{\int I_{ref,BaSO_4} - \int I_{ref,sample}} \times 100\% = \frac{N_{em}}{N_{abs}} \times 100\% \quad (1)$$

Emission and excitation spectra were done by using an Edinburgh Instruments FLS980 spectrometer. The spectrometer uses an excitation and emission monochromators, 450 W Xe arc lamp, and to −20 °C cooled single-photon counting photomultiplier tube (Hamamatsu R928P) during measurement. Photoluminescence emission spectra were corrected using a correction file obtained from a tungsten incandescent lamp certified by NPL (National Physics Laboratory, UK). Excitation spectra were corrected by a reference detector.

Collection of excitation spectra in the VUV range was performed on a commercial Edinburgh Instruments FL920 spectrometer, which was modified by the integration of VUV monochromators for the excitation branch. The excitation branch consists of a D_2 lamp (DS-775) as VUV radiation source, an Acton Research VM-504 VUV monochromator and a mirror based focusing unit. The monochromator has manually adjustable (by a micrometer screw) inlet and outlet openings, as well as a 1200 grooves per mm (F/mm) grid. The inside of the monochromator and the focusing unit are operated under much reduced pressure ($<5 \times 10^{-}$ mbar the focusing unit are operated and the lamp radiates through an MgF_2 window directly into the radiation path being under vacuum. The remaining distance between the exit of the focusing unit, which is also closed by an MgF_2 window, and the sample is continuously flushed with dry nitrogen. The sample is fixed in the standard FLS920 sample chamber in a modified sample holder at a 45° angle to the excitation beam. The measurement is carried out in a 90° arrangement. The emission arm of the spectrometer consists of a convex quartz collecting lens, a TMS300 monochromator with an 1800 F/mm grating (Czerny-Turner Optics) and a photomultiplier tube (PMT, Hamamatsu R928) which is operated in single photon counting mode and is cooled to −20 °C by a Peltier element. To consider that the excitation source exhibits intensity fluctuations over the measured spectral range, all VUV excitation spectra are divided by the excitation spectrum of a standard compound. Sodium salicylate (≥99.5 %, Merck KGaA) was used for this

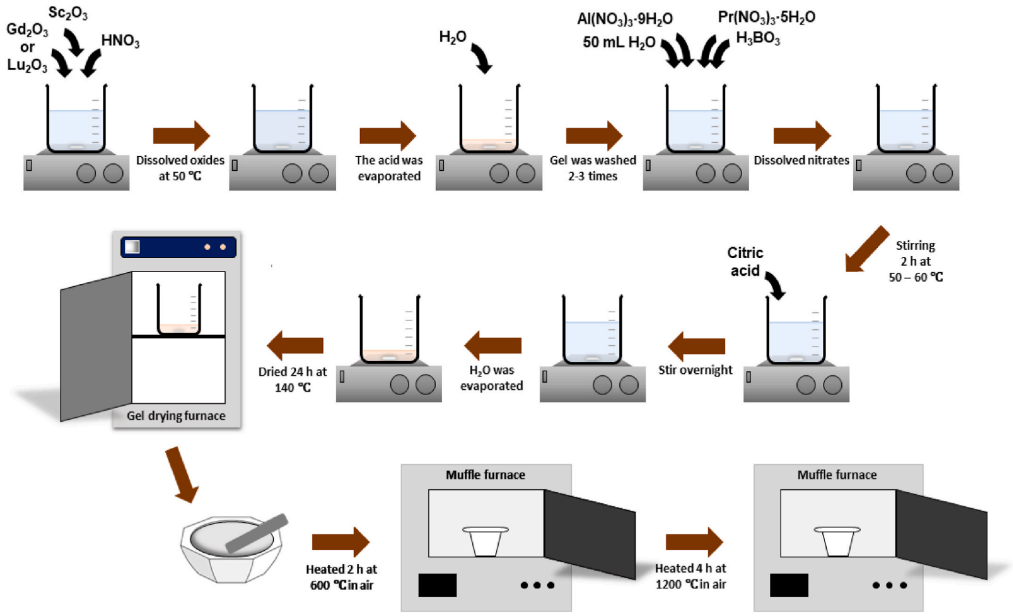

Fig. 1. Scheme of praseodymium doped garnet sol-gel synthesis procedure.

purpose because it exhibits relatively constant excitability over the relevant spectral range.

Temperature resolved spectroscopy was performed by using Edinburgh Instruments FLS920 spectrometer. The spectrometer uses an ozone lamp (450 W Xe; Osram AG) and a single-photon counting photomultiplier tube (Hamamatsu R928). Spectra in temperature range from 77 K to 500 K was measured. These spectra were recorded by using a liquid nitrogen cooled cryostat (Oxford Instruments MicrostatN2).

Time resolved spectroscopy, i.e. The photoluminescence decay curves of the garnet samples were recorded by using an Edinburgh Instruments FLS920 spectrometer. For lutetium aluminum/scandium garnet samples, photoluminescence decay times were measured using a 265 nm laser excitation source. For gadolinium aluminum scandium garnets decay times were performed with a millisecond pulsed xenon flashlamp (Edinburgh Instruments μF920H).

Radioluminescence measurements were performed on an Edinburgh Instruments FLS980 spectrometer equipped with a photomultiplier tube (PMT, Hamamatsu R928P) which is cooled to −20 °C by Peltier elements. For the generation of X-rays an Oxford Instruments Neptune 5200 tube was used, while the whole spectrometer set-up was cladded by Pb foil to absorb scattered x-rays.

3. Results and discussion

3.1. Inductively coupled plasma optical emission spectroscopy

All synthesized garnet samples were doped with 1 % of praseodymium and different amounts of boron. The $Gd_3Al_3Sc_2O_{12}$ garnets were analyzed by ICP-OES to determine the molar concentration of Pr^{3+} and B^{3+} in the samples. The results are shown in Table 2. The analysis results show that the praseodymium amount varies slightly but is close to 1 %, the discrepancies may most likely be caused by the small amount present and the inaccuracies of the analysis itself. The amount of boron in the compounds varied from 0 % to 5 % during the synthesis. From the obtained results, it can be seen that the actual measured amount is not identical to the calculated one. However, the difference is quite small in all cases. Despite the existing differences and the overall trend remains as expected, the more B^{3+} was added to the structure, the more was detected. Garnets, which should contain 3 % and 5 % boron, show slightly lower values of 2.6 % and 4.2 % respectively. This reduction may have occurred because of the low melting point of boric acid which causes some of the B^{3+} to evaporate.

Table 2
Praseodymium and boron content in% in GdASG samples measured by ICP-OES.

Sample	Praseodymium		Boron	
	Weighed in	Determined	Weighed in	Determined
$Gd_3Al_3Sc_2O_{12}$:1%Pr	1.0 %	1.2 %	0 %	0 %
$Gd_3Al_3Sc_2O_{12}$:1% Pr,1%B	1.0 %	1.0 %	1.0 %	1.3 %
$Gd_3Al_3Sc_2O_{12}$:1% Pr,3%B	1.0 %	1.3 %	3.0 %	2.6 %
$Gd_3Al_3Sc_2O_{12}$:1% Pr,5%B	1.0 %	1.3 %	5.0 %	4.2 %

3.2. X-ray diffraction

Since luminescence properties are dependent on the phase composition of the materials it is imperative to fully investigate the compositional makeup of each sample. As such, the phase purity of the samples was investigated by X-ray diffraction analysis and Rietveld refinement. The XRD patterns and the results of Rietveld refinement of GdASG doped with Pr^{3+} and B^{3+} are plotted in Fig. 2, while the results for LuAG, and LuASG doped with Pr^{3+} and B^{3+} can be found in Supplementary material as figures SM1 and SM2. The reliability factors as well as cell

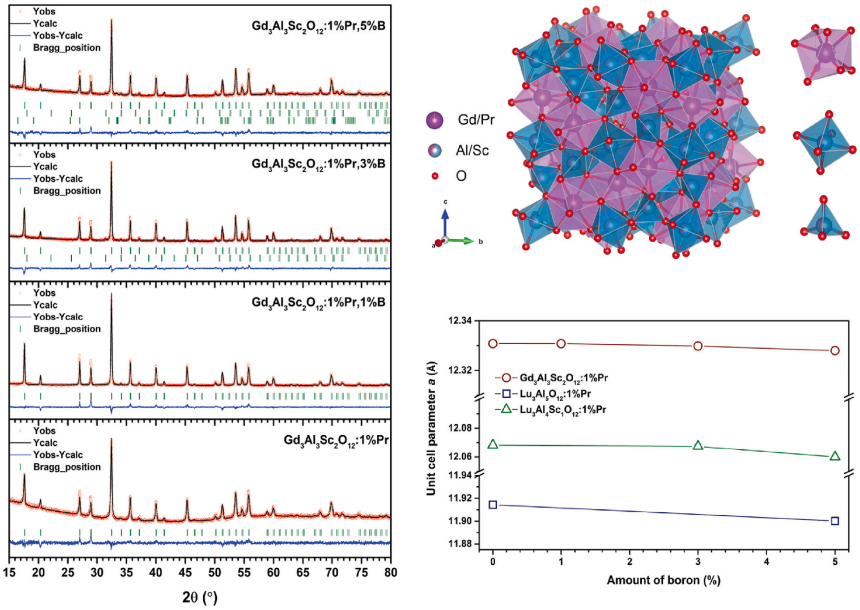

Fig. 2. Rietveld refinement results of XRD data recorded for Pr^{3+} and B^{3+} doped $Gd_3Al_3Sc_2O_{12}$ at room temperature (red dots are the experimental data; black lines are calculated data), Bragg reflections are indicated by vertical ticks. Top right – a structure of garnet cell after Rietveld refinement. Bottom right – unit cell parameter *a* after Rietveld refinement of all synthesized samples. (For interpretation of the references to color in this figure legend, the reader is referred to the Web version of this article.)

parameter values obtained after refinement are given in Supplementary materials as table SM1. From the Rietveld refinement results displayed in Fig. 2 (left), it can be observed that samples containing 0 and 1 % of boron possess a single phase garnet structure with a space group $Ia\bar{3}d$. The model shows quite a good fit with no unattributed reflections. However, when the sample is doped with 3 % of B^{3+} an additional diffraction peak is observed at around 32 2θ(°). This impurity phase was identified as Sc_2O_3 with a space group of $I\bar{3}a$ and when 5 % B^{3+} is added, another impurity phase of $GdAl_3(BO_3)_4$ with an *R*32 space group (Powder Diffraction File, (PDF) #04-002-9348) is observed as indicated by new reflection at around 33.5 2θ(°). However, while the impurities in these cases are indeed present, their fractions are rather insignificant. In the case when 3 % of boron was used the impurities consisted of only 0.64 %, and in the second case (5 % of Boron) – 1.73 %. In the case of LuAG and LuASG, the compounds (figures SM1 and SM2) have pure garnet phase (space group – $\bar{3}d$, Powder Diffraction File, (PDF) #00-056-1646) with no formation of impurity phases as indicated by no additional reflections being observed after the refinement procedure. Fig. 2 (bottom right) shows the variation of unit cell parameters based on the B^{3+} content in the samples. In all cases when boron was introduced into the unit cell a reduction of the lattice parameter was observed. This is due to the ionic radii difference between Al^{3+} (0.53 Å) and B^{3+} (0.27 Å) [23]. In GdASG:Pr, the unit cell parameter *a* slightly reduces from 12.331 Å to 12.328 Å, in LuASG:Pr from 12.068 Å to 12.060 Å, and in LuAG:Pr from 11.914 Å to 11.900 Å. The unit cell parameter of $Lu_3Al_5O_{12}$ garnet was reported to be around 11.906 Å [24]. Overall, the gadolinium based garnet showed the largest size, followed by the Al–Sc garnet, and the simple Lu–Al garnet exhibited the smallest lattice parameter. Overall, it can be stated that Sc^{3+} (0.75 Å) and Pr^{3+} (2.47 Å) doping causes an expansion of the crystal lattice, while the introduction of B^{3+} ions causes it to contract as is expected from the ionic radii differences [23].

The visualization of the garnet structure from the data obtained after Rietveld refinement can be found in Fig. 2 (top right). Visualization was made with the "Vesta" software [25]. Garnets have a cubic crystal structure with the $Ia\bar{3}d$ space group. In such a structure there are three independent positions, an 8-fold coordinated dodecahedral, a 6-fold coordinated octahedral, and a 4-fold coordinated tetrahedral. Depending on the size, elements can occupy different positions in the structure. In this case, Sc^{3+}, Al^{3+}, and B^{3+} occupy tetrahedral and octahedral sites, and Lu^{3+}, Gd^{3+}, and Pr^{3+} the dodecahedral sites. All of the coordination polyhedrons are shown in Fig. 2. Overall, the obtained crystallographic results fit well with the ones reported in the literature [26–28].

3.3. Particle morphology analysis

All synthesized samples were subjected to particle morphology determination by scanning electron microscope (SEM). To observe the complete view of the particles, the images were taken at different magnifications. The lower magnification images performed under 10 k magnification represent a broader view of the sample morphology, while images done under higher magnification of 50 k, were performed to observe particle boundaries and their arrangement more closely. SEM images of $Lu_3Al_5O_{12}$ and $Lu_3Al_4Sc_1O_{12}$ garnets doped with Pr^{3+} and different amounts of boron are shown in Fig. 3. $Gd_3Al_3Sc_2O_{12}$ garnets – in Fig. 4. Garnet samples that are prepared by the sol-gel method, are commonly are characterized by irregularly shaped individual and interconnected particles that may have unfilled pores between them [29–31]. A similar case was observed for all samples under study as well. As can be seen from the given SEM micrographs, morphological properties of all lutetium, lutetium/scandium, and gadolinium aluminum/scandium garnets are dependent on the B^{3+} ion doping. It can be

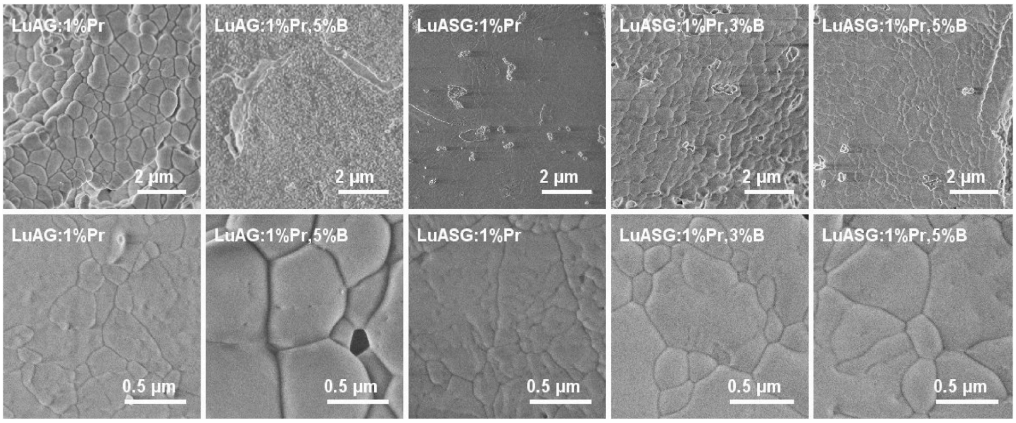

Fig. 3. SEM images of 1 % Pr^{3+} and different amounts of B^{3+} doped $Lu_3Al_5O_{12}$ and $Lu_3Al_4Sc_1O_{12}$ garnet samples in different magnifications.

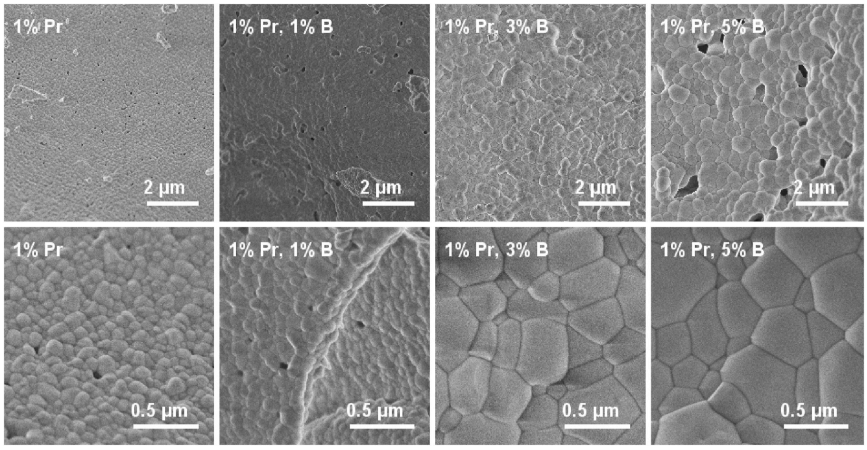

Fig. 4. SEM images of 1 % Pr^{3+} and different amounts of B^{3+} doped $Gd_3Al_3Sc_2O_{12}$ garnet samples in different magnifications.

seen that samples without boron have smaller particles as compared to those containing B^{3+} ions. As the boron content increases, the particle size also increases. This is observed for LuAG and LuASG samples. However, it is especially noticeable in the $Gd_3Al_3Sc_2O_{12}$ samples. This may be caused by the fact that the initial particle size for this composition is much smaller as compared to the Lu based garnets as well as by a more gradual increase in boron content. In this case, particle size increases from nanometer scale to micrometer one. These changes in particle size are related to the B^{3+} acting as a flux, since the melting point of boric acid is 170 °C, which allows for faster particle size growth. Furthermore, the incorporation of boron may also lead to a reduced melting point of the final garnet compound which would allow for faster mass transport and result in larger grains as well [20]. Particle agglomeration due to B^{3+} acting as a flux also causes a significant effect on the porosity of all samples. In Fig. 4, it can be observed that the porosity of garnets decreases as the boron content increases. Overall, the incorporation of B^{3+} leads to a larger particle size as well as a reduction in porosity.

The size distribution of the garnet particles was measured using the "Horiba LA-950-V2 organic" device. Histograms of the particle size distribution and calculated d10, d50, d90 values of gadolinium aluminum scandium garnets doped with praseodymium and boron can be seen in Fig. 5. Pr^{3+} and B^{3+} doped lutetium aluminum/scandium garnet particle distributions can be seen in the supplementary material figure SM3. Fig. 5 shows that the data correlates well with the data from the SEM images. As the B^{3+} content increases, the particle size also increases. Of course, deviations can be observed, but the trend remains. A particularly pronounced increase in particles size is observed when 3 % boron was doped in the gadolinium aluminum scandium garnets (Fig. 5). Arguably, this sample has the largest particle size. Garnet doped with 5 % boron may have slightly smaller particles due to the presence of a slight amount of impurities. However, it is worth noting that during the measurement not the individual particles, but the size of agglomerates may also be measured. As such while the sizes tend to correlate discrepancies may also be caused by this fact. At the same time, figure SM3 shows a similar tendency.

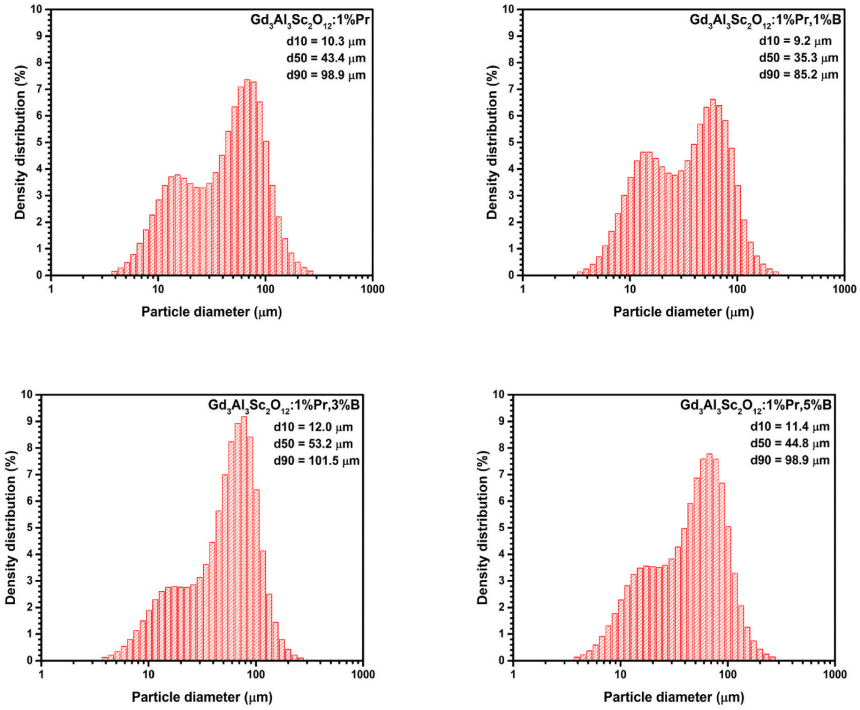

Fig. 5. Particle size histograms of 1 % Pr^{3+} and different amounts of B^{3+} doped $Gd_3Al_3Sc_2O_{12}$ garnet samples.

3.4. Luminescence properties

Reflection spectra of all synthesized compounds are shown in Figs. 6 and 7. It can be seen that all samples ($Lu_3Al_5O_{12}$, $Lu_3Al_4Sc_1O_{12}$, $Gd_3Al_3Sc_2O_{12}$) doped with Pr^{3+} ions exhibit electron transitions characteristic to that of praseodymium ions. $^3H_4 \rightarrow [Xe]4f^15\,d^1$, and $^3P_0 \rightarrow {}^3H_{4,5,6}$ also $^1D_4 \rightarrow {}^3H_4$ transitions describe the Pr^{3+} absorption in compounds [32]. These electron transitions are responsible for the slight

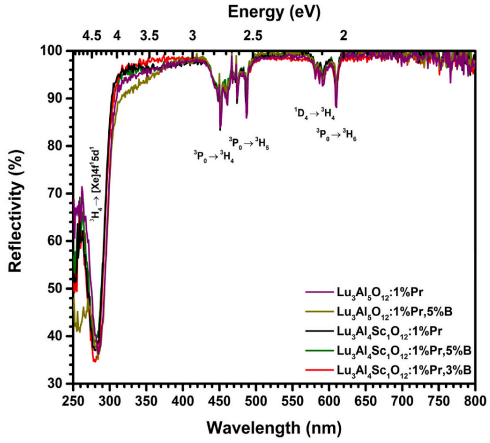

Fig. 6. Reflection spectra of 1 % of praseodymium and different amounts of boron doped $Lu_3Al_5O_{12}$ and $Lu_3Al_4Sc_1O_{12}$.

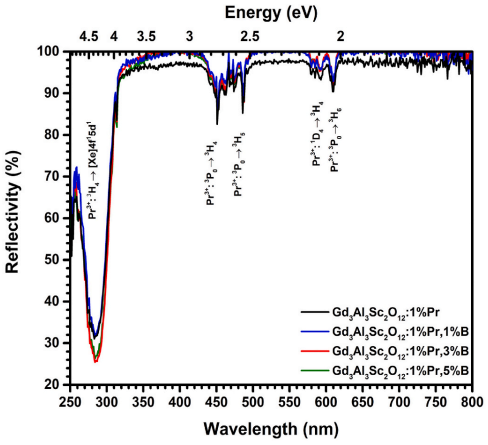

Fig. 7. Reflection spectra of 1 % of praseodymium and different amounts of boron doped $Gd_3Al_3Sc_2O_{12}$.

greenish color in the samples which is typical for Pr^{3+} doped materials [33]. A slight shift from 451 to 453 nm can be observed between the reflectance spectra bands of lutetium and gadolinium garnets. The spectra of $Gd_3Al_3Sc_2O_{12}$ garnets are shifted to longer wavelengths. This can be explained by the different radii of Lu^{3+} (0.98 Å) and Gd^{3+} (1.05 Å) ions and the covalence effect [34]. Furthermore, a rather high reflectance value is observed in the spectral ranges where there are no electron transitions. This value is between 90 % and 100 % relatively to the white $BaSO_4$ standard and shows a high optical quality of the synthesized materials. Based on the reflection spectra, the band gap energies were also calculated for all samples, which are listed in table SM2 in the Supplementary material file. It can be seen that lutetium aluminum garnets have a slightly smaller band gap energies than gadolinium aluminum garnets. Furthermore doping of boron increases the band gap energy for all samples. Scandium also has the same effect.

VUV and UV excitation spectra were measured for all synthesized samples using 312 nm as emission wavelength. Fig. 8 shows the normalized excitation spectra of lutetium garnets in the range from 120 nm to 310 nm with an intense band being visible at 172 nm. It is assigned to host the absorption of LuAG. From 230 nm two intense bands are assigned to praseodymium ion excitation [35]. The normalized excitation spectra of the GdASG samples are shown in Fig. 9. It is quite difficult to ascribe the bands existing in the 120 nm–200 nm region as not much data is present in the literature for such composition, however similarly as before, at least in part it could arise from the band gap of the matrix compound. Bands from 200 nm are attributed to Pr^{3+} ions centered $^3H_4 \rightarrow [Xe]4f^15\ d^1$ transitions and Gd^{3+} ions centered $^8S_{7/2} \rightarrow {}^6I_J$ and $^8S_{7/2} \rightarrow {}^6P_J$ transitions.

Figs. 10 and 11 show the excitation (a) and emission (b) spectra of LuAG, LuASG, and GdASG phosphors measured at room temperature. From the data given in Fig. 10, it can be observed that $Lu_3Al_5O_{12}$ and $Lu_3Al_4Sc_1O_{12}$ garnets exhibit characteristic excitation spectra of praseodymium ions with (a) and $^3H_4 \rightarrow [Xe]4f^15\ d^1$ electron transitions. Additionally, a peak shift is observed between different samples. LuAG samples have excitation peaks at lower energy values than samples containing Sc^{3+}. This shift occurrence can be explained by the covalency effect, because of the reduction of the energy between the lowest 5d and lowest 4f energy levels [36]. The presence of Sc^{3+} in the structure also affects the intensity of the excitation spectra, mainly resulting in a

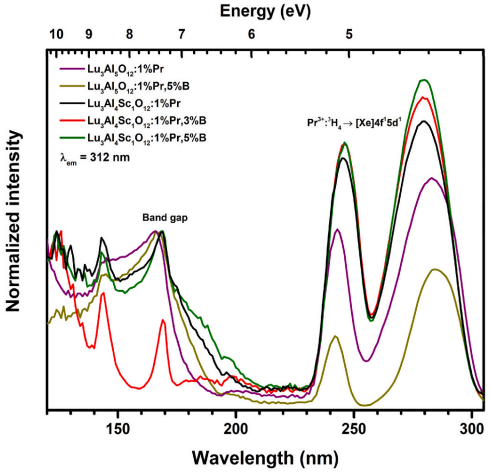

Fig. 8. VUV and UV excitation spectra of 1 % of praseodymium and different amounts of boron doped $Lu_3Al_5O_{12}$ and $Lu_3Al_4Sc_1O_{12}$ samples.

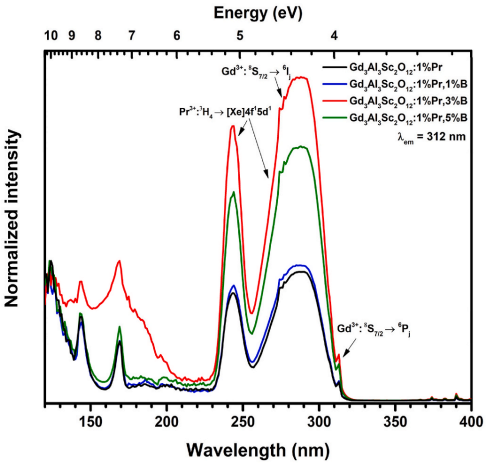

Fig. 9. VUV and UV excitation spectra of 1 % of praseodymium and different amounts of boron doped $Gd_3Al_3Sc_2O_{12}$.

reduction in intensity. However, samples containing B^{3+} have higher intensity, with the most intense emission being observed at 3 % of B^{3+} doping. Electron transitions ascribed to praseodymium ions are also visible in the emission (b) spectra [15,37]. During the measurement of emission spectra λ_{ex} = 285 nm was used for the excitation. In the wavelength range of 300–460 nm, characteristic, allowed, and more intense $[Xe]4f^2 \rightarrow [Xe]4f^15\ d^1$ electron transitions are visible. As in the excitation spectra, garnets without Sc^{3+} have the most intense emission, while out of the LuASG samples, garnet doped with 3 % of boron showed the most intense emission. The $[Xe]4f^2 \rightarrow [Xe]4f^2$ transitions of lower intensity are seen in the 450–800 nm wavelength spectral range. In this case, the LuASG sample with 3 % of B^{3+} has the most intense emission ($4f^15\ d^1 \rightarrow {}^3H_j, {}^3F_j$ transition). It can be observed that in the case of $[Xe]4f^2 \rightarrow [Xe]4f^2$ transitions boron significantly improves the emission intensity. This may be most likely caused by the increase in particle size, which was induced by the use of B^{3+} as a flux. Fig. 11 (a) shows the excitation spectra of GdASG samples. In this case, electron transitions characteristic not only of praseodymium ions but also of gadolinium ions are observed [15,38]. At 242 nm and 285 nm Pr^{3+} ($^3H_4 \rightarrow [Xe]4f^15\ d^1$) and at 312 nm – Gd^{3+} ($^8S_{7/2} \rightarrow {}^6P_J$). In this case, the B^{3+} in the structure has a totally positive effect and all compounds containing boron have a stronger excitation, with the highest intensity sample being the one with doped 5 % of B^{3+}. Interestingly, this sample has the highest amount of impurities, as such it is possible that they are in part responsible for the high excitation intensity. Since a large amount of scandium and gadolinium quenches the $[Xe]4f^2 \rightarrow [Xe]4f^15\ d^1$ emission of praseodymium, no emission of these transitions is observed in Fig. 11 (b) [39,40]. The effect of Sc^{3+}/Gd^{3+} ion on luminescence quenching can be explained by a non-radiative relaxation process from the 5d excited state to the 4f ground state, it may also be caused by photoionization process as well [41–43]. However, more intense $[Xe]4f^2 \rightarrow [Xe]4f^2$ emission is observed in this case (compared to LuAG and LuASG). Furthermore, the compound with 5 % of B^{3+} is also characterized by the most intense emission. As with excitation, the intensity is believed to be driven by the resulting impurities and changing particle size [20,44].

The application of scintillators is based on the excitation of samples with high energy radiation. Figs. 12 and 13 show the emission spectra in conventional and heatmap forms with the integrated emission intensities of synthesized garnets under X-ray excitation at 50 kV and 1.8 mA. The conventional spectra of LuAG and LuASG can be seen in Fig. 12

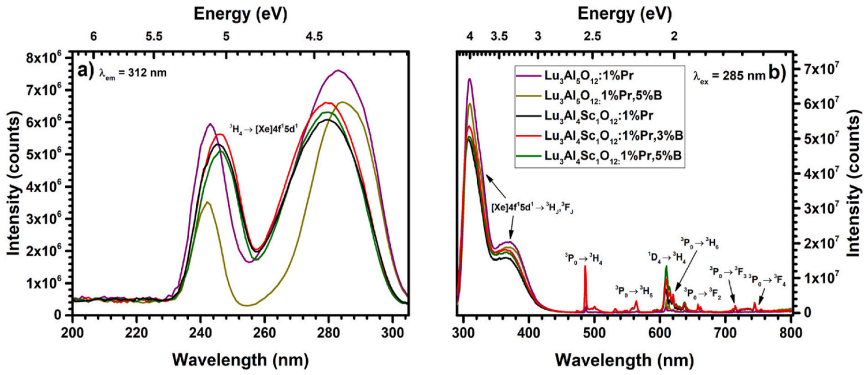

Fig. 10. Excitation (a) and emission (b) spectra of 1 % of praseodymium and different amounts of boron doped $Lu_3Al_5O_{12}$ and $Lu_3Al_4Sc_1O_{12}$.

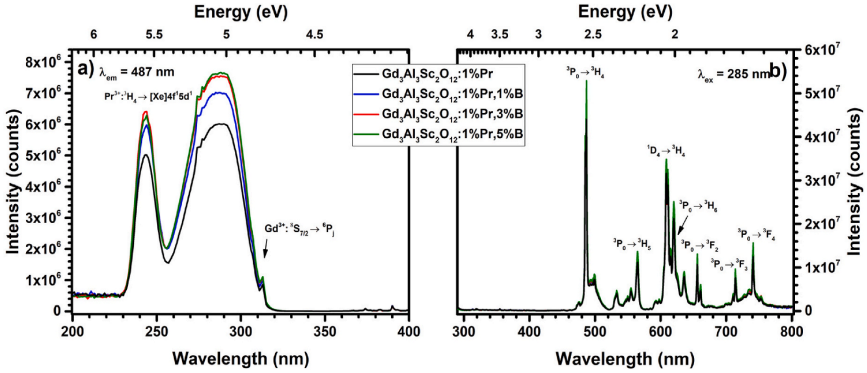

Fig. 11. Excitation (a) and emission (b) spectra of 1 % of praseodymium and different amounts of boron doped $Gd_3Al_3Sc_2O_{12}$.

left part. Both [Xe]$4f^2$ → [Xe]$4f^1$5 d^1 and [Xe]$4f^2$ → [Xe]$4f^2$ electron transitions characteristic of Pr^{3+} are observed under X-ray excitation. From the given data, it can be seen that the introduction of scandium into the garnet lattice reduces the intensity of [Xe]$4f^2$ → [Xe]$4f^1$5 d^1 electron transition but increases [Xe]$4f^2$ → [Xe]$4f^2$ emission intensity. LuAG:1%Pr, as under UV excitation, exhibits the highest [Xe]$4f^2$ → [Xe] $4f^1$5 d^1 emission intensity, as shown by the conventional emission spectrum (left) and heatmap (right). Meanwhile, the most intense [Xe] $4f^2$ → [Xe]$4f^2$ transitions are observed for LuASG:1%Pr,5%B sample. These differences are more clearly visible in the heatmap and in the graph of integrated intensity since the increase in intensity (red color) for this sample at 610 nm is readily observable. Similarly, under UV excitation, the increase in intensity may result from the increase in particle size upon the doping of B^{3+}. Fig. 13 left part shows the emission spectra of GdASG under X-ray excitation. The [Xe]$4f^2$ → [Xe]$4f^1$5 d^1 electron transitions should be quenched by Sc^{3+} and Gd^{3+} ions, but for the GdASG:1%Pr,3%B sample are visible in the 300–400 nm spectral range. Furthermore, the introduction of B^{3+} leads to an increase in the emission intensity for the [Xe]$4f^2$ → [Xe]$4f^2$ transitions. The most intense emission was observed for the GdASG:1%Pr,3%B sample, which is even 1.2×10^5 counts more intense than the sample without boron. The discussed changes can be more clearly visible in the heatmap (right side), which shows a yellow color at this sample and wavelength. These observations also are also confirmed by the graph of integrated intensities. Overall, B^{3+} has a positive effect on the emission intensity when X-ray excitation is used. Thus, indicating that such garnets could potentially be better scintillators than the boron-free samples.

The measured decay times (excited at 265 nm for lutetium garnets and 285 nm for gadolinium garnets) and quantum efficiency values of the compounds at room temperature are given in Table 3. Decay time of Pr^{3+} in the garnet matrix were calculated by fitting the curves using the first-order exponential equation. Due to the different existing electron transitions in Gd and Lu based garnets, decay times were measured using different emission wavelengths (for lutetium aluminum garnets - 312 nm, and for gadolinium aluminum scandium garnets - 487 nm). This was done in order to analyze the most intense emission bands. Furthermore, due to the differing nature of electron transitions for these bands ([Xe] $4f^2$ → [Xe]$4f^1$5 d^1 for Lu based, and [Xe]$4f^2$ → [Xe]$4f^2$ for Gd) a difference between micro and nano second range in decay times was measured. The faster decay times in Lu based garnets were observed due to the allowed nature of [Xe]$4f^2$ → [Xe]$4f^1$5 d^1 transitions, which are in general much faster than forbidden [Xe]$4f^2$ → [Xe]$4f^2$ ones that were analyzed in Gd based garnet. However, gadolinium ions may also affect the decay times and increase them even further. While the decay time curves are shown in Figs. 14 and 15, the obtained data exhibit that all the curves vary exponentially and are typically characteristic of Pr^{3+} ions. The decay time of lutetium garnets is in the nanoseconds range, while that of gadolinium garnets is in microseconds. As there is energy

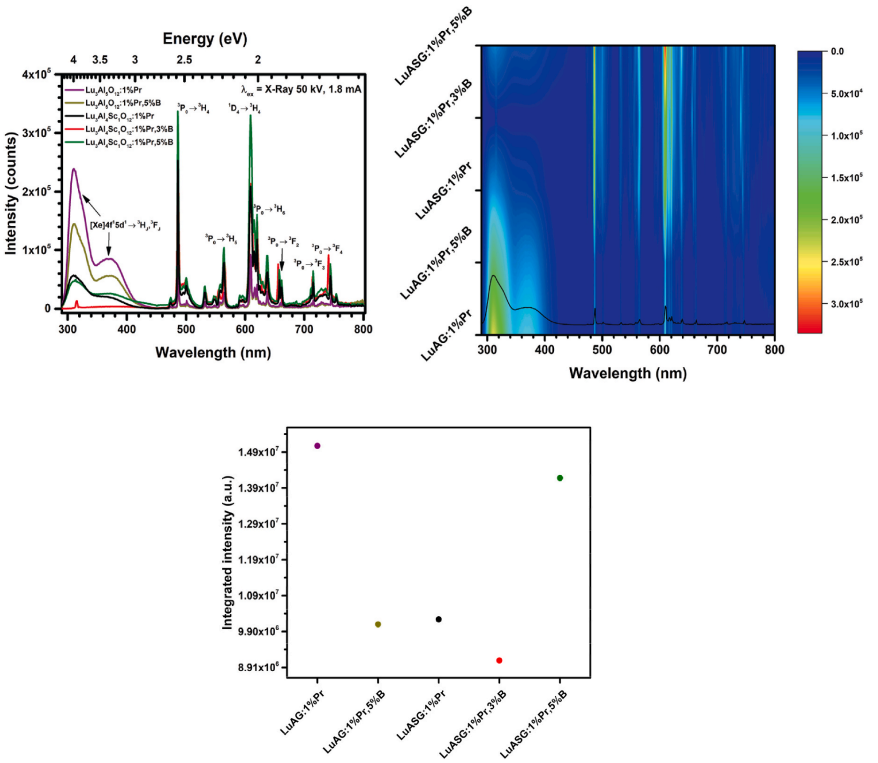

Fig. 12. (Top) Emission spectra under X-Ray excitation (left), heatmap (right) of 1 % of praseodymium and different amounts of boron doped $Lu_3Al_5O_{12}$ and $Lu_3Al_4Sc_1O_{12}$. (Bottom) integrated intensities of samples emission spectra (integration errors are not included due to their extremely small values as compared to the measured results).

migration through the Gd^{3+} sublattice, it acts as a slow component and the garnets' decay time becomes longer with Gd^{3+} than with Lu^{3+} ion [45]. The decay time of LuAG decreases as much as 3.6 ns when garnet is doped with boron. LuAG:1%Pr,5%B has the shortest decay time of all synthesized samples, and it is equal to 19.5 ns. The presence of boron in the garnet structure has a positive effect on the reduction of decay time values. The shortening of the decay times themselves can be based on the fact that the boron has a higher electronegativity than that of aluminum. The decrease in the decay time is due to the effect of B^{3+} ions, which can be explained by the polarization of the local environment of the activator ions. The polarization decreases when the electronegativity of the ions increases, and as a result decay time becomes shorter. As such the difference in the electronegativity between Al^{3+} and B^{3+} ions causes this effect, which in turn causes the changes in decay time values [46]. The decay times of the GdASG samples vary from 8.8 to 8.3 μm. As with LuAG and LuASG samples, values are reduced by doping compounds with B^{3+} ions. $Gd_3Al_3Sc_2O_{12}$:1%Pr,3%B has the lowest decay time. This reduction in value is due to the optimal amount of boron ions and the relatively low amount of impurities (just 0.64 %). Further, increase in B^{3+} doping leads to an increase in the amount of impurities (up to 1.73 %), as a result the decay time may also increase.

In terms of quantum efficiency, $Lu_3Al_4Sc_1O_{12}$:1%Pr,5%B has the highest value of 87 %. Meanwhile, the values of the other samples vary widely, although they tend to be greater than 50 %. Table 3 shows that gadolinium garnets have lower EQE values than lutetium garnets. Interestingly, only in the LuAG case, a decrease in EQE was observed when boron was introduced. As in the LuASG and GdASG cases, a quite steady increase in the efficiency values was observed based on the B^{3+} content in the sample. The higher the doping content, the higher the values obtained, in LuASG ranging from 49 % to 87 %, and in GdASG values changed from 10 % to 46 %. This positive change in EQE may be related to the different polarization of the activator ion environment. The changes in the local environment in this case are caused by the dopant ions. As they have different electronegativity values as compared to the base ones. As the polarization decreases, the EQE values increase. Since boron ions have a higher electronegativity than aluminum ions, it caused changes in polarization and as result and increase in EQE is observed [47,48].

To obtain a more fundamental view of the doping effects in $Gd_3Al_3Sc_2O_{12}$ system, garnets were further characterized by means of temperature dependent luminescence analysis. The excitation (a), emission (b) spectra, heatmap of the emission spectra, and graph of integrated intensities (bottom) of the compound doped with 1 % of praseodymium and 3 % of boron are shown in Fig. 16. The spectra of the other garnets are depicted in the supplementary material, viz. figures SM4, SM5, and SM6. Similarly, to that of room temperature measurements, the same excitation and emission spectra are observed at different temperatures. In the conventional spectra (part a of the figure) the characteristic bands of Pr^{3+} ions at 242 nm and 285 nm due to $^3H_4 \rightarrow [Xe]4f^15\ d^1$ electron transitions can be seen. Bands at 275 nm and 312

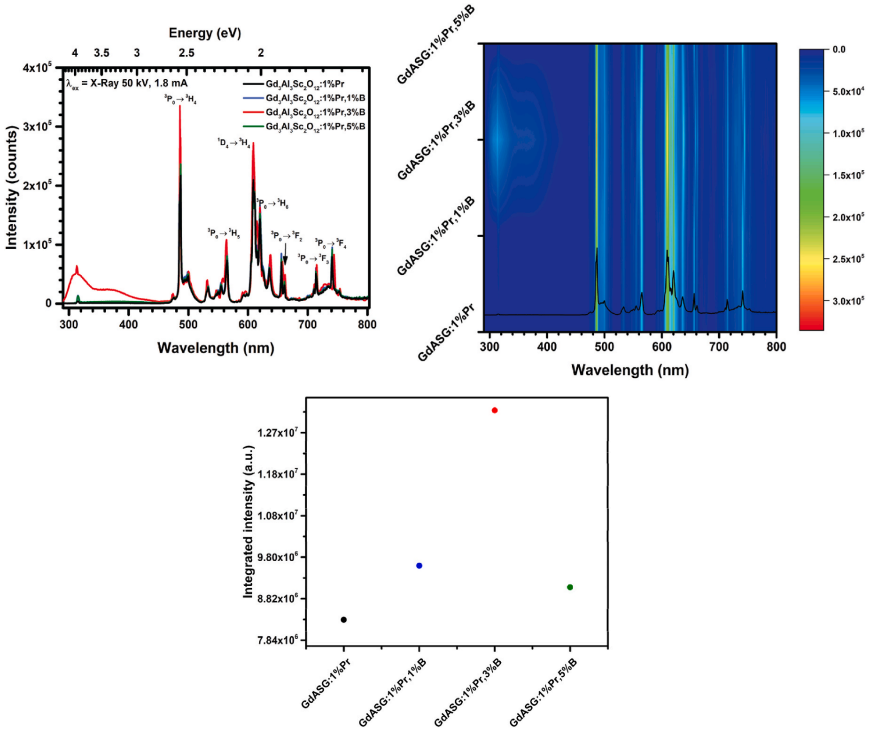

Fig. 13. (Top) Emission spectra under X-ray excitation (left), heatmap (right) of 1 % of praseodymium and varying amounts of boron doped $Gd_3Al_3Sc_2O_{12}$. (Bottom) integrated intensities of samples emission spectra (integration errors are not included due to their extremely small values as compared to the measured results).

Table 3
Synthesized samples decay time and quantum efficiency.

Sample	Decay time	χ^2 value	Quantum efficiency [%]
$Lu_3Al_5O_{12}$:1%Pr	23.1 ± 0.1 ns	1.198	70
$Lu_3Al_5O_{12}$:1%Pr,5%B	19.5 ± 0.1 ns	1.118	52
$Lu_3Al_4Sc_1O_{12}$:1%Pr	22.4 ± 0.1 ns	1.260	49
$Lu_3Al_4Sc_1O_{12}$:1%Pr,3%B	19.7 ± 0.1 ns	1.050	60
$Lu_3Al_4Sc_1O_{12}$:1%Pr,5%B	19.9 ± 0.1 ns	1.114	87
$Gd_3Al_3Sc_2O_{12}$:1%Pr	8.8 ± 0.2 μs	1.164	10
$Gd_3Al_3Sc_2O_{12}$:1%Pr,1%B	8.6 ± 0.2 μs	0.946	33
$Gd_3Al_3Sc_2O_{12}$:1%Pr,3%B	8.3 ± 0.2 μs	1.221	39
$Gd_3Al_3Sc_2O_{12}$:1%Pr,5%B	8.5 ± 0.2 μs	1.181	46

nm are attributed to electron transitions caused by Gd^{3+} ions. Emission spectra (b) also show $[Xe]4f^2 \rightarrow [Xe]4f^2$ electron transitions characteristic of praseodymium ions, when 285 nm excitation light was used. The most intense emission feature is ascribed to the $^3P_0 \rightarrow {}^3H_4$ transition. Both excitation and emission spectra show the same tendency, mainly that the luminescence intensities decrease with increasing temperature, samples at 77 K have the highest intensity and at 500 K – the lowest. As the temperature is raised, the resulting vibrations cause the Pr^{3+} ions to transfer energy to the surrounding lattice. For this reason, the probability of non-radiative transition increases. Especially at high temperatures, an even greater decrease in intensity is observed due to thermal quenching [49]. The emission spectra heatmap and the displayed integrated intensities (Fig. 16 bottom) yield a clearer image of the decreasing emission intensity, as a change in color from red-yellow to a more white-blue is observed for electron transitions upon an increase in temperature. All of the measured praseodymium and boron doped gadolinium aluminum scandium garnet samples show the same trend.

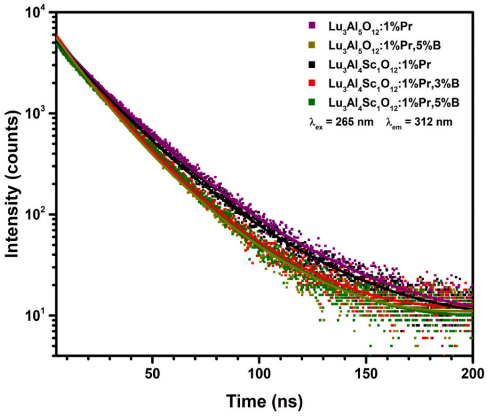

Fig. 14. Decay curves of 1 % of praseodymium and different amounts of boron doped $Lu_3Al_5O_{12}$ and $Lu_3Al_4Sc_1O_{12}$.

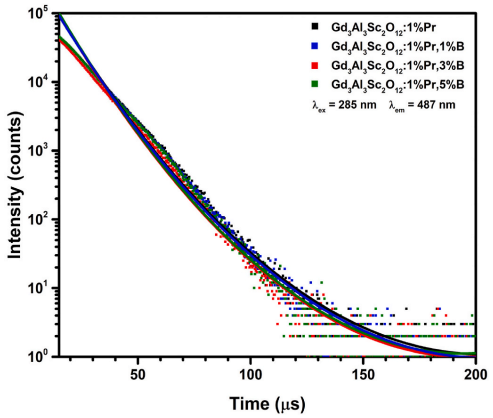

Fig. 15. Decay curves of 1 % of praseodymium and different amounts of boron doped $Gd_3Al_3Sc_2O_{12}$.

Activation energies were calculated for all praseodymium doped gadolinium aluminum scandium garnets and the obtained data is presented in Table 4. Activation energy is characterized by low values ranging from 0.029 to 0.034 eV. The obtained activation energy values, are similar to those reported in the literature, for garnets with similar chemical compositions [50]. However, it is worth noting that the available data especially for the Gd based garnets is scarce. Furthermore, the activation energy changes unevenly when increasing the amount of boron. When 1 % of boron is introduced a reduction of activation energy is observed, however further additions lead to increase in value. The changes increase of activation energy may be related to the formation of impurities. As, at 3, 5 % of boron not only the garnet but also secondary phase were observed. Overall, the addition of boron to the structure produces only minor, insignificant changes to the activation energy.

As a results in the room temperature, in different temperatures decay time of Pr^{3+} in the garnet matrix were calculated by fitting the curves using the first-order exponential equation. The values of the decay time measured using $\lambda_{ex} = 285$ nm and $\lambda_{em} = 487$ nm at different temperatures are plotted in Fig. 17. In this case, the thermal quenching of luminescence as already mentioned in the discussion of the excitation and emission spectra, is particularly visible. Upon increasing the temperature, the decay time decreases from 11 μs to 3 μs. $Gd_3Al_3Sc_2O_{12}$:1% Pr,3%B garnet decay curves are shown in Fig. 18 (the decay curves of the remaining samples are presented in supplementary material figure SM7), measured at different temperatures show a typical shape for garnet doped with Pr^{3+} ions in all temperatures. The curve shape and angle (lowest at highest temperature, and highest at lowest temperature) confirm that the thermal quenching occurs, and the obtained decay times decrease as the temperature increases.

Table 4
Praseodymium and boron doped $Gd_3Al_3Sc_2O_{12}$ activation energies.

Sample	Activation energy (eV)	R^2
$Gd_3Al_3Sc_2O_{12}$:1%Pr	0.034 ± 0.002	0.977
$Gd_3Al_3Sc_2O_{12}$:1%Pr,1%B	0.029 ± 0.003	0.936
$Gd_3Al_3Sc_2O_{12}$:1%Pr,3%B	0.033 ± 0.002	0.970
$Gd_3Al_3Sc_2O_{12}$:1%Pr,5%B	0.034 ± 0.002	0.965

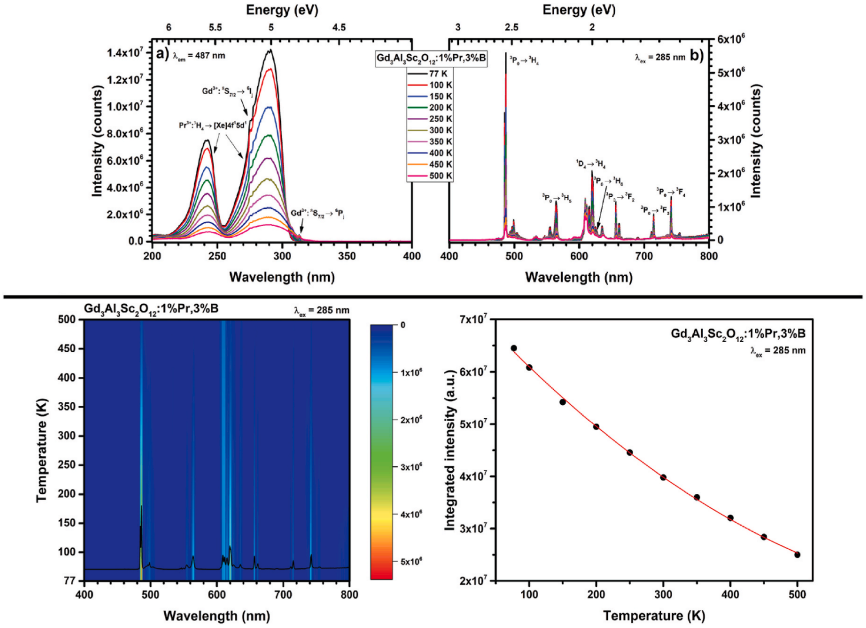

Fig. 16. a) Conventional excitation, b) emission spectra in different temperatures (top), emission heatmap and integrated intensities (bottom) of 1 % of praseodymium and 3 % of boron doped $Gd_3Al_3Sc_2O_{12}$ (integration errors are not included due to their extremely small values as compared to the measured results).

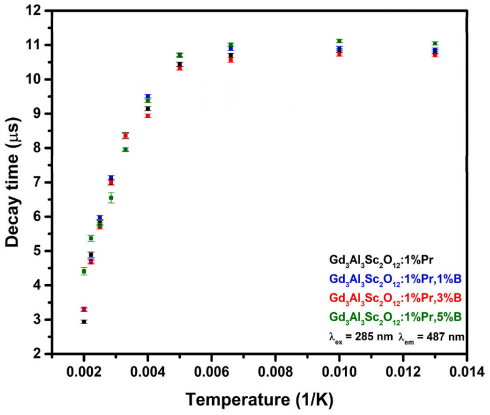

Fig. 17. Decay times at different temperatures of 1 % of praseodymium and different amounts of boron doped $Gd_3Al_3Sc_2O_{12}$.

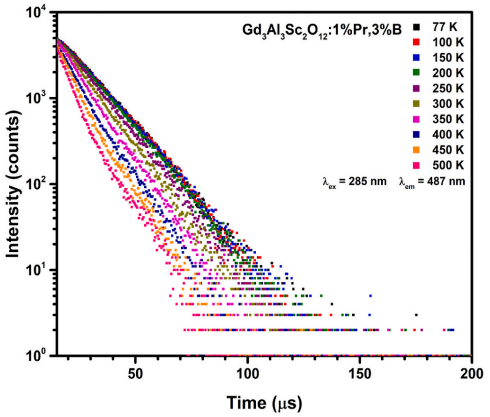

Fig. 18. Decay curves in different temperatures of 1 % of praseodymium and 3 % of boron doped $Gd_3Al_3Sc_2O_{12}$.

4. Conclusions

$Lu_3Al_5O_{12}$, $Lu_3Al_4Sc_1O_{12}$, and $Gd_3Al_3Sc_2O_{12}$ garnets doped with 1 % of praseodymium and different amounts of boron were synthesized by using an aqueous sol-gel synthesis method. All samples, except the gadolinium garnets doped with 3 and 5 % of boron, are of single phase. Furthermore, Rietveld analysis revealed that the introduction of boron led to a slight contraction of the unit cell. ICP-OES analysis in addition confirmed that all Gd^{3+} based garnets (which were doped with boron) contained an appropriate amount of B^{3+} ions, indicating the successful incorporation of the boron into the crystal structure. Boron doping may have lowered melting point of garnets, while also acting as a flux, as a result of which the particle size increased – as indicated by the SEM images and particle size distribution measurements. The luminescence measurements revealed that a larger particle size has a positive effect on the emission intensity as well. Compounds doped with boron ($Lu_3Al_4Sc_1O_{12}$:1%Pr,3%B and $Lu_3Al_4Sc_1O_{12}$:1%Pr,5%B; GdASG:1% Pr,3%B and GdASG:1%Pr,5%B) had the most intense emission under excitation by UV and X-rays. Doping with boron ions also has a positive effect on the decay time and quantum efficiency values. Increasing the boron content shortens the decay time and increases the quantum efficiency up to 87 % for $Lu_3Al_4Sc_1O_{12}$:1%Pr,5%B. Thus, it can be summarized that the doping of garnet samples with B^{3+} ions has a positive and necessary influence on the luminescent and radioluminescence properties of studied garnets. As such, the overall increase in the emission intensity, and shorter decay times are a significant improvement and could be a valuable route for the preparation of better scintillator materials for practical application.

CRediT authorship contribution statement

Greta Inkrataite: Writing – original draft, Visualization, Validation, Methodology, Investigation, Formal analysis, Data curation, Conceptualization. **Jan-Niklas Keil:** Writing – review & editing, Validation, Methodology, Data curation, Conceptualization. **Agne Kizalaite:** Writing – review & editing, Methodology, Formal analysis, Data curation. **Thomas Jüstel:** Writing – review & editing, Validation, Supervision, Investigation, Data curation, Conceptualization. **Ramunas Skaudzius:** Writing – review & editing, Visualization, Validation, Supervision, Methodology, Investigation, Formal analysis, Data curation, Conceptualization.

Declaration of competing interest

The authors declare that they have no known competing financial interests or personal relationships that could have appeared to influence the work reported in this paper.

Appendix A. Supplementary data

Supplementary data to this article can be found online at https://doi.org/10.1016/j.ceramint.2024.08.041.

References

[1] E. Matioli, C. Weisbuch, Internal quantum efficiency in LEDs, Top. Appl. Phys. (2013) 121–152, https://doi.org/10.1007/978-94-007-5863-6_6.
[2] X. Li, C. Guo, H. Wang, Y. Chen, J. Zhou, J. Lin, Q. Zeng, Green emitting $Ba_{1.5}Lu_{1.5}Al_{3.5}Si_{1.5}O_{12}:Ce^{3+}$ phosphor with high thermal emission stability for warm WLEDs and FEDs, Ceram. Int. 46 (2020) 5863–5870, https://doi.org/10.1016/j.ceramint.2019.11.037.
[3] T.C. Wang, S.Y. Yao, S.P. Yan, J. Yu, Z.Y. Deng, A.N. Yakovlev, B. Meng, J.B. Qiu, X.H. Xu, High thermal stability of copper-based perovskite scintillators for high-temperature X-ray detection, ACS Appl. Mater. Interfaces 15 (2023) 23421–23428, https://doi.org/10.1021/ACSAMI.3C02041/SUPPL_FILE/AM3C02041_SI_001.MP4.
[4] P. Schauer, O. Lalinský, M. Kučera, Overview of S(T)EM electron detectors with garnet scintillators: some potentials and limits, Microsc. Res. Tech. 84 (2021) 753–770, https://doi.org/10.1002/JEMT.23634.
[5] D.S. McGregor, Materials for gamma-ray spectrometers: inorganic scintillators, Annu. Rev. Mater. Res. 48 (2018) 245–277, https://doi.org/10.1146/annurev-matsci-070616-124247.
[6] J.W. Cates, C.S. Levin, Evaluation of a clinical TOF-PET detector design that achieves 100 ps coincidence time resolution, Phys. Med. Biol. 63 (2018), https://doi.org/10.1088/1361-6560/aac504.
[7] X. Qiu, Z. Luo, J. Zhang, H. Jiang, J. Jiang, Mechanical properties and machinability of GYGAG:Ce ceramic scintillators, Ceram. Int. 46 (2020) 4550–4555, https://doi.org/10.1016/j.ceramint.2019.10.183.
[8] C. Foster, M. Koschan, Y. Wu, C.L. Melcher, Boron codoping of Czochralski grown lutetium aluminum garnet and the effect on scintillation properties, J. Cryst. Growth 486 (2018) 126–129, https://doi.org/10.1016/j.jcrysgro.2018.01.028.
[9] R. Baba, A. Yoneyama, M. Kawamoto, Quantitative analysis of the physical properties of CsI, GAGG, LuAG, CWO, YAG, BGO, and GOS scintillators using 10-, 20- and 34-keV monochromated synchrotron radiation, Opt. Mater. Express 11 (2) (2021) 398–411, https://doi.org/10.1364/OME.409161, 398-411. 11.
[10] D. Kofanov, I. Gerasymov, O. Sidletskiy, S. Tkachenko, Y. Boyaryntseva, D. Kurtsev, O. Zelenskaya, O. Okrushko, T. Gorbacheva, O. Viagin, P. Maksimchuk, K. Lebbou, LuAG:Ce and LuYAG:Ce scintillation crystals grown under reducing conditions from W crucibles, Opt. Mater. 134 (2022) 113176, https://doi.org/10.1016/J.OPTMAT.2022.113176.
[11] D. Zhu, M. Nikl, W. Chewpraditkul, J. Li, Development and prospects of garnet ceramic scintillators: a review, J. Adv. Ceram. 11 (2022) 1825–1848, https://doi.org/10.1007/S40145-022-0660-9, 2022 1112.

[12] G. Inkrataite, J. Keil, A. Zarkov, T. Jüstel, R. Skaudzius, The effect of boron and scandium doping on the luminescence of LuAG:Ce and GdAG:Ce for application as scintillators, J. Alloys Compd. 966 (2023) 171634, https://doi.org/10.1016/j.jallcom.2023.171634.

[13] K. Kamada, M. Nikl, S. Kurosawa, Y. Shoji, J. Pejchal, Y. Ohashi, Y. Yokota, A. Yoshikawa, Growth and scintillation properties of praseodymium doped (Lu, Gd)$_3$(Ga,Al)$_5$O$_{12}$ single crystals, J. Lumin. 169 (2016) 811–815, https://doi.org/10.1016/J.JLUMIN.2015.05.057.

[14] L. Swiderski, M. Moszyński, A. Nassalski, A. Syntfeld-Kazuch, T. Szczęśniak, K. Kamada, K. Tsutsumi, Y. Usuki, T. Yanagida, A. Yoshikawa, W. Chewpraditkul, M. Pomorski, Scintillation properties of praseodymium doped LuAG scintillator compared to cerium doped LuAG, LSO and LaBr$_3$, IEEE Trans. Nucl. Sci. 56 (2009) 2499–2505, https://doi.org/10.1109/TNS.2009.2025040.

[15] L. Rößmann, F. Schröder, T. Jüstel, Effect of Gd^{3+} doping on the luminescence and up-conversion of Pr^{3+} activated Ca$_2$(Lu$_{0.99-x}$Gd$_x$Pr$_{0.01}$)Hf$_2$Al$_3$O$_{12}$, J. Lumin. 263 (2023) 120033, https://doi.org/10.1016/J.JLUMIN.2023.120033.

[16] S.V. Kuznetsov, V.S. Sedov, A.K. Martyanov, S.C. Batygov, D.S. Vakalov, K. N. Boldyrev, I.A. Tiazhelov, A.F. Popovich, D.G. Pasternak, H. Bland, S. Mandal, O. Williams, M.S. Nikova, V.A. Tarala, Cerium-doped gadolinium-scandium-aluminum garnet powders: synthesis and use in X-ray luminescent diamond composites, Ceram. Int. 48 (2022) 12962–12970, https://doi.org/10.1016/J.CERAMINT.2022.01.169.

[17] J. Li, J.G. Li, Z. Zhang, X. Wu, S. Liu, X. Li, X. Sun, Y. Sakka, Gadolinium aluminate garnet (Gd$_3$Al$_5$O$_{12}$): crystal structure stabilization via lutetium doping and properties of the (Gd$_{1-x}$Lu$_x$)$_3$Al$_5$O$_{12}$ solid solutions (x = 0-0.5), J. Am. Ceram. Soc. 95 (2012) 931–936, https://doi.org/10.1111/J.1551-2916.2011.04991.X.

[18] D.M. Revenko, O.M. Chapura, E.A. Bondarenko, L.V. Mikhnev, D.L. Gazdinsky, V. V. Mizina, V.V. Ovsyannikov, D.V. Mitrofanov, A.A. Zakharov, Influence of scandium on luminescence YSAG:Yb^{3+}, J. Phys. Conf. Ser. 1989 (2021) 012017 https://doi.org/10.1088/1742-6596/1989/1/012017.

[19] G. Inkrataite, M. Kemere, A. Sarakovskis, R. Skaudzius, Influence of boron on the essential properties for new generation scintillators, J. Alloys Compd. 875 (2021) 160002, https://doi.org/10.1016/j.jallcom.2021.160002.

[20] S. Cho, C. Yun, Y.S. Kim, H. Wang, J. Jian, W. Zhang, J. Huang, X. Wang, H. Wang, J.L. MacManus-Driscoll, Strongly enhanced dielectric and energy storage properties in lead-free perovskite titanate thin films by alloying, Nano Energy 45 (2018) 398–406, https://doi.org/10.1016/j.nanoen.2018.01.003.

[21] G. Inkrataite, A. Zabiliute-Karaliune, J. Aglinskaite, P. Vitta, K. Kristinaityte, A. Marsalka, R. Skaudzius, Study of YAG : Ce and polymer composite properties for application in LED devices, Chempluschem 85 (2020) 1504–1510, https://doi.org/10.1002/cplu.202000318.

[22] J. Grigorjevaite, A. Katelnikovas, Luminescence and luminescence quenching of K$_2$Bi(PO$_4$)(MoO$_4$):Eu^{3+} phosphors with efficiencies close to unity, ACS Appl. Mater. Interfaces 8 (2016) 31772–31782, https://doi.org/10.1021/acsami.6b11766.

[23] R.D. Shannon, IUCr, Revised Effective Ionic Radii and Systematic Studies of Interatomic Distances in Halides and Chalcogenides, vol. 32, Urn:Issn:0567-7394, 1976, pp. 751–767, https://doi.org/10.1107/S0567739476001551.

[24] L. Ding, Q. Zhang, J. Luo, W. Liu, W. Zhou, S. Yin, Preparation, structure and photoluminescence of nanoscaled-Nd:Lu$_3$Al$_5$O$_{12}$, J. Alloys Compd. 509 (2011) 10167–10171, https://doi.org/10.1016/J.JALLCOM.2011.07.083.

[25] K. Momma, F. Izumi, VESTA: a three-dimensional visualization system for electronic and structural analysis, Urn:Issn:0021-8898 41 (2008) 653–658, https://doi.org/10.1107/S0021889808012016.

[26] G. Inkrataite, A. Pakalniskis, D. Vistorskaja, R. Skaudzius, A. Kareiva, A novel sol-gel synthesis of Ca$_3$Nb$_{1.775}$Li$_{0.275}$Ga$_{2.95}$O$_{12}$ garnet, Mater. Lett. 316 (2022) 131990, https://doi.org/10.1016/J.MATLET.2022.131990.

[27] J. Ueda, S. Tanabe, Review of luminescent properties of Ce^{3+}doped garnet phosphors: new insight into the effect of crystal and electronic structure, Opt. Mater. X. 1 (2019), https://doi.org/10.1016/J.OMX.2019.100018.

[28] G. He, Y. Liu, H. Zhou, X. Chen, Sintering behavior, phase composition, microstructure, and dielectric characteristics of garnet-type Ca$_3$Fe$_2$Ge$_3$O$_{12}$ microwave ceramics, J. Mater. 9 (2023) 472–481, https://doi.org/10.1016/J.JMAT.2022.12.005.

[29] P. Maurya, R.C. Kamath, V. Gaddale Srinivas, Experimental investigation of suspension-type abrasive water jet machining of nitrile rubber for positive displacement motor applications, Int. J. Light. Mater. Manuf. 6 (2023) 367–378, https://doi.org/10.1016/J.IJLMM.2023.03.002.

[30] Y. Guo, H. Li, S. Li, L. Chen, Z. Li, Study on the structure, magnetic properties and mechanism of Zn-doped yttrium iron garnet nanomaterial prepared by the sol-gel method, Gels 8 (2022) 325, https://doi.org/10.3390/GELS8050325, 325. 8 (2022).

[31] M. Dioktyanto, A. Noviyanto, A.H. Yuwono, Influence of mechanical activation on the formation of yttrium aluminum garnet (YAG) at lower temperature, Solid State Phenom. 339 (2022) 69–75, https://doi.org/10.4028/P-98UO37.

[32] A. Katelnikovas, H. Bettentrup, D. Dutczak, A. Kareiva, T. Jüstel, On the correlation between the composition of Pr^{3+} doped garnet type materials and their photoluminescence properties, J. Lumin. 131 (2011) 2754–2761, https://doi.org/10.1016/J.JLUMIN.2011.06.012.

[33] R.J. Xie, M. Mitomo, K. Uheda, F.F. Xu, Y. Akimune, Preparation and luminescence spectra of calcium- and rare-earth (R = Eu, Tb, and Pr)-Codoped α-SiAlON ceramics, J. Am. Ceram. Soc. 85 (2002) 1229–1234, https://doi.org/10.1111/J.1151-2916.2002.TB00250.X.

[34] M.G. Brik, Fully relativistic analysis of the covalence effects for the isoelectronic 3d3 ions (Cr^{3+}, Mn^{4+}, Fe^{5+}) in SrTiO$_3$, J. Phys. Chem. Solid. 67 (2006) 856–861, https://doi.org/10.1016/j.jpcs.2005.12.006.

[35] M. Laube, T. Jüstel, On the temperature and time dependent photoluminescence of Lu$_3$Al$_5$O$_{12}$:Gd^{3+}, J. Lumin. 216 (2019) 116729 https://doi.org/10.1016/J.JLUMIN.2019.116729.

[36] N.S. M Viswanath, J. Hyeong In, H. Jun Kim, V. Hugo López-Lugo, M. Judith Rivera-Medina, J. Carlos Alonso, G. Seon Park, K. Min Kim, S. Wook Mhin, First-principles analysis of the effects of covalency and ionicity on the 4f–5d transition energy of Ce^{3+} in garnet-type oxides, ECS J. Solid State Sci. Technol. 12 (2023) 076013, https://doi.org/10.1149/2162-8777/ACE84A.

[37] A. Pakalniskis, A. Marsalka, R. Raudonis, V. Balevicius, A. Zarkov, R. Skaudzius, A. Kareiva, Sol-gel synthesis and study of praseodymium substitution effects in yttrium aluminium garnet Y$_{3-x}$Pr$_x$Al$_5$O$_{12}$, Opt. Mater. 111 (2021) 110586.

[38] G. Inkrataite, G. Laurinavicius, D. Enseling, A. Zarkov, T. Jüstel, R. Skaudzius, Characterization of GAGG doped with extremely low levels of chromium and exhibiting exceptional intensity of emission in NIR region, Cryst 11 (2021) 673, https://doi.org/10.3390/CRYST11060673, 11 (2021) 673.

[39] H.P. Labaki, F.H. Borges, F.J. Caixeta, R.R. Gonçalves, Widely dual tunable visible and near infrared emission in Pr^{3+}-doped yttrium tantalate: Pr^{3+} concentration dependence on radiative transitions from ^{3}P$_0$ to the ^{1}D$_2$, J. Lumin. 236 (2021) 118073, https://doi.org/10.1016/J.JLUMIN.2021.118073.

[40] X. Shi, Q. Wang, S. Song, X. Wang, J. Feng, H. Zhang, The influence of Pr^{3+} ions on the emission characteristics of Er^{3+}-doped YSGG single crystal fibers in the 1–3 μm wavelength range, Opt. Mater. 145 (2023) 114468, https://doi.org/10.1016/J.OPTMAT.2023.114468.

[41] R.A. Hansel, S.W. Allison, D.G. Walker, Temperature-dependent luminescence of Ce^{3+} in gallium-substituted garnets, Appl. Phys. Lett. 95 (2009) 114102, https://doi.org/10.1063/1.3216583/927332.

[42] J. Ueda, S. Tanabe, T. Nakanishi, Analysis of Ce^{3+} luminescence quenching in solid solutions between Y$_3$Al$_5$O$_{12}$ and Y$_3$Ga$_5$O$_{12}$ by temperature dependence of photoconductivity measurement, J. Appl. Phys. 110 (2011), https://doi.org/10.1063/1.3632069/990774.

[43] M. Nikl, K. Kamada, S. Kurosawa, Y. Yokota, A. Yoshikawa, J. Pejchal, V. Babin, Luminescence and scintillation mechanism in Ce^{3+} and Pr^{3+} doped (Lu,Y,Gd)$_3$(Ga,Al)$_5$O$_{12}$ single crystal scintillators, Phys. Status Solidi Curr. Top. Solid State Phys. 10 (2013) 172–175, https://doi.org/10.1002/PSSC.201200499.

[44] T. Yang, C.M.R. de Almeida, D. Han, L. Meng, J. Deng, E.L. da Silva, M.C. Santos, S. Shi, Hydrothermal synthesis and optimization of boron doped LiZr$_2$(PO$_4$)$_3$ Li-ion solid electrolyte, Appl. Surf. Sci. 474 (2019) 250–255, https://doi.org/10.1016/j.apsusc.2018.02.158.

[45] N.J. Cherepy, Z.M. Seeley, S.A. Payne, P.R. Beck, O.B. Drury, S.P. O'Neal, K. M. Figueroa, S. Hunter, L. Ahle, P.A. Thelin, T. Stefanik, J. Kindem, Development of transparent ceramic Ce-doped gadolinium garnet gamma spectrometers, IEEE Trans. Nucl. Sci. 60 (2013) 2330–2335, https://doi.org/10.1109/TNS.2013.2261826.

[46] S. Kurumada, S. Takamori, M. Yamashita, An alkyl-substituted aluminium anion with strong basicity and nucleophilicity, Nat. Chem. 12 (2020) 36–39, https://doi.org/10.1038/s41557-019-0365-z.

[47] C. Netzel, A. Knauer, M. Weyers, Impact of light polarization on photoluminescence intensity and quantum efficiency in AlGaN and AlInGaN layers, Appl. Phys. Lett. 101 (2012) 242102, https://doi.org/10.1063/1.4770364/125182.

[48] G. Muziol, H. Turski, M. Siekacz, K. Szkudlarek, L. Janicki, M. Baranowski, S. Zolud, R. Kudrawiec, T. Suski, C. Skierbiszewski, Beyond quantum efficiency limitations originating from the piezoelectric polarization in light-emitting devices, ACS Photonics 6 (2019) 1963–1971.

[49] J. Wang, K. Zhu, H. Zhou, J. Qiu, L. Ye, J. Zhang, L.G. Wang, Impacts of Ce^{3+} doping on temperature sensing characteristics of LuAG: Yb^{3+}/Ho^{3+} up-conversion fluorescent materials, J. Alloys Compd. 960 (2023) 171046, https://doi.org/10.1016/J.JALLCOM.2023.171046.

[50] J. Ueda, A. Meijerink, P. Dorenbos, A.J.J. Bos, S. Tanabe, Thermal ionization and thermally activated crossover quenching processes for 5d-4 f luminescence in Y$_3$Al$_{5-x}$Ga$_x$O$_{12}$:Pr^{3+}, Phys. Rev. B 95 (2017) 14303 https://doi.org/10.1103/PhysRevB.95.014303.

Synthesis of Praseodymium Doped Lutetium and Gadolinium Aluminum Garnets Modified by Scandium and Boron to Improve Luminescence Properties

Greta Inkrataite[1], Jan-Niklas Keil[2], Agne Kizalaite[1], Thomas Jüstel[2], and Ramunas Skaudzius[1]

[1] Institute of Chemistry, Faculty of Chemistry and Geosciences, Vilnius University, Naugarduko 24, LT-03225 Vilnius, Lithuania
[2]Department of Chemical Engineering, FH Münster University of Applied Sciences, Stegerwaldstrasse 39, D-48565 Steinfurt, Germany

SUPPLEMENTARY MATERIAL

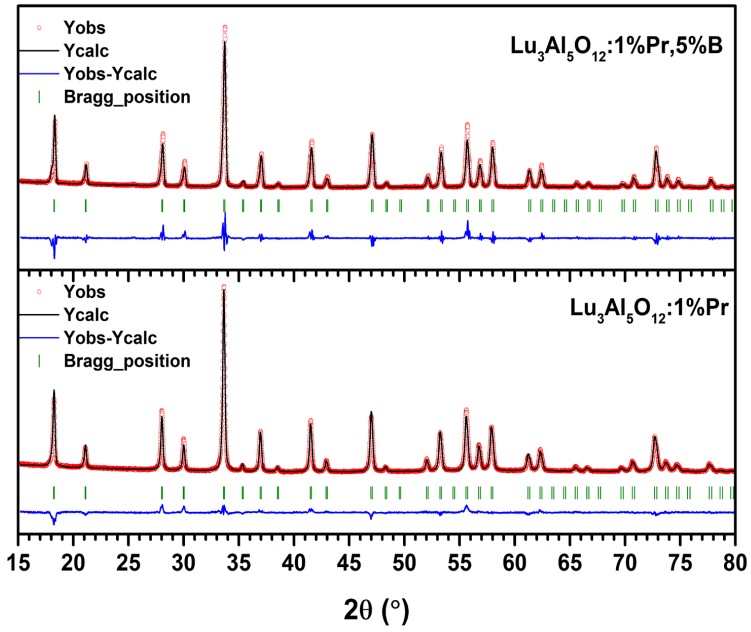

Figure SM1. Rietveld refinement results of XRD data recorded for Pr^{3+} and B^{3+} doped $Lu_3Al_5O_{12}$ at room temperature (red dots are the experimental data; black lines are calculated data), Bragg reflections are indicated by vertical ticks.

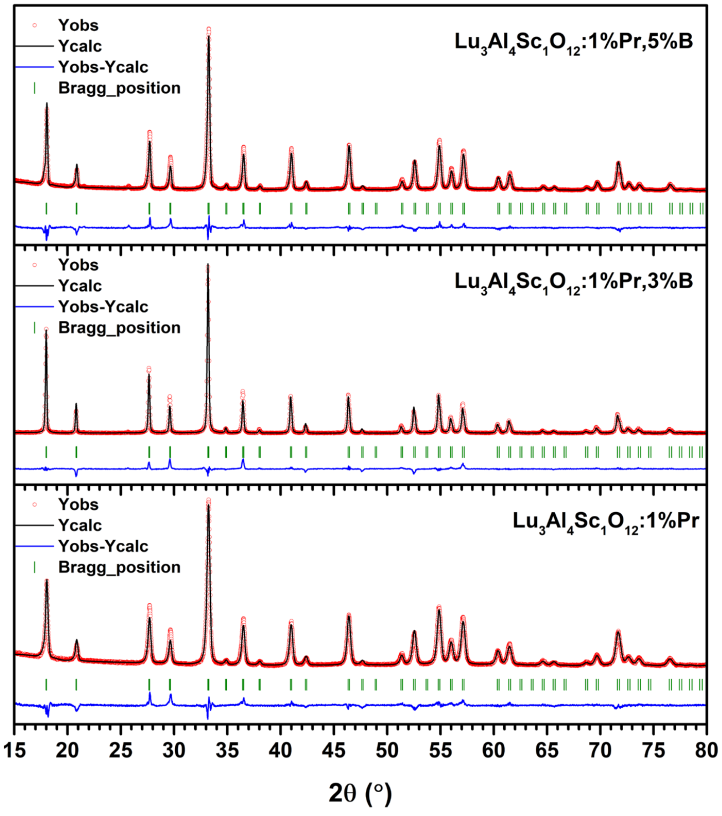

Figure SM2. Rietveld refinement results of XRD data recorded for Pr^{3+} and B^{3+} doped $Lu_3Al_4Sc_1O_{12}$ at room temperature (red dots are the experimental data; black lines are calculated data), Bragg reflections are indicated by vertical ticks.

Table SM1. Rietveld refinement results.

Sample	Unit cell parameter A (Å)	R_p	R_{wp}	R_{exp}
$Lu_3Al_5O_{12}$:1%Pr	11.914(3)	4.61	6.01	4.03
$Lu_3Al_5O_{12}$:1%Pr,5%B	11.900(2)	6.62	9.15	4.02
$Lu_3Al_4Sc_1O_{12}$:1%Pr	12.068(2)	5.06	6.73	3.90
$Lu_3Al_4Sc_1O_{12}$:1%Pr,3%B	12.067(4)	7.92	11.2	4.54
$Lu_3Al_4Sc_1O_{12}$:1%Pr,5%B	12.059(9)	5.69	7.51	3.67
$Gd_3Al_3Sc_2O_{12}$:1%Pr	12.330(8)	3.32	4.29	4.80
$Gd_3Al_3Sc_2O_{12}$:1%Pr,1%B	12.330(8)	8.17	10.40	7.31
$Gd_3Al_3Sc_2O_{12}$:1%Pr,3%B	12.329(8)	3.84	5.30	4.00
$Gd_3Al_3Sc_2O_{12}$:1%Pr,5%B	12.327(9)	3.53	4.67	4.38

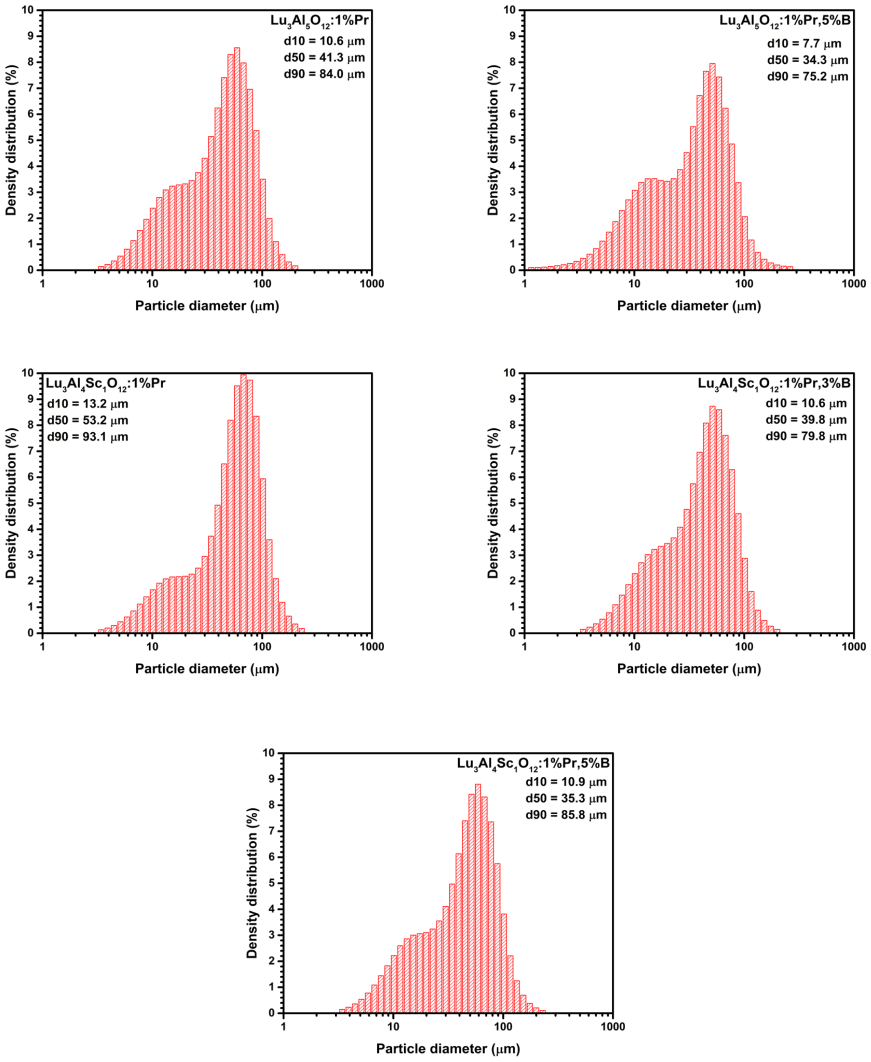

Figure SM3. Particles size histograms of 1 % Pr^{+3} and different amount of B^{+3} doped $Lu_3Al_5O_{12}$ and $Lu_3Al_4Sc_1O_{12}$ garnet powder samples.

Table SM2. Calculated band gap energies for synthesized samples.

Sample	Band gap energy (eV)
$Lu_3Al_5O_{12}$:1%Pr	4.096
$Lu_3Al_5O_{12}$:1%Pr,5%B	4.105
$Lu_3Al_4Sc_1O_{12}$:1%Pr	1.146
$Lu_3Al_4Sc_1O_{12}$:1%Pr,3%B	4.160
$Lu_3Al_4Sc_1O_{12}$:1%Pr,5%B	4.132
$Gd_3Al_3Sc_2O_{12}$:1%Pr	4.031
$Gd_3Al_3Sc_2O_{12}$:1%Pr,1%B	4.033
$Gd_3Al_3Sc_2O_{12}$:1%Pr,3%B	4.055
$Gd_3Al_3Sc_2O_{12}$:1%Pr,5%B	4.059

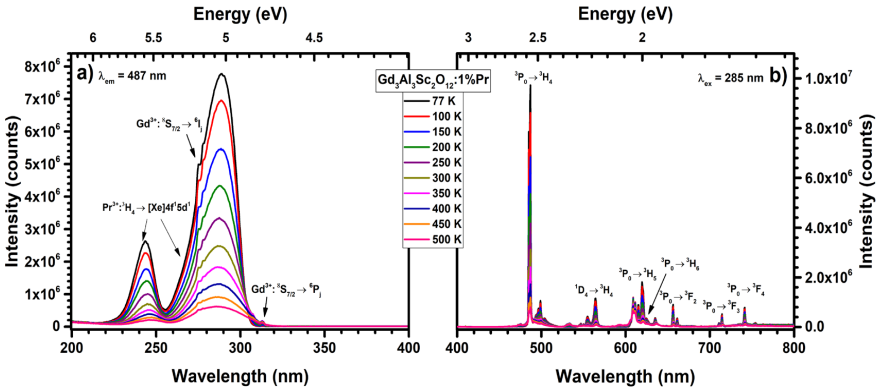

Figure SM4. Temperature dependency emission (b) and excitation (a) of 1 % praseodymium doped $Gd_3Al_3Sc_2O_{12}$.

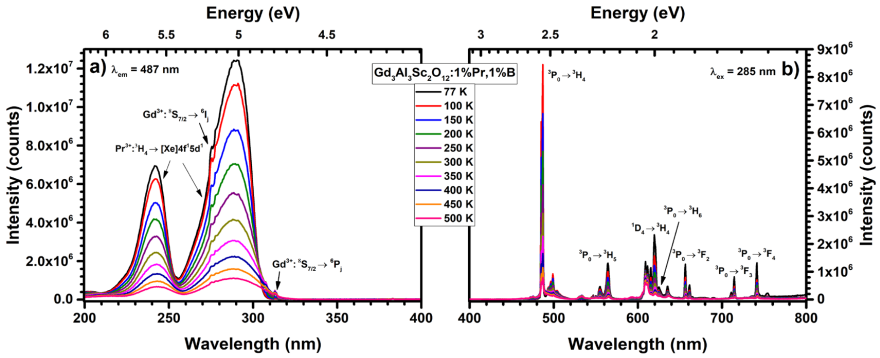

Figure SM5. Temperature dependency emission (b) and excitation (a) of 1 % praseodymium and 1 % boron doped $Gd_3Al_3Sc_2O_{12}$.

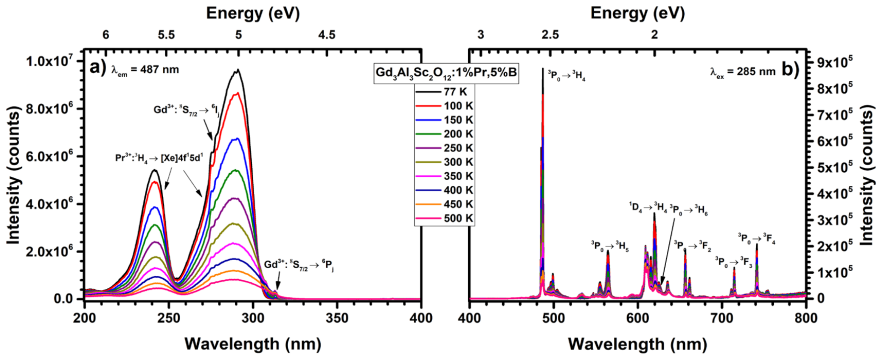

Figure SM6. Temperature dependency emission (b) and excitation (a) of 1 % praseodymium and 5 % boron doped $Gd_3Al_3Sc_2O_{12}$.

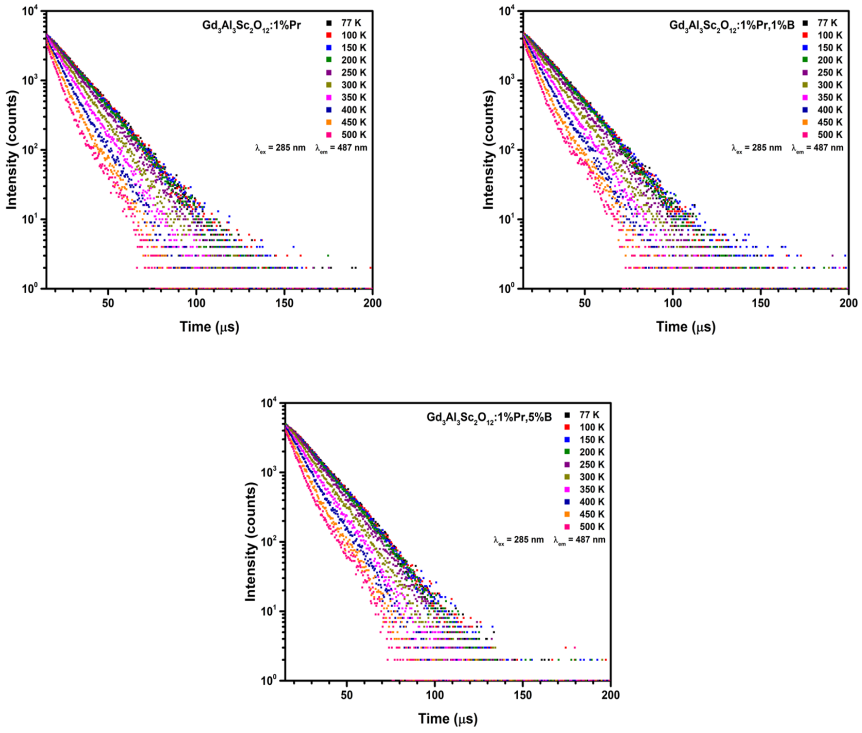

Figure SM7. Temperature dependency decay curves of 1 % praseodymium and different amounts of boron doped $Gd_3Al_3Sc_2O_{12}$.

Vilniaus universiteto leidykla
Saulėtekio al. 9, III rūmai, LT-10222 Vilnius
El. p. info@leidykla.vu.lt, www.leidykla.vu.lt
bookshop.vu.lt, journals.vu.lt
Tiražas 20 egz.